Title
Plasma Diagnostics and Plasma-Surface Interactions in Inductively Coupled Plasmas

Author
Titus, Monica Joy

Publication Date
2010

Plasma Diagnostics and Plasma-Surface Interactions in Inductively Coupled Plasmas

by

Monica Joy Titus

A dissertation submitted in partial satisfaction of the

requirements for the degree of

Doctor of Philosophy

in

Chemical Engineering

in the

Graduate Division

of the

University of California, Berkeley

Committee in charge:

Professor David B. Graves, Chair
Professor Roya Maboudian
Professor Michael A. Lieberman

Spring 2010

Plasma Diagnostics and Plasma-Surface Interactions in Inductively Coupled Plasmas

Abstract

Plasma Diagnostics and Plasma-Surface Interactions in Inductively Coupled Plasmas

By

Monica Joy Titus

Doctor of Philosophy in Chemical Engineering

University of California, Berkeley

Professor David B. Graves, Chair

The semiconductor industry's continued trend of manufacturing device features on the nanometer scale requires increased plasma processing control and improved understanding of plasma characteristics and plasma-surface interactions. This dissertation presents a series of experimental results for focus studies conducted in an inductively coupled plasma (ICP) system. First novel "on-wafer" diagnostic tools are characterized and related to plasma characteristics. Second, plasma-polymer interactions are characterized as a function of plasma species and processing parameters. Complimentary simulations accompany each focus study to supplement experimental findings.

Wafer heating mechanisms in inductively coupled molecular gas plasmas are explored with PlasmaTemp^{TM}, a novel "on-wafer" diagnostic tool. Experimental wafer measurements are obtained with the PlasmaTemp^{TM} wafer processed in argon (Ar) and argon-oxygen (Ar/O_2) mixed plasmas. Wafer heating mechanisms were determined by combining the experimental measurements with a 3-dimensional heat transfer model of the wafer. Comparisons between pure Ar and Ar/O_2 plasmas demonstrate that two additional wafer heating mechanisms can be important in molecular gas plasmas compared to atomic gas discharges. Thermal heat conduction from the neutral gas and O-atom recombination on wafer surface can contribute as much as 60 % to wafer heating under conditions of low-energy ion bombardment in molecular plasmas.

Measurements of a second novel "on-wafer" diagnostic sensor, the PlasmaVolt^{TM}, were tested and validated in the ICP system for Ar plasmas varying in power and pressure. Sensor measurements were interpreted with a numerical sheath simulation and comparison to scaling laws derived from the inhomogeneous sheath model. The study demonstrates sensor measurements are proportional to the RF-current through the sheath and the scaling is a function of sheath impedance. PlasmaVolt^{TM} sensor measurements are proportional to the square root of the plasma density at the plasma-sheath interface, one-fourth root of the electron temperature, and one-fourth root of the RF bias voltage under conditions where the sheath is predominantly capacitive. When the sheath impedance becomes increasingly resistive, the sensor measurements deviate from the scaling law and tend to be directly proportional to the plasma density.

Vacuum ultraviolet (VUV) emissions in Ar ICPs are characterized and the chemical and physical modifications to 193 nm photoresist (PR) polymer materials processed in Ar ICPs are investigated. Fourier transform infrared (FTIR) transmission measurements as a function of VUV photon fluence demonstrate that VUV-induced bond breaking occurs over a period of time. A numerical model demonstrates that VUV photons deplete near-surface O-containing bonds, leading to deeper, subsequent penetration and more bond losses, while the remaining near-surface C–C bonds absorb the incident radiation and slow VUV photon penetration.

The roughening mechanism of blanket and patterned 193 nm PR samples are explored in a well characterized Ar ICP. FTIR and atomic force microscopy (AFM) analysis of plasma processed 193 nm PR suggests that ion-induced generation of a graphitized layer at high energies, combined with VUV bulk modification of 193 nm PR may initiate PR roughening. The roughness of blanket samples increases as a function of VUV fluence, ion energy, and substrate temperature. Line width roughness (LWR) measurements of patterned samples demonstrate a similar trend suggesting that LWR may correlate with surface roughness of patterns. The results are compared to PR studies previously conducted in an ultra-high vacuum beam system demonstrating that the vacuum beam system is a useful tool that can deconvolute and simplify complex plasma systems.

To my mom, dad, and brother.

Table of Contents

List of Figures

Chapter 1

Chapter 2

Chapter 3

Chapter 4

Chapter 5

Chapter 6

Chapter 7

Chapter 8

Appendix A

Appendix B

Appendix C

List of Tables

Chapter 1

Chapter 3

Chapter 4

Chapter 5

Chapter 6

Chapter 7

Chapter 8

Appendix A

Appendix B

Appendix C

Appendix D

Appendix E

Acknowledgements

The number of people who have helped me with this endeavor over the past five years here at Berkeley is overwhelming and I find myself feeling very fortunate to have been surrounded by such supportive and inspiring family and friends.

First I would like to thank my advisor, David Graves, for allowing me the opportunity to study in his research group and to work on such novel, challenging, and industry relevant projects. Without his continued guidance and encouragement to steer me through my mental roadblocks, this work would not have been possible. I have been inspired by his enthusiasm for pursuing new ideas and have learned what it means to be a good researcher.

I'd also like to thank Cheng-Che Hsu for teaching me everything about the ICP system; his guidance was instrumental in providing me with the fundamental knowledge that I would use in all of my future experimental studies. In addition I would like to thank John Coburn, Harold Winters, and Dave Fraser for their expertise and insights. On numerous occasions I would find myself turning to them for advice whenever I'd be modifying or trouble-shooting the ICP system and designing new experimental setups.

The Graves' group – past and present – have made this research experience most memorable. The antics that ensued in our lab, the laughs that we've shared, and the disasters that we've survived have made working two floors underground, in the dungeon, more tolerable than it would have been otherwise.

Thank you to all of my friends – new and old – who listened to me gripe, provided entertainment, and kept me relatively sane. I won't list you all for fear of forgetting someone, but please know that without the dinners, dancing, hiking, shopping sprees, sight-seeing, and game nights I would not have survived.

Last, but not least, I'd like to thank my parents, Mark and Mieko, and my brother, Marcus. Their continued love and support have made this journey possible. Words cannot describe how much I've missed home, but their encouragement always lifted my spirits and motivated me to achieve my goal. This accomplishment is ours to share. I love you all.

Chapter 1 – Introduction

1.1 The Semiconductor Industry

Every two years the number of transistors on a microprocessor doubles while the critical dimensions (CD) of these features shrink by 0.7 times. This trend is known as Moore's law and is the primary source of motivation for the semiconductor industry. As a result, engineers manufacture more dies per wafer, on increasingly larger wafers, at a reduced cost. In addition, shrinking CDs have increased the number density of features to the hundreds of millions. As transistors are packed more densely, they leak less energy, produce less heat and switch faster. Thus consumers benefit in purchasing inexpensive microprocessors that run faster, use less power, and are more energy-efficient.

Key changes in the fabrication of these small features (i.e. transistors) have allowed the semiconductor industry to keep pace with Moore's law and develop technology nodes now on the nanometer (nm) scale. Technological and material changes were made in the photolithography, or patterning, step including the development and use of new photoresists and light sources. Simultaneously, technological changes in the etching, or pattern transfer, step including the use of plasmas were initiated, and has also allowed for fabrication of densely packed, nanometer-scale features. However, it is growing increasingly difficult to keep pace with Moore's law as the features are nearing the 22 nm technology node where transistor gate lengths are on the order of 15 nm[1]. High quality pattern transfer of these small features will require more stringent control of processing variables in the photolithography and etching steps and a better understanding of plasma-wafer interactions. Both experimental and modeling studies of plasma-surface interactions will become invaluable as engineers seek solutions to increasingly complex challenges in manufacturing high-quality, low-cost devices.

1.2 Photolithography

Photolithography is a series of steps used to pattern integrated circuits, comprised of numerous features often tens of nanometers in dimension. First, a film (e.g. metal) is deposited on the substrate surface (Figure 1.1a) and is then followed by photoresist (PR) deposition (b). The PR is optically irradiated through a patterned mask (c) with a light source of specified wavelength. The exposed area is then developed away by chemical means (d). The pattern left in the PR, is transferred to the underlying film by a subsequent etching process. Traditionally, etching was accomplished by dipping the substrate into a liquid bath where a vigorous chemical reaction between the liquid and exposed material yields the feature shape. The pattern, however is not faithfully transferred because the chemical reaction etches in all directions at the same rate (isotropic etching)[2]. This may result in feature undercutting (e). In the past when typical feature dimensions were several micrometers in length significant undercutting could occur without severely affecting device performance. However, current nanometer-scale features are so densely packed that undercutting can lead to electronic interference between adjacent features, and ultimately device failure. Thus, anisotropic etching (f) is essential for high quality pattern transfer and is accomplished with a plasma etching tool.

Significant changes in photolithography technology have allowed the semiconductor industry to keep pace with Moore's law, including changes in the light sources used during optical exposure. Photolithographers observed that shorter light wavelengths improved the resolution of small features; therefore wide-band light sources of constant illumination were preferentially replaced with Hg-arc lamps (emitting wavelengths at 436 nm and 365 nm) for patterning micrometer length-scale features (Table 1.1). Eventually Hg-arc lamps were replaced with KrF (248 nm) and ArF (193 nm) excimer laser light sources for patterning nanometer length-scale features[3].

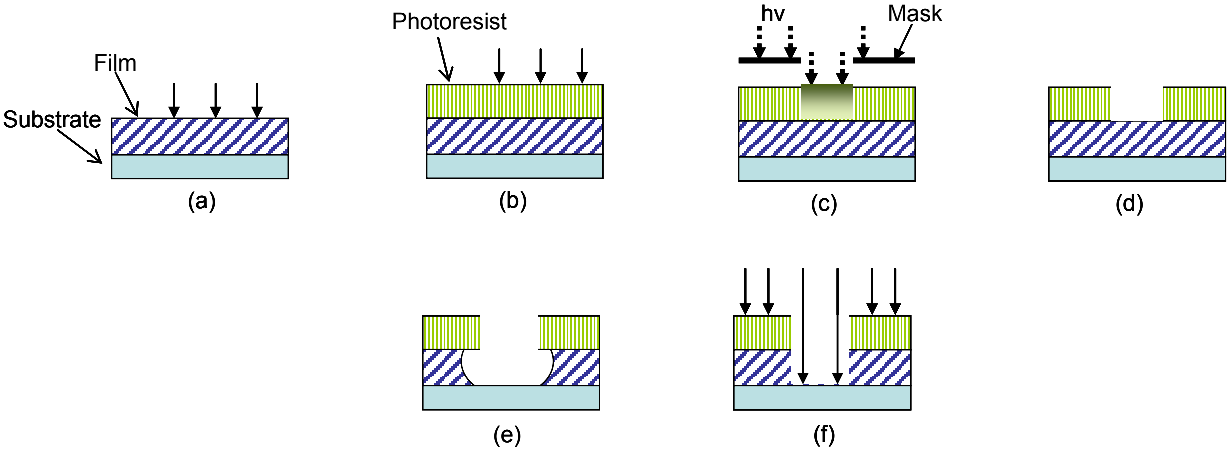

Figure 1.1: Photolithography steps: (a) Film deposition; (b) Photoresist deposition; (c) Optical exposure through a mask; (d) Photoresist development; (e) Chemical etching progress, leading to poor pattern transfer; (f) Anisotropic plasma etching

The change to lower wavelengths was accompanied by a change in photoresist (PR) chemistry. With Hg-arc lamps, features were patterned with diazonaphthoquinone (DNQ) PRs. However, for patterning with KrF excimer light sources, all of the photons (300 – 450 nm) necessary for photo-induced reactions in the PR were not available. Photolithographers were required to enhance the photoreactions by changing the polymer chemistry and this resulted in the chemically amplified 248 nm PR. With the use of ArF excimer lamps, 248 nm PR proved unsuitable as it was far too absorbent of 193 nm wavelength light. The PR chemistry required increased concentrations of oxygen to reduce the absorbency of 193 nm light; 193 nm PR resulted[3]. Ultimately, the change to ArF excimer lasers and 193 nm PRs, combined with other resolution enhancement techniques[4], allowed photolithographers to pattern features down to 10's of nanometers in the PR layer.

193 nm PRs processed in plasmas during the etch step, however, unfortunately undergo severe chemical and physical modification, causing enhanced roughness of the PR[5, 6]. The degradation of the PR (on the nanometer scale) prevents faithful pattern transfer to the underlying materials and that may result in device failure[7]. This is of increasing concern as CDs continue to shrink beyond the 32 nm technological node. The mechanism of 193 nm PR degradation in plasma processing environments is not well understood and is the focus of many experimental studies in an effort to develop treatment or prevention recipes[5-13].

Table 1.1 Evolution of light sources and photoresist materials used in patterning device features.

Time Line	Device Minimum Feature	Light Source	Photoresist	Structure
~'85 - ~'95	1000 nm – 350 nm	Hg-arc lamp	DNQ PR	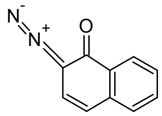
~'95 - ~'00	350 nm – 130 nm	KrF excimer laser	248 nm PR	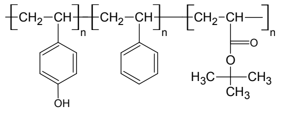
~'00 - present	130 nm – 22 nm	ArF excimer laser	193 nm PR	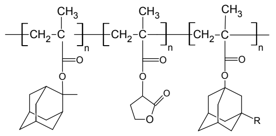

1.3 Plasma Discharges

Plasma discharges are utilized for anisotropic etching during pattern transfer. A plasma is a partially ionized gas consisting of several components, including ions, electrons, neutrals, and radicals. Many of the plasmas used in the etching process are weakly ionized; the ionization fraction, $x_i << 1$, therefore the ion (n_i) and electron (n_e) densities ($\sim 10^9 - 10^{12}$ cm^{-3}) are magnitudes lower than the neutral gas density (n_g). The bulk plasma, though, is considered quasi-neutral as $n_i \approx n_e$. Both elastic and inelastic collisions take place between all species in the plasma. One of the more important collision reactions is the electron-atom ionization: $e^- + X \rightarrow 2e^- + X^+$. This leads to a collision cascade where the reaction generates two electrons per collision that can in turn react and produce additional electrons. This reaction scheme is important in sustaining the plasma. However, only electrons that have energies greater than the ionization energy (ε_{iz}) and dissociation energy (ε_{diss}) can ionize an atom or dissociate a molecule, respectively. The electron energy is dependent upon the electron energy distribution function (EEDF) and is a function of the plasma operating condition.

A plasma is generated inside a typical etch tool by feeding electrical power into a gas[2]. One common etch tool is the inductively coupled plasma (ICP) etch tool typically used for etching processes that define the gate-electrode region. A simple schematic of an ICP is shown in Figure 1.2. A radio-frequency (RF) current is driven through the coils above the dielectric window at the top of the chamber. This couples the inductive field to the plasma[2]. Power transferred from the fields to the few free electrons initially within the gas excites the electrons to higher energies. These high energy electrons can then ionize the neutrals and initialize the collision cascade, thus creating and sustaining the plasma.

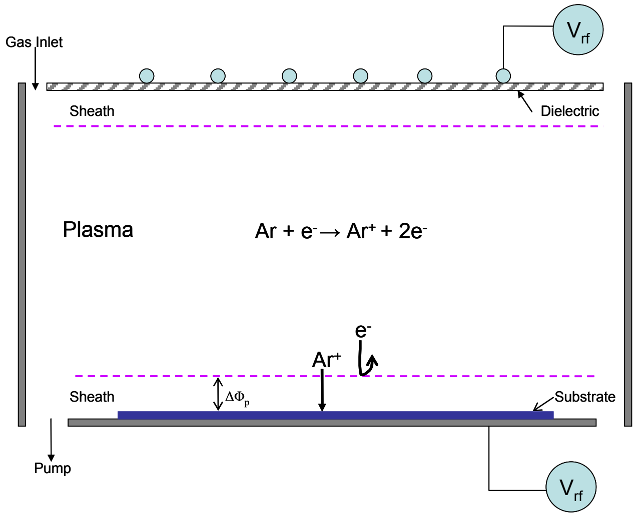

Figure 1.2 Schematic of an inductively coupled plasma (ICP) etch tool. Power is deposited through coils above a dielectric window, generating bulk plasma (of density n_e) and sheath regions. Bias voltages to the lower electrode control ion bombarding energies.

Initially within the system, the electrons rapidly move throughout the chamber and are lost to the walls, as opposed to the slower (heavier) ions. In order to maintain quasi-neutrality, i.e. an equal net flow of ions and electrons toward a surface, a confining potential (Φ) forms. This potential acts to repel the electrons back to the bulk, while accelerating the ions toward the walls, and ultimately forms a region of net positive charge: the sheath[2, 14]. The sheath thickness is on the order of a few Debye lengths, typically a few millimeters. The ion acceleration energy is typically 10 – 40 V, which is equivalent to the dc plasma potential (Φ_p). One of the key features of an ICP tool is the ability to control the ion energy by separately biasing the lower electrode where the substrate sits. Biasing the lower electrode increases the potential drop within the sheath. An ion falling through this potential drop will bombard the substrate surface with the equivalent potential drop energy[15], i.e. an ion falling through a 1 V potential drop gains 1 eV in kinetic energy. Therefore, in a low pressure system (collisions between species are minimized in the sheath) where the substrate is negatively biased, anisotropic etching can be accomplished.

1.4 Plasma & Wafer Diagnostics – Metrology

Although high-quality pattern transfer is more readily accomplished with a plasma etching tool, obtaining uniform pattern transfer across 200 – 300 mm diameter wafers is extremely challenging because practical control of these systems requires tuning of a number of process parameters, such as power, pressure, chemistry, and flow rates. A change in a single parameter may result in numerous changes to how plasma species behave and interact with the substrate. Automated control schemes are often very complicated and require several diagnostic tools to monitor both the plasma and wafer product[16-18]. Plasma and wafer diagnostic tools may be available in-line, *in-situ*, and *ex-situ* where each type of metrology has its respective merits and drawbacks.

1.4.1 Wafer Diagnostics

Traditionally, examination of wafer response to process control parameters of plasma etching tools used monitor or dummy wafers. These are a series of wafers inserted into production flow in place of production grade wafers and typically comprise 20 – 40 % of a fab’s total throughput[17, 19]. Once a monitor wafer is processed, *ex-situ* metrology such as scanning electron microscopy (SEM), spectrophotometry, and spectroscopic ellipsometry is employed to determine critical feature dimensions, film thickness, and etching uniformity (Table 1.2)[20, 21]. The advantages of these *ex-situ* monitoring techniques are the high-degrees of accuracy and ability to directly measure the wafer change in response to plasma processing conditions. Unfortunately, these post-processing analysis techniques are time consuming and delays in monitor-wafer characterization may prevent timely detection and correction of drifting processes.

There is a large trend towards *in-situ* and in-line metrology to complement monitor wafers for wafer processing and tool control. *In-situ* and in-line metrology employs diagnostic tools that are physically built or attached to the plasma etch tool. For example, the devices may be present in the load/lock chamber for pre or post processing measurements or mounted on the reactor wall. In-line sensors that monitor the wafer are categorized as “wafer state” sensors[22]. A wafer state sensor monitors changes directly observed on the wafer surface, such as etch rates or film thickness. Examples of such sensors include but are not limited to reflectometers, ellipsometers, and scatterometers (Table 1.2)[16, 21, 23]. The benefits of in-line metrology include improved process monitoring, reduced product variance, and higher throughput[19]. The drawback is that the entire wafer cannot be monitored and observed measurements (e.g. etch rate) are for single locations. Furthermore, due to design restrictions or financial limitations, installation of in-line "wafer-state" sensors are not always practical.

An alternative to monitor wafers and in-line "wafer-state" sensors are a new metrology tool called "on-wafer" sensors. These are wafers with sensors embedded onto the wafer surface, capable of measuring wafer parameters (e.g. temperature) at different radial positions (Table 1.2). These sensors wafers are inserted into production flow along with product wafers and act as autonomous measuring devices capable of capturing the temporal evolution of wafer processing states in real time. Real time, *in-situ* measurements at the wafer level improves diagnostic capabilities without requiring any integration of additional equipment to the plasma etching tools, saving both time and operational expenses[19, 24]. Furthermore, establishing the temporal and spatial evolution of wafer-surface will allow for more finely tuned control of the processing equipment. This will be necessary as feature dimensions continue to grow smaller and more compact.

1.4.2 Plasma Diagnostics

Monitoring plasma response to process control parameters, such as pressure, power, and flow rate are important since wafer uniformity can be controlled, for example, with the resulting etching rates or deposition rates. Therefore, there is a large effort to measure bulk plasma characteristics with traditional, in-line and *in-situ* techniques, or with new emerging technology "on-wafer" sensors.

Bulk plasma characteristics such as electron density and temperature are typically monitored with in-line or *in-situ* metrology tools. Similar to the "wafer-state" metrology tools, these diagnostic tools are mounted in or on the chamber and are called "process state" sensors. The process state sensor monitors the plasma's response to changes in the process control parameters; e.g. they may detect gas phase reactants and product species, bulk temperatures and densities, with residual gas analyzers (RGA), optical emission spectrometers (OES) or Langmuir probes, respectively[23, 25-28](Table 1.3). The benefits of in-line metrology include improved real-time monitoring of the plasma that reduces product variance and increases throughput[19]. Again, however, the metrology may be limited to line-of-sight measurements and may not directly account for the spatial variation across the plasma tool.

"On-wafer" sensors are also used to monitor the plasma in addition to wafer response. These "on-wafer" sensors have the potential to measure plasma characteristics, such as electron density, above the wafer surface, providing information on both the temporal and spatial variation of the plasma[29]. As this is yet an emerging technology, much study of these sensors is required. However, use of these sensors to couple plasma characteristics to sensor measurements will give significant insight on how to control a plasma etch tool for a desired wafer result.

Table 1.2 *Ex-situ*, *in-situ*, and “on-wafer” diagnostic tools for wafer characterization.

Method	**Wafer Feature/Variable**	**Diagnostic Tool**
Ex-situ	Surface Morphology	Atomic Force Microscopy
	Critical Dimensions	Scanning Electron Microscopy,
	Film Thickness	Waveguide-mode Spectroscopy[23]
		X-ray Photo Spectroscopy[23]
In-situ	Film Deposition	Ellispometry[21,30]
	Etching Rate	Interferometry[16,17]
	End Point Detection	Reflectometry[17,21]
		Optical Emission Spectroscopy[16,31]
		Fourier-Transform Infrared Spectroscopy[23]
		Quadrupole Mass Spectroscopy/Residual Gas Analyzer[16,22,31,32]
		Quartz-Crystal Microbalance[23]
On-Wafer	Etching Rate	Micromachined Reactive Ion Etching Sensor[16]
	Wafer Temperature	PlasmaTemp™ [24,33]
	Surface Charge	Charge Sensor: micromachined cantilever beam[34]

Table 1.3 *In-situ*, and “on-wafer” diagnostic tools for plasma characterization.

Method	**Wafer Feature/Variable**	**Diagnostic Tool**
In-line & *In-situ*	Ion Current/Flux	Ion (electrostatic) Probe[25]
		Langmuir Probe[15]
	Plasma Photo-emissions	Optical Emission Spectroscopy[35]
		Vacuum Ultraviolet Spectroscopy[36]
	Electron Density	Langmuir Probe[37-40]
		Microwave Interferometer[41]
		Spectroscopy[39]
	Electron Temperature	Langmuir Probe[37-40]
	Electron Energy Distribution	Langmuir Probe[37-40]
	Ion Energy Distribution	Gridded Ion Energy Analyzer[15]
		Mass Spectroscopy with ion energy analyzer[15]
	Neutral Gas Temperature	Optical Emission Spectroscopy[28]
	Plasma Species (mass & flux)	Mass Spectroscopy/Residual Gas Analyzer[2,15,16]
		Optical Emission Spectroscopy[28]
On-Wafer	Radio-Frequency Currents	PlasmaVolt™[29]
	Ion Current/Flux	PlasmaPilot™
		Ion Flux Sensors (double-probe version)[42-44]
	Plasma Photo-emissions	PlasmaLux™
		LED Sensors[45,46]

1.5 Numerical Modeling

The complexities of plasma discharges are extensive, covering a range of topics from gas-phase kinetics, mass and heat transport, and plasma chemistry. It is clear from experimental studies that a deeper understanding of plasma discharges and improvement of process control requires investigation of time and space variations. Thus numerical models of plasmas and plasma-surface interactions are of increasing importance as engineers strive to improve fabrication of nanometer-scale devices.

Fluid[47], finite element[48], and particle-in-cell simulations have been widely used to study bulk plasma physics in inductively coupled and capacitively coupled discharges[2]. The effects of process control parameters such as power and pressure on electron energy distribution functions[49], recombination rates of species on surfaces[47], and formation of concentration and thermal gradients have been investigated. Increasingly, plasma-surface interactions are simulated to study the effects of bulk plasma characteristics on the wafer surface. For example, sheath simulations are a useful tool in studying ion energy distributions[50], ion currents and trajectories[51], and potential drops[52], which can directly impact etching rates and wafer uniformity. Lastly, as feature density increases and critical dimensions shrink, the capability to control the evolution of patterns in plasma discharges is of increasing interest. Many simulation studies model profile evolution and the effects of ion angles and deposition and recombination of species on the patterns[53]. Feature evolution can also be investigated on the microscopic level with molecular dynamic simulations[54].

1.6 Thesis Outline

This dissertation work focuses on plasma and wafer diagnostics as a method to improve understanding of process control parameter effects on bulk plasma characteristics and wafer response. Three focus studies using a combination of experimental work in an inductively coupled plasma and numerical simulations will be presented. The first two focus studies will concentrate on a novel technology, "on-wafer" sensors. The third focus study examines plasma-surface interactions and will concentrate on 193 nm photoresists processed in inductively coupled plasmas. Chapter 2 provides an overview of the experimental apparatus and diagnostic tools utilized in all of the focus studies. In addition, Chapter 3 provides data analysis techniques and characterizes an Ar ICP that may be of use for future users of the inductively coupled plasma chamber and its accompanying diagnostic tools.

1.6.1 "On-wafer" Sensors

Recent commercial developments now provide a powerful platform – "on-wafer" sensors – that allows quasi-real time and *in-situ* measurements of plasma and wafer characteristics. Because this technology is relatively new, much work remains to develop truly reliable sensors that can relate sensor measurements to plasma dynamics and process control variables. However, it can be readily anticipated that this technology will be the new front in wafer and plasma metrology with the ultimate goal of developing sensors capable of measuring feature etching rates and feature profile evolution.

Two commercially manufactured "on-wafer" sensors, the PlasmaTemp^{TM} and PlasmaVolt^{TM}, are investigated and the results are coupled with numerical simulations of an inductively coupled plasma, sheath, and wafer heat-transport in order to increase confidence in and understanding of the experimental measurements. The objective was to correlate sensor measurements to plasma characteristics (such as ion flux and electron density) and to process control parameters (such as power and bias voltages). Both qualitative and quantitative agreement between sensor measurements and numerical simulations demonstrate that "on-wafer" sensors are powerful diagnostic tools that can be interpreted to yield much more than face-value measurements.

Specifically, Chapter 4 will focus on the PlasmaTemp^{TM} studies and address wafer heating mechanisms in inductively coupled, molecular-gas plasmas. Chapter 5 will focus on the PlasmaVolt^{TM} studies and demonstrate that sensor measurements can be coupled to plasma density. Appendices A and B contain supplemental experimental data and simulation user guides for the PlasmaTemp^{TM} and PlasmaVolt^{TM} focus studies, respectively. In addition, Appendix C outlines a numerical simulation of the ICP system used to study Ar and Ar/O_2 plasma discharges in the PlasmaTemp^{TM} study and outlines the modifications made to study the generation of Ar-metastable species.

1.6.2 193 nm Photoresist

Current photolithography standards use ArF excimer lasers and 193 nm photoresist (PR) for patterning features on the nanometer scale. Research has shown that 193 nm PRs processed in plasmas during the etch step are less etch resistant and experience significant chemical and physical modification[5, 55-58]. The degradation and roughening of 193 nm PR is of increasing concern as the roughness prevents the pattern from being faithfully transferred to the underlying layer and is increasingly becoming of the same order as the feature size. Many studies have explored the cause of 193 nm PR roughening and have attributed it to synergistic effects between energetic ion bombardment and vacuum ultraviolet (VUV) photon irradiation[6, 10].

Chapter 6 characterizes the VUV emissions from an inert Ar plasma and measures the effects on 193 nm PR. Chapter 7 presents a numerical simulation modeling the VUV photoabsorption behavior of 193 nm PR. Chapter 8 focuses on the synergistic roughening effects due to VUV photons and ions, and effects of varying process control parameters. A roughening mechanism for 193 nm PR is proposed. Appendix C also contains updates to the ICP numerical model that allows for monitoring of both metastable and resonance states of Ar. Comparison between experimental and simulated VUV fluxes are demonstrated.

Chapter 2 – The Inductively Coupled Plasma System & Diagnostic Tools

2.1 Abstract

This chapter will introduce the reader to the inductively coupled plasma system used in these studies, along with the installed diagnostic tools that allow for plasma characterization. Diagnostic tools include a wall-mounted ion current probe, an optical emission spectrometer (OES), a vacuum ultraviolet (VUV) spectrometer, an ion mass spectrometer (IMS), an appearance potential mass spectrometer (APMS), a quartz-crystal microbalance (QCM), and a Langmuir probe. Data analysis techniques are provided with each equipment description.

2.2 Inductively Coupled Plasma Chamber

The inductively coupled plasma (ICP) system used in these studies was originally built by former graduate student Harmeet Singh[59], and previously modified and used by former graduate student Cheng-Che Hsu to study etching of ruthenium coatings in O_2 and Cl_2 containing plasmas[48]. The ICP reactor consists of a cylindrical, stainless steel chamber, 20 cm in diameter and 10 cm in height (Figure 2.1). The process gas enters through an annulus at the chamber top and the pressure is controlled by modulating the gas flow rate at the chamber outlet. The chamber pressure (1 – 100 mT) is measured with an MKS Baratron (type 660) capacitance manometer gauge. The plasma chamber is pumped by a 1000 L/s Seiko-Seiki turbo pump, backed by a mechanical roughing pump. A typical base pressure of $\sim 5 \times 10^{-7}$ Torr is achieved.

The plasma density and ion energy are controlled with two, independent, radio frequency (RF) power sources. First, a five-turn planar coil delivers 13.56 MHz RF power through the alumina dielectric window at the chamber top. A Faraday shield placed between the coil and the dielectric plate minimizes the capacitive coupling. The set power and pressure control the plasma density. A bias voltage is delivered through the second 13.56 MHz power source through the stainless steel electrode (chuck) at the chamber bottom. This bias voltage independently controls ion bombarding energies and is measured with a 1000x 3pF attenuated high voltage probe (Tektronix P6015) and recorded by a Tektronix TDS 2022B oscilloscope. Wafers (up to 150 mm in diameter) are mechanically clamped to the chuck. Backside helium cooling is available to improve heat transfer between the wafer and chuck.

The ICP chamber is equipped with sampling ports located 2.54 cm above the lower electrode surface (Figure 2.2). Diagnostic tools include a wall-mounted ion current probe, an optical emission spectrometer (OES), a vacuum ultraviolet (VUV) spectrometer, an ion mass spectrometer (IMS) and a neutral mass spectrometer. In addition, a port equipped with a radial-motion, linear feed-through system can be interchanged with a sample holder, Langmuir probe and a quartz-crystal microbalance (QCM).

2.3 Sample Holder

A temperature and bias controlled sample holder can be mounted in the radial-motion, linear feed-through port (Figure 2.3). Samples (1 – 2 cm^2) are mounted on the 1.1-inch diameter holder in the load-lock chamber, and translated into the ICP system until flush at the chamber wall. The holder temperature (0 – 100 °C) is controlled with an external Neslab RTE-111 water bath. Samples are held on the holder with thermal paste (Apiezon H Hi Temp Vacuum Grease) and kapton tape. The bias is controlled with a 13.56 MHz RF power supply, measured with a high voltage probe and recorded by a Tektronix TDS 2022B oscilloscope.

2.4 Quartz Crystal Microbalance

A quartz crystal microbalance is available to measure mass change corresponding to material etching or deposition. Although not used in this study, a brief description will be given herein. For detailed operation, the reader is referred to the dissertation of Hsu[48].

A Phelps Electronics (model 18020) quartz crystal microbalance (QCM) is exchangeable with the previously described sample holder, as well as with the Langmuir probe in the radial-motion, linear feed-through port mounted on the chamber wall. The microbalance head supports 6 MHz Au-coated quartz crystals, monitored for changes in oscillation frequency via a thickness/rate monitor (STM-100/MF, Sycon Instruments) interfaced with a PC. The Au-coated quartz crystals are transferred to the microbalance through the load-lock chamber (*cf* Figure 2.2) isolated from the main chamber via a gate valve, and pumped down with a supporting roughing pump. The samples are translated into the ICP chamber to sit flush at the reactor wall. The microbalance head is cooled through an external water supply to prevent changes in frequency oscillations due to ion bombardment induced sample heating. A 1 Hz change in the oscillation frequency corresponds to a mass change of 12.1 ng/cm^2.

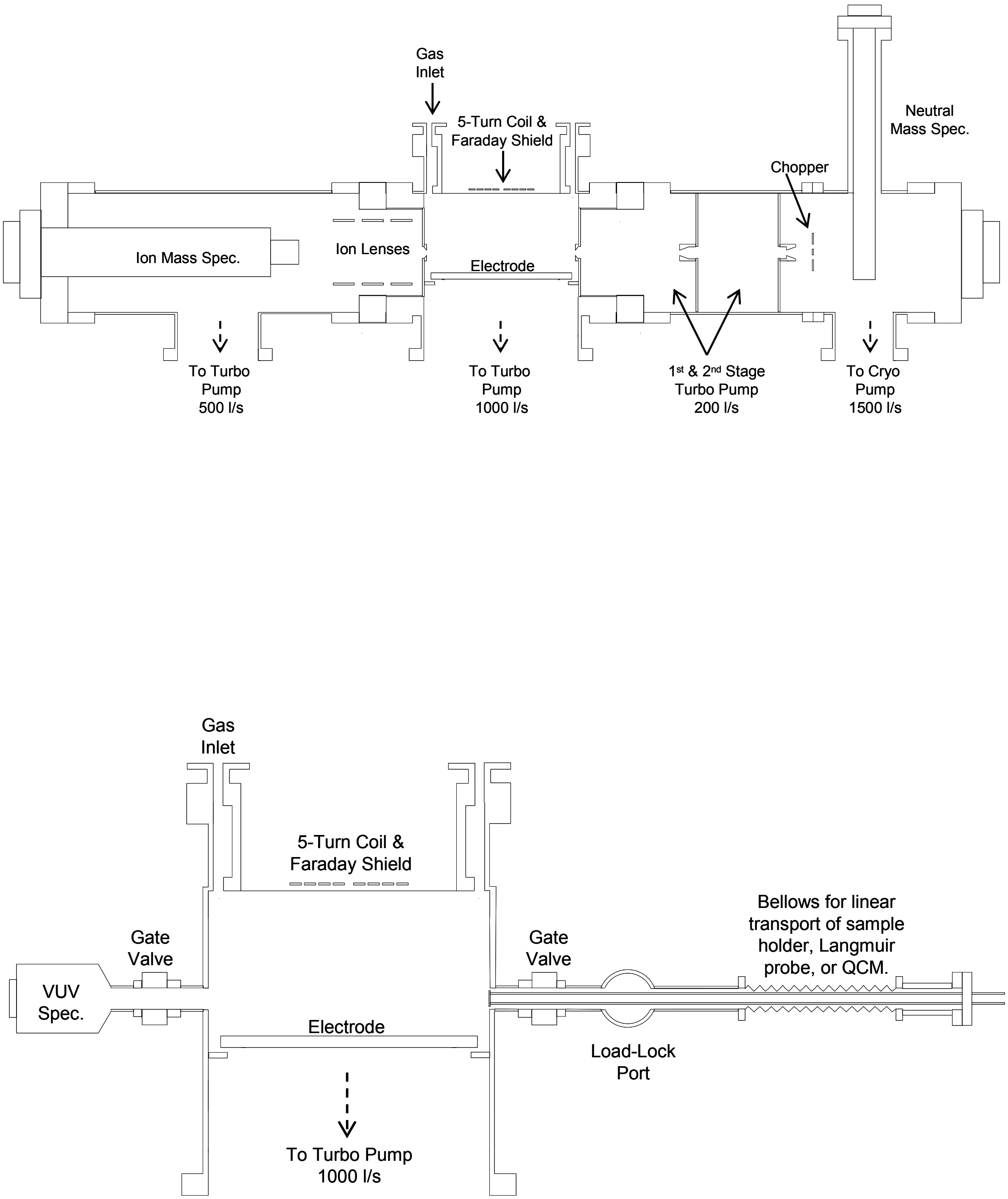

Figure 2.1 Two side views (180 ° rotation) of the inductively coupled plasma system and diagnostic tools.

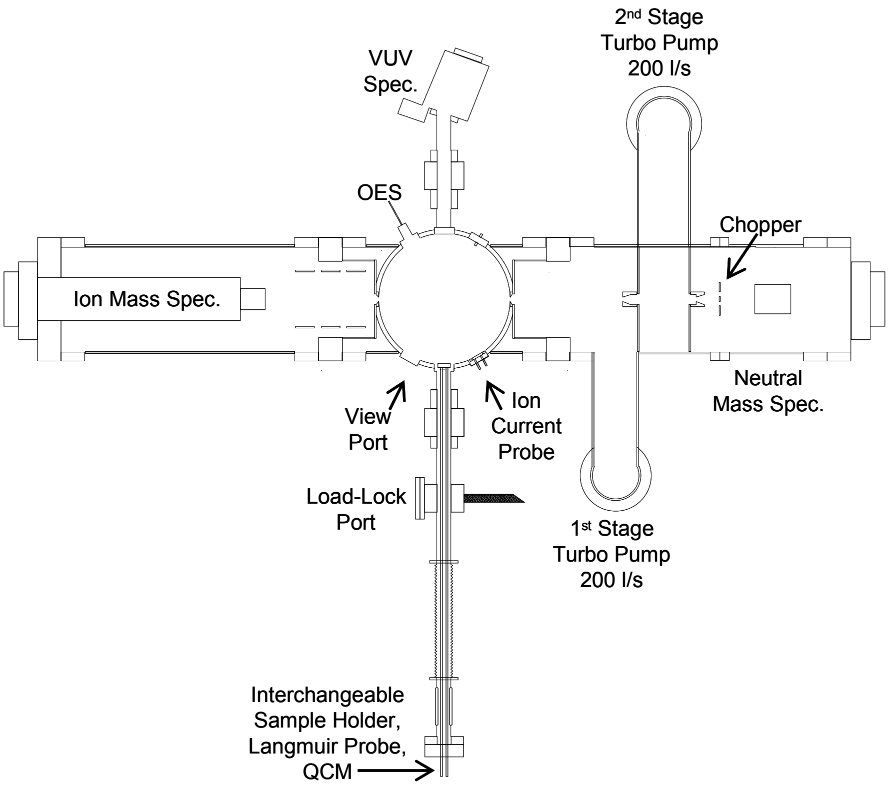

Figure 2.2 Top-down view of the inductively coupled plasma system, equipped with diagnostic tools.

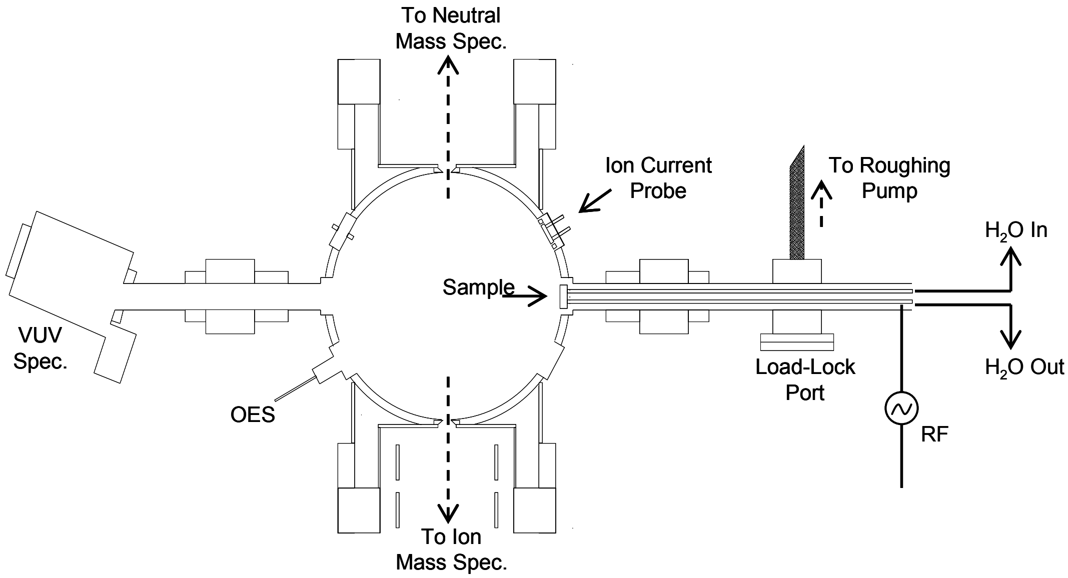

Figure 2.3 Top-down view of the inductively coupled plasma system equipped with the temperature and bias controlled sample holder, mounted in the radial-motion, linear feed-through port.

2.5 Langmuir Probe

The Langmuir probe is introduced into the plasma chamber through the differentially pumped radial-motion, linear feed-through port (inter-exchangeable with the sample holder and QCM) and can access different radial positions ranging from the chamber center to edge (r = 0 cm to r = 7.5 cm). The probe is designed according to the guidelines of Godyak *et al*. by former graduate student Harmeet Singh[27,38]. The telescopic probe design ensures that probe measurements do not significantly perturb the plasma[38,60,61] while the Faraday shield between the coil and plasma minimize the RF potential distortion[59].

The Langmuir probe is used to measure the electron temperature (T_e), electron density (n_e) and plasma potential (Φ_p) by measurement of the electron energy probability function (EEPF) and application of the second derivative method[27,38]. For this purpose, a platinum wire tip (125 μm diameter, ~ 5 mm length) performs a voltage sweep, V_p, measuring the collected current, I_p (Figure 2.4).

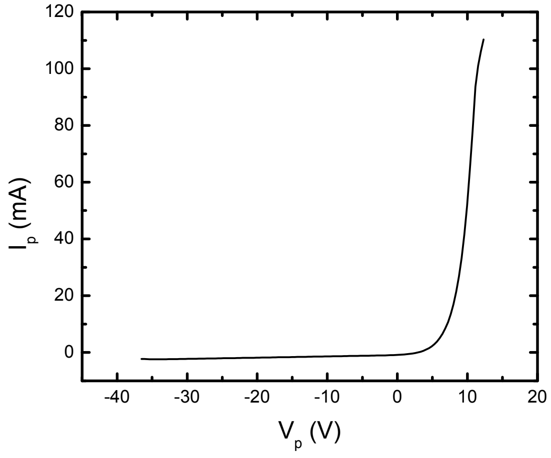

Figure 2.4 Langmuir probe voltage sweep.

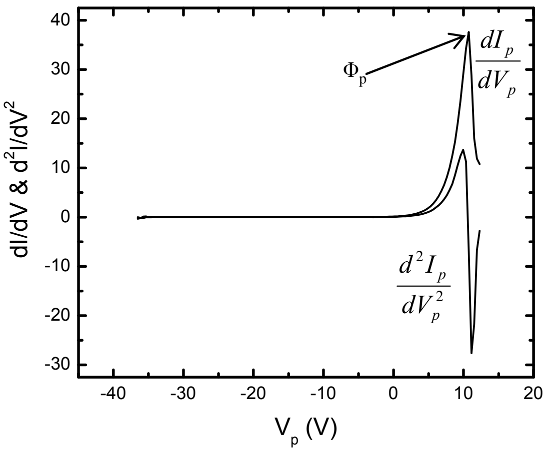

Figure 2.5 The first and second derivative of the Langmuir probe voltage sweep.

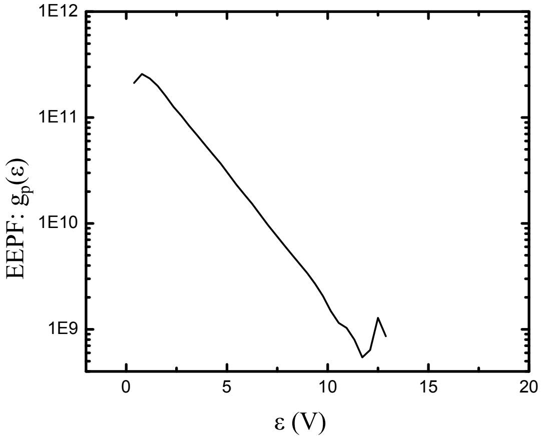

Figure 2.6 The electron energy probability function plotted as a function of electron energy.

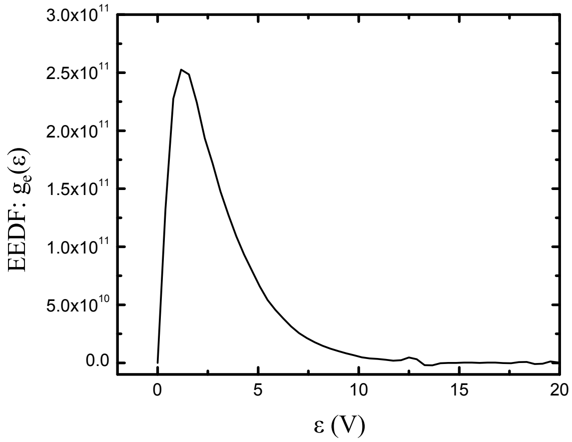

Figure 2.7 The electron energy distribution function (EEDF) vs. electron energy. Integration yields n_e.

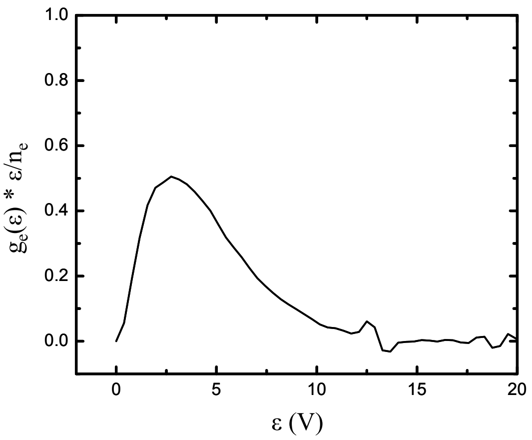

Figure 2.8 Integration yields ‹ε› according to Equation 2.4.

The plasma potential is obtained from the maximum of the first derivative of the V_p-I_p curve (Figure 2.5). The V_p-I_p curve is used to obtain the EEPF[2], $g_p(\varepsilon)$:

$$g_p(\varepsilon) = \frac{2m}{e^2 A}\left(\frac{2e}{m}\right)^{1/2} \frac{d^2 I_p}{dU_p^2} \ , \qquad (2.1)$$

where ε is the electron energy (eV), m is the electron mass (kg), e is the electron charge (C), A is the probe tip surface area ($2\pi rL$) and U_p is the probe potential with respect to the plasma potential ($U_p = \Phi_p - V_p$) (Figure 2.6). The electron energy distribution function (EEDF) is used to calculate n_e (Figure 2.7) and T_e where T_e is defined as 2/3 of the average energy $\langle\varepsilon\rangle$ (Figure 2.8).

$$g_e(\varepsilon) = \frac{2m}{e^2 A}\left(\frac{2e}{m}\right)^{1/2} \frac{d^2 I_p}{dU_p^2}\sqrt{\varepsilon} = g_p(\varepsilon)\sqrt{\varepsilon} \qquad (2.2)$$

$$n_e = \int_0^\infty g_e(\varepsilon)d\varepsilon \qquad (2.3)$$

$$\langle\varepsilon\rangle = \frac{1}{n_e}\int_0^\infty \varepsilon g_e(\varepsilon)d\varepsilon \qquad (2.4)$$

2.6 Ion Current Probe

A 0.4 cm^2 wall-mounted, planar, ion current probe is DC-biased to −40 V to measure the total positive ion current. A 2 mm wide guard ring surrounding the probe and similarly biased to – 40 V is used to suppress edge effects[25]. The temporal evolution of the DC ion current is recorded with an Agilent 34410A 6½-digit multimeter and allows for measurement of plasma stability.

The absolute value of a specific specie's ion flux can be determined with the total positive ion flux and the known percentages of each ion specie as measured by the ion mass spectrometer.

2.7 Ion Mass Spectrometer

A UTI-300C quadrupole mass spectrometer (QMS) is used to monitor positive ion species emitted from a plasma. A detailed description of the QMS setup can be found in the dissertations of Singh[59] and Hsu[48]. In brief, the QMS is differentially pumped with a 500 L/s turbomolecular pump (Pfeiffer Balzers TPU-510 with TCP-380 controller) producing a base pressure at the quadrupole mass filter, typically $10^{-8} - 10^{-7}$ Torr. Ion species are sampled (collisionlessly) through a 325 µm aperture in the chamber side wall and guided to the detector with charged ion lenses (*cf* Figure 2.1). The lenses focus the ion flux into the quadrupole filter while the voltages applied to the lenses amplify the ion signal. QMS detection of ion species is applicable for low pressure (~ 3 – 25 mT) plasma conditions. At higher pressures (> 40 mT) the plasma neutral density scatters the ion flux and the QMS ion signal is lost.

A mass scan of the ion signal is performed, detecting ions with varying mass to charge ratios. The resulting energy vs. intensity data is acquired on a PC with a Keithley-Metrabyte 12-bit analog-to-digital board (Figure 2.9). By identifying known ion emissions (e.g. Ar ion 40 amu and 80 amu) in the plasma and the corresponding peaks in the energy vs. intensity spectra, the energy is converted to the respective mass signal via a linear relationship (Figure 2.10). The intensity signal is corrected for transmission and detection efficiencies provided by the manufacturer (Figure 2.11). The transmission efficiency (TE) for ions < 32 amu is 1 while ion masses > 32 amu varies as $10^{(32-m)/155}$. The detection efficiency (DE) varies as $m^{-0.45}$. The detected ion signal is proportional to the ion flux originating from the plasma, therefore the percentage of each ion species emitted from the plasma can be determined (Figure 2.12).

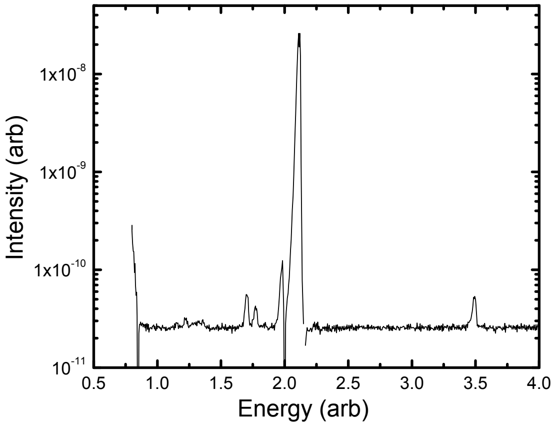

Figure 2.9 Quadrupole mass spectrometer data for an Ar plasma: Energy vs. Intensity.

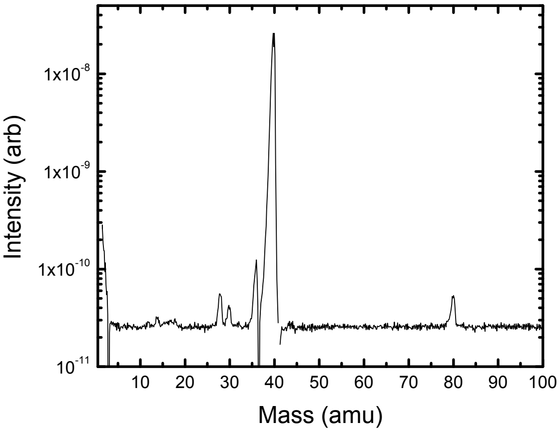

Figure 2.10 Quadrupole mass spectrometer data for an Ar plasma: Mass vs. Intensity.

Mass (amu)	Intensity (I)	TE	DE	Corrected Intensity (CI)	Specie Fraction
1		1	$m^{-0.45}$	I / (TE x DE)	CI /∑
↓		↓	↓	↓	↓
32		1			
33		$10^{(32-m)/155}$			
↓		↓	↓	↓	↓
				∑	

Figure 2.11 Quadrupole mass spectrometer calculation template.

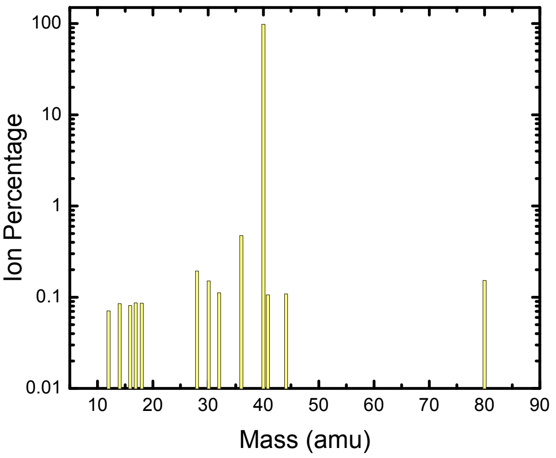

Figure 2.12 Ar plasma ion fractions

2.8 Appearance Potential Mass Spectrometer

A Hiden Analytical PIC300 quadrupole mass spectrometer is mounted in cross-beam mode and attached to the ICP system (*cf* Figures 2.1 and 2.2). Although the appearance potential mass spectrometer (APMS) is not used in these studies, a brief description will be given here. For further details, refer to the dissertations of Singh[59] and Hsu[48].

The APMS chamber is 3-stage, differentially pumped. The first two stages are differentially pumped with 200 L/s turbomolecular pumps (Seiko Seiki STP-H200C and Pfeiffer Balzers TPU-240 with controller TCP380). The third stage, housing the quadrupole mass filter chamber, is pumped down with a 1000 L/s cryogenic pump (On-Board 8F, CTI-Cryogenics, Helix Technology Corp.). The differentially pumped stages allow for improved signal to noise ratios.

The neutral plasma species are sampled through a 900 μm diameter aperture in the chamber wall. The APMS selectively ionizes species with an ionizer in line-of-sight with the sampling aperture. The background noise is measured when a slotted-wheel, rotary-beam chopper is rotated to block the beam signal. The rotary chopper is located in the third differential pumping stage between the ionizer and the aperture.

The radical number density of species ‘X’ measured with the APMS is calculated with the following expression and respective variable definitions[48,59]:

$$n_X^{on} = n_{Ar}^{off}\left(\frac{A^{X\to X^+}}{A^{Ar\to Ar^+}}\right)\left(\frac{\lambda^{Ar\to Ar^+}}{\lambda^{X\to X^+}}\right)\left[\frac{t(m_{Ar^+})\theta(m_{Ar^+})}{t(m_{X^+})\theta(m_{X^+})}\right] \tag{2.5}$$

n_X^{on}	Plasma on: Density of radical ‘X’ at the aperture.
n_{Ar}^{off}	Plasma off: Density of reference specie, Ar, at the aperture (ideal gas law)
$A^{X\rightarrow X^+}$	Plasma off: Linear fit of the energy scan near the threshold energy, for radical ‘X$^+$’
$A^{Ar\rightarrow Ar^+}$	Plasma off: Linear fit of the energy scan near the threshold energy, for reference signal ‘Ar$^+$’
$\lambda^{Ar\rightarrow Ar^+}$	Plasma on: Linear fit of the cross sections near the threshold energy for direct ionization of radical Ar
$\lambda^{X\rightarrow X^+}$	Plasma on: Linear fit of the cross sections near the threshold energy for direct ionization of reference specie X
$t(m)$	Mass (amu) dependent transmission efficiency
$\theta(m)$	Mass (amu) dependent detection efficiency
$t(m)\theta(m)\propto m^{-0.81}$	Correlation derived by Singh[59]

2.9 Optical Emission Spectrometer

The optical emission (OE) emitted from the plasma is collected with an Ocean Optics PC2000-UV-VIS-ISA OES. A 2048 element, linear CCD array collects the electromagnetic spectrum ranging from 200 nm to 850 nm with a 1.5 nm FWHM resolution. The OE is collected with a collimating lens and guided through an optical fiber to the spectrometer that is interfaced (ISA-bus) with a PC. The OES can capture a full spectrum in 1 ms, however the integral time is adjusted to achieve high signal to noise ratio for a desired acquisition rate.

In these studies, the OES is used to monitor the plasma and ensure the plasma has reached steady-state soon after plasma ignition. The temporal evolution of a line emission is used to indicate plasma stability[48]. In addition, the spectra are monitored for changes in plasma chemistry due to chamber contaminants or product emissions from sample surfaces. For example the 420.06 nm and 811.5 emission lines of a pure Ar plasma are often monitored for plasma stability, while the 777.4 and 844.6 nm lines and 656.3 nm line are monitored for O_2 and H_2 contamination, respectively.

2.10 Vacuum Ultraviolet Spectrometer

The plasma generated vacuum ultraviolet (VUV) emissions are monitored with a Resonance LTD VSFS92 VUV spectrometer mounted on a side-wall port, opposite the sample holder, with line-of-sight at 2.54 cm above the lower electrode surface (*cf* Figures 2.1 and 2.2). To minimize ion bombarding damage, the VUV spectrometer is offset from the main plasma chamber by a branch of specified distance (r). The VUV spectrometer is pumped down directly by the ICP chamber’s turbomolecular pump through the branch and spectrometer entrance slit (150 μm length). The spectrometer is comprised of a concave holographic grating (1,800 grooves/mm) and linear CCD detector (0.2 × 28 mm).

The VUV hardware dial may be adjusted to change the grating and the respective wavelength collection window (ranging ~ 25 nm – 450 nm) (Figure 2.13). The calibration of the hardware was conducted for the wavelength range of 100 – 200 nm and for the purposes of these studies was maintained at the respective dial setting of 150. The integration time is adjusted to achieve high signal to noise ratio for a desired acquisition rate and tends to scale linearly with intensity (Figure 2.14).

Calibration of the VUV spectrometer (with a NIST-calibrated CsI diode supplied by Resonance Ltd.) was completed in the ultra-high vacuum beam system for a Resonance Ltd. VUV source emitting high intensity 147 nm Xe VUV photons[62]. The VUV emission from the plasma system was converted to an absolute VUV photon flux with the calibrated Xe VUV photon flux (2.14×10^{12} photons/cm^2/s) to emission intensity (5731.45) ratio. An integration time of 4,000 ms was used in the calibration. Any change to the integration time must be reflected in scaling the emission intensity accordingly. In addition, emission intensities must be corrected by the manufacture-recommended factor (S) of 10 for wavelengths < 120 nm due to decreasing spectrometer sensitivity.

The VUV photon flux from the ICP system was also corrected for a solid-angle factor, accounting for the spectrometer offset from the chamber by distance 'r_2' (Figure 2.15). Assuming the plasma is a sphere of radius 'a_1' filling the ICP chamber of radius 'r_1' then the total illumination, E_1, on a given plane (i.e. the sample port) is calculated via Equation 2.6 [63].

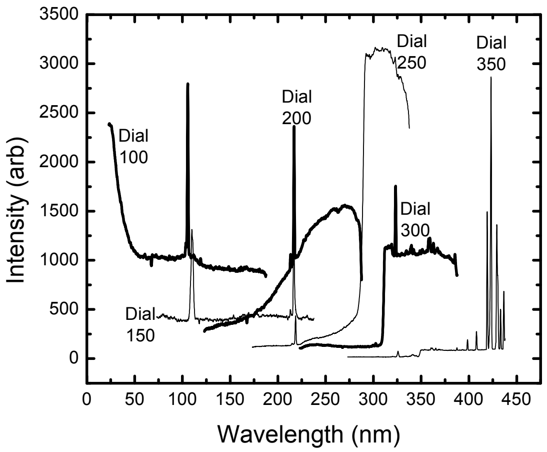

Figure 2.13 VUV hardware dial setting effects on the spectra collection window. VUV spectra for a 10 mT, 200 W Ar plasma.

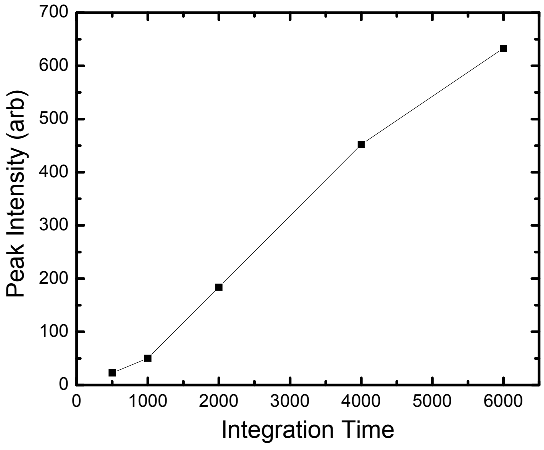

Figure 2.14 VUV peak intensity variation with integration time. Data representative of a 10 mT, 85 W Ar plasma.

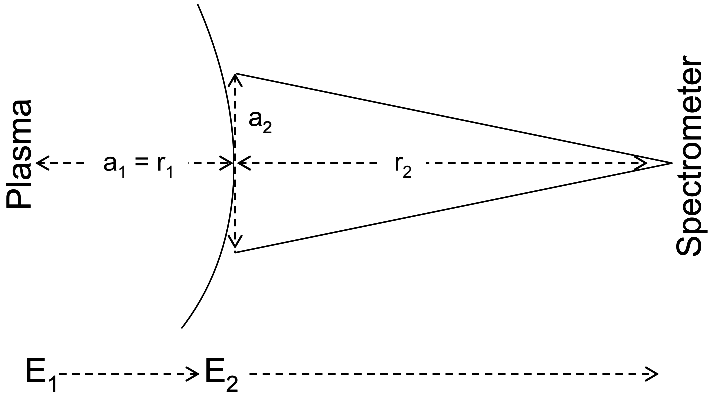

Figure 2.15 Diagram for the solid angle correction factor in determining the absolute VUV photon flux emitted from the plasma. A spherical plasma of radius a_1 illuminates the sample port entrance with E_1. The sample port, of radius a_2, illuminates the planar, spectrometer entrance slit with E_2.

$$E_1 = \frac{\pi a_1^2 b}{r_1^2} \tag{2.6}$$

Here, b is the brightness of the surface. For $r_1 = a_1$, then the illumination is that of an infinite plane and Equation 2.6 reduces to:

$$E_1 = \pi b \tag{2.7}$$

Assuming the sampling port is a disk of radius 'a_2' then the illumination on the spectrometer a distance r_2 away is given as[63]:

$$E_2 = \frac{\pi a_2^2 b}{a_2^2 + r_2^2} \tag{2.8}$$

The lost emission intensity is calculated by taking the ratio for the illumination on the sampling port (E_1) versus the illumination on the spectrometer (E_2), yielding the solid angle correction factor (SA).

$$SA = \frac{E_1}{E_2} = \frac{a_2^2 + r_2^2}{a_2^2} \tag{2.9}$$

For the present set of studies, the correction factor was ~ 517. A sample equation is given below to demonstrate the factors utilized to calculate the total VUV flux (Γ_{hv}) emitted from Ar lines at 104.8 nm and 106.7 nm in the ICP chamber. This flux calculation represents the absolute flux of VUV photons irradiating the chamber wall, or sample holder flush with the chamber wall.

$$\Gamma_{\mathrm{hv}}\ \frac{photons}{cm^2 s} = \text{VUV Intensity} \times \frac{2.14\times10^{12}\ \frac{photons}{cm^2 s}}{5731.45} \times 10 \times 517 \tag{2.10}$$

Chapter 3 – Argon Plasma Characterization

3.1 Abstract

A number of diagnostic tools were utilized to characterize the plasma for the PlasmaTemp^{TM}, and PlasmaVolt^{TM} "on-wafer" studies, as well as the 193 nm photoresist (PR) studies. Diagnostic tools include the Langmuir probe, ion current probe, ion mass spectrometer, optical emission spectrometer (OES) and vacuum ultraviolet (VUV) spectrometer that have been previously described in Chapter 2. An Ar/O_2-mix plasma was investigated for the PlasmaTemp^{TM} study, in addition to the pure, inert Ar plasmas generated for all other studies. In characterizing the plasmas, much attention was given in understanding effects of pressure and power on plasma species such as ions, metastables, and VUV photons. Effects of bias voltage application and Langmuir probe measurements on plasma stability were also investigated. In this chapter the general characteristics of the Ar plasmas utilized in the "on-wafer" sensor studies and 193 nm PR studies are given. Supplementary reference data can be found in Appendices A and B.

3.2 Langmuir Probe

The plasma density (n_e), electron temperature (T_e) and plasma potential (Φ_p) are measured 2.54 cm above the lower electrode with the Langmuir probe for the pure Ar plasmas utilized in the PlasmaTemp^{TM}, PlasmaVolt^{TM} and 193 nm PR experimental studies. The radial variation of the plasma characteristics were also investigated by linearly translating the probe from chamber center to edge. The effects of changing ICP power, operating pressure and plasma chemistry were investigated. Issues of plasma stability during Langmuir probe measurements were also considered. Scaling of the plasma density measurements to the lower electrode surface is also discussed.

3.2.1 Power and Pressure Effects

The n_e, T_e, and Φ_p were measured for a range of operating conditions used in the PlasmaTemp™ and PlasmaVolt™ studies. The dependence on power and pressure are given in Figures 3.1 – 3.3 for Langmuir probe measurements taken at r = 0 cm (chamber center). Supplementary operating conditions and diagnostic measurements are given in Appendices A and B. Note that n_e is determined from an energy balance and is proportional to the total power absorbed, congruent with the global model[2]. In contrast, the T_e is determined by particle conservation and is independent of plasma density (or ICP power).

n_e measurements depend on radial position whereas T_e and Φ_p measurements remain fairly independent of radial position for Langmuir probe measurements 2.54 cm above the lower electrode surface. T_e and Φ_p values used in the PlasmaTemp™, PlasmaVolt™, and 193 nm PR studies neglect any spatial variation. However, significant spatial variation in n_e is observed – as much as 50 % in high pressure cases and 30 % in low pressure cases. Figures 3.4 – 3.6 demonstrate radial dependence for measurements at the chamber center and edge. As the operating pressure increases, the radial gradient of the density increases because the plasma transport becomes collisionally dominant. This produces a larger difference between center and edge density measurements.

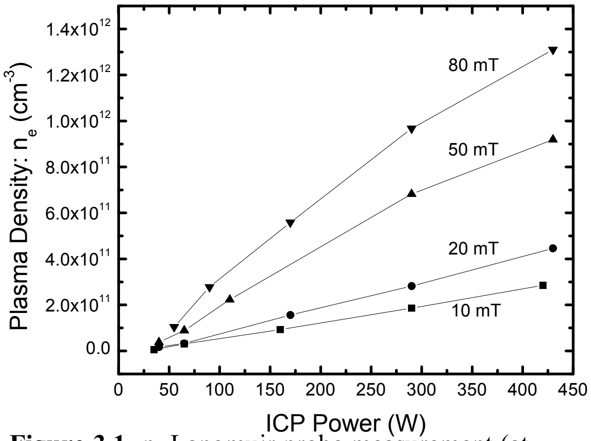

Figure 3.1 n_e Langmuir probe measurement (at chamber center) for Ar plasmas.

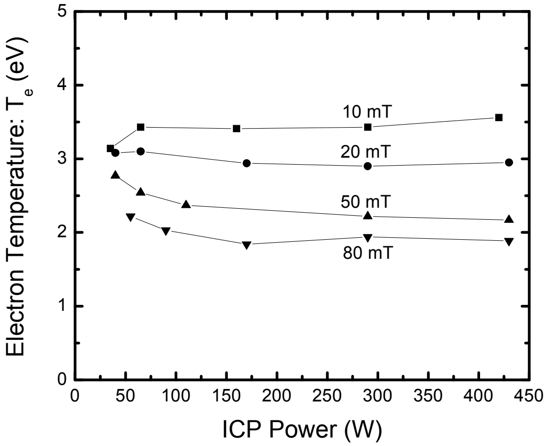

Figure 3.2 Φ_p Langmuir probe measurement (at chamber center) for Ar plasmas.

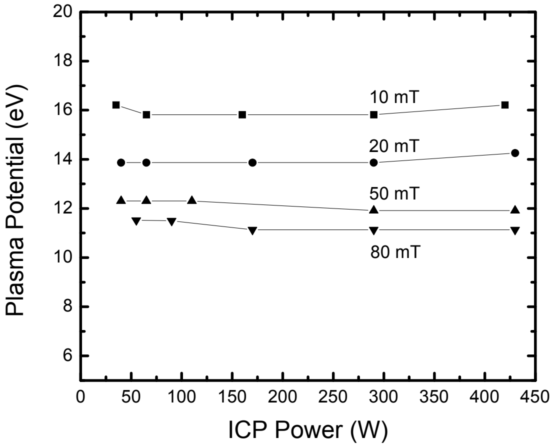

Figure 3.3 T_e Langmuir probe measurement (at chamber center) for Ar plasmas.

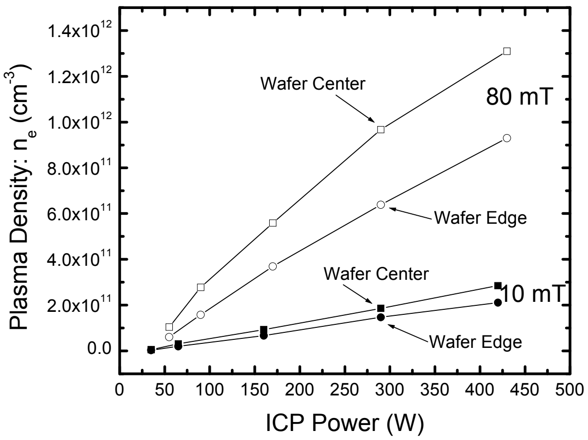

Figure 3.4 Electron density spatial variation for Ar plasmas at 10 mT.

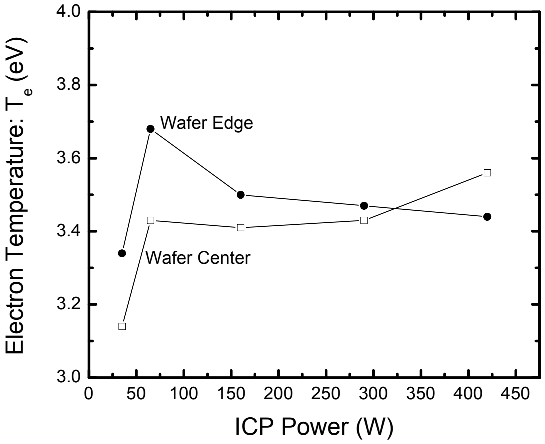

Figure 3.5 Electron temperature spatial variation for Ar plasmas at 10 mT.

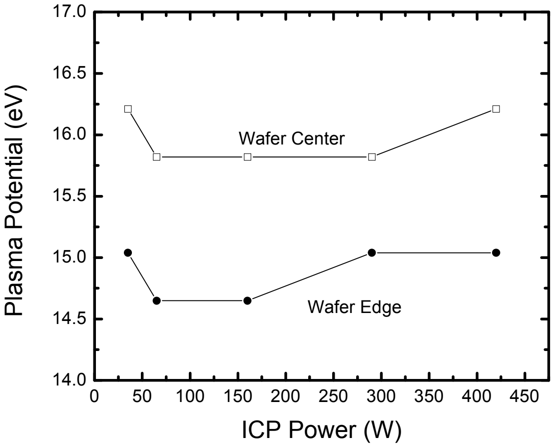

Figure 3.6 Plasma potential spatial variation for Ar plasmas at 10 mT.

3.2.2 Plasma Perturbation Effects

Langmuir probe measurements introduce local plasma perturbations as the probe is translated into the plasma with the radial-motion, linear feed-though mechanism. Plasma density depletion around the probe scales as α/λ_i, were α is the probe radius and λ_i is the ion mean free path[64]. For Ar plasmas, λ_i (in cm) is defined as $1/(330P)$, where P is the operating pressure in Torr[2]. The plasma perturbation can be neglected when $\alpha << \lambda_i$. The density and ion current perturbations are typically ignored for a 10 mT Ar plasma where $\lambda_i = 0.3$ cm and $\alpha = 0.1$ cm. At 50 mT, $\lambda_i = 0.06$ cm, therefore, the perturbations become increasingly significant. For the relatively high pressure (50 – 90 mT) studies conducted in this dissertation, however, plasma density changes due to Langmuir probe perturbations are neglected.

3.2.3 Scaling Experimental Measurements to Substrate Surfaces

The Langmuir probe measurements are taken at 2.54 cm above the lower electrode (or wafer) surface, giving radial profiles of the bulk plasma. Many of the studies, including the PlasmaTemp^{TM} and PlasmaVolt^{TM} studies, require plasma density measurements at the wafer surface, or plasma-sheath interface. These density values were obtained by scaling the experimentally measured density with a factor (R) obtained from a numerical simulation of the plasma (Table 3.1)[48]. The details of the numerical simulation are provided in Appendix C.

Table 3.1 Factor (R) to scale experimentally measured n_e values down to the wafer/electrode surface.

Operating Pressure (mT)	R
10	2.4
25	5.0
58	14.2
80	11.9

3.3 Ion Current Probe

The ion current probe measures the positive ion flux to the wall as described in Chapter 2. In general, the ion current probe is used to monitor plasma stability during the PlasmaTemp^{TM}, PlasmaVolt^{TM} and 193 nm PR studies. Plasma perturbation is found typically during bias voltage application to the lower electrode and Langmuir probe measurements. The changes to plasma density and ion current, however, were considered negligible for these studies.

3.3.1 Effects of Power and Pressure

ICP power deposition and chamber pressure effects on the ion current probe measurements are given in Figure 3.7. The ion current increases with power due to an increase in plasma density, and tends to increase linearly at higher powers. A slight increase in ion current is observed for higher pressures at ICP powers > 200 W. As pressure increases, the radial gradient of the density increases because the plasma transport processes become collisionally dominant. This produces a larger difference between the chamber center and edge density values. Therefore, although the plasma center density increases, a significant change in ion current at the chamber wall is not observed due to the steep density gradient.

Ion current for Ar/O_2-mix plasmas behave differently than in inert Ar plasmas. The hollow data points represent ion current measurements for a 35 sccm:100 sccm Ar/O_2-mix plasma. More power is required to maintain the Ar/O_2 plasma to achieve an approximately equal ion current compared to the Ar plasma because there are additional collisional energy loss mechanisms in a molecular gas, including excitation of vibrational and rotational energy levels, molecular dissociations and negative ion formation[2].

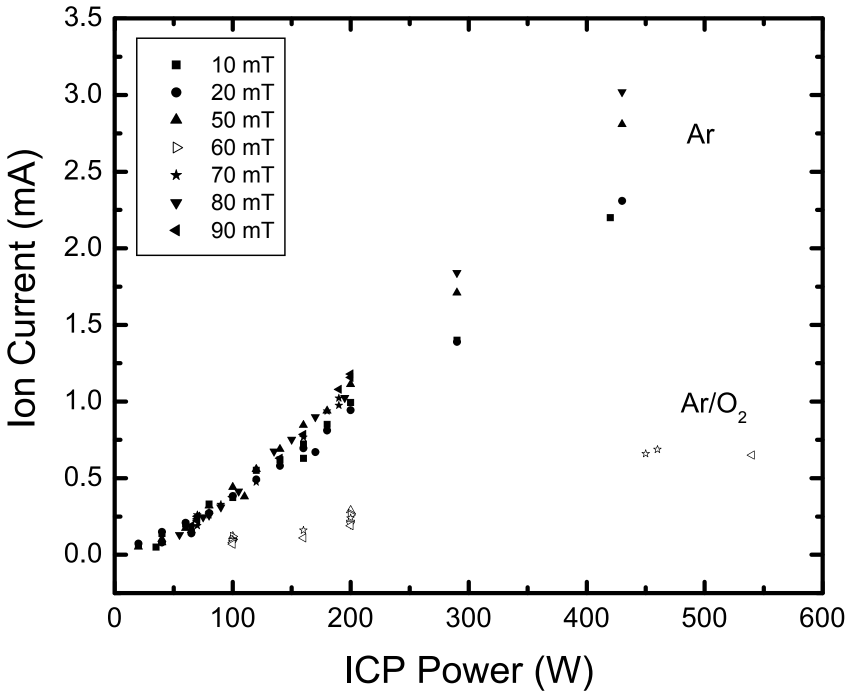

Figure 3.7 Ion current measurements (multimeter values). Solid: pure Ar. Hollow: 35:100 sccm Ar/O_2

3.3.2 Effects of Bias Voltage

The temporal evolution of the ion current is monitored to ensure plasma stability for the duration of an experiment. The stability of the plasma may be disrupted due to application of a bias voltage on the lower electrode necessary for plasma ignition or substrate biasing. Figure 3.8 depicts a typical ion current (or ion flux) measurement for a 10 mT, 70 W, Ar plasma. Plasma variation is minimal except for the initial 1~2 seconds. Biasing the lower electrode, required to supply enough capacitive coupling for plasma ignition, produces a burst in plasma density and ion current, as much as ~ 25 % times greater before reaching the stable condition.

Bias voltages applied to the lower electrode (as in the PlasmaVolt^{TM} studies) also result in ion current and plasma density instability. Typical changes in ion current measurements are given in Figure 3.9 for a 10 mT, 35 W and 155 W Ar plasma. Applied bias voltages are given in Table 3.2. The ion current increases in the low plasma density case (35 W) up to 22 %, while for the mid-range plasma density case (155 W) the ion current increases ~ 3%. For low density plasmas (e.g. 35 W) the ICP RF-power is equal to or less than the RF-bias power and capacitive coupling becomes increasingly important. Capacitive coupling increases electron heating and consequently the plasma density increases uniformly from chamber center to edge[65]. In contrast, high density plasmas experience little-to-no capacitive coupling since RF-ICP power >> RF-bias power. Bias applications in high density plasmas tend to cause only the plasma density at the chamber center to decrease due to gas composition change[65]. For mid-range plasma densities (e.g. 155 W) the two effects cancel each other out, and very little change is observed in plasma density during bias application[65].

Table 3.2 Peak-to-peak bias voltages applied to the substrate in a 10 mT, 35 W and 155 W Ar plasma. The respective change in ion current (I_p) for each voltage application is given.

	35 W		155 W	
	$V_{pp,bias}$ (V)	I_p % Change	$V_{pp,bias}$ (V)	I_p % Change
1	76	12	12	1 – 3 %
2	140	20	40	
3	185	22	70	
4	230	13	92	
5	255	2	160	

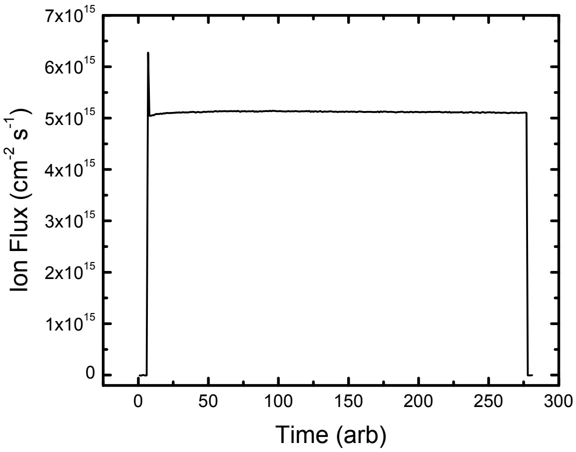

Figure 3.8 Ion flux for a 10 mT, 70 W Ar plasma. Lower electrode biasing required for plasma ignition results in a sudden increase in plasma density and ion current.

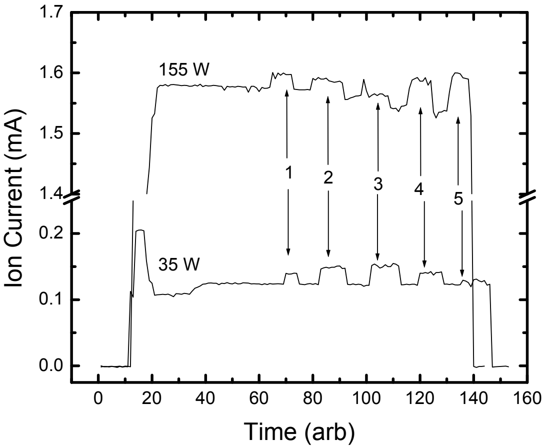

Figure 3.9 Ion current measurements for a 10 mT, 35 W and 155 W Ar plasma. Electrode biasing results in ion current perturbations.

3.3.3 Effects of Surface Area

Plasma density is not only dependent on ICP power and operating pressure, but also on the chamber geometry and surface area available for electron and ion loss. The dependency on surface area is most notable during Langmuir probe measurements as observed by the change in ion current (Figure 3.10). At (a) the plasma is ignited and reaches a stable operating condition, (b). As the Langmuir probe is inserted into the plasma (c) and measures the plasma density at varying chamber radii, r = 0 cm (d) and r = 5.8 cm (e), the available surface area for electron and ion loss increases, resulting in decreased plasma density and ion current. When the plasma density is measured at r = 0 and r = 5.8 cm, the wall ion current decreases by 12 % and 5 %, respectively, indicating that the Langmuir probe measured plasma densities are under-estimates of the true plasma density.

As discussed previously in section 3.1.2, Langmuir probes introduce local plasma perturbations, as is increasingly the case when the probe is translated into the plasma with the radial-motion, linear feed-through mechanism. The perturbations are typically ignored for low pressure plasmas, and although they grow increasingly significant for higher pressures, the effect on plasma density and ion current is uncorrected in these studies.

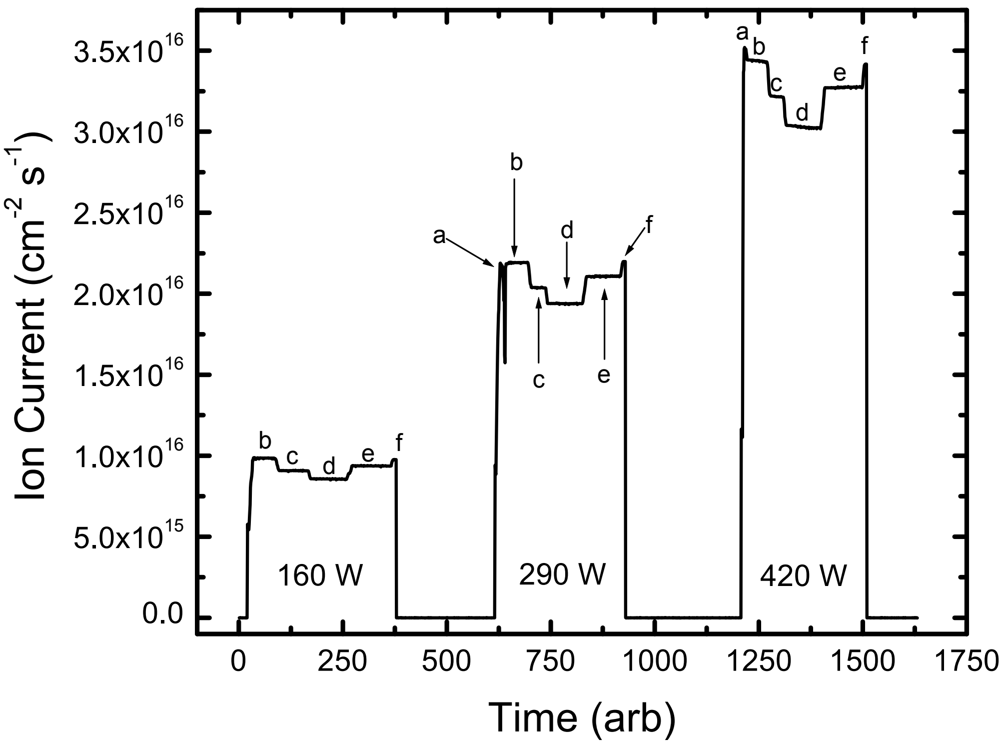

Figure 3.10 Ion current for a 10 mT, 160 W, 290 W and 420 W Ar plasma. (a) Plasma ignition, (b) Stable ion current, (c) Langmuir probe translated to chamber center, r = 0 cm, (d) Stable ion current during Langmuir probe measurement at r = 0 cm, (e) Stable ion current for Langmuir probe measurement at wafer edge, r = 5.8 cm (f) Removal of Langmuir probe from chamber.

3.4 Ion Mass Spectrometry

Ion mass spectrometry (IMS) is utilized in the low-pressure conditions of the 193 nm photoresist (PR) studies. In all studies, a pure Ar plasma at low pressure (10 mT) was generated and the plasma ion chemistry prior to and during photoresist processing in the ICP chamber was measured. The Ar plasma is typically inert, except for CO_2 and H_2O residual contaminants that ionize and generate $C_xH_yO_z$ ion species (Figure 3.11 a). When a PR sample is processed in the chamber, non-Ar^+ peaks increase (Figure 3.11 b). The increase in $C_xH_yO_z$ species is attributed to possible product off-gassing, as well as CO_2 and H_2O contamination introduced when PR samples are loaded through the side-wall, load-lock port.

The fractions of each ion specie generated in a 10 mT, 70 W, Ar plasma are given in Table 3.3. Increases in contaminant/product ion species are observed when a PR sample is introduced to the ICP chamber. The H_2O, CO, and ArH ion fractions increase by 3, 2, and 1.4 times, respectively. With the total positive ion flux measured with the ion current probe (~ 5.15×10^{15} ions/cm^2/s) the individual ion flux can be calculated.

Table 3.3 Fraction of ion species for a 10 mT, 70 W, Ar plasma

Mass (amu)	Specie	No Sample	With Sample
12	C	0.07	0.07
14	CH_2	0.09	0.08
16	O	0.08	0.11
17	OH, CH_3	0.09	0.13
18	H_2O	0.09	0.22
28	CO	0.19	0.27
30	CH_2O	0.15	0.22
32	O_2, CH_3OH	0.11	0.13
36	Ar	0.47	0.47
40	Ar	98.30	97.72
41	ArH	0.11	0.32
44	CO_2	0.11	0.12
80	Ar	0.15	0.14

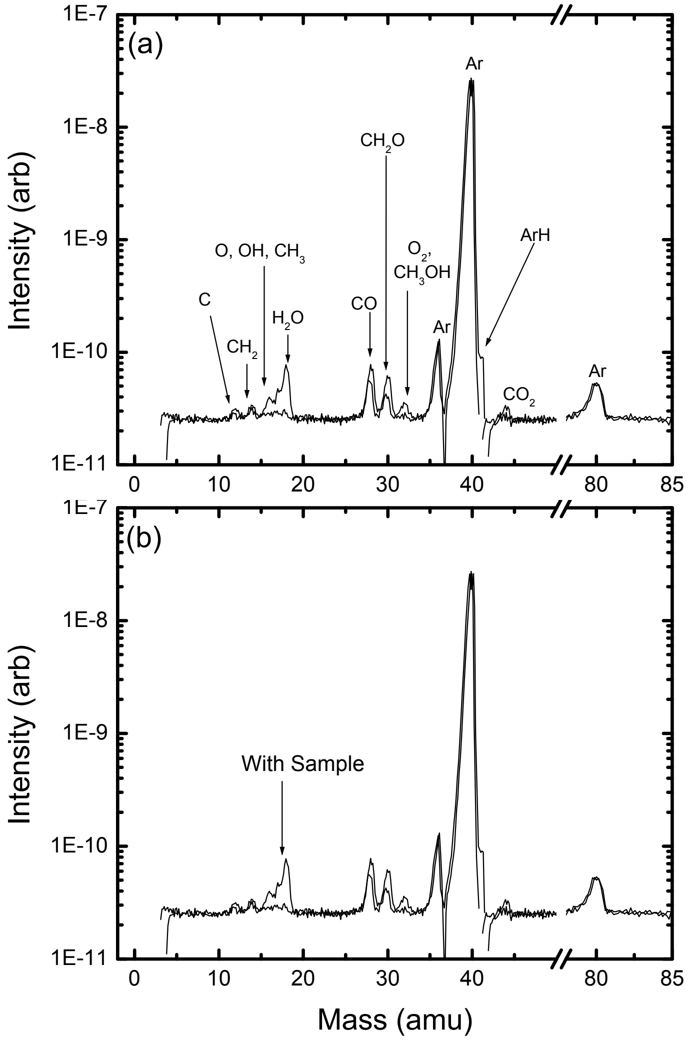

Figure 3.11 Ion mass spectra for a 10 mT, 70 W Ar plasma. (a) Ion peaks labeled. (b) Sample vs. No Sample spectra. $C_xH_yO_z$ species are due to residual contaminant and product off-gassing.

3.5 Optical Emission Spectrometry

Optical emission spectrometry (OES) is used in addition to the ion current probe to monitor plasma stability. For example, the effects of bias voltage application to the lower electrode on plasma density can be clearly seen in increases of the Ar emission lines at 420.6 nm and 811.5 nm. Other diagnostic techniques such as actinometry[26] can be used to measure plasma density and understand the behavior of metastable and resonant states[35].

3.5.1 Plasma Stability Measurements

Plasma stability is monitored by plotting the temporal evolution of emission line intensities. For pure Ar plasmas, the 420.6 nm, 750 nm and 811.5 nm emission lines are plotted as a function of time (Figure 3.12). As plasma "on" time increases, a drift in the plasma intensity (< 10 %) is observed due to an increase in plasma temperature (and chamber wall heating) and decrease in plasma density. This type of drift in the plasma density is considered negligible.

Additional instabilities in the plasma are observed when the lower electrode is biased. Figure 3.13 plots the respective changes in the OES for a 10 mT, Ar plasma for the biases applied in Table 3.2. The observed change in the OES is similar to that observed in the ion current measurements. Applied bias voltages at low plasma densities increase the electron heating from capacitive coupling. The resulting increase in plasma density is reflected in the increase in the OE intensity (Figure 3.13 a). At mid-densities, (155 W), the effect of bias voltage on plasma density is negligible (Figure 3.13 b).

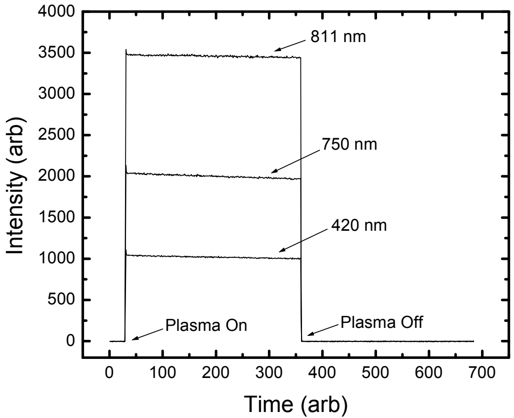

Figure 3.12 Optical emission line intensities for a 10 mT, 70 W Ar plasma plotted as a function of time. The steady temporal evolution of the line intensities indicates plasma stability.

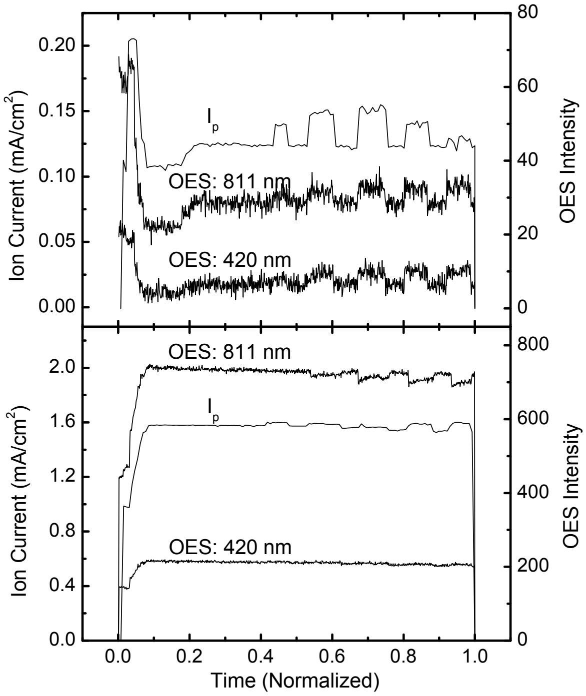

Figure 3.13 The temporal evolution of the 811.5 nm and 420.6 nm optical emission line intensities and ion current (I_p) measurements for a 10 mT (a) 35 W and (b) 155 W Ar plasma.

3.5.2 Monitoring Plasma Resonance and Metastable States

In addition to using OEs to monitor plasma stability, OEs are used to monitor the generation and consumption of resonance and metastable states. In particular, the OEs of the $1s_2$ and $1s_4$ resonance states and $1s_3$ and $1s_5$ metastable states of an Ar plasma were monitored during the 193 nm PR experiments (Table 3.4).

At low pressures, the ratios of optical transitions to the $3p^54s$ manifold from the $3p^54p$ manifold (e.g. A/F, B/G, E/H) increase indicating that the plasma grows optically thick for transitions into the $1s_2$ and $1s_4$ resonance states (Figure 3.14). Under these conditions, the $1s_3$ and $1s_5$ metastable state densities increase. As the operating pressure is increased, the metastable-to-resonance state line ratios (i.e. A/F, B/G, E/H) tend to decrease. This is accompanied by an increase in the $1s_2$ and $1s_4$ resonance state densities. The densities increase until they saturate and begin to decrease slightly for very large pressures. The variation of the OE line ratios measured in the ICP chamber are in good agreement with work done by Schulze, *et al*[35].

Figures 3.15 – 3.17 show the ratio of VUV (104.8 nm and 106.7 nm) emission intensities to OE intensities emitted during transition from the $3p^54p$ to $3p^54s$ manifold, i.e. $1s_2$ and $1s_4$ generation. As the pressure is increased from 10 mT to 50 mT, the ratios decrease. Therefore, the optical thickness for line emissions into the ground state is greater than for emissions into the $1s_2$ and $1s_4$ states, further increasing the $1s_2$ and $1s_4$ densities. As power is increased, $1s_3$ and $1s_5$ densities tend to remain constant while $1s_2$ and $1s_4$ densities increase until saturation[35].

Table 3.4 Optical transitions for $1s_2$ – $1s_5$ Ar resonance and metastable states.

	Optical Transition	Wavelength (nm)	E_{th} (eV)	A_{ij} (s^{-1})	Lifetime (ns)
A	$2p_2 \rightarrow 1s_5$	696.54	13.33	6.39×10^6	28.4
B	$2p_3 \rightarrow 1s_5$	706.72	13.30	3.80×10^6	28.9
C	$2p_2 \rightarrow 1s_4$	727.29	13.33	1.83×10^6	28.4
D	$2p_3 \rightarrow 1s_4$	738.40	13.30	8.47×10^6	28.9
E	$2p_4 \rightarrow 1s_3$	794.82	13.28	1.86×10^6	30.4
F	$2p_2 \rightarrow 1s_2$	826.45	13.33	1.83×10^6	28.4
G	$2p_3 \rightarrow 1s_2$	840.82	13.30	2.23×10^7	28.9
H	$2p_4 \rightarrow 1s_2$	852.14	13.28	1.39×10^7	30.4
I	$1s_2 \rightarrow$ ground	104.8	11.82	5×10^8	2
J	$1s_4 \rightarrow$ ground	106.7	11.62	1×10^8	10

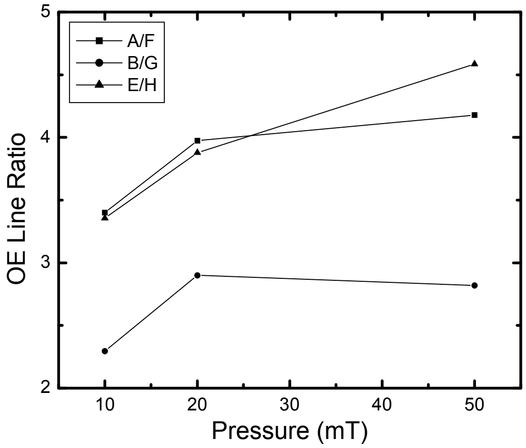

Figure 3.14 Ratios of OE transition lines from the $3p^54p$ manifold to the $3p^54s$ manifold given in Table 3.4.

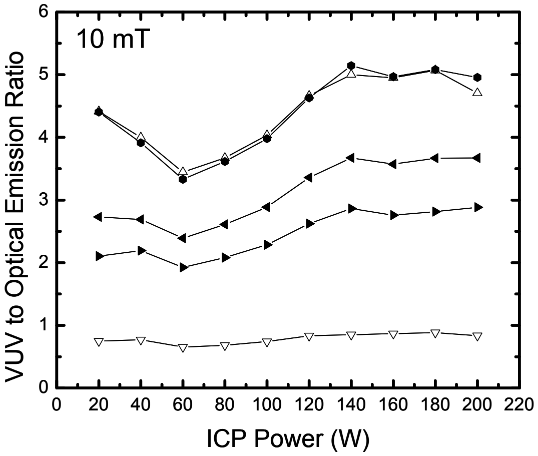

Figure 3.15 Ratios of VUV peak emission intensities to OE peak intensities for a 10 mT pure Ar plasma. Legend given in Figure 3.17.

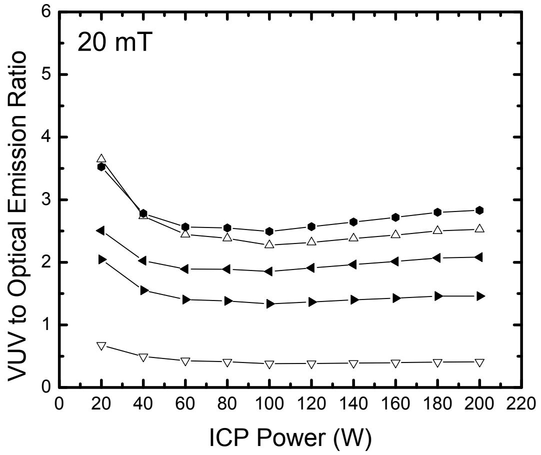

Figure 3.16 Ratios of VUV peak emission intensities to OE peak intensities for a 20 mT pure Ar plasma. Legend given in Figure 3.17.

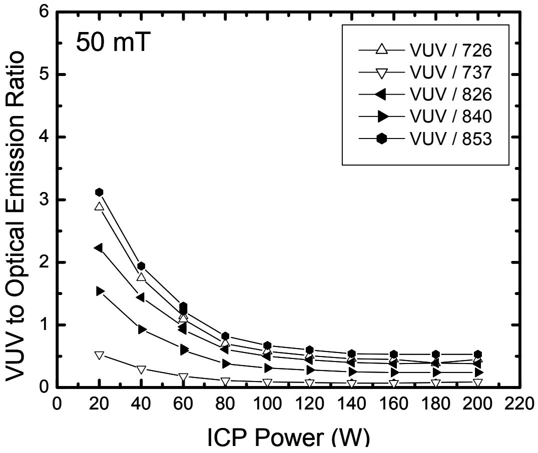

Figure 3.17 Ratios of VUV peak emission intensities to OE peak intensities for a 50 mT pure Ar plasma.

3.6 Vacuum Ultraviolet Spectrometry

Vacuum ultraviolet (VUV) spectroscopy is used to monitor wavelength emissions in the 80 nm to 210 nm range, as discussed in Chapter 2, and is used primarily in the 193 nm PR studies. The 193 nm PR studies required measurements of the absolute VUV photon flux emitted from a plasma in order to study the chemical and physical effects of VUV photons and energetic ions on the PR. For the purposes of those experiments, a nearly pure, relatively inert Ar plasma was generated and the VUV emissions were characterized. Reported observations of VUV intensities for pure Ar plasmas focus on the dominant 104.8 nm and 106.7 nm emission lines[66-68]. To prevent radical and ion damage to the spectrometer, chemically reactive plasmas, such as Ar/O_2 mixtures were not observed. Process control parameters (e.g. ICP power deposition and pressure) were varied to monitor the effects on VUV photon generation.

Figure 3.18 displays the VUV spectrum for an Ar plasma at 10 mT and a range of ICP powers. As power is increased, the dominant 104.8 nm and 106.7 nm Ar emission line intensities increase due to an increase in plasma density and excitation rates of $1s_2$ and $1s_4$ resonance states responsible for the VUV emissions[69]. Furthermore, the intensities tend to increase with ICP power at higher powers for low pressures, while the VUV intensity appears to saturate at higher pressures (Figure 3.19). A VUV band from ~140 nm – 210 nm is likely due to carbon monoxide (CO) emissions from the 4th positive band[70,71] and is a residual contaminant in the ICP system. The high intensity peaks at ~209 nm and 213 nm are double-peaks of the 104.8 nm and 106.7 nm emissions and is an artifact of the spectrometer. This was verified by inserting a MgF_2 window[36,72] with cut-off wavelength of 112 nm between the plasma source and the spectrometer (Figure 3.20).

The VUV emission intensities are highly dependent on the operating pressure of the ICP system (Figure 3.21 and 3.22). The VUV peak intensities increase as pressure increases from 1 mT to 10 mT and is attributed to the increasing plasma density that enhances $1s_2$ and $1s_4$ production from ground state or other $1s$ levels[69]. The 104.8 nm and 106.7 nm peaks are distinct at lower pressures and merge as the pressure increases. The dominant line broadening mechanism is attributed to Doppler broadening for the range of powers (0 – 200 W) and pressures investigated[64]. As pressure increases to 20 mT and 50 mT, the peak intensities decrease, apparently due to radiation trapping and an increase in quenching, and is congruent with the OE measurements (*cf* section 3.5.2). Absorption and quenching in the gas-filled region between the VUV spectrometer and the plasma also increases at higher pressure[69,73,74]. The dominating intensity of the 106.7 nm peak is attributed to its smaller absorption coefficient, typically four times less than the 104.8 nm peak[64].

Again, the band between 140 – 210 nm is attributed to CO VUV emissions from the fourth positive band. As the pressure is varied, the CO emission intensifies and appears comparable to the Ar 104.8 nm and 106.7 nm emission lines. However, the Ar emission intensity must be corrected by a factor of 10 to account for spectrometer sensitivity at lower wavelengths. Thus, integrating over both the Ar lines and CO-band emissions the CO-band intensity is at most 2.8 %, 2.5 %, 5.2 %, and 20.8 % the intensity of the Ar lines at 1, 10, 20, and 50 mT, respectively.

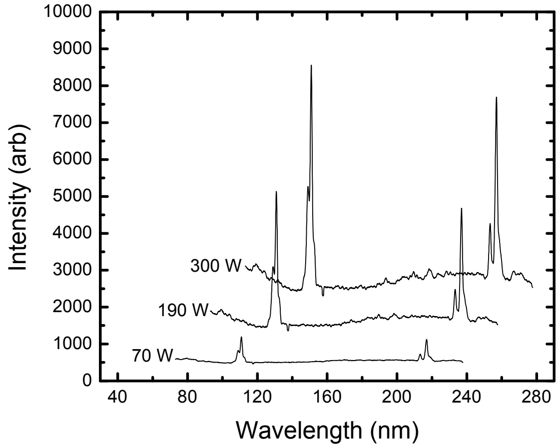

Figure 3.18 VUV spectra for a 10 mT Ar plasma at varying ICP powers.

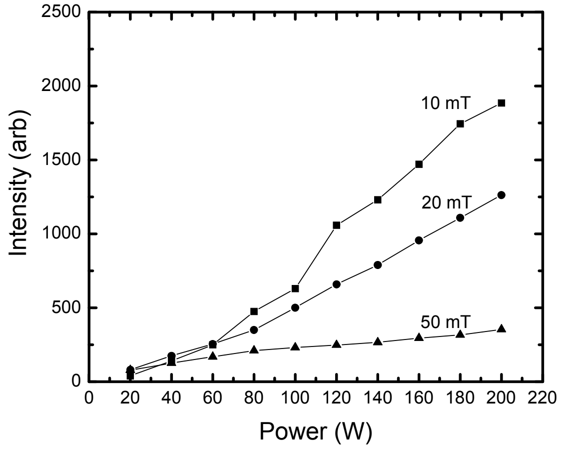

Figure 3.19 Peak 104.8 and 106.7 nm Ar intensities for varying ICP power at 10, 20, and 50 mT pressures.

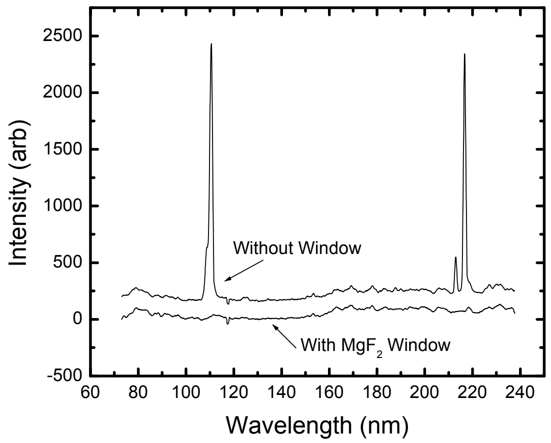

Figure 3.20 VUV spectra for a 10 mT, 200 W Ar plasma. The artificial peaks at 209 and 213 nm are confirmed with a MgF$_2$ window.

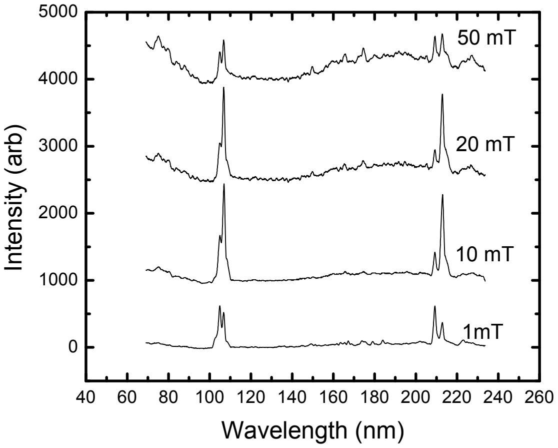

Figure 3.21 VUV spectra for a 110 W Ar plasma for a range of operating pressures.

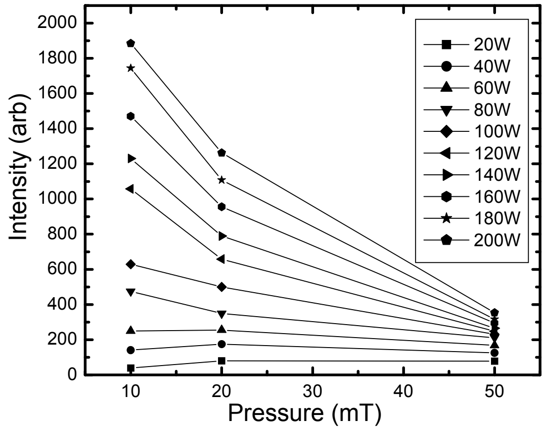

Figure 3.22 Peak 104.8 and 106.7 nm Ar intensities plotted for varying operating pressures for ICP powers ranging from 20 – 200 W.

The total Ar VUV flux emitted from the Ar ICP is on the order of 10^{15} – 10^{16} photons/cm^2/s (Figure 3.23) and is in good agreement with the range of VUV fluxes reported by Woodworth *et al.*[74](3 × 10^{16} cm^{-2} s^{-1}) in the Gaseous Electronics Conference reference cell experiments, and Piejak *et al.*[64] (1 × 10^{16} – 5 × 10^{16} cm^{-2} s^{-1}) in their ICP experiments. The resulting photon-to-ion flux (PI) ratio ranges from ~0.1 to 0.7 (Figure 3.24) and tends to decrease with power since the ion flux scales linearly with power[36].

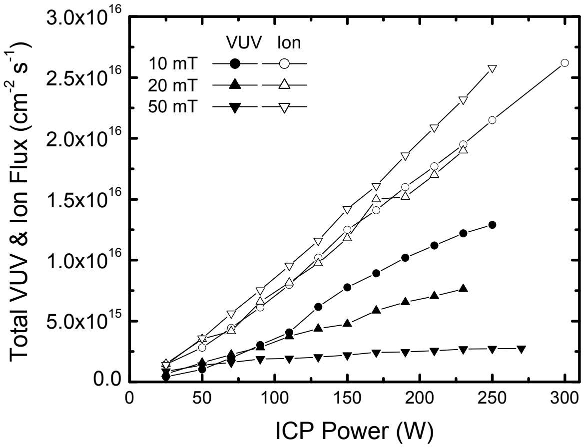

Figure 3.23 Total VUV and ion fluxes for an Ar plasma at 10, 20, and 50 mT operating pressures and a range of ICP powers.

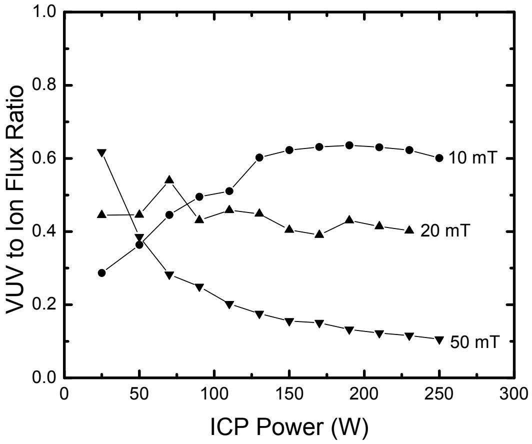

Figure 3.24 The VUV photon-to-ion flux ratio for an Ar plasma.

Chapter 4 – Wafer Heating Mechanisms in a Molecular Gas, Inductively Coupled Plasma

4. 1 Abstract

In this chapter, measurements and modeling of wafer heating mechanisms in an Ar and Ar/O_2 inductively coupled plasma (ICP) are reported. Experimental wafer temperature measurements are obtained with a commercially available on-wafer sensor system (PlasmaTemp^{TM} developed by KLA-Tencor) consisting of an on-board electronics module housing battery power and data storage with 30 temperature sensors embedded onto the wafer at different radial positions. This system allows for real-time, *in-situ* wafer temperature measurements. Wafer heating mechanisms were investigated by combining temperature measurements from the PlasmaTemp^{TM} sensor wafer with a 3D heat transfer model of the wafer and a model of the ICP. Comparisons between pure Ar and Ar/O_2 discharges demonstrated that two additional wafer heating mechanisms can be important in molecular gas plasmas compared to atomic gas discharges. The two mechanisms are heating from the gas phase and O-atom surface recombination. These mechanisms were shown to contribute as much as 60 % to wafer heating under conditions of low bias power. This study demonstrated how the "on-wafer" temperature sensor not only yields a temperature profile distribution across the wafer, but can be used to help determine plasma characteristics, such as ion flux profiles or plasma processing temperatures.

4.2 Introduction

Wafer temperature control is an important parameter in the semiconductor industry, especially in plasma etching and deposition processes. It is well known that etching rates, uniformity and selectivity often have an Arrhenius-type dependence on wafer temperature[2]. Thus, temperature variation in the radial direction may introduce variations in critical feature dimensions across the wafer. Many experimental and modeling studies have been conducted in order to establish an understanding of wafer temperature response to plasma processing conditions[33,64,75-78]. These cases often investigate heat transfer to, from, and within the wafer in processing regimes with relatively high source or bias power and inert atomic gases (such as Ar) where ion-bombardment and ion-electron recombination have been identified as the major source of heat transfer[33,75,76,78]. Wafer heating mechanisms in molecular gas plasmas, however, can involve effects in addition to those identified in atomic gas plasmas. These mechanisms include thermal conduction from the neutral gas, where bulk temperatures can be in excess of ~1000 K, and heat release associated with atom recombination on the wafer surface.

The ability to make *in-situ* measurements of the wafer temperature during plasma processing is therefore a powerful diagnostic tool. The relative importance of wafer heating mechanisms can then be determined by combining experimental measurements of substrate temperatures with heat transport simulations and discharge physics calculations. This study utilizes the PlasmaTemp^{TM} sensor wafer that is capable of measuring wafer temperature profiles *in-situ*. The objective of this study was to determine the wafer heating effects in an Ar/O_2 inductively coupled plasma over a range of gas pressures (70 – 90 mT) and source powers (70 – 550 W), in the limit of no bias power. The following study demonstrates how a combination of experimental measurements and modeling of the PlasmaTemp^{TM} sensor, along with plasma diagnostics and modeling elucidate the various wafer heating mechanisms.

4.3 Experimental Methods

The experimental setup and diagnostic tools applied for this study have been described in detail in Chapter 2 and will be briefly reviewed here. In addition, the experimental methodology employed here are similar to a previous study conducted by C.C. Hsu *et al.*[33] with the PlasmaTemp^{TM} under pure Ar conditions and has been extended to study Ar/O_2 plasma conditions.

4.3.1 The "on-wafer" sensor: PlasmaTemp^{TM}

PlasmaTemp^{TM} is a commercially available sensor tool developed by KLA-Tencor made of production grade silicon wafer, covered with a layer of thermal oxide. It contains 30 temperature sensors, located at different radial positions (see Appendix A) and also houses a battery and data storage module. The sensors are protected with a layer of polyimide coating and the electronic module is hermetically sealed. The module is used for high speed, autonomous data acquisition and wireless data transfer (Figure 4.1). A 150 mm diameter version of the product is used for the present experiments. The PlasmaTemp^{TM} sensor wafer was mechanically clamped to the stainless steel chuck in a university built inductively coupled plasma (ICP) chamber.

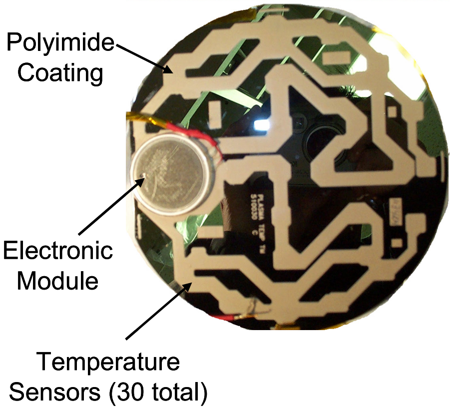

Figure 4.1 A snapshot of the 150 mm diameter version of the PlasmaTemp^{TM}. 30 temperature sensors are protected with a layer of polyimide coating and communicate with a hermetically sealed electronic module.

4.3.2 Experimental Apparatus & Diagnostic Tools

The ICP reactor consists of a cylindrical, stainless steel chamber, 20 cm in diameter and 10 cm in height. A five-turn planar coil delivers 13.56 MHz radio frequency (RF) power through the alumina dielectric window at the chamber top. A Faraday shield placed between the coil and the dielectric plate minimizes capacitive coupling. Backside helium (He) cooling was not used to cool the wafer in order to study the early transient temperature rise of the wafer. Additional experimental measurements were obtained from a Langmuir probe used to measure the electron temperature (T_e), electron density (n_e) and sheath potential by measurement of the electron energy probability function (EEPF) and application of the second derivative method[27,38]; an ion current probe used to measure the total positive ion current to the chamber surfaces[33]; and an optical emission spectrometer Ocean Optics PC2000-UV-VIS-ISA was used to monitor the plasma and ensure steady-state after plasma ignition.

4.3.3 Experimental Conditions

A series of experiments under the conditions displayed in Tables 4.1 and 4.2 were conducted to determine the wafer heating and cooling mechanisms in an Ar/O_2 mix plasma (see Appendix A for supplemental data). Approximately 70 % of the power listed in the tables (forward minus reflected power) is deposited into the ICP chamber[48,59]. The sensor wafer was exposed to a plasma for 30 seconds and the resulting temperature rise was observed to establish wafer heating trends. Additional measurements, after the plasma was extinguished and processing gas turned off, were obtained to observe wafer cooling behavior. A pure Ar plasma was used as a basis for comparison to the Ar/O_2 plasma in order to distinguish relative heating contributions from ion-bombardment and ion-electron recombination (the main mechanism in inert atomic gas plasma[20,33]), and thermal conduction and surface recombination (key additional mechanisms for molecular gas containing plasmas like O_2). In order to simplify the comparison between the Ar and Ar/O_2 plasma cases, the total ion flux to the wafer surface was maintained constant so that heating contributions due to ion bombardment kinetic energy would be similar. Note that more power is required to maintain the Ar/O_2 plasma to achieve an approximately equal ion current compared to the Ar plasma because there are additional collisional energy loss mechanisms in a molecular gas, including excitation of vibrational and rotational energy levels, molecular dissociations and negative ion formation[2] (*cf* Chapter 3, section 3.3.1).

Table 4.1 Experimental conditions investigated for a pure Ar plasma.

Chemistry	Pressure (mT)	Power (W)	Ion Current (mA/cm^2)
Ar – 70 sccm	70	70	1.18
Ar – 70 sccm	70	80	0.65
Ar – 70 sccm	70	95	0.82
Ar – 70 sccm	70	160	1.93
Ar – 70 sccm	70	190	2.44
Ar – 70 sccm	90	70	0.55
Ar – 70 sccm	90	70	0.58
Ar – 70 sccm	90	100	0.95
Ar – 70 sccm	90	130	1.57
Ar – 70 sccm	90	150	1.96
Ar – 70 sccm	90	200	2.90

Table 4.2 Experimental conditions investigated for comparing pure Ar to Ar/O_2 mixed inductively coupled plasmas.

Chemistry	Pressure (mT)	Power (W)	Ion Current (mA/cm^2)
Ar – 70 sccm	70	70	0.48
Ar – 70 sccm	70	70	0.65
Ar – 70 sccm	70	170	2.35
Ar – 70 sccm	90	65	0.48
Ar – 70 sccm	90	70	0.63
Ar – 70 sccm	90	190	2.65
Ar – 35 sccm : O_2 – 100 sccm	70	180	0.39
Ar – 35 sccm : O_2 – 100 sccm	70	200	0.45
Ar – 35 sccm : O_2 – 100 sccm	70	490	1.66
Ar – 35 sccm : O_2 – 100 sccm	90	170	0.28
Ar – 35 sccm : O_2 – 100 sccm	90	200	0.38
Ar – 35 sccm : O_2 – 100 sccm	90	550	1.64

4.4 PlasmaTemp^{TM} Thermal Model

A three-dimensional (3D) model of the PlasmaTemp^{TM} wafer was developed to simulate heat transfer to, from, and within the wafer. In a previous study by C.C. Hsu *et al.*[33] a 2D axisymmetric model of the sensor wafer was utilized. The 2D axisymmetric model near-quantitatively captures the wafer heating for short times (< 30 seconds); however, for longer times, the electronic module on the PlasmaTemp^{TM} (*cf* Figure 4.1) begins to act as a heat sink while heating or a heat source while cooling. The axisymmetry is thus lost for the longer time experiments, necessitating a 3D model. The 3D model, as displayed in Figure 4.2, more accurately accounts for the thermal properties of the wafer, sensors, and electronic module. The 3D model only differs in the addition of the electronic module, which is assumed to have quartz crystal thermal properties and is 3.94 cm in diameter and 3.6 mm thick. Therefore, the 3D model contains one additional transient thermal heat conduction equation to be solved and the reader is referred to C.C. Hsu *et al.*[33] for a detailed description of the model setup. The key points of the model are briefly reviewed here.

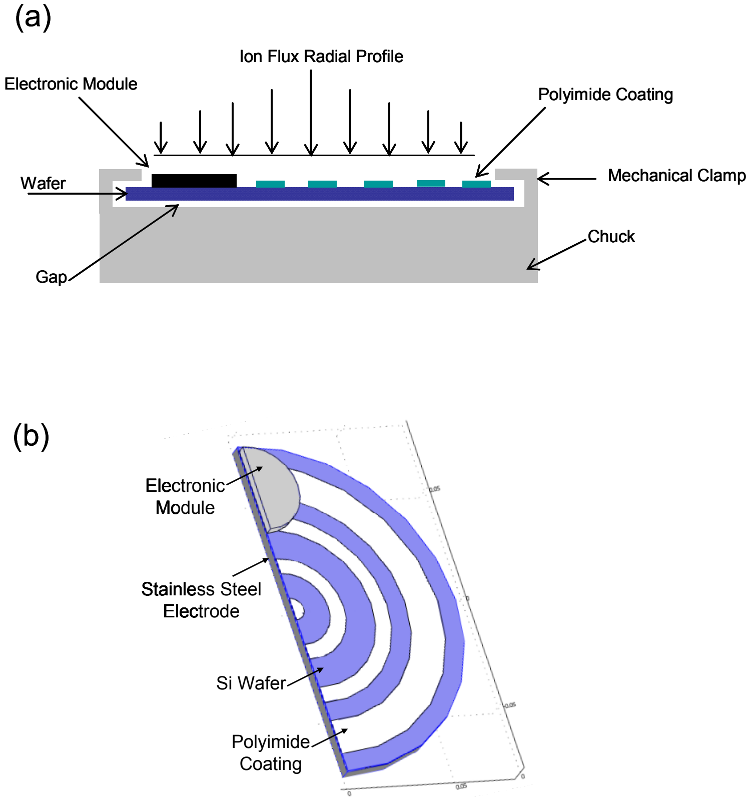

Figure 4.2 A 3-dimensional model of the PlasmaTemp^{TM} sensor wafer. (a) Side view: The model consists of 5 domains including a stainless steel chuck, a gap, Si wafer, polyimide coating, and an electronic module of thicknesses, 5 mm, 50 µm, 675 µm, 40 µm, and 3.6 mm, respectively. (b) The polyimide coating is modeled as concentric rings covering 42 % of the wafer.

The 3D model consists of 5 coupled domains: the electronic module, polyimide coatings, wafer, gap, and chuck, within which the conductive heat flux equation is solved:

$$\rho C_p \frac{\partial T}{\partial t} + \nabla \cdot (-k \nabla T) = 0 \tag{4.1}$$

The initial temperature, T_0, of the system was set at 300 K. An effective heat transfer coefficient (h_{eff}) used to described the heat lost from the backside of the Si wafer to the stainless steel chuck through the gap is determined in a semi-empirical manner and is defined as the ratio of the gap thermal conductivity to gap thickness,

$$h_{eff} = \frac{k_{gap}}{d_{gap}} . \tag{4.2}$$

It was found that using a value of $h_{eff} = 10$ W m^{-2} K^{-1} at the wafer center and $h_{eff} = 40$ W m^{-2} K^{-1} at the wafer edge where the wafer is mechanically clamped (improving thermal contact) yields near-quantitative agreement between the model predicted transient radial temperature profile and PlasmaTemp^{TM} measurements. The boundary conditions for all sides of the chuck, gap, wafer and polyimide coatings are set to be thermally insulated. The chuck bottom surface is defined as a constant temperature surface, T_0 = 300 K. The wafer surface, i.e. the exposed Si wafer, polyimide coatings, and electronic module experience an incident heat flux from the plasma. The sides of the electronic module are also defined as having an incident heat flux due to sheath formation around the electronic module. The sheath forms between the quasi-neutral plasma region and the bounding chamber walls and also around plasma-immersed objects such as probes[2,38]. The sheath formation around immersed objects is, in general, geometry-dependent[79]. For simplicity, an incident heat flux is defined for the electronic module surface and sides, while ignoring any heat flux to the adjoining edges of the surfaces.

The total heat flux to the wafer surface is the sum of a variety of heating mechanisms and is dependent on radial position and plasma type. For a pure Ar plasma it was found that there are two important heat sources: transfer of kinetic energy from the Ar ions (Ar^+) and electrons (e^-) bombarding the surface and the absorption of energy released during ion-electron recombination[33,48]. However, in molecular gas plasmas such as an Ar/O_2 plasma, there are additional heating mechanisms. Ion and electron bombardment still play a significant role, therefore kinetic energy transferred from Ar^+ and e^- as well as from the molecular and atomic oxygen ions (O_2^+ and O^+) will be important (q_{ions}). However, two new terms, thermal conduction (q_{cond}) heating from the neutral gas, and O-atom recombination (q_{rec}) heating must also be included.

q_{cond} is important especially when bulk (neutral gas) temperatures are in excess of 1000 K. The neutral gas temperature of molecular gas plasmas may exceed temperatures of equivalent density atomic gas plasmas due to additional heating mechanisms. Heat may be transferred to the neutral gas via electron-neutral dissociation reactions, electron-neutral momentum transfer, electron-neutral energy transfer, ion-neutral energy transfer, gas phase thermochemistry and exothermic wall recombination reactions[28,80,81]. One proposed cause of the neutral gas temperature increase of molecular gas plasmas is the Franck-Condon effect and inelastic collisions that lead to vibrational or rotational excitation of molecules[28,80]. Franck-Condon heating occurs when electron-impact dissociation leads to dissociation products with excess kinetic energy. These hot dissociation products in turn heat the neutral species through collisions. Estimates of the magnitude of this heating indicate that it can lead to peak neutral gas temperatures on the order of 1000 K.

q_{rec} is important because atoms can recombine on surfaces and release heat equivalent to the molecule's dissociation energy (ε_{diss}). Some fraction of this energy release is retained by the wafer thus contributing to the temperature increase.

The contribution of each type of heat flux, q_{ions}, q_{cond}, and q_{rec}, is included in the thermal model. Because radially-resolved experimental values for the flux of ions, metastables, and neutrals to the wafer surface and values for the neutral temperature above the wafer surface cannot be readily measured, they are obtained from an ICP chamber model. The ICP model simulation is adjusted (through the applied source power) until the simulation wall ion current is equivalent to the experimentally measured ion current, thus normalizing experiment to model. This allows for extrapolation of the experimental data from the position of the Langmuir probe above the surface down to the wafer surface (*cf* Chapter 3, section 3.2.3). This model has been described in detail by Hsu[48] and has been found to accurately simulate the ICP reactor chamber. Appendix C contains the ICP numerical model and describes the modifications made for generation of Ar-metastable (Ar^m) species.

The heat flux expressions for the Ar and Ar/O_2 ion contributions, and the q_{cond} and q_{rec} terms are defined in Equations 4.3 – 4.6, respectively.

$$q_{Ar} = n_{Ar^+} u_{B,Ar^+} e\left(\Phi_p + 0.5T_e + 2T_e + \varepsilon_{iz}\right) + \frac{1}{4} n_{Ar,m} \bar{v}_{Ar} \varepsilon^* \tag{4.3}$$

$$q_{Ar/O2} = q_{Ar} + n_{O2^+} u_{B,O2^+} e\left(\Phi_p + 0.5T_e + 2T_e + \varepsilon_{O2,iz}\right) + n_{O^+} u_{B,O^+} e\left(\Phi_p + 0.5T_e + 2T_e + \varepsilon_{O,iz}\right) \tag{4.4}$$

$$q_{rec} = \frac{1}{4} n_O \bar{v}_O \gamma_{rec} \varepsilon_{O2,diss} \tag{4.5}$$

$$q_{cond} = \frac{16}{15\pi} \frac{k}{\lambda} \left(\frac{T_g}{T_w} \right)^{1/2} \left(T_g - T_w \right) \tag{4.6}$$

The ion bombardment energy is determined from the measured floating potential, Φ_p (eV). Zero bias voltage is applied to the chuck and there are large grounded walls adjacent to the chuck, therefore the sheath voltage is set equal to Φ_p. Φ_p is obtained experimentally from Langmuir probe measurements by taking the first derivative of the I-V characteristic[27]. The pre-sheath potential energy is defined as $0.5T_e$ and the electron thermal energy is $2T_e$ [2]. ε_{iz} for Ar^+, O_2^+, and O^+, are set equal to 15.8 eV, 12.14 eV and 13.61 eV, respectively. ε^* is 11.6 eV and it is assumed that all Ar^m quench with unity probability on all surfaces. $\varepsilon_{O2,diss}$ is 5.12 eV, and the O-atom recombination probability is γ_{rec}. For simplicity, it is assumed that all electron-ion and atomic recombination energy is retained by the wafer The q_{cond} expression is equivalent to the jump boundary condition at the chamber walls utilized in the ICP model[47,48]. k is the neutral gas thermal conductivity, λ is the neutral mean free path, and T_g is the neutral gas temperature above the wafer surface. T_w is the wafer temperature.

4.5 Results & Discussion

The PlasmaTemp™ sensor wafer was exposed to a pure Ar and Ar/O_2 mix plasma under the conditions listed in Table 4.1 and 4.2. These conditions enabled rapid and stable plasma ignition so that the initial temperature rise could be studied without transients due to power adjustments. Furthermore, recall that experiments were conducted without chuck bias so that wafer heating effects are not dominated by kinetic energy transfer from bombarding ions alone and other heating effects could be observed. Pure Ar conditions were first examined to ensure that other heating mechanisms, such as Ar^m and thermal heat conduction did not play a major role. This was followed by an examination of heating mechanisms for Ar/O_2 plasmas focusing on heating contribution from thermal heat conduction and O-atom recombination.

4.5.1 Wafer Heating Mechanisms in Ar Plasmas

In the previous PlasmaTemp™ study[33], wafer heating in inert, atomic plasmas, such as Ar, were attributed to kinetic energy transfer due to ion bombardment ($n_i u_b e \Phi_P$) and ion-electron recombination ($n_i u_b e \varepsilon_{iz}$). Although additional heating mechanisms such as presheath energy transfer ($0.5 n_i u_b e T_e$), electron thermal energy transfer ($2 n_i u_b e T_e$) and Ar-metastable quenching ($0.25 n_{Ar,m} v_{Ar} \varepsilon^*$) are insignificant factors, the terms were included in the 3D model study for completion. Figure 4.3 demonstrates good agreement between experimental and simulation results that includes the additional heating terms for 90 mT 70 W, 0.55 mA/m^2 and 130 W, 1.57 mA/cm^2 cases. For low powers (i.e. low ion fluxes) the model tends to slightly underestimate the temperature rise since the model-predicted plasma density is more underestimated at lower powers. Examination of the time evolution of $\partial T/\partial t$ demonstrates that the model well predicts the rate of wafer temperature increase (Figure 4.4).

The fraction of heat transfer from ion bombarding energy, ion/electron recombination, electron thermal energy, Ar^m and presheath energy are ~32 %, ~51 %, ~13 %, ~0.8 %, and ~3 %, respectively (see Appendix A). Other heating mechanisms such as photon irradiation contributed to ~ 0.25 % of the total heat flux and were considered negligible. The modeled total heat flux to the wafer surface scales linearly with the experimental ion current (Figure 4.5). Note, the Ar^+ and Ar^m fluxes were determined from the ICP model as described in the section 4.4.

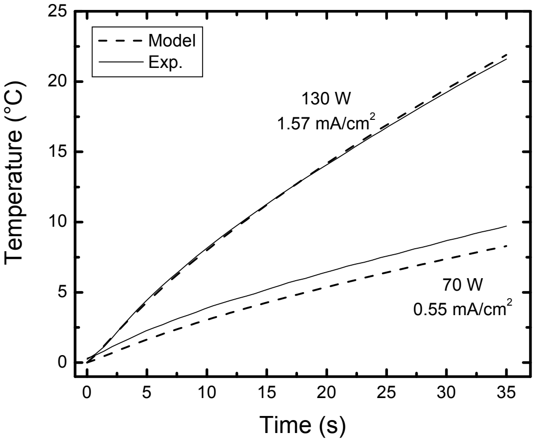

Figure 4.3 PlasmaTemp^{TM} vs. simulation temperature rise for pure Ar plasmas at 90 mT, 130 W and 70 W.

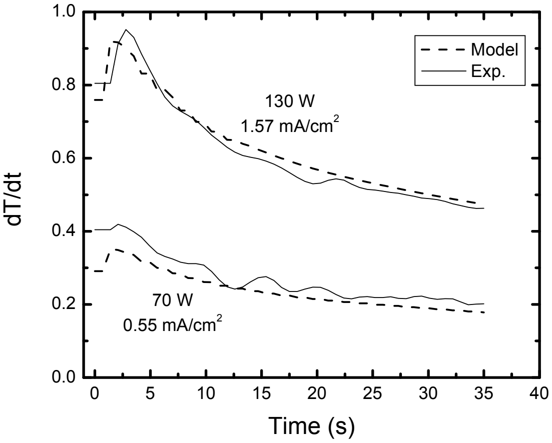

Figure 4.4 PlasmaTemp^{TM} vs. simulation evolution of $\partial T/\partial t$ with time for pure Ar plasmas at 90 mT, 130 W and 70 W.

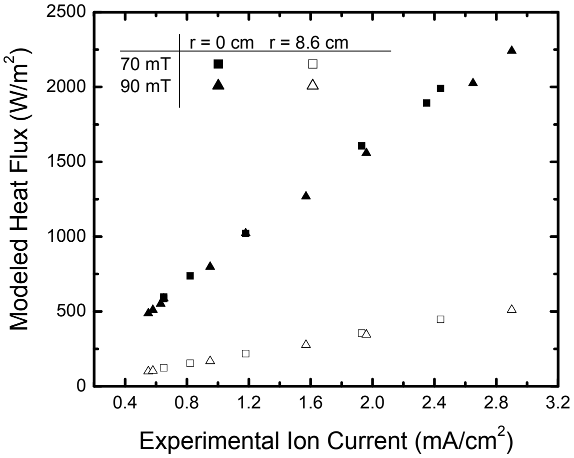

Figure 4.5 Modeled heat flux to wafer surface at chamber center (r = 0 cm) and edge (r = 8.6 cm) in pure 70 mT and 90 mT Ar plasmas.

4.5.2 Wafer Heating Mechanisms in Ar/O_2 Plasmas

The role of ion-bombardment induced wafer heating in Ar/O_2 plasmas were studied by generating a plasma with ion currents similar to that generated in Ar plasmas. Figure 4.6 displays results obtained with the PlasmaTemp^{TM} sensor wafer at different radial positions (r = 0 cm to r = 6.47 cm). A 70 mT Ar discharge with a total ion current of 0.48 mA/cm^2 is compared to a 70 mT Ar/O_2 discharge with a similar ion current of 0.45 mA/cm^2.

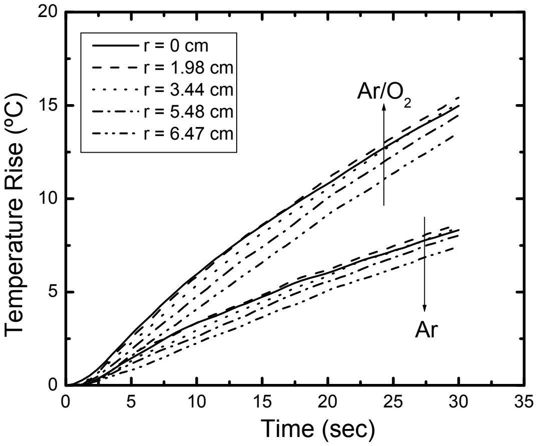

Figure 4.6 PlasmaTemp^{TM} temperature rise for a 70 mT, 70 W, 0.48 mA/cm^2 Ar plasma and an Ar/O$_2$ plasma at 70 mT, 200 W, 0.45 mA/cm^2.

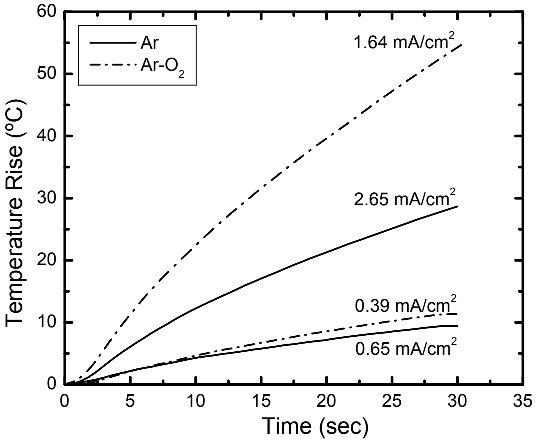

Figure 4.7 PlasmaTemp^{TM} temperature rise at r = 0 cm, in Ar vs. Ar/O$_2$ plasmas. See Table 4.2 for experimental conditions.

A similar total ion current in an Ar and Ar/O$_2$ discharge should yield a nearly identical temperature rise if wafer heating can be solely attributed to kinetic energy transfer from ion bombardment and ion-electron recombination. However, it was observed under nearly identical total ion fluxes that the temperature rise for the Ar/O$_2$ plasma is two times greater. The larger temperature rise suggests additional heating mechanisms arise in molecular gas plasmas. In other experiments (Figure 4.7), PlasmaTemp^{TM} measurements show that for a 30 s exposure to an Ar discharge having an ion flux ~1.6 times greater than the Ar/O$_2$ discharge, the wafer temperature is ~30 degrees lower than the wafer exposed to the Ar/O$_2$ plasma. Therefore, even in conditions where the ion current is far smaller in the Ar/O$_2$ discharge (i.e. less kinetic energy transfer due to ion bombardment) there is a significant amount of heating that must be attributed to another source.

In previous studies by C.C. Hsu *et al.*[33] and as demonstrated in section 4.5.1, modeling showed that the PlasmaTemp^{TM} temperature rise for a pure Ar plasma was due to the sum of ion bombardment, ion-electron recombination, electron thermal energy, Ar^m quenching, and pre-sheath ion energy. If the wafer response for an Ar/O$_2$ discharge is similarly modeled with respect to an Ar discharge, i.e. exclude the q_{cond} and q_{rec} terms and only consider heat transfer due to the flux of O_2^+, O^+ and Ar^+ and their respective ion-electron recombination reactions, then a significant under-prediction of the temperature rise results. Figure 4.8 shows a comparison between experimental and modeling results for a 90 mT Ar/O$_2$ plasma with an ion flux of 1.64 mA/cm^2. Here, the model accounts for heating due only to ion bombardment and ion-electron recombination. Simulation results show a temperature rise 32 degrees less than the experimental temperature rise after a 35 s exposure to the plasma. When the evolution of the time derivative of the temperature, $\partial T/\partial t$ vs. t (Figure 4.9) is examined, it is found that within the first three seconds of plasma exposure, the simulation predicts a rate of temperature rise 2.4 times smaller than in the experiment. The model is therefore missing some heating terms. For the Ar/O$_2$ discharge at these conditions, kinetic energy transfer from ion bombardment and ion-electron recombination contributes to only 45 % of the total wafer heating.

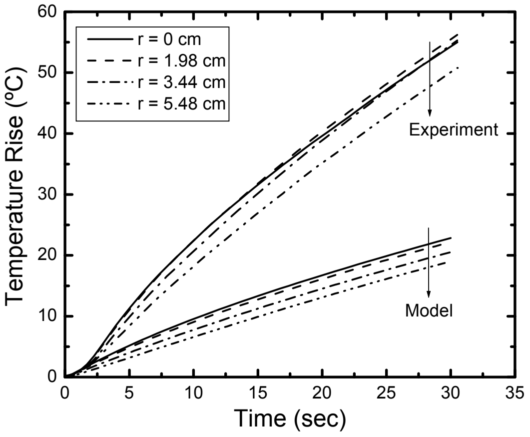

Figure 4.8 PlasmaTemp™ temperature rise for a 90 mT, 550 W Ar/O_2 plasma vs. modeled temperature rise: $q_{Ar\text{-}O2}$ (excluding q_{cond} and q_{rec}).

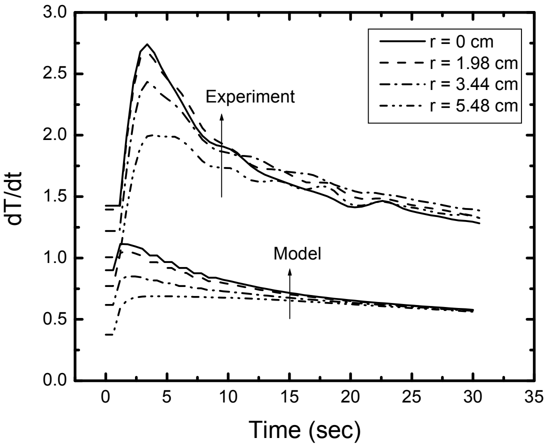

Figure 4.9 PlasmaTemp™ $\partial T/\partial t$ for a 90 mT, 550 W Ar/O_2 plasma vs. modeled $\partial T/\partial t$: $q_{Ar\text{-}O2}$ (excluding q_{cond} and q_{rec}).

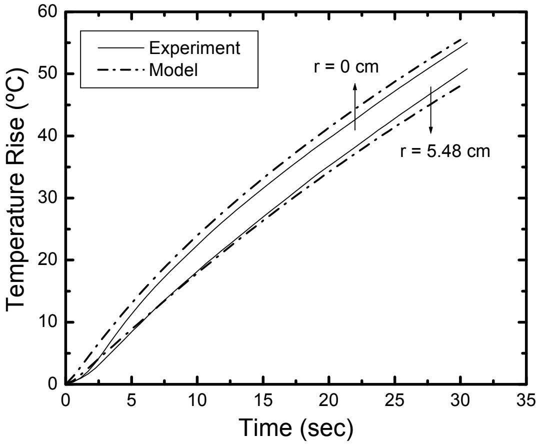

Figure 4.10 Temperature rise for 90 mT, 550 W Ar/O_2 plasma. PlasmaTemp™ vs. modeled temperature rise: $q_{Ar\text{-}O2} + q_{cond} + q_{rec}$.

Better agreement is achieved when q_{cond} and q_{rec} terms are included in the model (Figure 4.10). Plot 4.10 displays near-quantitative agreement between the experimental and model temperature rise (at r = 0 cm and r = 5.48 cm), showing that q_{cond} from the neutral gas and O-atom recombination on the wafer surface can account for the remaining 55 % of wafer heating. Under these conditions a γ_{rec} of 0.02 was used and contributed 15 % of total wafer heating. The neutral gas temperature above the wafer surface originally predicted from the ICP model was 500 K at r = 0 cm. The uncertainties in the plasma model are such that this value is only an estimate. Therefore the temperature was increased by 10 % to improve agreement between the wafer thermal model and the experimental results. The same trend is obtained for other experimental conditions as well, although not shown here.

It is important to note that distinguishing the heat contribution due to either q_{cond} or q_{rec} individually is difficult. In this analysis, the O-atom surface recombination coefficient and the peak neutral gas temperature were treated as adjustable parameters in the model in order to match measurements and model. As is well known precise values of γ_{rec} are difficult to experimentally measure due to various complicating factors such as coupling with ion bombardment, among other effects[82]. A typical value reported for γ_{rec} for O atoms on insulating materials is 0.01[83]. For this study, a value of 0.02 for γ_{rec} was chosen as an approximate value and fixed for all modeling conditions. Similarly, plasma neutral gas temperatures are difficult to experimentally measure or model, with precision. Bulk plasma temperatures can be measured through optical emission spectroscopy (OES)[28]. The neutral gas temperature, or translational temperature, can be estimated by observing the rotational energy of a diatomic species, such as N_2, that has been introduced into the gas flow. The rotational energy mode is generally assumed to be in thermal equilibrium with the translational energy mode due to efficient kinetic energy transfer during collisions[28]. Measurements with OES, however, are line of sight averages that yield rotational temperatures that may be only within ± 200 K of the actual peak neutral gas temperature[28]. Even if accurate (± 1~10 K) experimental measurements for the bulk temperature could be utilized to determine the accuracy of the ICP model's temperature predictions, there is still the matter of determining the gas temperature above the wafer surface. For the purposes of the present study, the ICP model-predicted gas temperature above the wafer surface was used as a first estimate of T_g and was accordingly increased or decreased (± 10 %) to achieve the best fit to the measured temperature vs. time data.

Table 4.3 displays the relative heat contribution from each modeled heat flux component at r = 0 cm and t = 0 s for Ar/O_2 90 mT, 550 W, 1.64 mA/cm^2 and 90 mT, 170 W, 0.28 mA/cm^2 experiments. The percent contributions are based on only the seven mechanisms studied in the heat flux calculations. Under these conditions, heating from Ar^m quenching is less than 1 % and is in agreement with other studies[64,77]. Therefore, heating due to Ar^m quenching is considered negligible in comparison to other heat sources. q_{cond}, however, does play a significant role in wafer heating (up to 50 % under certain processing conditions).

Table 4.3 The relative heat flux contributions as determined by the 3D thermal model for Ar/O_2 plasma cases.

Ar/O_2	90 mT, 550 W, 1.64 mA/cm^2	90 mT, 170 W, 0.28 mA/cm^2
Ion Bombardment	14.7 %	10.4 %
Ion/Electron Recombination	7.1 %	13.7 %
Electron Thermal Energy	1.8 %	1.1 %
Ar^m Quenching	0.1 %	0.1 %
Thermal Heat Conduction	46.4 %	36.5 %
O-atom Recombination	12.7 %	33.6 %
Total Modeled Heat Flux	3,850 W/m^2	950 W/m^2

Heating and cooling mechanisms, such as radiation, may also play an important role in wafer temperature response, although they weren't included in this study. For the investigated conditions a heat flux generated by photon radiation was ~ 2 – 5 W/m^2, which is less than 0.25 % of the total heat flux and was determined to be negligible[64,84,85]. Also, calculations showed that for these short time (~ < 60 s) experiments where maximum temperature rises varied between 10 ~ 70 K above room temperature depending on the processing conditions, radiative cooling was negligible. Other heat sources such as energy released due to combustion of polyimide on the wafer surface were also not included. Energies released by dissociating CO bonds would release ~ 7 – 11 eV to the wafer surface[85]. This heat release would significantly increase the wafer temperature rise, which was not observed in experimental results. This could be validated by testing with a uniform polyimide or polysilicon coating on the sensor wafer, which was not done in this study. Lastly, other effects such as fast neutrals were eliminated since the sheaths are nearly collisionless for the investigated conditions.

4.5.3 Wafer Cooling Mechanisms

Heat transfer to, from, and within the wafer is best captured with a 3D model that considers the thermal effects of the electronic module. The electronic module is a 3.6 mm thick device with a relatively large heat capacity value (820 J kg^{-1} K^{-1}) that acts as a heat sink during wafer heating, or a heat source during wafer cooling (Figure 4.11 – 4.12). Wafer cooling trends were captured with the PlasmaTemp^{TM} by monitoring the wafer after being exposed to a plasma for ~30 seconds.

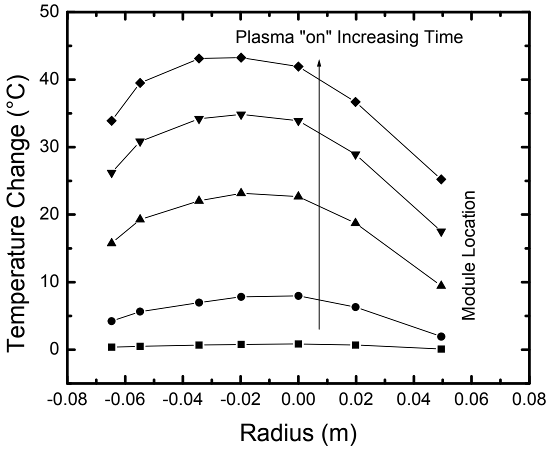

Figure 4.11 PlasmaTemp^{TM} temperature rise, at various times, during exposure to a 90 mT, 550 W Ar/O$_2$ plasma.

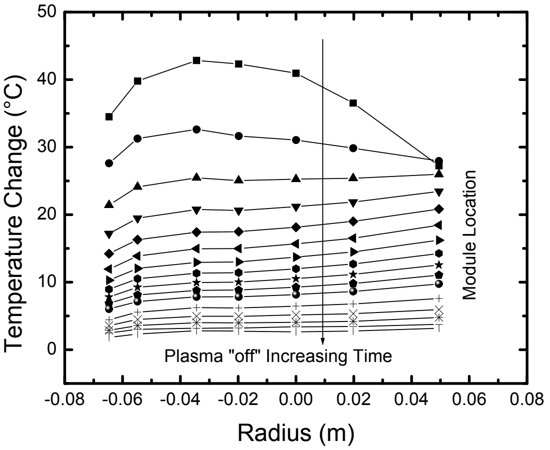

Figure 4.12 PlasmaTemp^{TM} cooling trend, at various times, after exposure to a 90 mT, 550 W Ar/O$_2$ plasma.

The temperature decrease as a function of time is the sum of two exponential decays. Figure 4.13 shows the PlasmaTemp™ cooling trend after being exposed to a 90 mT, 550 W Ar/O_2 plasma for 35 seconds. The measured wafer temperature transient behavior of the wafer is modeled with the following exponential decay expression,

$$T_w \propto \exp\left(\frac{-h_1 t}{\rho_1 Cp_1 \delta_1}\right) + \exp\left(\frac{-h_2 t}{\rho_2 Cp_2 \delta_2}\right) \tag{4.7}$$

where h_i, ρ_i, Cp_i, and δ_i, are the heat transfer coefficient, density, heat capacity and thickness of (1) the wafer and (2) the module respectively. The characteristic time delay constant is defined as

$$\tau = \frac{\rho Cp \delta}{h}. \tag{4.8}$$

Fits to the experimental data show that the first characteristic time constant (τ_1) is ~ 72 seconds and the second characteristic time constant (τ_2) is ~340 seconds. τ_1 is attributed to the thermal heat capacity of the sensor wafer and the heat transfer resistance between the wafer and the chuck. Using the effective heat transfer coefficient of the wafer-chuck gap, i.e. $h_1 = 10$ W m^{-2} K^{-1}, and assuming the wafer is a composite material consisting of Si and polyimide coating, yields a value for τ_1 of 67 seconds. τ_2 is almost five times larger than τ_1 and can be shown to be due to the thermal inertia of the electronic module which acts as a significant heat sink or source, affecting the transient thermal behavior of the wafer. This effect can be readily observed in temperature contour plots of the wafer surface as illustrated in Figure 4.14 (also Figure 4.11 and 4.12), and yields significant insight into the effects of sensor wafer design. Note, that convective heat transfer must be considered if neutral gas flow is not turned off after the plasma is extinguished.

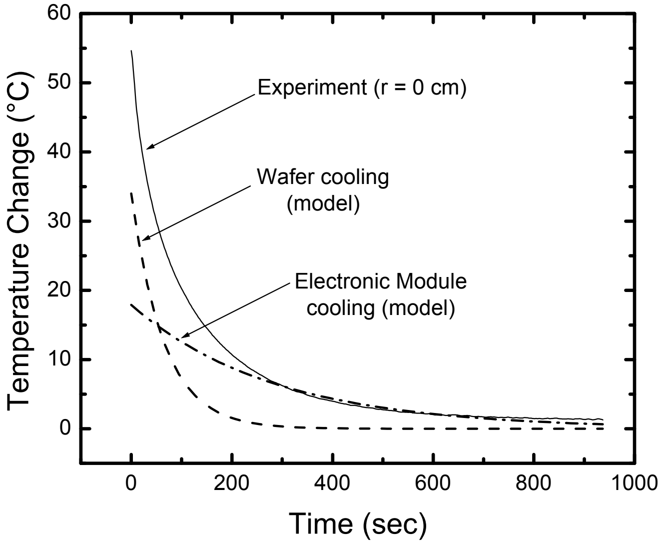

Figure 4.13 PlasmaTemp™ cooling trend after exposure to a 90 mT, 550 W Ar/O_2 plasma for 35 s. Model fits demonstrate wafer cooling is the sum of two exponential decays, each due to the cooling of the Si wafer and electronic module.

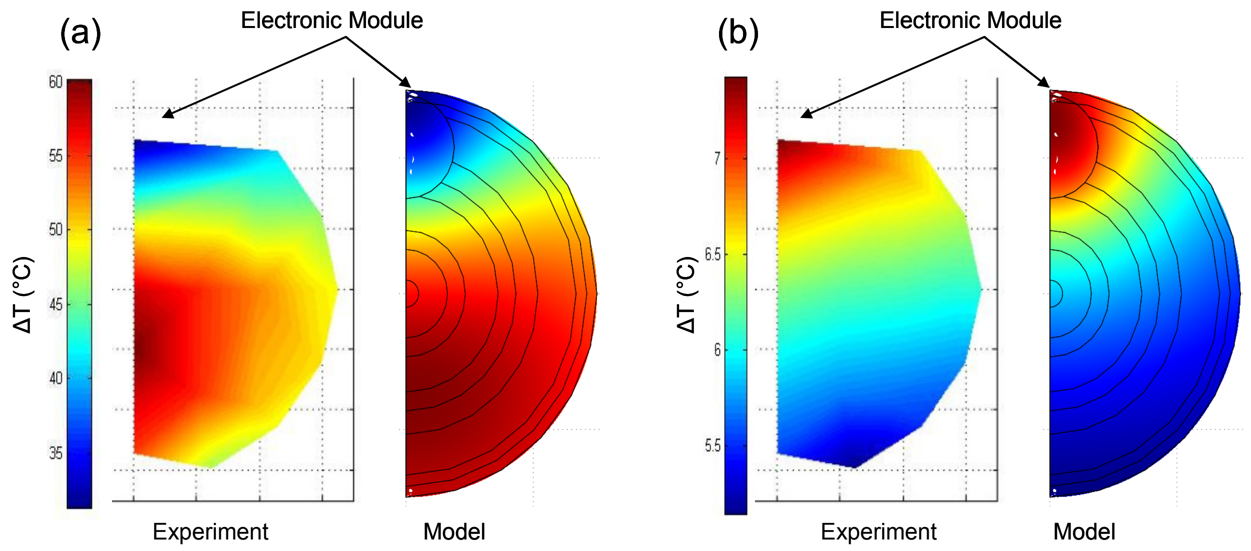

Figure 4.14 A qualitative comparison between the experimental and modeling temperature contour profiles of the PlasmaTemp^{TM} wafer processed in a 90 mT, 550 W Ar/O_2 plasma. (a) Temperature rise after 35 s plasma exposure. (b) Cooling profile after the plasma has been extinguished for 200 s.

4.6 Conclusion

Wafer heating mechanisms in an Ar/O_2 ICP were investigated by combining *in-situ*, real time temperature measurements from the PlasmaTemp^{TM} sensor wafer with a 3D heat transfer model of the wafer. Comparisons between pure Ar and Ar/O_2 discharges demonstrated that heating from the gas phase and O-atom recombination can be important in molecular gas plasmas. These mechanisms were shown to contribute as much as 70 % to wafer heating under conditions of low bias power. This study demonstrated how the "on-wafer" temperature sensor not only yields a temperature profile distribution across the wafer, but can be used to help determine plasma characteristics, such as ion flux profiles or plasma processing temperatures. The 3D model also successfully captured the thermal behavior of each domain and accounted for the 3D temperature distortion that arose due to the heat capacity of the electronic module. This result gives insight into the role of sensor wafer design on performance under transient conditions.

Chapter 5 – “On-Wafer” Voltage Sensor Analysis in an Inductively Coupled Plasma

5.1 Abstract

This chapter presents a second study on a novel, “on-wafer” sensor, the PlasmaVolt^{TM}. The commercially manufactured PlasmaVolt^{TM} sensor wafer was studied in the inductively coupled plasma reactor in an effort to validate sensor measurements. A pure Ar plasma at various powers (25 – 420 W), for a range of pressures (10 – 80 mT) and bias voltages (0 – 250 V) was utilized. A numerical sheath simulation was simultaneously developed in order to interpret experimental results. It was found that PlasmaVolt^{TM} sensor measurements are proportional to the RF-current through the sheath. Under conditions such that the sheath impedance is dominantly capacitive, sensor measurements follow a scaling law derived from the inhomogeneous sheath model of Lieberman[2]. Under these conditions, sensor measurements are proportional to the square root of plasma density at the plasma-sheath interface, one-fourth root of the electron temperature, and one-fourth root of the RF-bias voltage. When the sheath impedance becomes increasingly resistive, the sensor measurements deviate from the scaling law and tend to be directly proportional to the plasma density. The measurements and numerical sheath simulation demonstrate the scaling behavior as a function of changing sheath impedance for various plasma conditions.

5.2 Introduction

The semiconductor industry’s need for continuous improvement of feature and chip scaling requires stringent process control and a thorough understanding of the dynamic relationships between process control variables and plasma characteristics. Therefore, plasma and wafer diagnostics that couple processing control parameters to plasma and wafer characteristics are essential tools that will bring an understanding of how chip features evolve as a function of processing conditions. Traditional plasma diagnostic tools are typically *in-situ* or in-line and are typically attached to the plasma etch tool. These devices may be present in the load/lock chamber for pre or post processing measurements or mounted on the reactor wall. In-line sensors are categorized as either "wafer state" or "process state" sensors[22]. A process state sensor monitors the process, i.e. they may detect gas phase reactants and product species, and bulk temperatures and densities, with residual gas analyzers (RGA), optical emission spectrometers (OES) or Langmuir probes, respectively[25-28]. A wafer state sensor monitors changes directly observed on the wafer surface, such as etch rates or film thickness. Examples of such sensors include but are not limited to reflectometers, ellipsometers, and scatterometers[16,21,23].

These diagnostic tools aren't without merit, but they do have drawbacks especially in commercial applications. In-line and *in-situ* metrology typically measure bulk parameters such as plasma temperature, density and species type. The metrology may also be limited to monitoring single-locations on a wafer thus yielding average thickness values or etching rates. These monitoring tools may not directly take into account the spatial variation in etching rate or film thickness across the wafer, which is important when dealing with wafers 300 mm in diameter[17]. Furthermore, in-line metrology often requires modification of commercial tools to accommodate the installation of monitoring devices, thus increasing the cost and complexity of integrating sensors onto the equipment.

New metrology tools that are capable of providing spatially-resolved wafer-state information are called "SensArray^{TM}" or "on-wafer" sensors. These are wafers with sensors embedded onto the wafer surface, capable of measuring parameters such as wafer temperature at different radial positions. These sensor wafers are entered into production flow with standard product wafers and act as autonomous measuring devices capable of capturing the temporal evolution of wafer processing states in real time. Real time, *in-situ* measurements at the wafer level improves diagnostic capabilities without requiring integration of additional equipment to the plasma etching tools, saving both time and operational expenses[19,24]. Furthermore, establishing the temporal and spatial evolution of wafer-surface or plasma characteristics will allow for more finely tuned control of the processing equipment. This will be necessary as feature dimensions continue to grow smaller and demands for robust sensors and process controllers increase. For plasma etch, process objectives include critical dimension control, minimizing damage and contamination, and increasing uniformity and selectivity. "On-wafer" sensors in plasma processes have the potential to enhance process control by providing important information about the plasma at the wafer location.

One commercially available "on-wafer" sensor system is PlasmaVolt^{TM}, manufactured by KLA-Tencor. PlasmaVolt^{TM} records spatially resolved, real-time, and *in-situ* measurements of RF-current at the wafer surface. These measurements have the potential to yield information on the physical interaction between the plasma, sheath, and wafer surfaces at any time and location, which would allow for better process control capabilities. For example, in an inductively coupled plasma (ICP) etch tool, an important feature is the capability to separately control the bias voltage or power of the wafer electrode and the source power. Bias voltage controls the energy of ions impacting the wafer and source power controls the ion flux[2]. Control over the ion flux and ion bombarding energies at the wafer surface are important because they help determine the etch rates, etch selectivities and profile evolution of features. Many studies have utilized *in-situ* diagnostic tools, such as gridded ion energy or retarding field ion energy analyzers, to measure the ion energy distribution (IED) profiles over a wafer surface[86-88] or Langmuir probes to measure plasma densities over the wafer surface[38]. These experimental studies are often limited to single location analyses within the chamber and generally require modification of the etch tool. If an "on-wafer" wafer like the PlasmaVolt^{TM} could be utilized to take measurements that were related to a plasma characteristic such as density, PlasmaVolt^{TM} would allow for spatially resolved, real-time measurements without disturbing the plasma environment or requiring tool modification.

Because sensor wafers like PlasmaVolt^{TM} are still relatively new, information about the relationship between the sensor measurements and the plasma characteristics are limited. Therefore the objective of this study is to establish a more quantitative understanding of the relationship between the PlasmaVolt^{TM} sensor measurements and the plasma characteristics. This was done by combining measurements of the plasma with a sheath model and comparing the results to the sensor measurements. The plasma density, electron average energy, and ion flux to the wall were measured in an ICP tool under a variety of conditions. In addition, the voltage waveform applied to the wafer-bearing electrode was measured as well. The sheath models relate plasma characteristics such as plasma density and electron temperature to RF-voltage and current at the electrode. The combined plasma diagnostics and models are then related to sensor measurements.

5.3 Experimental Methods

5.3.1 Experimental Apparatus & Diagnostic Tools

The PlasmaVolt^{TM} sensor wafer was tested in a university built ICP etch system that has been described in Chapter 2. Briefly, the ICP reactor consists of a cylindrical, stainless steel chamber, 20 cm in diameter and 10 cm in height. A five-turn planar coil delivers 13.56 MHz radio frequency (RF) power through the alumina dielectric window at the chamber top. A Faraday shield placed between the coil and the dielectric plate minimizes the capacitive coupling. The bias voltage is delivered through a second 13.56 MHz power source through the stainless steel electrode (chuck) at the chamber bottom. The bias voltage applied to the chuck is measured with a high voltage probe connected directly to the chuck and is recorded with a TDS 2022B Tektronix oscilloscope. The bias power is a few watts (10 – 30 W), therefore minimizing the capacitive coupling between the chuck and plasma. The measured peak-to-peak bias voltage is approximately twice the DC-bias voltage.

The ICP chamber is also equipped with several diagnostic tools, including a Langmuir probe, a wall-mounted ion current probe, and an optical emission spectrometer (OES). All experimental sampling ports are located 2.54 cm above the chuck. The Langmuir probe is designed according to the guidelines of Godyak *et al.*[27,38]. The probe is introduced into the plasma chamber through a differentially pumped radial motion feed-through and can access different radial positions ranging from r = 0 cm to r = 7.5 cm. The probe is used to measure the electron temperature (T_e), electron density (n_e) radial profiles and the sheath potential by measurement of the electron energy probability function (EEPF) and application of the second derivative method[27,38]. The electron temperature is defined as 2/3 of the average electron energy[2]. The ion current probe is a circular, 0.4 cm^2 wall-mounted planar probe DC biased to –40 V. A 2 mm wide guard ring surrounding the probe and similarly biased to –40 V is used to suppress edge effects[25]. The probe is used to measure the total positive ion current to the chamber wall[33]. The temporal evolution of the DC ion current is measured by an Agilent 34410A 6½ Digit Multimeter, thus also establishing the relative plasma stability over time. The optical emission collected with an Ocean Optics PC2000-UV-VIS-ISA OES is used to monitor the plasma and ensure the plasma has reached steady-state soon after plasma ignition. The temporal evolution of the 811.5 nm Ar emission line is used to indicate plasma stability[33].

5.3.2 The "on-wafer" sensor: PlasmaVolt™

PlasmaVolt™ is a commercially available 200-300 mm diameter sensor wafer produced by KLA-Tencor. For the present experiments, a 150 mm diameter version of the wafer, modified with an electronic tether is utilized (Figure 5.1). The electronic tether is fed through a vacuum compatible electrical feed-through located in the ICP chamber wall and is attached to a DC power supply. The ICP chamber lacks a load-lock mechanism for rapid transfer of the wafer into and out of the chamber. This electronic tether modification therefore allows consecutive experiments to be carried out rapidly, avoiding the time-consuming process of repetitively opening and closing the chamber.

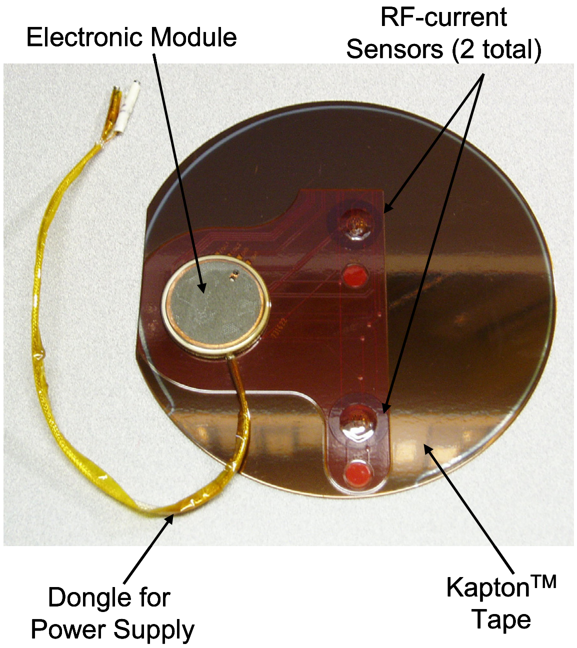

Figure 5.1 150 mm diameter version of the PlasmaVolt™ sensor wafer.

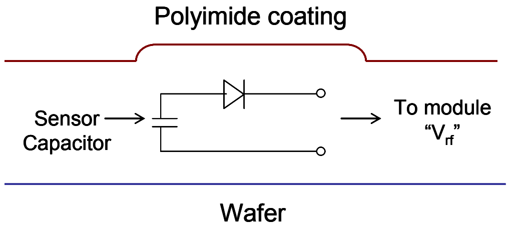

Figure 5.2 Diagram of the PlasmaVolt™ RF-current sensor.

The sensor wafer contains two RF-current sensors located at 5 mm and 66 mm away from the wafer center and is protected with a layer of Kapton tape. The sensors consist of thin film, copper capacitors connected to RF-diodes (Figure 5.2). The sensor diameter is 0.81 cm and the disk thickness is 0.0018 cm; the spacing between disks is 0.0025 cm. RF-current flowing along the wafer at the sensor location creates a DC voltage across the sensor capacitor. The sensor capacitor is ohmically isolated from the plasma and a decoupling capacitor between the sensor capacitor and diode, ensures only the AC measurement is transmitted. Sensor measurements are proportional to the rectified and period-averaged RF peak voltage across the capacitor[48]. This measurement is subsequently referred to as 'V_{rf},' or peak-to-peak voltage from the sensor. The wafer is equipped with an electronic module that allows for high speed, autonomous data acquisition and wireless data transfer. Data is downloaded to a computer equipped with PlasmaView™, a software package.

5.3.3 Experimental Conditions

The PlasmaVolt™ sensor wafer was tested in the ICP chamber with an Ar plasma under a variety of conditions, 10 – 80 mT, 0 – 400 W ICP power, 0 – 250 V bias voltage. For the experimental results described in this chapter, the conditions are listed in Table 5.1. Supplemental conditions can be found in Appendix B.

Table 5.1 Experimental and simulation conditions for the PlasmaVolt™ study. Ion current density at the chamber wall, and n_e and T_e values are measured 2.54 cm above the wafer surface. For all conditions, 10 – 250 V of bias voltage is applied.

Pressure (mT)	ICP Power (W)	Ion Current Density (mA/cm^2)	Edge n_e x 10^{10} (cm^{-3})	Center n_e x 10^{10} (cm^{-3})	T_e (eV)
10	25	0.25	1.08	1.50	3.1
10	35	0.13	3.40	5.50	3.1
10	50	0.60	2.36	3.45	3.4
10	65	0.38	2.00	3.10	3.4
10	100	1.27	4.88	6.91	3.4
10	160	1.58	6.70	9.30	3.4
10	200	2.61	9.96	13.5	3.4
10	290	3.50	1.50	1.90	3.4
10	400	5.67	19.7	25.3	3.5
10	420	5.50	2.10	2.80	3.6
50	50	0.56	5.47	9.86	2.6
50	200	3.19	31.1	37.8	2.2

5.4 Sheath Model Formulation

A one-dimensional (1D) model of a sheath was developed in a numerical software package, COMSOL™. A sketch of the domain is shown in Figure 5.3; the electrode is located at x = 0, and the total domain length (L) is adjusted from 5 to 10 mm depending on the biasing conditions, i.e. the length is adjusted to minimize solution convergence time. An initial length of 5 – 10 mm was chosen based on the analytical solution for the limiting case of the Child-Law sheath, discussed later. The domain length is chosen to be slightly greater than the sheath so that the plasma-sheath boundary conditions of plasma density, plasma potential and ion velocity can be applied consistently. The plasma is assumed to consist of a single positive ion species and electrons in a static neutral background of argon. For simplicity, electron temperature is assumed to be constant through the sheath and secondary electron emission and electron impact ionization are neglected in the model. It is known that in Ar plasmas for pressures below 100 mT and driven at 13.56 MHz, secondary electrons are typically not important[2]. Spatial and temporal profiles of ion velocity (u_i), potential (Φ), and density (n_i, n_e) are calculated by solving Poisson's equation and the fluid equations for ion-continuity and ion-momentum. Electrons are assumed to follow a Boltzmann distribution. The present model is intended to represent an RF-biased electrode in an inductively coupled plasma under conditions such that the plasma potential has little or no RF component. This is a good approximation in the experimental chamber utilized in this study.

The sheath model equations are,

$$\frac{\partial^2 \Phi}{\partial x^2} = -\frac{e}{\varepsilon_0}\left(n_i - n_e\right) \tag{5.1}$$

$$\frac{\partial u_i}{\partial t} + u_i \frac{\partial u_i}{\partial x} = \frac{eE}{m_i} - \nu_m u_i \tag{5.2}$$

$$\frac{\partial n_i}{\partial t} + \frac{\partial\left(n_i u_i\right)}{\partial x} = 0 \tag{5.3}$$

$$n_e = n_{es} \exp\left(\frac{\Phi}{T_e}\right) \tag{5.4}$$

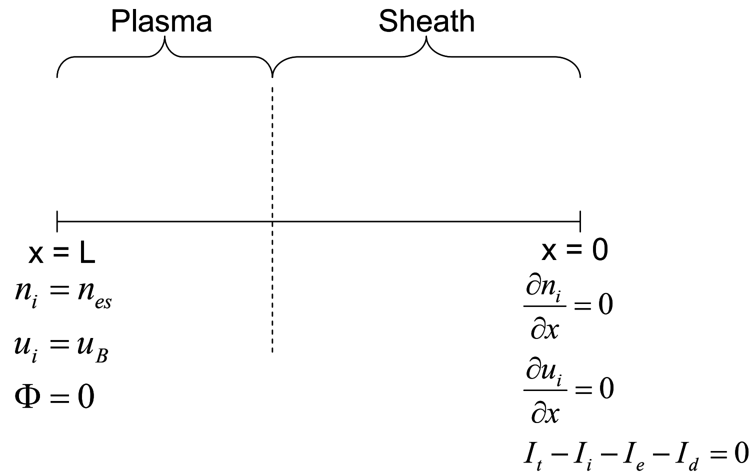

Figure 5.3 One-dimensional sheath model setup in COMSOL^{TM}. The electrode is located at x = 0, and the domain extends into the plasma by L = 5 ~ 10 mm. The boundary conditions at each endpoint are displayed. The electrode is driven by a sinusoidal RF-current, I_t, that is user defined.

In Equations 5.1 – 5.4, ε_0 is the permittivity of free space, m_i is the ion mass, n_{es} is the electron density near the plasma-sheath boundary, and ν_m is the ion-neutral momentum transfer frequency. Equation 5.2 contains the Krook collision term $(\nu_m u_i)$[2,89], assuming that only ion-neutral elastic and charge exchange collisions occur within the sheath. ν_m is a function of the ion mean free path, λ_i (cm), which here is given as a function of pressure, P (Torr). ν_m is given by the following expression:

$$\nu_m = \frac{u_i}{\lambda_i} = \frac{u_i}{330P} \tag{5.5}$$

At the electrode, x = 0, the potential boundary condition is determined by a current balance, in an approach similar to sheath models developed by Sobolewski *et al.*[51] and Aydil *et al.*[90]. The total current, I_t, is the sum of ion (I_i) and electron (I_e) conduction currents and the displacement current (I_d),

$$I_t(t) = I_i(x,t) + I_e(x,t) + I_d(x,t) \tag{5.6}$$

where,

$$I_t(t) = I_{rf}\sin(2\pi f t) \tag{5.7}$$

$$I_i(x,t) = -e n_i(x,t) u_i(x,t) A \tag{5.8}$$

$$I_d(x,t) = -\varepsilon_0 A \frac{\partial E(x,t)}{\partial t} \tag{5.9}$$

$$I_e(x,t) = eAn_{es}\left(\frac{eT_e}{2\pi m_e}\right)^{1/2}\exp\left(\frac{\Phi}{T_e}\right) \tag{5.10}$$

A is the area of the electrode. The RF-current amplitude, I_{rf}, is assumed to be known and f is the electrode driving frequency (13.56 MHz). The voltage at the electrode is calculated as part of the solution to Poisson's equation.

At x = L, the plasma potential is set as $\Phi = 0$, consistent with the assumption of no RF component in the plasma potential. Positive ions are required to enter the sheath with at least the Bohm velocity[2]. Therefore the ion velocity at x = L (just outside the sheath) is set equal to the Bohm velocity. The Bohm velocity is defined as,

$$u_B = \left(\frac{kT_e}{m_i}\right)^{1/2}. \tag{5.11}$$

The ion and electron density are nearly equal in the plasma bulk. n_{es} at x = L can be estimated using a Langmuir probe measurement that is scaled down to the wafer surface according to a simulation of the ICP chamber, explained in detail later[33,48]. The Bohm velocity is calculated via Equation 5.11 using the value of T_e obtained from Langmuir probe measurements 2.54 cm above the wafer surface.

5.5 Results & Discussion

5.5.1 Sheath Model Validation

The accuracy of the sheath model was tested in part by comparing results to experimental and numerical sheath model data produced by Sobolewski[51]. Sobolewski created a 1D sheath model similar to the one described here, extending from the electrode to an arbitrary position into the plasma. The simulation predicts ion and electron density profiles by solving the ion continuity, ion momentum, and Poisson's equations using the oscillating-step approximation for electrons, i.e. $n_e = n_i$ on the plasma side of the step (x < W(t)) and $n_e = 0$ on the sheath side of the step (x > W(t)). W(t) is calculated as a part of the solution. Sobolewski's model applies the Bohm criterion (i.e. the ions are accelerated by the electric field ($E = kT_e/2e\lambda_d$) to the Bohm velocity at the sheath edge) to the electrode surface. For consistency, the same BCs were applied for this study's sheath model. Also, Sobolewski's model uses the measured voltage across the sheath as an input parameter. As this was not available for input into the COMSOL™ simulation, Sobolewski's RF-current output (a nearly sinusoidal 0.8 A RF-current) was instead used as input. Sobolewski's model and the present simulation showed good agreement for the following condition, which was close to the conditions relevant for this study: 10 MHz driving frequency, 120 W source power, 0.319 A ion current at the electrode, plasma/sheath electron density of 1.25×10^{-11} cm^{-3}, and an electron temperature of 3.0 eV. Figure 5.4 from the present model is a plot of the sheath voltage and current components for this case, and it is in good agreement with the corresponding result in Figure 8 of Sobolewski[51].

It is noted that for a sinusoidal RF-current input, the resulting voltage drop across the sheath is highly non-sinusoidal and, as mentioned above, the waveform is similar to the sheath voltage measured by Sobolewski. During the cathodic phase of the cycle, electrons are repelled from the electrode surface and the corresponding electron current to the electrode is nearly zero. During this part of the cycle, the sum of the positive ion and displacement currents maintain the total current within the sheath. Note that inclusion of the time derivatives in the ion continuity and momentum equations allows the sheath model to capture transients in ion current and density through the period.

The present sheath simulation was also validated by comparing it to the limiting case of a direct current (DC) Child's Law analytical solution. In the Child Law DC sheath model, the electron density is assumed to be zero, and in this limit an analytical solution can be found for sheath thickness, *s*.

$$s = \left[\frac{\frac{2}{3}\left(\frac{5}{3}\right)^{3/2} \varepsilon_0 \left(\frac{2e\lambda_i}{\pi M}\right)^{1/2} V_{bias}^{3/2}}{e n_p u_B} \right]^{2/5} \tag{5.12}$$

Here λ_i is the ion mean free path and V_{bias} is the electrode DC voltage[2]. Sheath thickness results from the numerical simulation and the analytical Child Law sheath solutions are shown in Figure 5.5 for an Ar plasma at 10 mT. The points represent simulation solutions while the line represents the analytical solution to the collisional Child-Law sheath. It is clear that the collisional Child-Law sheath model and the collisional numerical sheath model are in reasonable agreement. The small differences are attributed to the fact that the numerical solution assumes Boltzmann-distributed electrons rather than zero electron density in the case of the Child's Law solution. The analytical Child-law solution also provides a good initial estimate for the domain length of the numerical simulation.

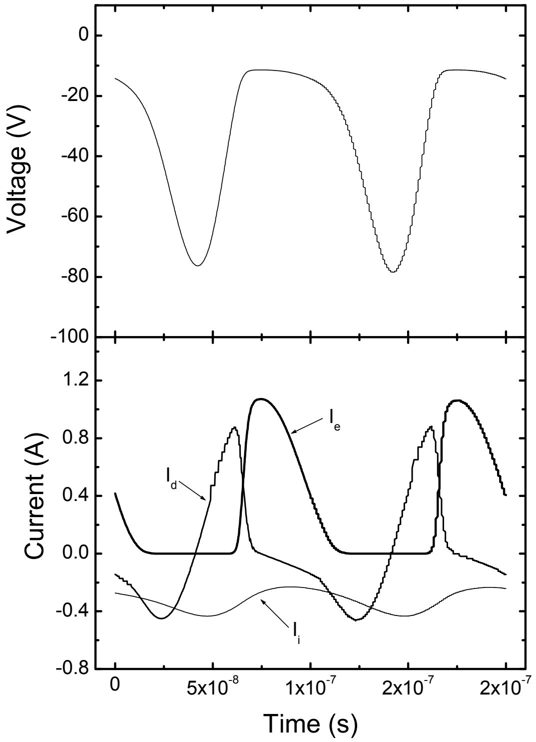

Figure 5.4 Simulation results for a 120 W, 10 MHz, plasma. Ion current: 0.319 A. Plasma/sheath density: 1.25×10^{-11} cm^{-3}. Electron temperature: 3.0 eV. (a) Voltage at the electrode. (b) Displacement, ion, and electron currents through the sheath.

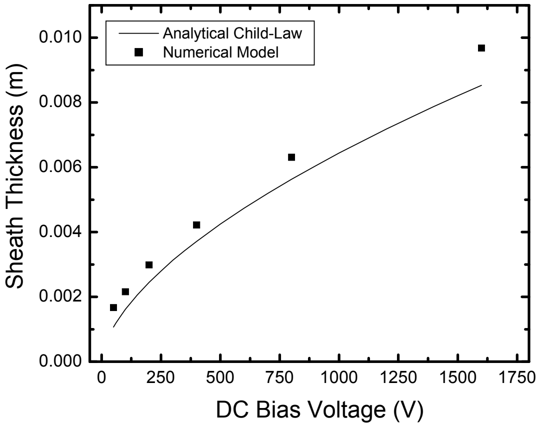

Figure 5.5 Numerical simulation vs. collisional Child-Law sheath analytical solution for a 10 mT, Ar plasma .

5.5.2 Sheath Simulation Results

The benefit of an inductively coupled plasma is the ability to independently control ion energy and plasma density. The deposition power controls plasma density while the bias power to the lower electrode controls the potential drop through the sheath, hence the ion energy[2]. The sheath simulation is useful in demonstrating the effects of bias voltages on plasma characteristics, such as electron density and current, through the sheath and onto the wafer surface for a range of operating pressures, powers, and frequencies. Figure 5.6 demonstrate typical plasma potential, ion velocity, and ion/electron density profiles through a sheath for an applied bias voltage (in this case I_{rf}). As the RF-current amplitude (I_{rf}) is increased, the potential drop through the sheath increases, generating a thicker sheath and causing a greater acceleration of ions toward the electrode. Ions tend to follow the period averaged potential drop in these thick sheaths, while the instantaneous drop is followed for thinner sheaths. The respective I_d, I_i, and I_e profiles, for reference are shown in Appendix B, and qualitatively agree well with the sheath simulation studies by Nitschke[91].

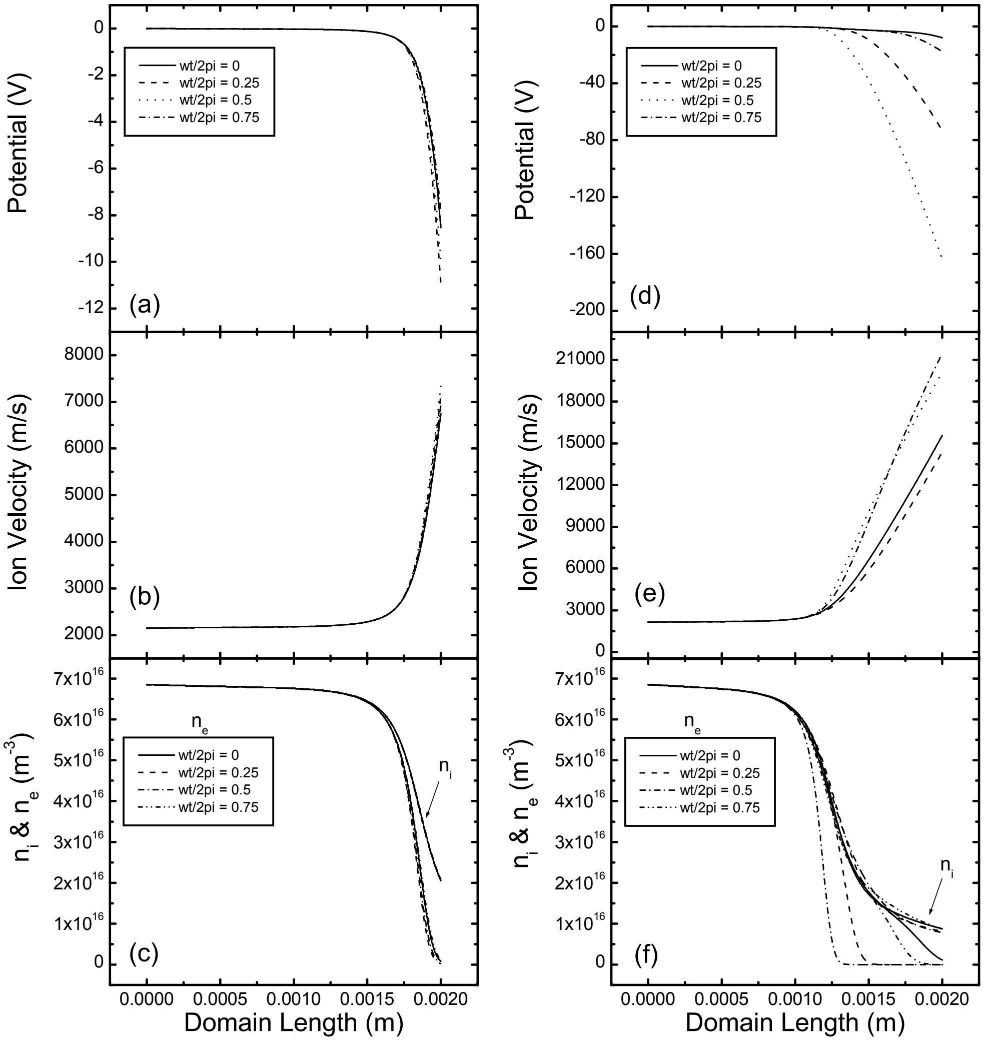

Figure 5.6 Simulation results: potential, ion velocity, n_i, and n_e profiles for a 10 mT, Ar plasma. (a) – (c): I_{rf} = 0.2 A. (d) – (f): I_{rf} = 1.0 A.

The sheath thickness is dependent on both the bias voltage and plasma density and is derived from the simulation according to Equation 5.13. Figure 5.7 clearly demonstrates that the sheath thickness increases with bias voltage while simultaneously the increasingly larger potential repels electrons from and accelerates ions toward the electrode (Figures 5.9 – 5.12). In contrast, as the plasma density increases, the sheath thickness decreases (Figure 5.8). This behavior agrees well with analytical solutions for sheath thicknesses (Equation 5.14) of low-density plasmas and high voltage applications derived from Lieberman[2]:

$$s(t) = \frac{\varepsilon_0 A \,{}^{\partial V}\!/_{\partial t}}{I_d} \tag{5.13}$$

$$s = 1.23\omega\varepsilon_0 \frac{V_{pp,bias}}{I_{rf}} \tag{5.14}$$

Comparing the sheath thickness to the ion mean free path (λ_i) demonstrates the degree of sheath collisionality. For $s < \lambda_i$ the sheath is collisionless, while $s > \lambda_i$ indicates the sheath is collisional. At low pressures, 10 mT, $\lambda_i \sim 0.003$ m and the sheath is considered collisionless throughout the entire RF-cycle (13.56 MHz), while at 20 mT, $\lambda_i \sim 0.0015$ m and the sheath is collisional for part of the RF-cycle. As the pressure increases to 50 mT and 80 mT ($\lambda_i \sim 0.0006$ m and 0.0004 m, respectively), the sheath is collisional for the entire RF-cycle. See Appendix B for plots.

Much like the sheath thickness, the dynamic behavior of the displacement, electron, and ion currents also depend on bias voltage and plasma density. Figure 5.13 shows the behavior of Φ_P, I_d, I_i, and I_e at the electrode surface, biased to 200 V, for a low density (35 W) and high density (420 W) plasma. At low plasma densities the potential is nearly sinusoidal and I_d is the primary current in the sheath while I_e and I_i can be considered negligible. As the plasma density increases, however, the potential grows increasingly non-sinusoidal and I_e and I_i become a significant fraction of the total current and begins to affect the sheath impedance (Figure 5.14).

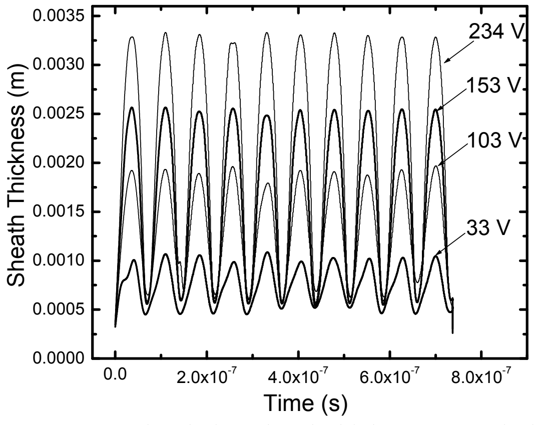

Figure 5.7 Simulation sheath thickness. Trends for a 10 mT, 25 W, Ar plasma, driven at 13.56 MHz for 33 V, 103 V, 153 V and 234 V bias voltage applications.

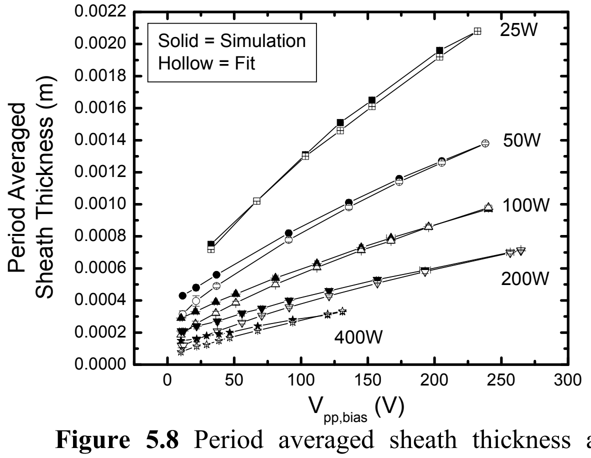

Figure 5.8 Period averaged sheath thickness and analytically derived sheath thickness, for a 10 mT, 25 W, 50 W, 100 W, 200 W, and 400 W Ar plasma.

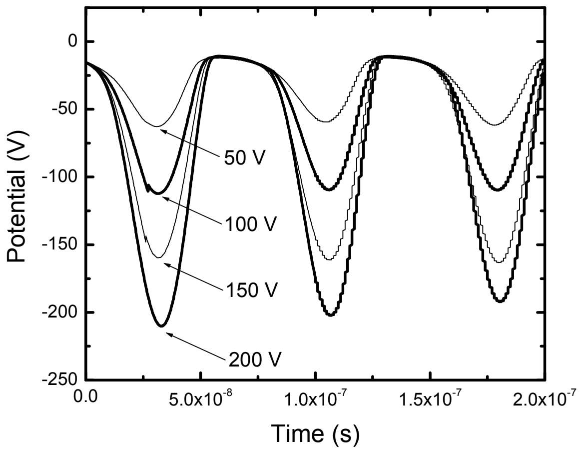

Figure 5.9 Simulation results: potential at the electrode biased at 50 V, 100 V, 150 V, 200 V for a 10 mT, 420 W Ar plasma.

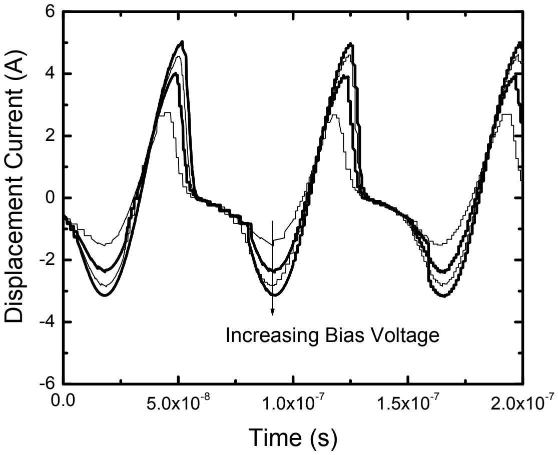

Figure 5.10 Simulation results: displacement current at the electrode biased at 50 V, 100 V, 150 V, 200 V for a 10 mT, 420 W Ar plasma.

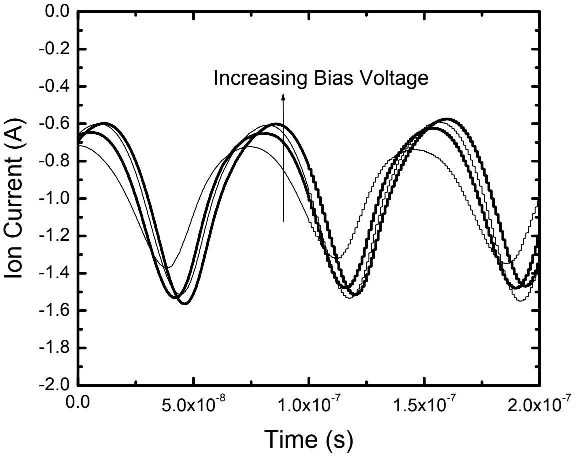

Figure 5.11 Simulation results: ion current at the electrode biased at 50 V, 100 V, 150 V, 200 V for a 10 mT, 420 W Ar plasma.

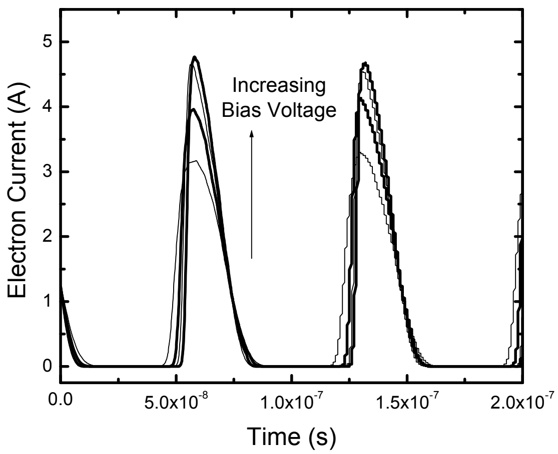

Figure 5.12 Simulation results: electron current at the electrode biased at 50 V, 100 V, 150 V, 200 V for a 10 mT, 420 W Ar plasma.

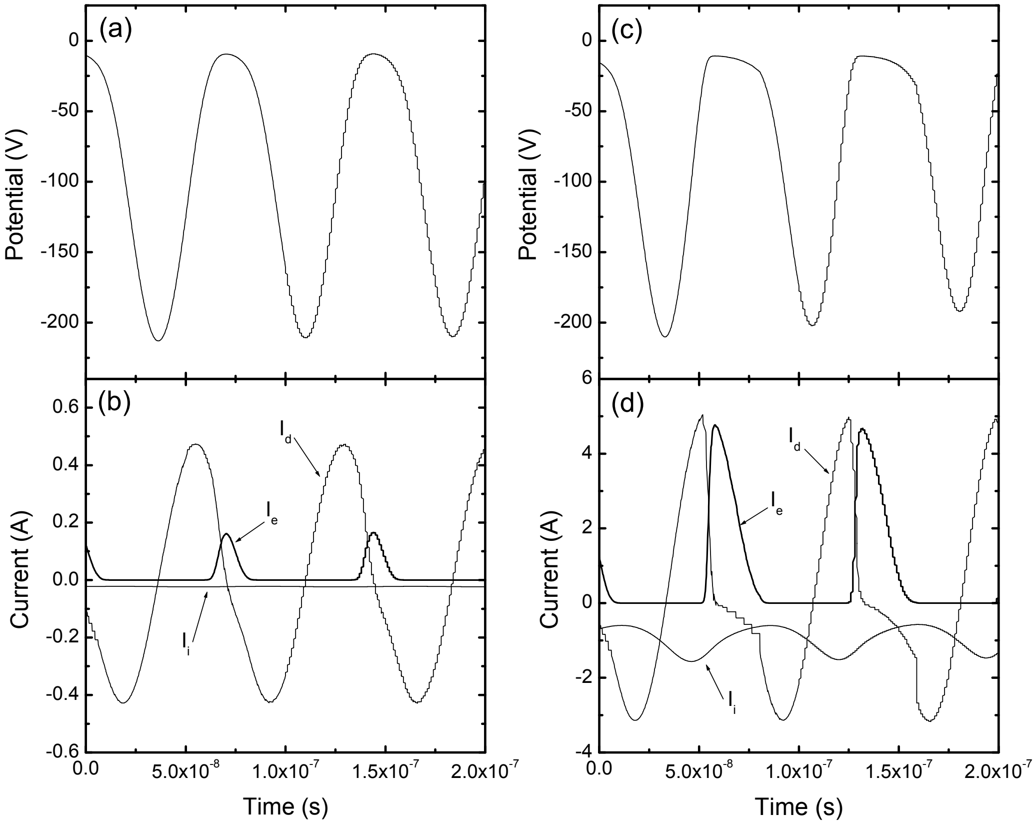

Figure 5.13 Sheath simulation generated potential, displacement current, ion current and electron current at the electrode surface. The electrode is biased to 200 V in a 10 mT (a – b) 35 W plasma, and (c – d) 420 W plasma.

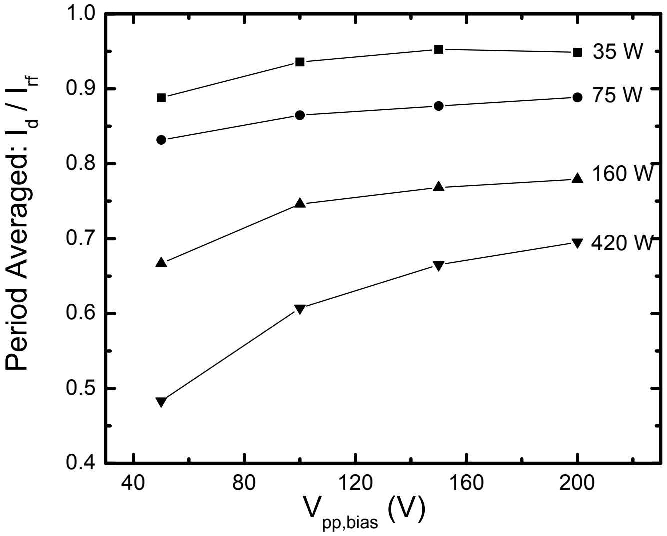

Figure 5.14 Simulation results: Period averaged fraction of displacement current for a 10 mT, Ar plasma.

5.5.3 Validating PlasmaVolt^{TM} Measurements

PlasmaVolt^{TM} sensor measurements (V_{rf}) as a function of the measured applied RF peak-to-peak bias voltage magnitude ($V_{pp,bias}$) are plotted (Figure 5.15) for two of the plasma conditions investigated (10 mT at 50 W and 400 W ICP power). Figure 5.15 shows that V_{rf} increases non-linearly with increasing $V_{pp,bias}$ for each ICP condition. Note, $V_{pp,bias}$ is measured closest to the chuck as possible (minimizing circuit length) and half the $V_{pp,bias}$ amplitude is approximately the DC-bias voltage. The difference between the center sensor measurement (solid points) and edge sensor measurement (hollow points) is attributed to the radial variation of the electron density at the plasma/sheath interface (n_{es}). As the pressure increases, the radial gradient of the density increases because the plasma transport processes becomes collisionally dominant. This produces a larger difference between center and edge density values and is reflected by the increasing difference between center and edge V_{rf} measurements. In the 10 mT case demonstrated in Figure 5.15, there is a center-to-edge average difference in n_{es} of 27 %. For a higher pressure, 50 mT, case (Figure 5.16) the average center-to-edge difference is 54 %. A more quantitative assessment of this effect requires interpretation with the sheath model as will be discussed later.

The numerical sheath simulation was utilized to test whether sensor measurements were proportional to the RF-current density. The simulation was run for the various ICP conditions, where input parameters n_{es} and T_e were obtained from experimental measurements. I_{rf} was changed until the simulated peak-to-peak bias voltage at the electrode ($V_{pp,bias}$) matched the experimental peak-to-peak bias voltages obtained with the oscilloscope (see Appendix B, section B.4). If V_{rf} is proportional to I_{rf} then a plot of I_{rf} vs. $V_{pp,bias}$ should resemble Figures 5.15 – 5.16. In fact, when plotting I_{rf} vs. $V_{pp,bias}$ and V_{rf} vs. $V_{pp,bias}$ (Figure 5.17), a one-to-one correspondence is observed, i.e. the superimposed experimental and simulation data points demonstrate that I_{rf} is in fact proportional to the sensor measurement, V_{rf}, for the cases considered here. This relationship, V_{rf} is proportional to I_{rf}, is used in the remaining data analysis.

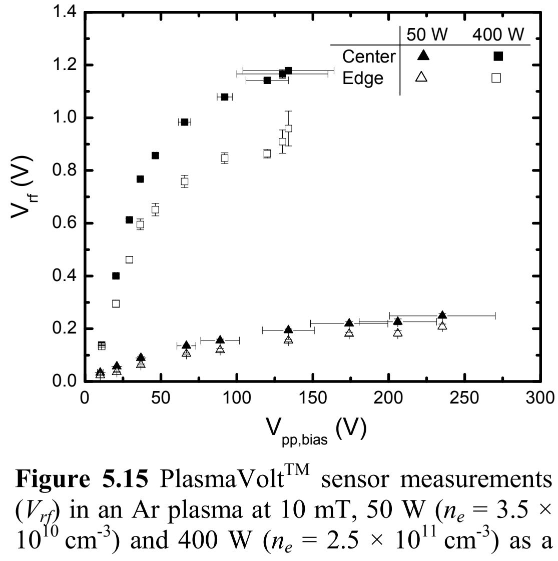

Figure 5.15 PlasmaVolt^{TM} sensor measurements (V_{rf}) in an Ar plasma at 10 mT, 50 W ($n_e = 3.5 \times 10^{10}$ cm^{-3}) and 400 W ($n_e = 2.5 \times 10^{11}$ cm^{-3}) as a function of the applied RF-bias voltage ($V_{pp,bias}$).

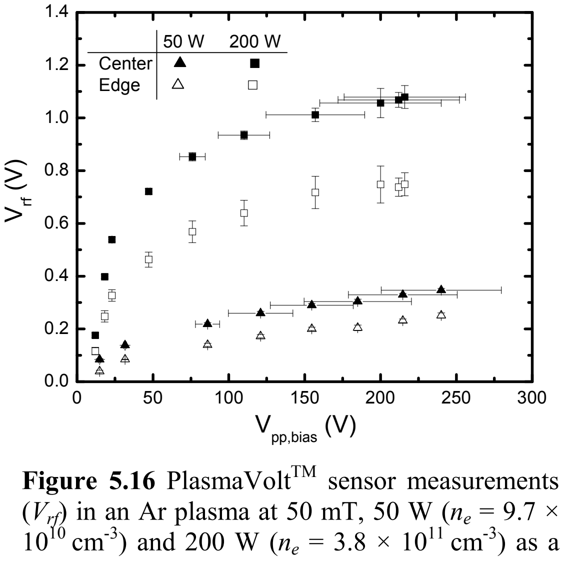

Figure 5.16 PlasmaVolt^{TM} sensor measurements (V_{rf}) in an Ar plasma at 50 mT, 50 W ($n_e = 9.7 \times 10^{10}$ cm^{-3}) and 200 W ($n_e = 3.8 \times 10^{11}$ cm^{-3}) as a function of the applied RF-bias voltage ($V_{pp,bias}$).

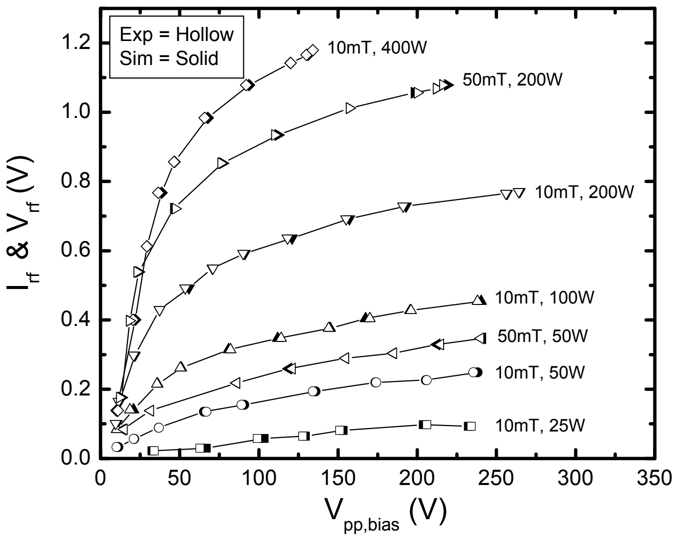

Figure 5.17 Sheath simulation results (solid) normalized to the experimental PlasmaVolt^{TM} measurements (hollow) for Ar 10 mT and 50 mT conditions displayed in Table 5.1. The results are superimposed, thus demonstrating that experimental sensor measurements (V_{rf}) are proportional to the RF-current through the sheath.

5.5.4 Correlating PlasmaVolt^{TM} Measurements to Plasma Density

Another goal of the study was to develop a quantitative model of the sensor response in terms of plasma quantities such as n_e and T_e. Since it is established that V_{rf} is proportional to I_{rf}, the next objective is to find a plasma sheath model that can relate how I_{rf} depends on plasma parameters. First an analytical sheath model is sought to apply to experimental measurements to obtain relevant scaling laws, if they can be found for the conditions chosen. Then the numerical sheath model is used to check that the analytical model can be applied to the conditions chosen. Finally, the numerical sheath model can be used to suggest plasma sheath conditions for which the analytical model will no longer suffice.

First the analytical inhomogeneous sheath model developed by Lieberman *et al.*[2] is tested. This model should be valid if the following conditions hold:

(1) The magnitude of the RF displacement current ($\tilde{I}_{disp}$) dominates over the conduction current.

(2) Ion density does not modulate through the RF period, implying $\omega^2 >> \omega_{pi}^2$, where ω_{pi} is the ion plasma frequency.

(3) The electrons respond rapidly to the RF-potential, implying $\omega^2 << \omega_{pe}^2$, where ω_{pe} is the electron plasma frequency.

(4) The electron density in the sheath is zero, implying $T_e << V_{dc}$ (DC voltage across the sheath) and the electron Debye length is less than the sheath thickness ($\lambda_{De} << s$).

(5) No electron-neutral inelastic collisions occur within the sheath, such as ionization.

(6) A sinusoidal RF-current passes through the sheath.

(7) No transverse variation exists along the electrodes, i.e. 1-dimensional treatment is valid.

To ensure the validity of these conditions during the experiments, a high voltage to the chuck is applied, such that $T_e \ll V_{dc}$ and $\lambda_{De} \ll s$, where V_{dc} is ½ $V_{pp,bias}$. The RF-bias power is relatively low, ~10 – 20 W, thus minimizing the capacitive coupling with the plasma The plasma potential is therefore approximated as constant. Even at low ICP powers, the ion transit time is several RF cycles, therefore the ions traverse the sheath with an average potential. In addition, although there is spatial variation in the plasma density across the chuck (as measured with the Langmuir probe), the sheath variation from center to edge is neglected for simplicity. It is later demonstrated that this is a reasonable assumption.

With these assumptions the following relationship was derived[2]:

$$\tilde{I}_{disp}^{2} = 1.73 e\varepsilon_0 \omega^2 n_{es} T_e^{1/2} V_{pp,bias}^{1/2} \tag{5.15}$$

Note, due to assumption (6) where a sinusoidal RF-current is assumed, self consistent equations can be derived to quantitatively determine the average ion sheath current and voltage expressions needed for Equation 5.15. Thus the constant plasma potential approach taken in the sheath model is also consistent with this derivation. This equation states that the square of $\tilde{I}_{disp}$ is proportional to n_{es} and the square roots of T_e and $V_{pp,bias}$. Given the previous result that V_{rf} is proportional to $\tilde{I}_{disp}$, Equation 5.15 becomes

$$\frac{V_{rf}}{n_{es}^{1/2} T_e^{1/4}} \propto V_{pp,bias}^{1/4}\,. \tag{5.16}$$

Plotting $V_{rf}/(n_{es}^{1/2}\ T_e^{1/4})$ vs. $(V_{pp,bias})^{1/4}$ (equivalently, $I_{rf}/(n_{es}^{1/2}\ T_e^{1/4})$ vs. $(V_{pp,bias})^{1/4}$) will test if this relationship is valid for the ICP conditions investigated.

The application of this model requires values for electron density at the plasma-sheath interface (n_{es}) and a bulk $T_{e.}$ The Langmuir probe that is available to measure n_e and T_e is taken 2.54 cm above the wafer. n_e values must be scaled down to the wafer surface and is accomplished by using a numerical model of the ICP chamber that gives fully resolved, spatial profiles of specie densities, velocities, and temperatures (*cf* Chapter 3, section 3.2.3). The ICP model has been described in detail previously[48] and has been used for similar purposes[33]. The ICP simulation is run under the experimental conditions observed and the resulting spatial scaling is applied to the experimental Langmuir probe data to determine n_{es}. Note there is a center-to-edge variation in the electron energy distribution function measurement and this is reflected in n_e measurements at the chamber center and edge (*cf* Table 5.1). The measured T_e values indicate there is very little spatial variation (< 10 %) (see Appendix B, Table B.1). In addition, the OES and ion current data used to monitor plasma stability does not significantly drift or change during bias-voltage applications (*cf* Chapter 3, sections 3.3 and 3.5). Therefore, the plasma is assumed stable even when bias voltages are applied and that n_e and T_e are not affected by the applied bias voltage.

The proposed model scaling law from the inhomogeneous sheath model (Equation 5.16) is tested in Figure 5.18, using the PlasmaVolt^{TM} sensor data and the scaled Langmuir probe data. The scaling law is demonstrated with three of the 10 mT plasma conditions. As can be seen, the data appear to follow the proposed scaling for the low density, 50 W and 100 W cases. The deviation in the 10 mT, 400 W case is attributed to the increasingly resistive nature of the sheath impedance and will be discussed in detail later. Note that when the appropriate edge and center n_{es} values are utilized in the scaling, the respective data points nearly collapse to a single line for both the 10 mT, 50 W and 100 W plasma conditions. With the scaling law, the center-to-edge data points now demonstrate only a 1 % (previously 27 %) difference for the 10 mT cases and a 7 % (previously 54 %) difference for the higher pressure, 50 mT cases (Figure 5.19). The superimposed center and edge data points show that the scaling law derived from the inhomogeneous sheath model accurately describes the relationship between the square-root of the electron density (accounting for spatial variation across the wafer) and V_{rf} sensor measurement. In addition, this demonstrates that assumption (7) is valid in that there is no significant transverse variation across the plates, allowing only for differences in n_{es} values.

Although not shown here, a similar linear result is obtained when Equation 5.16 is applied to the simulation data, i.e. plotting $(V_{pp,bias})^{1/4}$ vs. $I_{rf} / (n_{es}^{1/2}\ T_e^{1/4})$. For the low density cases, the simulation data behaves linearly and I_{rf} scales to the square-root of n_{es}. However, for the same higher density cases, (i.e. 10 mT, 400 W of Figure 5.18) the simulation data also does not follow the scaling derived from the inhomogeneous sheath model. As with the experimental case, this difference is attributed to the changing nature of the sheath impedance. The assumptions used to derive the scaling from the inhomogeneous sheath model stipulate that the sheath must be highly capacitive in nature. For the higher density cases where the scaling does not suffice to describe the relationship between measurement and plasma density, the sheath impedance is growing increasingly resistive in nature.

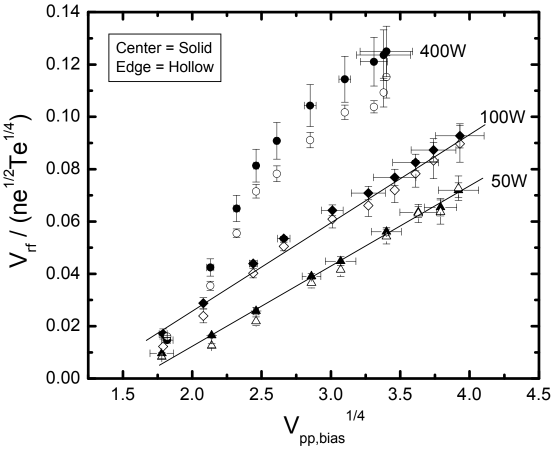

Figure 5.18 Scaling law derived from the inhomogeneous sheath model correlation applied to the PlasmaVolt^{TM} sensor data for a 10 mT Ar plasma at 50 W, 100 W, and 400 W.

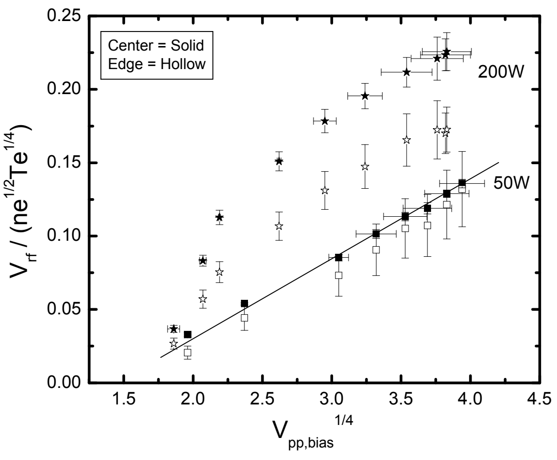

Figure 5.19 Scaling law derived from the inhomogeneous sheath model correlation applied to the PlasmaVolt^{TM} sensor data for a 50 mT Ar plasma at 50 W and 200 W.

The sheath impedance is a function of the sheath thickness, which is dependent upon the electron density and the voltage drop through the sheath[2] (*cf* section 5.5.2). Lower density and higher voltage tend to increase sheath thickness. Thicker sheaths result in following the period averaged potential drop and are highly capacitive. Higher density plasmas, at lower bias voltages, tend to develop thinner sheaths where the ions follow the instantaneous potential drop. These sheaths are more resistive in nature. The resistive or capacitive nature of the sheath is determined by taking the ratio of the displacement to conduction currents (I_{disp} / I_{cond}) from the numerical sheath simulation. In addition, the ratio of I_{disp} / I_{cond} is calculated based on experimental measurements, where $I_{disp} / I_{cond} \approx \omega / \omega_i$ and ω_i is the ion plasma frequency. Excellent agreement is found between experimental and simulation results for I_{disp} / I_{cond} (Figure 5.20). For I_{disp} / I_{cond} >> 1 the sheath is capacitive in nature; conversely, for I_{disp} / I_{cond} << 1 the sheath is resistive in nature[2]. The calculated ratios of I_{disp} to I_{cond} from the simulation are plotted as a function of the bias voltage and plasma-sheath interface density (Figure 5.21). This resulting figure obtained from the numerical sheath model demonstrates the plasma conditions (densities and bias voltages) for which the scaling law will no longer suffice.

As a further test of the limits of validity of the scaling law, Figure 5.22 displays the simulated RF-current values (solid lines) plotted as a function of density (at the plasma/sheath interface) for electrode bias ($V_{pp,bias}$) values ranging from 50 V – 200 V in a 10 mT Ar plasma. The scaling law applied from the inhomogeneous sheath model (dashed lines) follows the simulation results when the plasma density is relatively low and the applied voltage relatively high. Under these conditions, current through the sheath tends to be dominated by displacement current and is capacitive. However, as plasma density increases and/or sheath voltage decreases, the sheath thickness decreases and conduction current becomes more important relative to displacement current. Here, the sheath model scaling no longer holds and the RF-current becomes directly proportional to n_{es}.

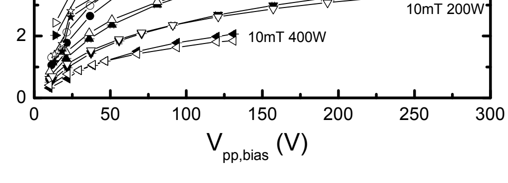

Figure 5.20 Ratio of displacement to conduction current as a function of applied bias voltage ($V_{pp,bias}$). Simulation results are compared to ratios (ω/ω_i) calculated from experimental data.

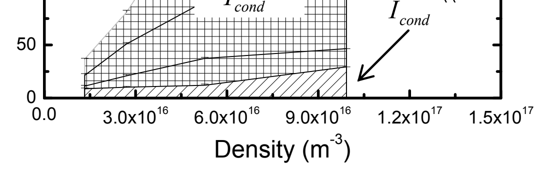

Figure 5.21 Simulation results for I_{disp} / I_{cond} values are plotted as a function of plasma density and $V_{pp,bias}$ and define the nature of the sheath impedance.

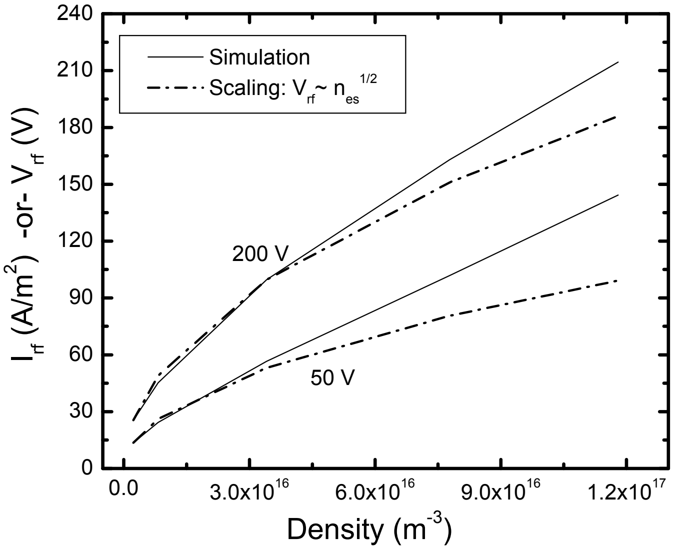

Figure 5.22 Numerical simulation results for high density plasmas at electrode bias values ($V_{pp,bias}$) ranging from 50 V – 200 V. Simulation results are compared to the scaling fit. For lower density plasmas and capacitive sheaths the RF-current is proportional to the square-root of plasma density. At higher densities with resistive sheaths the RF-current is proportional to the plasma density.

One unexpected result is the flexibility of the scaling law. First, the scaling law is applicable in the transition regime, where the sheath is neither fully capacitive nor resistive. For many of the low density conditions investigated in Table 5.1, the sheath simulations show the experiments fall into the transition regime where $\tilde{I}_{disp}$ is not dominant and a significant I_e flows through the sheath to the electrode. Surprisingly, the scaling of $\tilde{I}_{disp}$ with $V_{pp,bias}$ and n_{es} still holds quite well. The scaling may improve, i.e. different pressure (and thus density) conditions may superimpose if the sheath is entirely capacitive and $\tilde{I}_{disp} >> I_e$ and I_i. This may explain why the Ar 10 mT and 50 mT experimental studies did not collapse to the same line during the application of Equation 5.16.

Secondly, the inhomogeneous sheath model's scaling law performs well for both the collisionless and collisional sheath conditions. In this study, the 10 mT plasma condition is the only collisionless regime ($\lambda_i >> s$). For 20 – 80 mT conditions the sheaths become increasingly collisional. However, when the scaling law derived from the collisional inhomogeneous sheath model[2] is applied to the PlasmaVolt^{TM} data, the relationship between $\tilde{I}_{disp}$ with $V_{pp,bias}$, and n_{es} is worse. This demonstrates that the collisionless inhomogeneous sheath model is fairly applicable to a wide range of processing conditions.

5.5.5 Industry Relevant Applications

In industry, it is often important to know the ion flux and sheath impedance behavior during wafer processing since it may have direct impact on the ion energy distribution, etching rates and ultimately profile evolution. However, due to processing limitations, it may be impractical to measure the plasma densities and bias voltages. The experimental and simulation study with the

PlasmaVolt^{TM} sensor wafer demonstrates that the ion flux (plasma density) as well as resistive or capacitive behavior of the sheath can be predicted with this novel diagnostic tool and can be done so with minimal supplementary measurements. Since n_e scales with ICP deposition power (P_{ICP}) and bias power (P_{bias}) scales with the ion current and bias voltage ($J_{ions}V_{pp,bias}$), a plot of $V_{rf} / P_{ICP}^{1/2}$ vs. $P_{bias}^{1/4}$ should yield results similar to that in Figure 5.18. With this substitution of easily measured variables (power) combined with the PlasmaVolt^{TM} measurements, n_e can be readily back-calculated, and the sheath processing regime determined.

5.6 Summary & Concluding Remarks

In this chapter, it was demonstrated that PlasmaVolt^{TM} "on-wafer" measurements were proportional to the RF-current through the adjacent sheath at the wafer surface. A numerical simulation of an RF-sheath was developed and the simulated RF-bias voltage was matched to the experimental results by adjusting the total RF-current density boundary condition. By this method the RF-current density was shown to be proportional to the sensor measurement. In order to correlate radial variations in sensor measurement to plasma characteristics, such as plasma density, a relation between RF-current and plasma characteristics was needed. A scaling law derived from Lieberman's inhomogeneous sheath model predicted that sensor measurements were proportional to $n_{es}^{1/2}$, $T_e^{1/4}$ and $V_{pp,bais}^{1/4}$ for capacitive sheath conditions. The scaling law was shown to match experimental data and the RF sheath simulation reasonably well under conditions of lower plasma density and higher RF bias voltage. For thinner, resistive sheaths typical of higher density and lower RF bias voltages, the scaling derived from the inhomogeneous sheath model was no longer sufficient. For these conditions, the sensor measurement was directly proportional to the plasma density.

In order to improve the results, a more complex sheath model could be developed. Consideration of a 2D sheath model would better account for the center-to-edge variation of the plasma across the sheaths. In addition, other species such as the role of secondary electrons could be considered. Coupling the sheath model to a global plasma model would also allow for consideration of the effects of the electron energy distribution function at the plasma-sheath edge.

Chapter 6 – Absolute Vacuum Ultraviolet (VUV) Photon Flux in Inductively Coupled Plasmas and Chemical Modifications of 193nm Photoresist

6.1 Abstract

Vacuum ultraviolet (VUV) photons in plasma processing systems are known to alter surface chemistry and may damage gate dielectrics and photoresist. In this chapter the absolute VUV photon fluxes to surfaces exposed in an argon inductively coupled plasma (1 mT – 50 mT, 25 W – 400 W) are characterized using a calibrated VUV spectrometer. In addition, an alternative method to estimate VUV fluence in an inductively coupled plasma (ICP) reactor using a chemical dosimeter-type monitor is demonstrated. The technique is illustrated with argon ICP and xenon lamp exposure experiments, comparing direct VUV measurements with measured chemical changes in 193 nm photoresist-covered Si wafers following VUV exposure. A practical application is demonstrated by characterizing an atmospheric dielectric barrier discharge.

6.2 Introduction

Low temperature plasmas create vacuum ultraviolet (VUV) photons, primarily via electron impact excitation of neutral atoms and molecules. These photons may be re-absorbed, re-emitted, quenched, or interact with surfaces. At low pressures, < 50 mT, VUV photon fluxes to substrates exposed to the plasma may be considerable, potentially affecting surface chemical processes and material properties. Thus, understanding the effects of VUV emissions in plasma processing for semiconductor device manufacturing is becoming increasingly important, especially as critical dimensions shrink to nanometer scale and process control requirements grow more stringent.

VUV photons are known in some cases to alter electrical properties of dielectrics and morphology of polymers. Charge buildup and gate dielectric breakdown have been attributed to plasma-generated VUV exposure[67,68,74]. Roughening studies of polymethyl methacrylate

(PMMA)-based 193 nm photoresist (PR) have also addressed the effects of VUV exposure. Plasma pre-treatment with HBr or H_2-containing plasma have been reported to smooth PR line edge and line width roughness due to the VUV generated in the plasma[8]. Conversely, in other plasma-etching studies, the synergistic effects of simultaneous VUV exposure and energetic ion bombardment were shown to increase 193 nm PR roughening[5,10].

Current techniques utilized to measure plasma-generated VUV emission include chamber-mounted VUV spectrometers, optical emission spectroscopic interpretation of line intensity ratios[35], and "on-wafer" monitoring by measurement of electron/hole pair generation in dielectric films[68]. While these techniques are proven successful, they generally require special sensors, modification of equipment, or *a priori* knowledge of plasma kinetics (e.g. specie energies, cross-sections, and escape factors).

In this study, the VUV spectrum and plasma characteristics of an Ar ICP are examined with standard diagnostic tools. An alternative method is proposed for estimating the VUV flux to substrate surfaces by monitoring the chemical changes of 193 nm PR induced by VUV exposure. It is shown that the changes in chemical composition in the film are a function only of photon fluence (or dose). This approach uses standard Si wafers and commonly available materials and instruments. The method is illustrated in an Ar ICP chamber with comparisons made to Xe resonant lamp exposure under high vacuum conditions. A practical application is also demonstrated by characterizing the VUV emissions of an atmospheric dielectric barrier discharge (DBD) used in bio-medical applications.

6.3 Experimental Setup

6.3.1 Inductively Coupled Plasma System

An Ar plasma is generated in the ICP system described in Chapter 2. The diagnostic tools used in this study will be briefly discussed. The VUV spectrum is measured using a calibrated Resonance LTD VSFS92 VUV spectrometer. Reported observations of VUV emitted from pure Ar plasmas focus on the intensities of the dominant 104.8 nm and 106.7 nm resonance lines[66-68]. In some experiments, a MgF_2 window was mounted between the VUV spectrometer to filter wavelengths < 112 nm[92]. The VUV spectrometer was mounted facing the load-locked sampling port through which the PR samples were exposed to the plasma, and should therefore experience the same VUV flux as the samples. The positive ion current to the chamber wall is measured with a 0.4 cm^2 wall-mounted planar probe DC biased to –40 V and surrounded by a 2 mm wide guard ring, also biased to –40 V to suppress edge effects[33]. The temporal evolution of the DC ion current is measured with an Agilent 34410A 6½ Digit Multimeter. A Langmuir probe measures the electron temperature, electron density (n_e) and sheath potential (Φ_p) and an optical emission spectrometer (Ocean Optics PC2000-UV-vis-ISA) monitors the plasma to ensure steady-state after plasma ignition.

193 nm PR samples were cleaved from a Si wafer spin-coated with 250-300 nm thick PR film (commercial 193 nm PMMA-based; Rohm & Haas). ~1 cm^2 pieces were mounted on the radial-motion, linear feed-through stage and exposed to the plasma via the load-lock sidewall

port of the ICP chamber. The sample was placed flush with the reactor wall and was electrically floating. The sample received a flux of VUV photons and low energy ions (no bias) generated in a 1 – 50 mT, 25 – 400 W Ar plasma, for short times (sample temperature ~25 – 60 °C). Table 6.1 lists the experimental conditions investigated.

Table 6.1 Ar ICP experimental conditions for 193 nm PR processing

ID	Pressure (mT)	ICP Power (W)	Φ_p (eV)	Time (s)	VUV Flux ($\times 10^{10}$ cm^{-2} s^{-1})
1	10	20	16.2	10	0.41
2	10	20	16.2	20	0.41
3	10	20	16.2	40	0.41
4	10	85	15.8	30	2.8
5	10	85	15.8	60	2.8
6	10	85	15.8	20	2.8
7	10	140	15.8	20	6.9
8	10	200	15.8	15	10.7
9	20	40	13.9	20	1.1
10	20	80	13.9	20	2.6
11	20	200	13.9	20	6.8
12	50	60	12.3	20	1.5
13	50	200	12.1	20	2.5
14	10	70	15.8	5-300	2.6

6.3.2 Ultra-high Vacuum Beam System

To examine VUV-only effects on 193 nm PR, complementary experiments were conducted in a vacuum beam system, described in the dissertation of Dustin Nest[62]. The vacuum beam system allows for study of plasma-specific components (e.g. ions or VUV photons) and their effects on semiconductor materials. In this set-up a 1 cm^2 piece of PR-coated Si wafer was mounted on a translational-rotational, temperature controlled holder, and was exposed to a Resonance Xe lamp VUV emission line source (147 nm) with a calibrated flux of ~1.9 × 10^{14} photons/cm^2/s. The VUV flux was held constant while the exposure time was varied (30 s – 1 hr), i.e. PR exposures were a function of VUV fluence only. The vacuum beam system pressure is maintained below 10^{-5} Torr ensuring rapid removal of any products.

6.3.3 193 nm Photoresist Characterization

193 nm PR is a commercially available photoresist used in fabrication of devices with sub-0.13 μm features[3]. It is a terpolymer consisting of methyl adamantyl methacrylate (MAMA) in the leaving group, α-gamma butyrolactone methacrylate (α-GBLMA) in the lactone group, and R-functionalized adamantyl methacrylate (RAMA) in the polar group for adhesion (Figure 6.1). Both pristine and processed samples were characterized with Fourier transform infrared spectroscopy (FTIR) (Digilab FTS-3000) where the changes in the C=O peaks for the lactone (1796 cm^{-1}) and ester functional groups (1720 cm^{-1} and 1738 cm^{-1}), C–O–C peaks (1050 – 1350 cm^{-1}) and CH_2/CH_3 (2800 – 3100 cm^{-1}) peaks were measured.

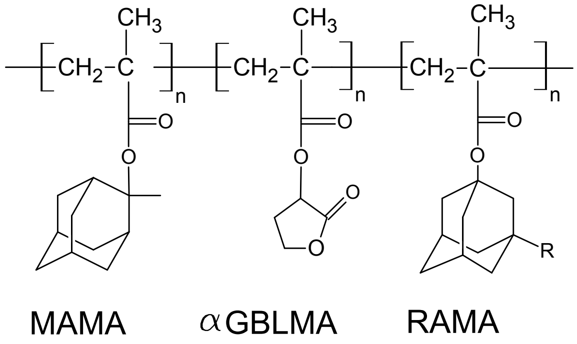

Figure 6.1 Chemical structure of 193 nm PR, comprised of methyl adamantyl methacrylate (MAMA) in the leaving group, α-gamma butyrolactone methacrylate (α-GBLMA) in the lactone group, and R-functionalized adamantyl methacrylate (RAMA) in the polar group for adhesion.

6.4 Results & Discussion

6.4.1 VUV and Ion Flux Characterization

In order to study the chemical modifications of 193 nm PR caused by VUV photons, the VUV spectra and flux generated in the ICP were first characterized by using the chamber-mounted VUV spectrometer. Figure 6.2 shows the VUV spectrum for a 110 W Ar plasma for a range of pressures. The two primary resonance peaks at 104.8 nm ($1s_2$) and 106.7 nm ($1s_4$) were identified and compare well to other published Ar plasma VUV spectra[66-68]. As discussed in Chapter 3, the VUV peak intensities increase as pressure increases from 1 mT to 10 mT due to increasing plasma densities that enhance $1s_2$ and $1s_4$ production from the ground state or other 1s levels[69]. As pressure increases to 20 mT and 50 mT, the peak intensities decrease, apparently due to radiation trapping and an increase in quenching. In addition, the 104.8 nm and 106.7 nm lines tend to merge as pressure increases, a result of the dominant Doppler line broadening mechanism for these investigated conditions[64]. Absorption and quenching in the gas-filled region between the VUV spectrometer and the plasma also increases at higher pressures[67,69,73]. The dominating intensity of the 106.7 nm peak is attributed to its smaller absorption coefficient, typically four times less than the 104.8 nm peak[64].

The total VUV flux as a function of ICP power is displayed in Figure 6.3 (solid points). These flux values are determined for line of sight measurements 2.54 cm above the electrode surface and directly opposite the load-lock sampling port. The measured VUV flux is $\sim 10^{16}$ photons/cm^2/s and is in good agreement with the range of VUV fluxes reported by Woodworth *et al.* ($\sim 3 \times 10^{16}$ cm^{-2} s^{-1}) in GEC reference cell experiments[74], and Piejak *et al.* ($\sim 1 \times 10^{16} - 5 \times 10^{16}$ cm^{-2} s^{-1}) in their ICP experiments[64]. The VUV flux increases with power since plasma density and therefore excitation rates, increase with power.

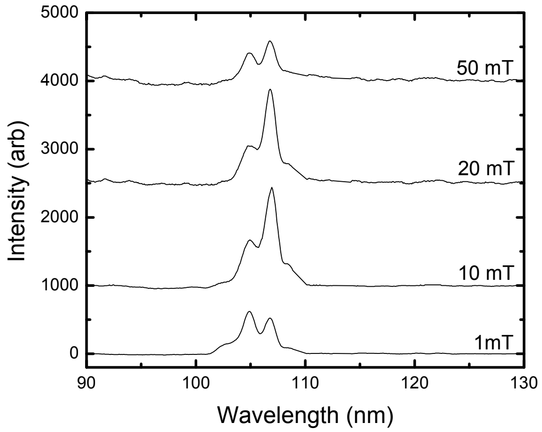

Figure 6.2 104.8 nm and 106.7 nm VUV emission lines for an Ar ICP at 110 W and 1 mT, 10 mT, 20 mT, and 50 mT.

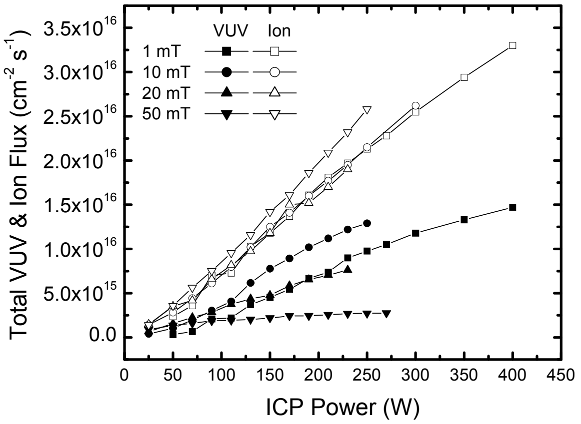

Figure 6.3 Total measured VUV flux (solid points) and ion flux (hollow points) for pure Ar plasmas.

The total ion flux measurements to the chamber wall are also given in Figure 6.3 (hollow points). The resulting VUV to ion flux ratio ranges from ~ 0.1 – 0.7 for the conditions examined and generally decreases with power since ion flux scales linearly with power. The exposed PR samples receive virtually the same low energy ion flux in the chemical dosimeter experiments. As shown next, the changes in chemical composition of the bulk 193 nm PR are due only to photon fluence and not to ion fluence.

6.4.2 VUV Modification of 193 nm Photoresist

193 nm PR samples were processed in the Ar ICP conditions listed in Table 6.1 and then analyzed with FTIR. FTIR spectra of 193 nm PR typically shows a decrease in the C=O and C–O–C peaks induced by UV/VUV exposure while little or no change is observed in the CH_2/CH_3 regions, indicating no etching loss of the PR[6,10,62]. Additionally, as VUV exposure time increases, a larger decrease in the C=O and C-O-C peaks are observed. The 193 nm PR samples processed in the Ar plasma with low energy ions (condition 14) demonstrate this effect (Figure 6.4).

From the FTIR spectra, the total peak intensity changes of C=O species are quantified and plotted as a function of the measured VUV fluence. Figure 6.5 displays a plot of the changes in C=O peak for both the Ar plasma experiments (squares & stars) and Xe lamp experiments (triangles) investigated. Figure 6.5 demonstrates that the chemical change in 193 nm PR is a function only of VUV fluence to the sample surface. This was verified by comparing test conditions, 5 and 8, 7 and 11, and 10 and 13. Each condition represents a significantly different plasma case, with varying VUV fluxes and photon/ion ratios. Exposure times were adjusted to maintain the same photon fluence, and this yielded the same change in FTIR spectra, thus confirming the dependence on VUV fluence. Furthermore, as in case 14 (stars) where the VUV flux was held constant and exposure time adjusted (5 sec – 5 min), it is clearly demonstrated that that C=O loss is a function of VUV fluence only.

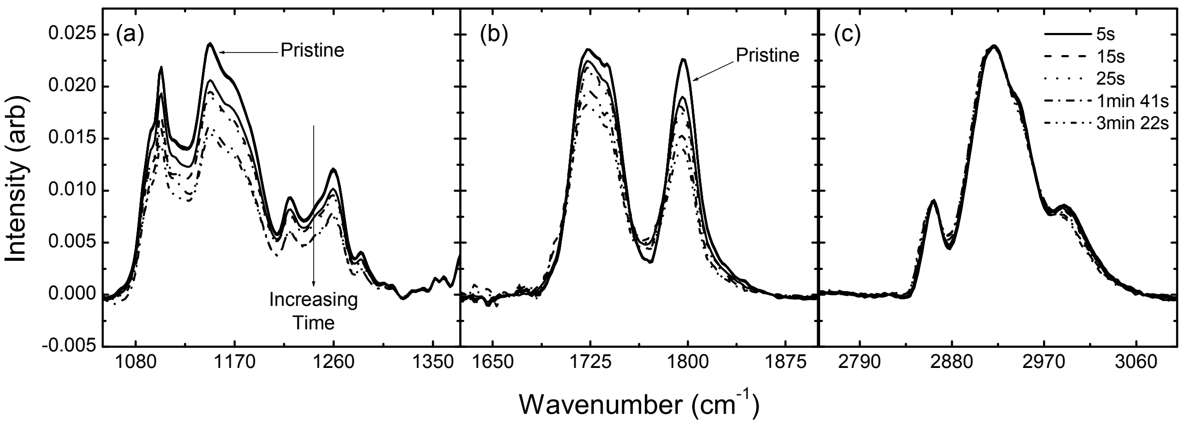

Figure 6.4 FTIR spectra of 193 nm PR processed in an Ar ICP at 10 mT, 70 W. Zero-bias. Substrate temperature: 50 °C. Processing times are varied from 5 s – 200 s. (a) C-O-C region. (b) C=O region. (c) CH_2/CH_3 region.

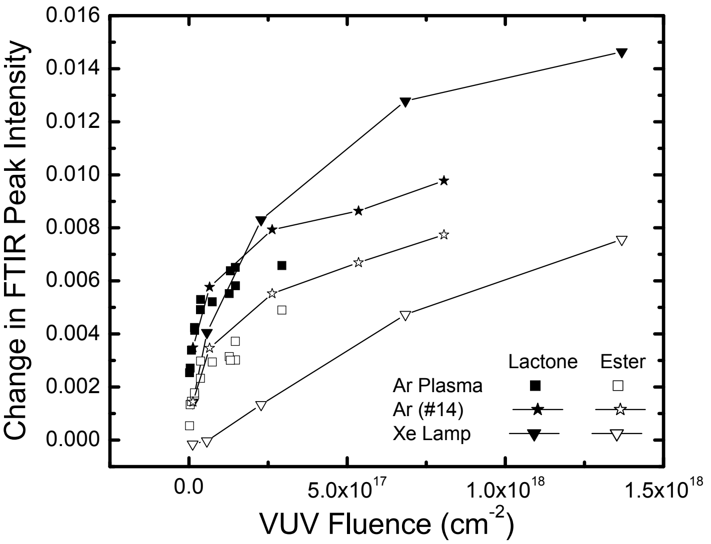

Figure 6.5 Change in FTIR peak intensity of C=O lactone and ester bonds as a function of total VUV fluence to the 193 nm PR sample. Results from the Xe lamp experiments (triangles) are compared to the Ar plasma exposure experiments of varying conditions (1–13) and times (14) (squares and stars). Lines are to guide the eyes.

The qualitative interpretation of the chemical changes as a function of photon fluence is as follows. Just after plasma ignition, VUV photons penetrate the top few nanometers of the film and break C=O and C–O–C bonds, liberating mostly CO[6,10,62]. Subsequent photons are able to penetrate deeper into the film past the less absorbent C-C and C-H bonds that are remaining. Typically, the absorption signal saturates to about 70 % of its original value when the films are ~300 nm thick. This is interpreted to mean that the VUV photons penetrate about 100 nm into the film before being absorbed. When about the top 100 nm of the polymer has been denuded of oxygen-containing bonds, the remaining C-C and C-H bonds in this region are sufficient to absorb most of the incident photons, and the decrease in FTIR peaks representing the oxygen-containing bonds saturates.

The difference between the Xe lamp and Ar plasma experiments are attributed to the difference in VUV wavelengths. Xe VUV emission at 147 nm vs. Ar VUV emissions at 104.8 and 106.7 nm have different absorption cross-sections, resulting in differences in bond breaking and penetration depth[72,93].

6.4.3 Chemical Dosimeter Application

The fact that the FTIR peaks for the C=O bonds decreased only as a function of VUV fluence suggests that this measurement can be utilized as a chemical dosimeter. Such a method has the advantage of simplicity and can be used with standard Si wafers and PR. As a practical application the chemical changes to 193 nm PR was measured after irradiation with a handheld, atmospheric, dielectric barrier discharge (DBD). Such devices are gaining interest in the bio-medical field as a portable and economical tool for sterilization and disinfection purposes. Performance studies have demonstrated the DBD to have bactericidal and fungicidal effects on *E. coli* and *candida albicans*, respectively[94]. A primary concern in the use of plasmas for medical treatments however lies in its possible damaging effect on eukaryotic cells. Therefore, measurement of UV and VUV emissions from these devices are of critical importance.

A schematic of the DBD prototype is shown in Figure 6.6. The plasma is generated between the grounded electrode and Teflon plate, separated by a distance, *d*, (1 – 8 mm) (Figure 6.7). 193 nm PR samples were placed above the grounded electrode and suspended (~6 mm) over the generated plasma discharge for 10 s – 120 s. Changes to the FTIR spectra were measured to determine VUV flux emissions from the DBD.

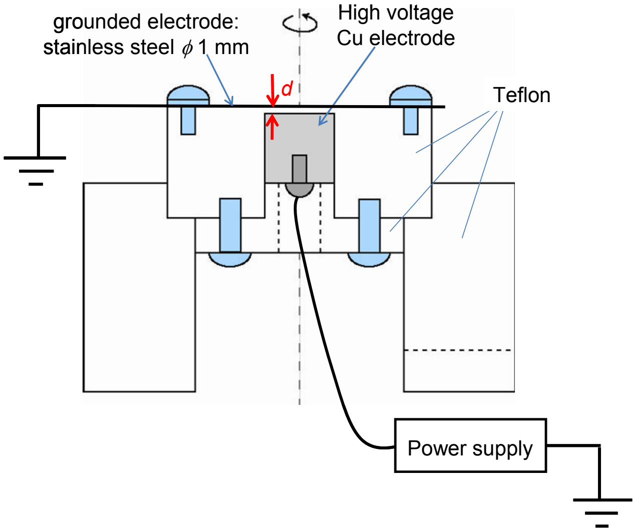

Figure 6.6 Schematic of the prototype dielectric barrier discharge (side view). The barrier thickness, *d*, is varied from 1 mm – 8 mm

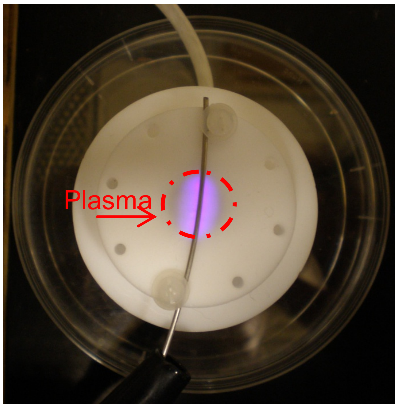

Figure 6.7 Top-down image of the prototype dielectric barrier discharge. The atmospheric plasma is generated between the grounded electrode and Teflon plate.

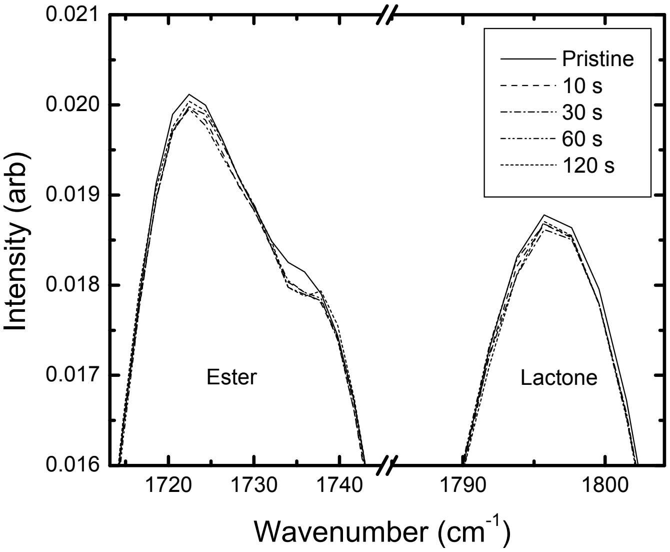

Figure 6.8 FTIR spectra for the C=O lactone and ester region of 193 nm PR samples suspended ~ 6 mm over the DBD for 10 s – 120 s.

The FTIR spectra demonstrate immeasurable change to the C=O and C–O–C regions of the 193 nm PR samples indicating few VUV emissions are reaching the sample surface (Figure 6.8). Although optical emission spectroscopy show N_2 UV/vis emissions were emitted from the discharge, VUV emissions are most likely re-absorbed in the atmosphere. Thus, the negligible change to 193 nm PR samples show VUV emissions from the prototype DBD are not an immediate concern for medical applications.

Successful application in characterizing VUV fluxes from plasma discharges with 193 nm PR, however, should undergo careful consideration. As illustrated in Figure 6.5, the FTIR peak changes in a non-linear fashion and saturates with respect to VUV fluence. This limits the utility of the method, as described here. Furthermore, the differences between Ar and Xe VUV exposure show that any dosimetry measurement would need to be calibrated for the plasma type. In order to improve the scheme, it is not difficult to envision alterations in which layers of different polymers are spin-coated on the wafer to allow an underlying polymer film to be partially protected, and to allow VUV exposure to be recorded in structural chemical changes. Multiple polymer layers with different functional groups may provide information about the VUV spectrum since different functional groups often absorb at different wavelengths[93,95]. This method of determining the VUV flux or fluence lends itself easily to spatially-resolved measurements on the wafer. Furthermore, unlike VUV or OES spectrometers that yield line of sight values within the bulk plasma and must account for radiation trapping or reabsorption[35,73] the VUV fluence directly to the wafer surface can be measured.

6.5 Conclusion

Vacuum ultraviolet (VUV) emissions from a 25 W – 400 W, 10 mT – 50 mT Ar ICP were characterized. The dominant 104.8 nm and 106.7 nm emission lines were identified and the absolute calibrated flux was on the order of ~10^{16} photons/cm^2/s. The chemical modifications (C=O and C–O–C depletion) to 193 nm PR processed under these Ar ICP conditions were attributed to VUV photoabsorption and were a function of VUV fluence (exposure time). Complementary experiments conducted in a vacuum beam system where 193 nm PR samples were irradiated with Xe VUV photons demonstrated similar bulk modifications as a function of VUV fluence. The C=O ester and lactone loss within the 193 nm PR were quantified as a function of the VUV fluences, consequently demonstrating the application of 193 nm PR as a chemical dosimeter for VUV fluence measurements. Practical application of 193 nm PR as a chemical dosimeter demonstrated that VUV emissions from a dielectric barrier discharge used in bio-medical antisepsis and sterilization applications emitted negligible VUV emissions apparently due to reabsorption in the atmosphere.

Chapter 7 – Modeling Vacuum Ultraviolet Photon Penetration Depth and C=O Bond Depletion in 193 nm Photoresist

7.1 Abstract

As demonstrated in Chapter 6, vacuum ultraviolet (VUV) photons are known to modify bulk chemical composition of 193 nm photoresist (PR), typically penetrating ~100 nm and depleting carbon-oxygen bonds. Fourier transform infrared (FTIR) transmission measurements as a function of VUV photon fluence demonstrate that VUV-induced bond breaking occurs over a period of time. This chapter presents a model based on the idea that VUV photons initially deplete near-surface O-containing bonds, leading to deeper, subsequent penetration and more bond losses, until the remaining near-surface C–C bonds are able to absorb the incident radiation. Fitted model photoabsorption cross sections compare well with literature values.

7.2 Introduction

Plasma-generated vacuum ultraviolet (VUV) radiation is known to affect surface and sub-surface processes during semiconductor manufacturing[8,68,74,96]. For example, studies have demonstrated charge build-up and dielectric breakdown from VUV photon exposure[68,88]. Roughening of poly-methyl methacrylate (PMMA) based 193 nm photoresist (PR) has been attributed to synergy between plasma generated VUV photons and high energy ion bombardment[5,6,10]. In addition, smoothing effects due to VUV photons have been observed in HBr and H_2-containing plasmas[8,96,97].

Fourier transform infra-red (FTIR) spectroscopy and x-ray photospectroscopy (XPS) analyses of VUV and ion exposed 193 nm PR reveal scissioning and cross-linking of C=O and C–O–C bonds[95,98]. These transformations are sometimes associated with film roughening and smoothing[12,93,95,98]. While damage due to ion bombardment is limited to the first few nm of the

PR[6,99], bulk changes are due to the VUV photons, often penetrating ~80 – 100 nm into the PR[6,8,10,95]. The penetration depth of VUV photons, often defined as depth of 90 % photon absorption, is determined by the VUV absorption spectra of the polymer, or the photoabsorption coefficients[93,95]. Many authors, including Wertheimer *et al.*[93] and Marasescu *et al.*[95] utilize these photoabsorption coefficients to characterize photon penetration for various VUV sources. However, these models are generally steady-state and do not account for transient photon-induced chemical changes in the polymer. Absorption spectra of bulk polymers can change with VUV fluence[100]. Furthermore, FTIR measurements clearly show that C=O and C–O–C bonds are broken within the bulk PR, and that the changes to absorption saturate after some fluence. In this chapter, a model of transient photon penetration into 193 nm PR is proposed. Model predictions are compared to experimental FTIR results for 193 nm PR exposed to VUV photons from a Xe lamp source in a vacuum beam system and an Ar inductively coupled plasma.

7.3 Model Development

193 nm PR (Figure 7.1) is modeled in COMSOL™ (a commercial software package) as a one-dimensional target material comprised of carbon (C) and oxygen (O) species (Figure 7.2). The divergence of photon flux through the PR (J_{hv}) is equal to the sum of the rates of the photon absorption processes. Photon transport is treated as pseudo-steady state, whereas the bond densities must be treated as time-varying. Only C–C bonds and ester and lactone groups (combining C=O and C–O–C bonds) are included in this simple version of the model. The key assumptions are that the photon is absorbed upon breaking the carbon-oxygen (CO) bonds, and that the bonds are simultaneously destroyed. The remaining C–C bonds are assumed to be unaffected by this process and other possible absorption sites in the polymer are ignored.

Photon absorption is governed by the density of bonds (N_{ester}, $N_{lactone}$ and N_{CC}) and their corresponding cross-sections (σ_{ester}, $\sigma_{lactone}$, σ_{CC}). These cross-sections are of course a function of wavelength. The bond site densities are computed using a simple transient continuity equation. The model equations are summarized as follows:

$$\frac{dN_{hv}}{dx} = -\left(\sigma_{ester} N_{exter} + \sigma_{lactone} N_{lactone} + \sigma_{CC} N_{CC,0}\right) N_{hv} \tag{7.1}$$

$$\frac{dN_i}{dt} = -\sigma_i N_i J_{hv} \tag{7.2}$$

In practice, the photoabsorption cross-sections (σ) are initially treated as adjustable parameters. The best fits to the experimental data are compared to literature values. For ester and lactone, the cross-sections (σ_i) are adjusted until the simulated ester and lactone bond density loss (integrated through the film depth) matches the experimental results of FTIR transmission for the corresponding absorption band. The C–C cross-section (σ_{CC}) is adjusted until the desired photon penetration depth of ~100 nm is achieved. The surface (x = 0 nm) VUV photon flux ($J_{hv,0}$) is arbitrarily defined and the simulation time is adjusted to match experimental VUV fluence measurements. Note that absolute photon fluxes are measured experimentally, allowing the model to be tested for absolute cross sections. Given the known polymer stoichiometry and density, the initial bond group concentrations ($N_{i,0}$ m^{-3}) are calculated (Table 7.1).

Table 7.1 Properties of 193 nm photoresist species.
Densities are calculated assuming a 250 nm × 250 nm surface area.

Property	Value
PR Density (g/cm^3)	1.2
MW (g/mol)	9200
$N_{ester,0}$ (m^{-3})	7.85 x 10^{27}
$N_{lactone,0}$ (m^{-3})	3.14 x 10^{27}
$N_{CC,0}$ (m^{-3})	1.22 x 10^{29}

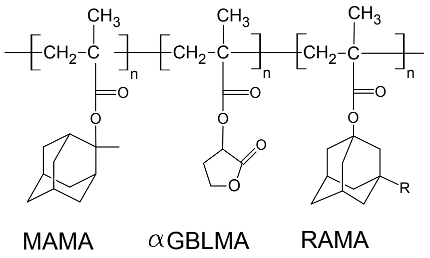

Figure 7.1 Chemical structure of 193 nm PR (Rohm and Haas), consisting of methyl adamantyl methacrylate in the leaving group, α-gamma butyrolactone methacrylate in the lactone group, and a polar group for adhesion.

Figure 7.2 One-dimensional, numerical model developed in COMSOL™ to simulate VUV photon penetration depth and C = O density profiles. The PR surface is defined x = 0 and receives a photon flux: $J_{hv,0}$.

7.4 Results & Discussion

Model results are compared to two sets of experimental studies carried out in a vacuum beam system and an inductively coupled plasma (ICP) system, respectively, both described previously in Chapter 6. In review, a temperature controlled, 1 cm^2 piece of PR-coated Si wafer is exposed to a Xe lamp VUV emission line source (147 nm) mounted in a vacuum beam system, where pressure is maintained below 10^{-5} Torr. The VUV spectrum was monitored with a calibrated Resonance LTD VSFS92 VUV spectrometer. Samples received a VUV flux of ~1.9 × 10^{14} photons/cm^2/s and the exposure time was varied (30 s – 60 min) to achieve VUV fluences similar to that of substrates exposed to typical low pressure plasmas during plasma etch processes. Similarly, a 1 cm^2 sample was placed in the ICP system on a temperature- (50 °C) and bias-controlled (zero bias used here) holder and exposed to a 10 mT, 70 W, Ar plasma for varying times. The plasma is also monitored with the calibrated VUV spectrometer (104.8 nm and 106.7 nm VUV lines), in addition to a wall-mounted ion current probe (~0.8 mA/cm^2), optical emission spectrometer (Ocean Optics PC2000-UV-vis-ISA), and a Langmuir probe (plasma potential ~ 16 eV). The PR samples were 250 nm – 300 nm thick films (commercial 193 nm PMMA-based; Rohm and Haas) coated on Si wafers. All processed samples were characterized with Fourier transform infrared spectroscopy (FTIR) (Digilab FTS-3000). Changes in the C=O peaks for ester and lactone groups (1720, 1738, and 1796 cm^{-1}), C–O–C peaks (1050 – 1350 cm^{-1}), and CH_2/CH_3 peaks (2800 – 3100 cm^{-1}) were monitored.

In Chapter 6, the experimental results demonstrated that 193 nm PR is chemically modified as it is exposed to VUV photons. For increasing VUV fluence, FTIR analysis shows a 30 – 50 % decrease in C=O and C–O–C peaks while CH_2/CH_3 stretching regions remain nearly unaffected. The observed drop in CO bonds is equivalent to ~100 nm of VUV photon-induced bond destruction, while the unaffected CH_2/CH_3 regions indicate no substantial etching of the PR has occurred[6,10,36]. The experimental data are reproduced here for the Xe-lamp exposures (Figure 7.3) and for the Ar plasma exposures (Figure 7.4), plotting the remaining fraction of ester and lactone species (from FTIR C=O measurements) as a function of VUV fluence. In addition, the simulation results for the remaining fraction of ester and lactone bond densities as a function of VUV fluence are also plotted.

The simulated FTIR measurements for each bond group are obtained by integrating the bond density (N_i) with depth. Good agreement is obtained between simulation and experiment for the ester and lactone groups in the Xe-lamp VUV exposure case, while slight differences are observed in the Ar-plasma case. This is attributed to differences in VUV wavelengths in the two experiments. In particular, for emissions from Ar plasmas (104.8 nm and 106.7 nm), photoionization may occur, thus changing the photochemistry within the PR[100,101]. Furthermore, PR samples processed in the Ar plasma are exposed to additional species such as low-energy ions (16 eV), metastables (~ 11.5 eV) and photons from the visible and near-UV spectrum. FTIR measurements indicate that lactone is sensitive to longer (UV-visible) wavelengths. This effect is neglected for simplicity.

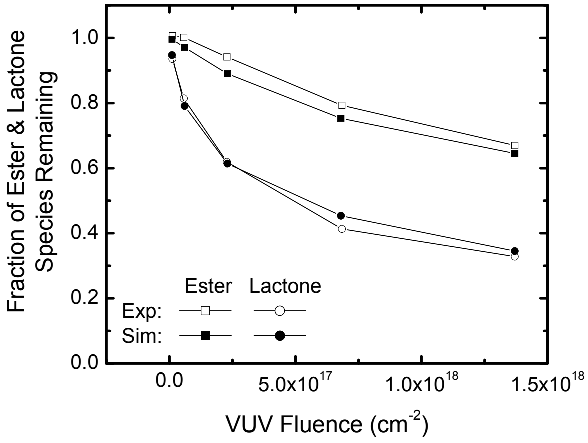

Figure 7.3 Xe-lamp experimental and simulation results for the fractional loss of ester and lactone bonds as a function of VUV fluence.

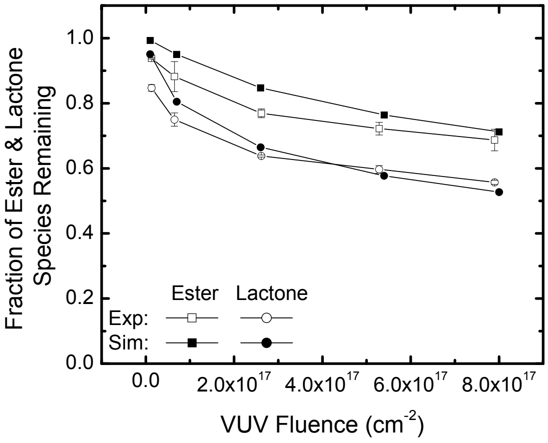

Figure 7.4 Ar plasma experimental and simulation results for the fractional loss of ester and lactone bonds as a function of VUV fluence.

As mentioned in section 7.3, the ester, lactone and C–C photoabsorption cross-sections were treated as adjustable parameters. The 'best fit' cross-sections for the Xe-lamp conditions and Ar-plasma conditions are given in Table 7.2. The ester and lactone cross-sections were adjusted to achieve similar C=O fractional losses to the experiment. The C–C cross-section was adjusted to achieve ~100 nm photon penetration at long times and resulted in ~91 nm and 87 nm penetration depth for the Xe and Ar cases, respectively. Xe lamp-generated photons tend to penetrate deeper (Figure 7.5) due to their smaller cross-section relative to photons generated in the Ar plasma[93,95].

Fitted cross-sections were compared to cross-sections of corresponding functional groups found in the literature. For ester ($HCOOCH_3$) species, reported cross-sections are on the order of $10 \sim 35 \times 10^{-18}$ cm^2 for VUV wavelengths between ~106 nm – 250 nm[102,103]. Cross-sections for alkane and alkene groups vary from $7 \times 10^{-19} - 6 \times 10^{-16}$ cm^2 for VUV wavelengths ranging between ~107 nm – 183 nm[104]. The fitted cross-section values for ester and C–C species fall well within the expected range for VUV wavelengths on the order of ~100 nm – 200 nm used in the experimental studies. The lactone group (cyclical ester) is also of the same order since absorption spectra of carboxyl compounds are often similar due to the active electrons in the C=O bond[103].

Table 7.2 Best-fit photoabsorption cross-sections for simulated VUV photon penetration of 193 nm PR.

Cross-section (cm^2)	Xe-Lamp	Ar-Plasma
σ_{ester}	5×10^{18}	10×10^{18}
$\sigma_{lactone}$	80×10^{18}	100×10^{18}
σ_{CC}	2×10^{18}	2.5×10^{18}

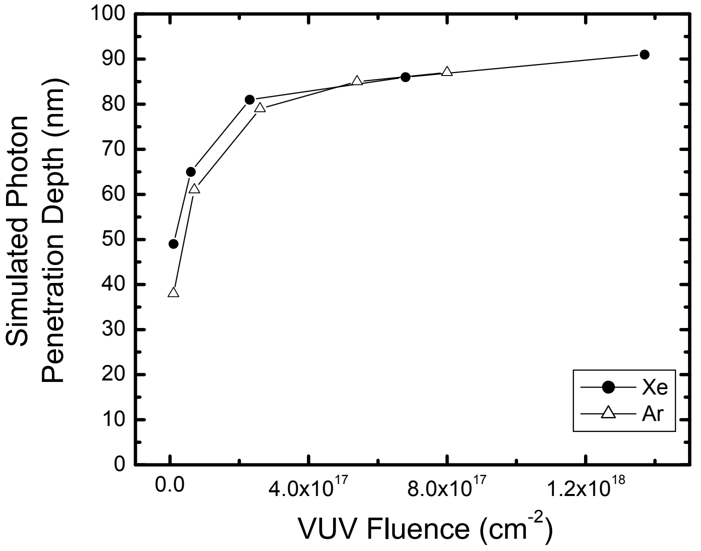

Figure 7.5 Simulated Xe and Ar VUV-photon penetration depths in 193 nm PR. Penetration depths are defined as the depth at which the photon flux is 10 % of its initial value.

Model results for integrated bond group densities vs. fluence (*cf* Figures 7.3 and 7.4) can be understood by examining how the transient photon fluxes through the film affect the bond density spatial profiles. Photons are readily absorbed by CO bonds due to their large cross-sections ($\sigma_{CO} > \sigma_{CC}$), thus preferentially breaking the CO bonds. After some fluence, the top region becomes depleted of CO species while the remaining C–C species continue to absorb photons. Eventually, the C–C region (i.e. the CO depleted region) is thick enough that most incident photons are absorbed without breaking any more CO bonds. Approaching steady state, the C–C species within the top layer of the PR limits the penetration depth of the photons to the top ~100 nm.

Figures 7.6 and 7.7 demonstrates model predictions of the changing concentration profiles of CO bond group densities and photon flux within the PR for the five Ar VUV fluences studied in Figure 7.4. As photons penetrate the surface, a propagating front develops, separating the photon-damaged region and the unaltered polymer. The concentration (or flux) of photons decreases with depth due to absorption. The photon flux reaches ~ 10 % of its initial value at ~ 100 nm. The separation between the de-oxygenated region and unprocessed polymer matches the experimental FTIR results that were interpreted to have lost 30 – 50% of the C=O and C–O–C species.

Of course, this simple model can be readily adapted to simulate photon penetration depths of varying VUV wavelengths by adjusting the photoabsorption cross-section values. The model may be improved by incorporating other functional groups in the polymer, to understand their impact on photon penetration. In addition, loss of C–C or addition of C=C species due to cross-linking may be included to determine their impact on photon penetration.

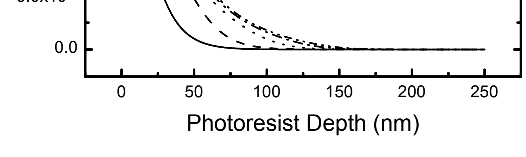

Figure 7.6 Simulated photon flux profile through 193 PR for the five Ar VUV fluences corresponding to Figure 7.4.

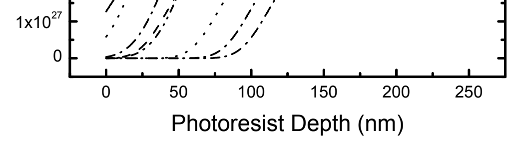

Figure 7.7 Simulated ester and lactone concentration profiles through 193 PR for the five Ar VUV fluences corresponding to Figure 7.4.

7.5 Conclusion

A numerical simulation of VUV-photoabsorption and C=O specie depletion in 193 nm PR was modeled after experimental results for Xe-VUV and Ar-VUV irradiation in the vacuum beam system and ICP system, respectively. The photoabsorption cross-sections of C–C and C=O ester and lactone species are a function of VUV wavelength and were used as adjustable parameters to achieve oxygen loss and photon penetration depths comparable to experiment. C=O cross-sections are responsible for the rate of oxygen depletion in the PR while C–C cross-sections are responsible for slowing the front of penetrating photons and limiting the damaged region to ~ 100 nm. For Xe irradiation, the ester, lactone, and C-C cross-sections were 5×10^{-18} cm^2, 80×10^{-18} cm^2, and 2×10^{-18} cm^2, respectively. The maximum photon penetration depth was ~ 91 nm. For Ar irradiation the ester, lactone, and C–C cross-sections were 10×10^{-18} cm^2, 100×10^{-18} cm^2, and 2.5×10^{-18} cm^2, respectively. The maximum photon penetration depth was ~ 87 nm.

Chapter 8 – Comparing 193 nm Photoresist Roughening in an Inductively Coupled Plasma System and Vacuum Beam System

8.1 Abstract

This chapter presents a comparison of blanket 193 nm photoresist (PR) roughening and chemical modifications of samples processed in a well characterized argon (Ar) inductively coupled plasma (ICP) system and an ultra-high vacuum beam system. In addition, patterned samples are processed in the ICP system to determine if roughening of features (line-width roughness, LWR) correlate with surface roughening behavior. In the ICP system, PR samples are irradiated with Ar VUV and Ar ions, while in the vacuum beam system, samples are irradiated with either a Xe-line VUV source or Ar-lamp VUV source with Ar ions. Sample temperature, photon flux, ion flux, and ion energy are controlled and measured. The resulting chemical modifications to bulk 193 nm PR and surface roughness are analyzed with Fourier transform infrared (FTIR) spectroscopy and Atomic Force Microscopy (AFM).

Results demonstrate that under VUV-only conditions in the vacuum beam and ICP systems, blanket and patterned 193 nm PR does not roughen. However, roughness increases with simultaneous high-energy (> 70 eV) ion bombardment and VUV-irradiation and is a function of VUV fluence, substrate temperature and photon-to-ion flux ratio. Analysis of patterned samples demonstrate a similar synergy between VUV photons and ions on LWR, however, the LWR remains independent of processing temperature. PR processed in the ICP system experience increased etching, probably due to release of H- and O-containing gaseous products and subsequent chemical etching, in contrast to samples in the vacuum beam system. The surface roughness structure and behavior between the two systems, however, remain similar and is attributed to the synergy between VUV-photons and positive ions.

8.2 Introduction

Photoresists based on polymethyl methacrylate (PMMA), designed for use with ArF (193 nm) excimer laser radiation, are known to be susceptible to surface roughening. Roughening often occurs during lithography steps (i.e. the exposure/development/post-exposure bake cycle), and can appear as top surface roughness and/or sidewall roughness on features such as lines and spaces or holes and vias. Additionally, plasmas used for etching-induced pattern transfer to underlying films are known to either smooth or further roughen features.

Plasma-induced roughening of 193 nm photoresist (PR) exists in many forms and generates significant problems in device performance due to degradation of features during the pattern transfer step. The term 'contact edge roughness' (CER) refers to the problem for rough contact holes (Figure 8.1a). Sidewall roughness in lines and spaces is described as 'line edge roughness' (LER) or 'line width roughness' (LWR), depending on whether the feature edge or width of the feature line is measured, respectively (Figure 8.1b). Surface roughening of non-patterned (blanket) samples are prevalent even in inert plasmas where chemistry effects are absent (Figure 8.1c).

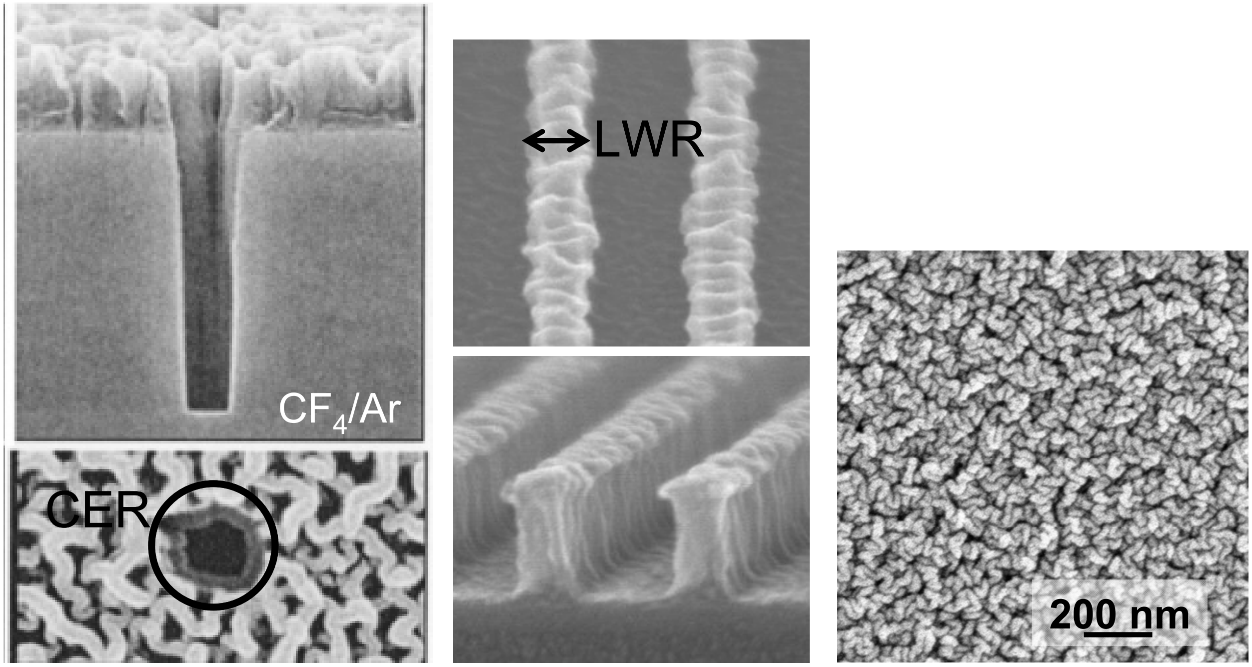

(a) (b) (c)

Figure 8.1 Examples of 193 nm photoresist degradation in plasmas. (a) SEM image of contact-edge roughness (CER) in 193 nm PR and the underlying BARC layer developed while etching in a CF_4/Ar mix plasma[105]. (b) SEM image of line-width roughness (LWR) for Xe vacuum-ultraviolet photon and 150 eV Ar^+ irradiation in a vacuum beam system. (c) SEM image of surface roughness of blanket 193 nm PR processed in an 800 W Ar plasma[6,10].

LWR is generally acknowledged to be a major problem for gate electrode leakage as well as other device performance characteristics as device sizes continue to shrink below the current 32 nm node[1,9]. LWR roughness is often characterized by the distribution of line widths (assumed Gaussian) along a feature edge such as a gate electrode. The difference between the root mean square (RMS) width of the distribution and the width at three times the mean of the distribution ('3σ') should be less than 2 nm for the 22 nm node devices, to minimize device gate leakage. This goal is proving difficult to meet, and the relative paucity of potential lithography-related means to meet minimal smoothness specs has prompted interest in seeking post-litho, plasma-based schemes, to achieve the goals.

Little is currently known, however, about the principles of plasma-based surface texturing for any polymer, including the complex polymer blends used for photoresists. More recent studies have investigated the cause of 193 nm PR roughening in a number of plasma systems. For example, effects of plasma chemistry and process control parameters such as power and pressure on 193 nm PR LER and LWR have been studied[12,56,57,96,106]. Results have shown that LER and LWR in C_4F_8/Ar plasma discharges are attributed to fluorine penetration in the polymer structure and fluorocarbon (FC) deposition on the sidewalls, where the FC sticking coefficients are dependent upon the plasma operating condition[56,57]. These studies typically consider the effects of neutral, radical and ion species on PR degradation and roughening. The roughening observed however neglects the effects of vacuum ultraviolet (VUV) radiation on the polymer structure, which has been proven to be a critical component of 193 nm PR roughening.

Focus on the effects of VUV photochemistry on polymers has greatly increased since VUV can be produced in significant quantities in processing plasmas[93,100,101]. An important feature of hydrocarbon-based polymers, such as 193 nm PR, is the large photoabsorption coefficients in the VUV region of the spectrum (< 200 nm)[36,93,95,100]. Depending on photon energy (or wavelength), photoexcitation or photoionization may occur in the bulk polymer and significantly transform the material via chain scissioning, radical formation, and cross-linking[93,100]. Thus it has grown increasingly important to study plasma-induced VUV effects on 193 nm PR in addition to effects associated with ion, neutral, and radical species.

Some groups have proposed plasma pre-treatment known as “plasma cures” and VUV/e-beam smoothing of 193 nm PR to eliminate LER and LWR[7,8,11,58,97,107,108]. Pargon *et al.* demonstrated that HBr and Ar plasma treatments reduce LWR and attributed the effect to VUV emission (110 – 210 nm) and low energy ion bombardment[7,11]. Smoothing was proposed to be due to the known effects of VUV light on chemical modification of the bulk PR through scissioning polymer chains and depleting the PR of C=O compounds. This removal of C=O species was thought to contribute to a lower molecular weight and mobile volume with a decreased glass transition temperature (T_g) that led to a final smaller PR roughness.

Most recently, the dissertation by Dustin Nest demonstrated that 193 nm PR roughening and degradation correlated with the synergistic effects of VUV radiation, ion bombardment and substrate heating[6,10,62]. His experiments conducted in a vacuum beam apparatus, demonstrated that 193 nm PR samples roughened most when heated and exposed to simultaneous VUV photon (from Xe and Ar resonance lines) and ion (Ar^+) bombardment. Roughening on the order of 1 – 5 nm RMS was observed along with accompanying degradation of carbonyl (C=O) bonds due to

VUV exposure. 248 nm PR (utilized as control samples) exposed to identical conditions, remained smooth.

Although these ultra-high vacuum beam studies demonstrate a synergy between ion bombardment and VUV photons leading to enhanced PR roughening, the question remains of whether this synergy exists in complex plasma systems where real device features are etched. Previous Ar plasma experiments showed PR roughening similar to that observed in the vacuum beam system, but the dependence of the roughening synergy on the various conditions in the plasma is not known. It is true that plasma etch processes generally utilize complex feed-gases and this no doubt influences the roughening mechanisms[5,56].

In order to begin to understand the roughening mechanism of 193 nm PR under realistic plasma etch conditions, preliminary experiments investigated smoothing and roughening effects in a relatively simple, well-characterized, mostly chemically inert, inductively coupled argon (Ar) plasma. First, "plasma cure" conditions were generated to measure the effects of VUV photons on bulk chemistry and surface morphology on blanket 193 nm PR samples. Secondly, the synergistic effects of substrate temperature, ion energy, VUV fluence, and photon-to-ion flux ratio on surface roughness of blanket samples were investigated and compared to experimental results obtained in the ultra-high vacuum beam experiments. Roughening mechanisms of 193 nm PR blanket samples are proposed from the results. Finally, the effects of VUV photons and ions on patterned samples are studied to determine if there is a correlation between LWR and surface roughness of features.

8.3 Photoresist Materials & Characterization Techniques

8.3.1 Blanket 193 nm and 248 nm Photoresists

Experiments focus on the surface roughening and degradation of polymethyl methacrylate (PMMA) based 193 nm PR (Dow Electronic Materials). The chemical structure (Figure 8.2) consists of methyl adamantyl methacrylate (MAMA) in the leaving group, α-gamma butyrolactone methacrylate (a-GBLMA) in the lactone group, and R-functionalized adamantyl methacrylate (RAMA) in the polar group for adhesion. Commercially available 248 nm PR materials are used in control experiments since they are known to remain smooth during plasma treatment. The polymer consists of hydroxystyrene, styrene, and tert-butylacrylate (Figure 8.3). Glass transition temperature (T_g) values for unprocessed 193 and 248 nm PRs are 180 °C and 100 °C, respectively.

193 nm PR polymers are spin-coated (250 – 300 nm) on 200 mm diameter wafers without photoacid generator or base quencher. 1 – 2 cm^2 samples are cleaved and mounted on a sample holder with thermal paste (Apiezon H Hi Temp Vacuum Grease) prior to plasma or beam exposures. Irradiated samples are analyzed with transmission Fourier transform infrared (FTIR) spectroscopy. 193 nm PR is monitored for changes in the C=O peaks for the ester and lactone groups (1720, 1738, and 1796 cm^{-1}), C-O-C peaks (1050 – 1350 $cm\text{-}^{1}$) and CH_2/CH_3 peaks (2800 – 3100 cm^{-1}) (Figure 8.4 a-c). Changes in 248 nm PR are monitored in the CH and ring

deformations (500 – 900 cm^{-1}), C=O/C-O-C/C=C regions (1000 – 1800 cm^{-1}), and $CH/CH_2/CH_3/OH$ regions (2800 – 3800 cm^{-1}) (Figure 8.4 d-f).

Tapping-mode atomic force microscopy (AFM) (Digital Instruments) is used to characterize the surface morphology of the PRs. Typically 1 μm × 1 μm surface areas are measured. Processed 193 nm PR samples are compared to the very smooth pristine sample, with typical RMS roughness values of ~ 0.3 nm (Figure 8.5).

After FTIR and AFM measurements, samples are dipped in neat tetrahydrofuran (THF) at room temperature and dried with N_2 gas. Samples are visually inspected for a remaining film, determined to be a graphitized layer, insoluble in THF[109]. Molecular dynamics (MD) simulations have demonstrated that graphitized, dehydrogenated layers 1 – 2 nm thick form on the surface of polymers during energetic ion bombardment (Figure 8.6)[99,110].

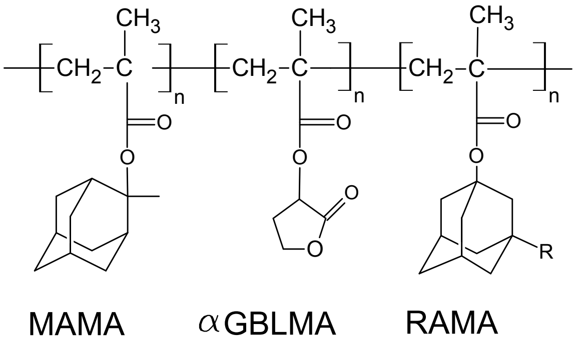

Figure 8.2 193 nm photoresist, consisting of methyl adamantly methacrylate (MAMA), α-gamma butyrolactone methacrylate (α-GBLMA) and R-functionalized adamantyl methacrylate (RAMA).

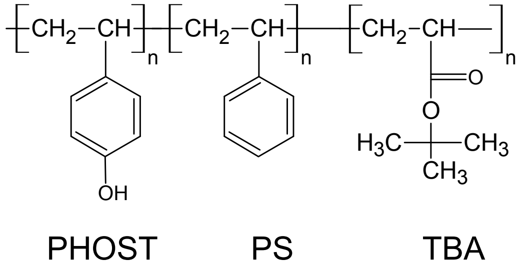

Figure 8.3 248 nm photoresist chemical structure consisting of a hydroxystyrene (PHOST), styrene (PS), and tert-butylacrylate (TBA).

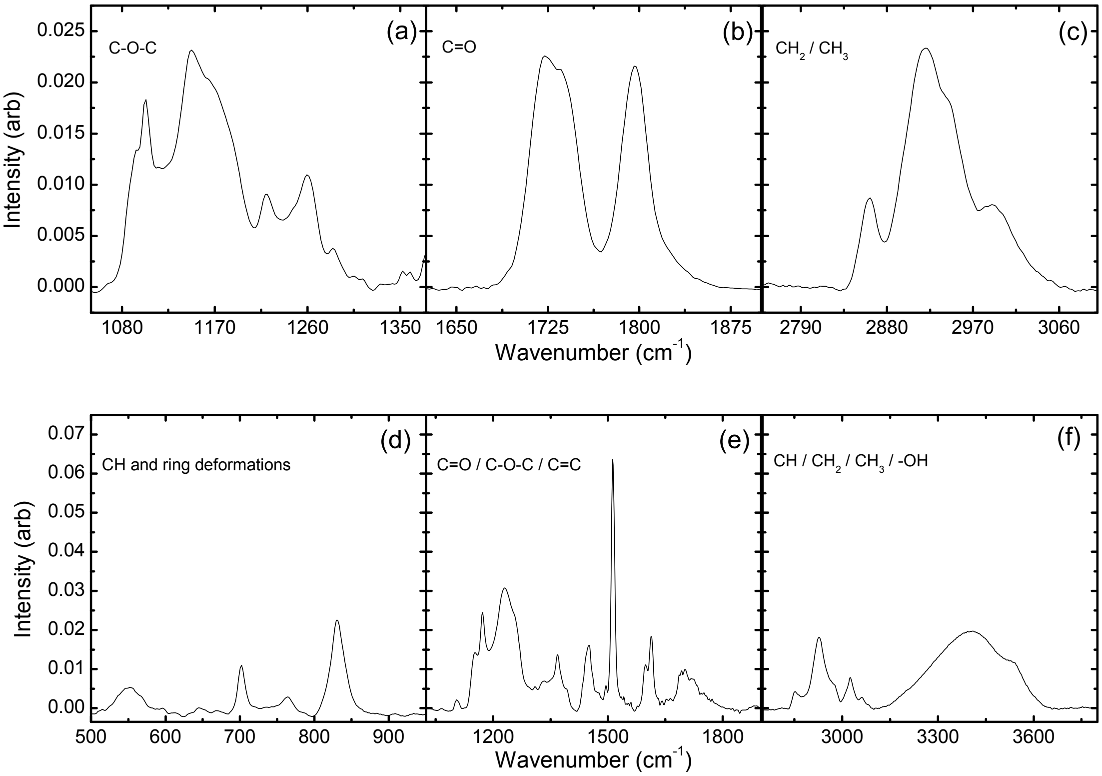

Figure 8.4 FTIR spectra of pristine 193 nm PR spincoated on Si wafers: (a) C-O-C region, (b) C=O region, (c) CH_2/CH_3 stretch region. FTIR spectra of pristine 248 nm PR spincoated on Si wafers: (d) CH and ring deformations, (e) C=O/C-O-C/C=C region, (f) CH_2/CH_3 and –OH region.

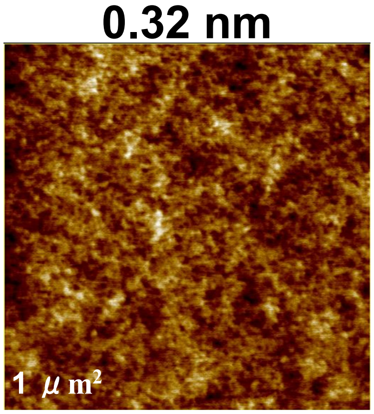

Figure 8.5 Surface morphology of pristine 193 nm PR, blanket sample, measured with AFM in tapping mode. Typical RMS ~ 0.3 nm.

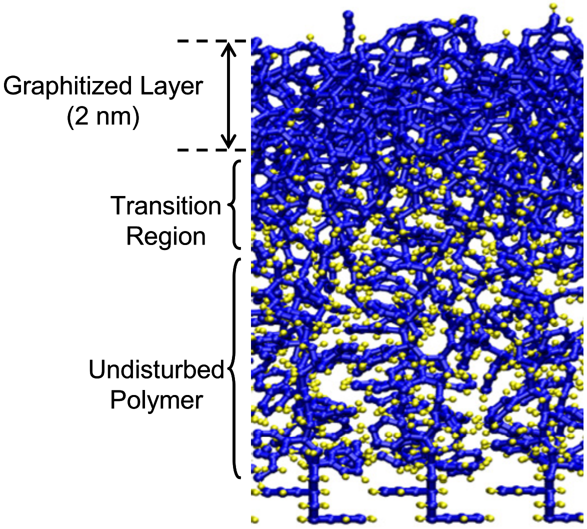

Figure 8.6 Molecular dynamic simulation results for polystyrene bombarded with 100 eV Ar^+, resulting in the formation of a ~ 2 nm graphitized layer.

8.3.2 Patterned 193 nm Photoresists

193 nm PR samples (~ 1 cm^2) patterned with lines of varying critical dimensions (Lam Research) were cleaved from 12 inch wafers and mounted on the temperature and bias controlled sample holder with thermal paste prior to plasma processing. Three patterned samples and one control blanket sample were processed per exposure condition. The line features are comprised of pad oxide, SiN, BARC, and 193 nm PR layers (Figure 8.7). Scanning electron microscope (SEM) scans taken at Lam Research measured line segments of varying length to yield high and low frequency LWR values. It has been observed in practice that high frequency LWR is typically easier to treat than low frequency LWR. Large surface areas of unpatterned PR were measured with AFM to determine RMS surface roughness (Figure 8.8). Initial roughness values of pristine patterned samples (RMS 1.88 nm) were quite high and most likely a result from previous photolithography steps.

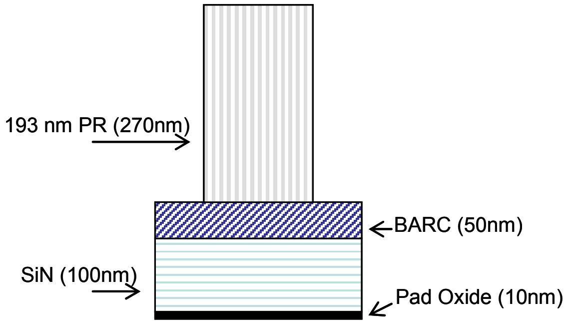

Figure 8.7 Diagram of 193 nm PR patterned lines from Lam Research. 270 nm tall PR lines are patterned on BARC (50 nm), SiN (100 nm) and pad oxide (10 nm) layers.

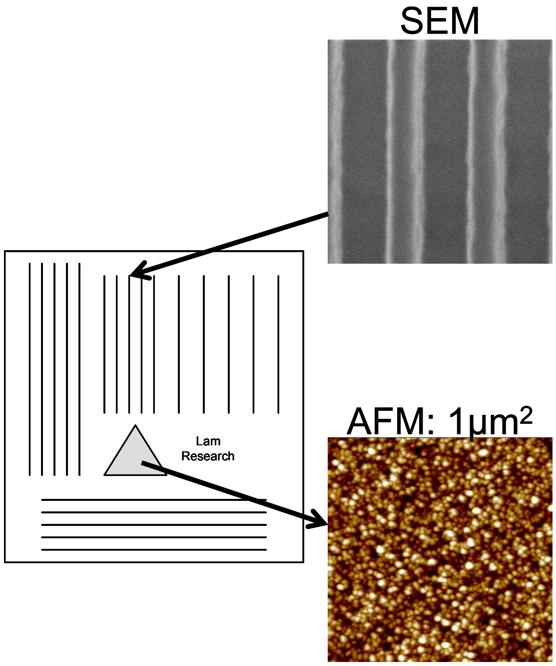

Figure 8.8 Plasma processed 1 cm^2 samples are analyzed with SEM and AFM to determine LWR and surface roughness, respectively.

8.4 Experimental Approach

8.4.1 Inductively Coupled Plasma System

Blanket and patterned 193 nm PR samples are processed in the inductively coupled plasma (ICP) chamber with the diagnostic tools and sample holder that have been described in detail in Chapter 2. The specific set-up relevant to this study is briefly repeated here. An argon (Ar) plasma is generated and sustained in the ICP reactor through a 5-turn, planar coil, powered with a 13.56 MHz RF power source. PR samples are introduced into the chamber through the side-wall, load-lock port, on the temperature (20 – 100 °C) and bias (0 – 420 V, peak-to-peak) controlled holder. The samples are placed flush with the chamber wall. The bias is controlled with a 13.56 MHz RF power supply and the temperature is set with a Neslab RTE-111 water bath. To monitor temperature control, sample temperatures in the ICP chamber were measured with Omega Four-Point irreversible temperature indicators attached to the sample.

A quadrupole mass spectrometer (QMS, UTI-300) is used to monitor positive ion species generated in the plasma, an optical emission spectrometer (OES, Ocean Optics PC2000-UV-VIS-ISA) is used to monitor the 811.5 nm Ar emission line to ensure plasma stability throughout the experiments, and a Langmuir probe is used to measure the plasma density (n_e), temperature (T_e), and potential (Φ_p). The total positive ion current is measured with an ion current probe, adjacent to the sample holder. The VUV flux is calculated from the total measured VUV intensities directly opposite the sample holder[13,36]. The ion energy is calculated as the sum of the plasma potential and average bias voltage. The VUV and ion fluences are controlled by adjusting the exposure times (5 s – 5 min). Table 8.1 summarizes the plasma experimental conditions studied and used for comparison to the vacuum beam system experiments.

Table 8.1 193 nm PR processing conditions in the inductively coupled plasma system for a 10 mT, Ar plasma

	Power (W)	Φ_P (eV)	Sample Temperature (°C)	Average Bias Voltage (V)	VUV Flux ($\times 10^{15}$ cm^{-2} s^{-1})	Ion Flux ($\times 10^{15}$ cm^{-2} s^{-1})	Photon-to-Ion Flux Ratio
1	25	16.2	50	~ 105	0.45 ± 0.02	1.44 ± 0.06	0.31
2	70	15.8	20 – 100	0 – 200	2.87 ± 0.25	5.51 ± 0.34	0.52
3	150	15.8	50	~ 105	7.87 ± 0.64	12.7 ± 0.48	0.62

8.4.2 Ultra High Vacuum Beam System

All 193 nm PR experiments conducted in the ICP system are compared to those previously done in the vacuum beam system. The vacuum beam system set-up, experimentation, and post processing techniques are described in detail by the dissertation of Dustin Nest[62]. For reference, a brief description will be given here.

The vacuum beam chamber is maintained at a base pressure of 5×10^{-8} Torr where a temperature-controlled, rotational-translational sample dock is introduced through a load-lock transfer arm (Figure 8.9). The chamber is equipped with a Commonwealth ion gun, accelerating Ar ions (Ar^+) to 150 eV at 90° incidence angle to the sample. The ion current is measured with a commercial Faraday cup (Kiethley). Samples were irradiated with Ar or Xe VUV photons from either an Oxford Applied Research (OAR) (HD25) inductively coupled plasma source with 13.56 MHz excitation frequency, or a Xe VUV line source (Resonance Ltd.). In addition, the vacuum beam system is equipped with a quartz crystal microbalance (QCM, Maxtek Inc. Model TM-400). QCM samples spin-coated with PR (250 nm thick) were used to measure mass change, *in-situ*, during exposure to ions and photons. All 193 nm PR samples were irradiated with ion-only, VUV-only, or simultaneous ion and VUV beams.

The vacuum beam system VUV sources are monitored with the same calibrated Resonance LTD VSFS92 VUV spectrometer as used in the ICP system. The VUV spectrometer is mounted directly opposite, line-of-sight, from the VUV sources. The VUV emission intensities (or VUV flux) from the OAR source are tuned by adjusting source power and pressure. The Resonance VUV line source, however, operates at fixed pressure and power; therefore the emission intensity can only be controlled by translating the source with respect to the sample. In some cases, LiF, MgF_2, CaF_2, and SiO_2 windows were mounted between the VUV source and spectrometer to filter wavelengths below 104 nm, 112 nm, 122 nm, and 160 nm, respectively[111]. The calculated Xe (147 nm) photon flux was 1.24×10^{13} and 1.9×10^{14} photons/cm^2/s for the OAR (190 mT, 100 W) and Resonance sources, respectively. The total photon flux from the OAR source with Ar was not calculated due to additional VUV peaks generated at lower wavelengths (below the 100 nm spectrometer cut-off) that could not be characterized[62]. Table 8.2 summarizes the experimental conditions studied in the vacuum beam system and used for comparison to the plasma exposures.

The advantage of a vacuum beam system is that it is a highly controlled processing environment in comparison to the ICP system. The effects of VUV photons and ions can be quantitatively monitored without interference from other plasma generated species (eg. neutrals and radicals). In addition, chemistry effects are negligible since sputtered products are rapidly swept away through the turbo-pump system. It should be noted, however, that processing times are orders of magnitude different. While ICP samples are processed a few seconds or minutes, due to the low-fluence VUV and ion sources of the vacuum beam system, processing times are on the order of hours.

Table 8.2 Ultra-high vacuum beam conditions used for 193 & 248 nm PR roughening and QCM studies. These conditions are used for comparison to Ar ICP experiments listed in Table 8.1.

ID	Species	Ar$^+$ Energy (eV)	Ar$^+$ Fluence (cm^{-2})	VUV Fluence (cm^{-2}) (or Time*)	Sample Temp. (° C)
1	Ar$^+$	150	$0 - 1 \times 10^{18}$ (1 hr)	~	65
2	Ar VUV (OAR)	~	~	5 min, 20 min, 2.5 hrs, 11.5 hrs	50
3	Xe VUV (Resonance)	~	~	1.14×10^{16} 5.70×10^{16} 2.28×10^{16} 6.84×10^{16} 1.36×10^{16}	20
4	Ar$^+$ + Ar VUV (OAR)	150	4×10^{17} (40 min)	40 min	50, 60, 75, 100
5	Ar$^+$ + Xe VUV (Resonance)	150	1×10^{18} (1 hr)	3.70×10^{17}	20, 40, 65
6	Ar$^+$ + Xe VUV (Resonance)	150	$0 - 1 \times 10^{18}$ (1 hr)	$0 - 6.8 \times 10^{17}$ (1 hr)	65

*Note, exposure times (and not fluence) are given for the Ar VUV (OAR) experiments because the Ar VUV emission spectra could not be fully characterized.

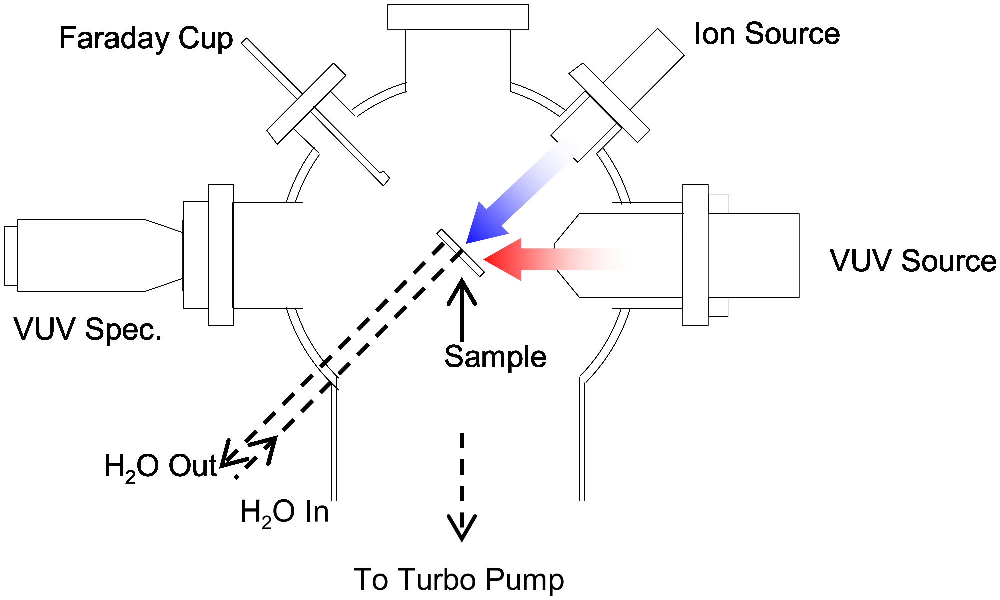

Figure 8.9 Side-view schematic of the ultra-high vacuum beam system used for 193 nm PR exposure studies.

8.5 Results & Discussion

8.5.1 VUV Characterization

Prior to evaluation of PR response to process control parameters, the ICP VUV spectrum was characterized in order to determine the appropriate exposure conditions for comparison to the vacuum beam experiments[36]. For a detailed discussion on VUV emission behavior for the Ar plasma, see Chapters 3 and 6. Here, the VUV emission characteristics relevant to this study are briefly discussed.

Figure 8.10 displays the VUV spectrum for an Ar plasma for four pressures at 110 W. For all pressures, the dominant 104.8 nm and 106.7 nm Ar emission lines are observed. The high intensity peaks at 209 nm and 213 nm are double-peaks of the 104.8 nm and 106.7 nm emissions and were verified with a MgF_2 window mounted in front of the VUV, filtering wavelengths < 112 nm[36,72]. The band between 140 – 210 nm is attributed to CO VUV emissions from the fourth positive band[70,71]. The 10 mT Ar plasma condition is chosen for PR exposure experiments reported here in order to minimize the VUV flux of the CO contaminant and maximize the Ar VUV flux. The VUV fluxes hitting the substrate, calculated from the measured Ar emission lines, are listed in Table 8.1. QMS measurements indicate that the CO^+ flux is ~140 times lower than the flux of Ar^+ for the primary condition investigated (10 mT, 70 W). The corresponding Ar^+ flux is also given in Table 8.1.

The Xe VUV line emission source used in the vacuum beam system experiments was characterized with the calibrated VUV spectrometer. The 147 nm VUV emission line from the Xe Resonance source is shown in Figure 8.11; the photon fluxes are given in Table 8.2. As previously mentioned, the OAR Ar lamp source could not be characterized with the VUV spectrometer due to additional peaks observed below the spectrometer's lower limit.

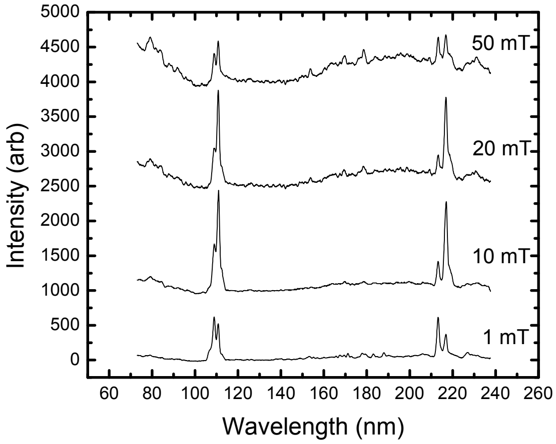

Figure 8.10 VUV spectra for a 110 W Ar plasma and varying pressure. The primary 104.8 nm and 106.7 nm VUV emission lines are observed.

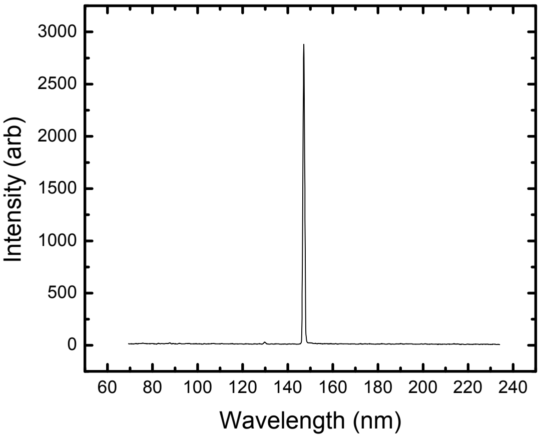

Figure 8.11 VUV emission line (147 nm) from the Xe Resonance source used in the vacuum beam system studies.

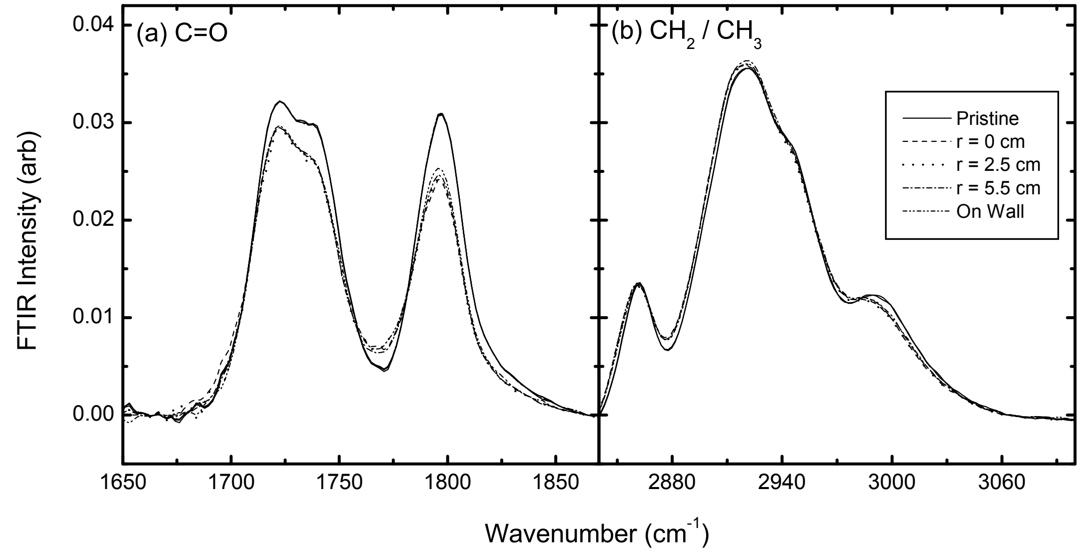

Figure 8.12 FTIR spectra of 193 nm PR processed in a 10 mT, 100 W Ar plasma for 20 s: (a) C=O region, (b) CH_2/CH_3 stretch. Samples were placed on the sample holder, flush with the wall, 2.54 cm above the wafer surface, and on the lower electrode at r = 0 cm, 2.5 cm, and 5.5 cm.

In the ICP system, chamber symmetry is assumed, therefore the VUV flux measured opposite the sample holder should be equivalent to that received by the 193 nm PR sample. This is a reasonable assumption since the spatial variations of the VUV emission generated in the Ar plasma are considered negligible for the conditions investigated. Figure 8.12 displays the FTIR spectra for 193 nm PR samples processed on the sample holder 2.54 cm above the lower electrode, and for samples placed at different radii (r = 0 cm, 2.5 cm, 5.5 cm) on the lower electrode in a 10 mT, 100 W Ar plasma for 20 s. (Simulation studies demonstrated the most significant spatial variation should occur for this plasma condition). The observed changes in the C=O and CH_2/CH_3 peaks for each sample location are identical, differing by only 1.5 % – 3 % indicating the plasma is likely optically thick.

8.5.2 Plasma Cure & VUV – Only Exposures

Plasma cure processing was conducted in the ICP chamber at 10 mT, 70 W, and zero-bias voltage (Table 8.1, condition 2). (All experiments conducted in the ICP system will henceforth be referred to as the Ar-ICP condition). Therefore, samples received only low energy (~16 eV) ions and Ar VUV flux (104.8 nm and 106.7 nm emissions). The resulting chemical modifications to the bulk PR was measured via FTIR analysis and compared to VUV-only exposures conducted in the vacuum beam system (Table 8.2, conditions 2 and 3). (All vacuum beam system experiments will henceforth be referred to as the Xe-beam and Ar-beam conditions). Figure 8.13 plots the transmission FTIR spectra for 193 nm PR samples exposed to Xe and Ar VUV photons for a range of fluence (*cf* Table 8.2, conditions 2 and 3) and for Ar VUV photon exposure (5 s – 5 min) in the plasma system. The FTIR spectra clearly demonstrate the dynamic dependence of the bulk modifications of 193 nm PR on VUV fluence and photon wavelength.

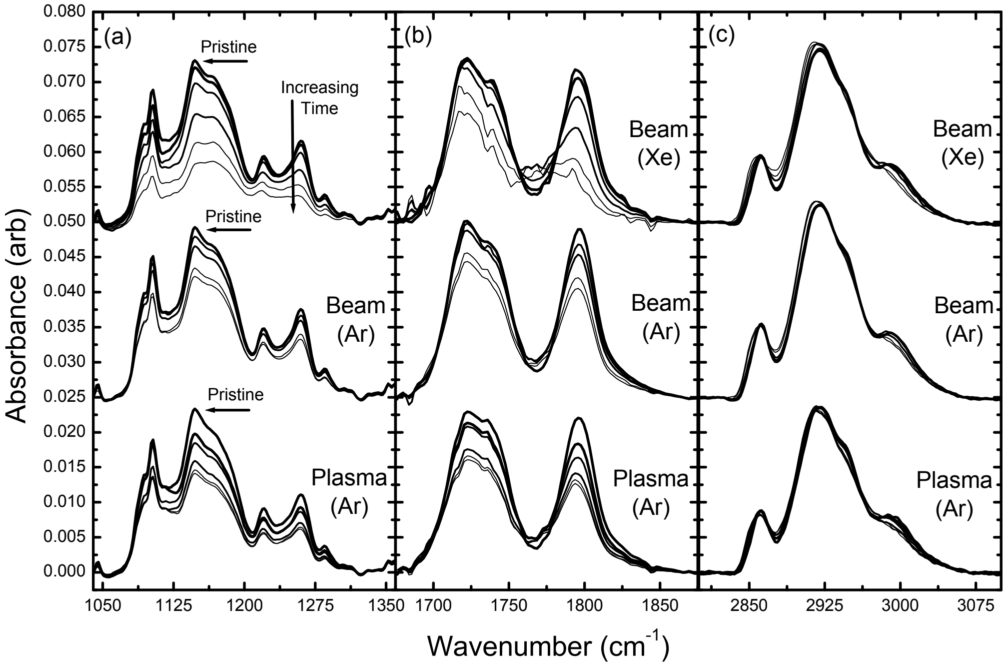

Figure 8.13 FTIR spectra of 193 nm PR: (a) C-O-C region, (b) C=O region, (c) CH_2/CH_3 stretch region. Ar plasma samples processed at 10 mT, 70 W, 50 °C, for 5 s – 300 s. Ar beam samples processed at 50 °C for 5 min – 11.5 hrs. Xe beam samples processed at 65 °C for 1 min – 120 min.

As the photon fluence increases, all irradiated samples show a corresponding depletion of C=O and C-O-C species. In both Xe-beam and Ar-ICP cases, the loss of carbon-oxygen (CO) bonds saturates after $\sim 1 \times 10^{18}$ photons/cm^2. A similar saturation (from 2.5 - 11.5 hrs) is observed in the Ar-beam experiment although the total VUV fluence is unknown. The saturated loss of CO species is attributed to photoabsorption cross-sections of the photons and the resulting penetration depth ~100 nm[6,10,36,112]. As the ester and lactone peaks (1724 and 1793 cm^{-1}) decrease, a rise in the free lactone peak (1772 cm^{-1}) is observed and is consistent with observations by other groups[10,11,62]. The additional free lactone peak observed in the Xe-beam case, however, is greater than that observed in both Ar-beam and Ar-ICP cases. Furthermore, an additional peak is observed in the Xe-beam case near 1680 – 1700 cm^{-1} and is associated with the formation of carboxylic acid dimers[11]. This difference between Ar and Xe VUV exposure is attributed to the difference in VUV wavelengths. At higher energy (lower) wavelengths such as those observed in the Ar-beam and Ar-ICP conditions (104.8 and 106.7 nm), photoionization may occur and thus change the photochemistry within the PR[100,101,112]. It should be noted that although each experiment was conducted with different sample temperatures, the temperature does not affect the bulk-chemical modification and only affects surface roughening[6], as discussed in section 8.5.3.4.

At early times ($\sim 1 \times 10^{16}$ photons/cm^2), the lactone peak decreases faster than the ester peak. This is attributed to the sensitivity of the lactone group to longer (UV-visible) wavelengths and is more pronounced in the Ar-ICP case where high intensity visible emissions from the plasma are present. The larger decrease in the ester peak for the Ar-ICP case appears to be due to the plasma ignition protocol. The lack of capacitive coupling from the coil prevents the discharge from igniting, and powering the lower electrode for several seconds allows the plasma to ignite. This appears to create a burst of VUV photons (i.e. initially higher VUV flux) and high energy ions (see Chapter 3, section 3.3.2).

FTIR peaks associated with the CH_2/CH_3 regions demonstrate little to no change after VUV exposure in both Xe-beam and Ar-beam cases. Similarly, the Ar-ICP case shows little change, even with ~16 eV ion bombardment. Therefore, no significant etching of the PR (or loss of the polymer backbone) due to VUV irradiation is observed and CO loss is attributed to bulk modifications of the PR caused by VUV photons. At higher fluence, a shift in the CH_2/CH_3 peak (2920 cm^{-1}) and rise at 2877 cm^{-1} is observed and is associated with the formation of C=C bonds[95]. Again, a larger change is observed in the Xe-beam case compared to both the Ar-beam and Ar-ICP cases and is attributed to the difference in wavelength and resulting photochemistry.

The fraction of remaining C=O lactone and CH_2/CH_3 species is calculated from the FTIR data and plotted in Figure 8.14 for the Ar-ICP and Xe-beam exposures. As previously noted, the lack of significant CH_2/CH_3 loss is interpreted as meaning no etching occurs due to VUV-only exposures. In contrast, a 40 – 60 % loss of C=O species is observed and attributed to the photoabsorption and destruction of CO bonds by VUV photons. As the VUV photons are absorbed by CO bonds (resulting in loss of O in the form of CO), the near-surface region of the PR is increasingly depleted of CO bonds. When this carbon-rich layer is about 100 nm thick, it is able to absorb most of the incident photons[112]. Ultimately, the CO loss saturates at $\sim 1 \times 10^{18}$ photons/cm^2 [6,112]. The larger decrease in CO species observed for PR irradiated with Xe photons is likely due to the difference in wavelength. The longer Xe wavelength can penetrate farther, thus scissioning more CO bonds[95,112] but is lower in energy therefore not inducing photoionization reactions in the PR[100,101,112].

AFM measurements of processed samples show 193 nm PR does not roughen with VUV-only exposures. A pristine 193 nm PR sample is typically on the order of 0.3 nm RMS (*cf* Figure 8.5). Ar-ICP and Xe-beam samples exposed to increasing VUV fluence demonstrate a similar roughness (Figure 8.15) confirming that VUV-only exposures do not induce 193 nm PR roughening[6,10,62]. In addition, samples dipped in concentrated THF do not show the formation of a graphitized layer on the PR surface.

As a control experiment 248 nm PR was exposed to VUV-only conditions in both the vacuum beam and ICP systems. Comparisons between FTIR and AFM measurements of samples processed in both systems show similar trends. FTIR measurements indicate little etching occurs (i.e. no decrease in the CH_2/CH_3 region) while the –OH band is reduced (Figure 8.16). Fewer bulk modification of the PR is observed and attributed to the lower oxygen content of 248 nm PR[10,62]. AFM measurements show roughening does not occur and remains similar to pristine roughness values (~0.3 nm) (Figure 8.17). In contrast to 193 nm PR, THF-dipped samples show strong cross-linking for VUV-only exposed samples.

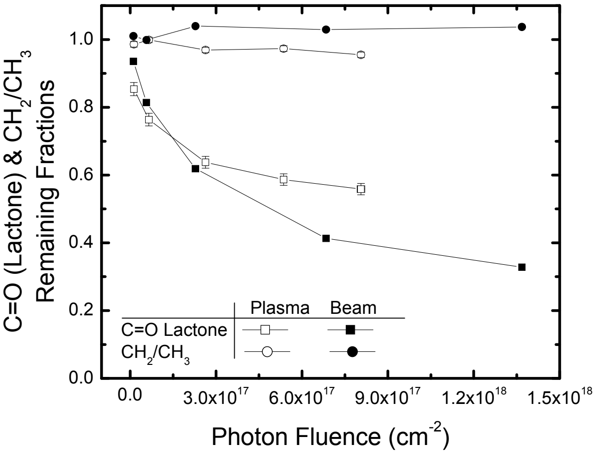

Figure 8.14 Remaining C=O and CH_2/CH_3 fractions in 193 nm PR, calculated from FTIR peak intensities. Ar plasma condition: 10 mT, 70 W, 50 °C. Xe beam condition: 65 °C.

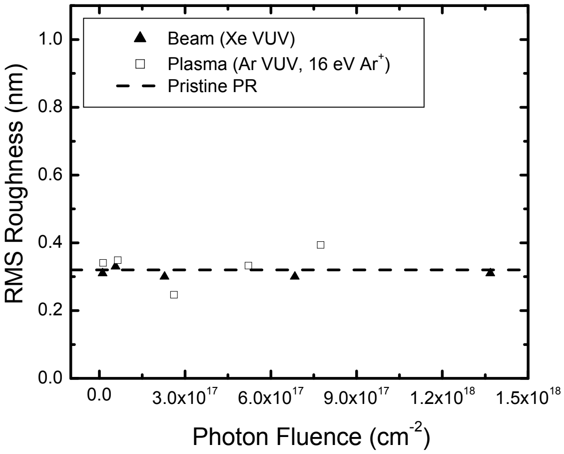

Figure 8.15 RMS surface roughness of 193 nm PR measured with AFM. Ar plasma condition: 10 mT, 70W, 50 °C. Xe beam condition: 65 °C.

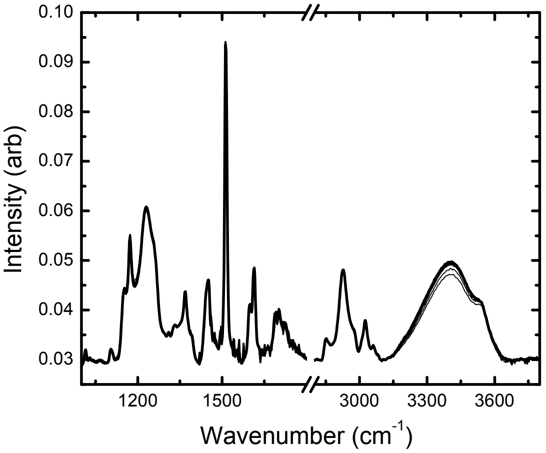

Figure 8.16 FTIR spectra of 248 nm PR after exposure to a 10 mT, 70 W Ar plasma for 5 s – 300 s. Substrate temperature: 50 °C.

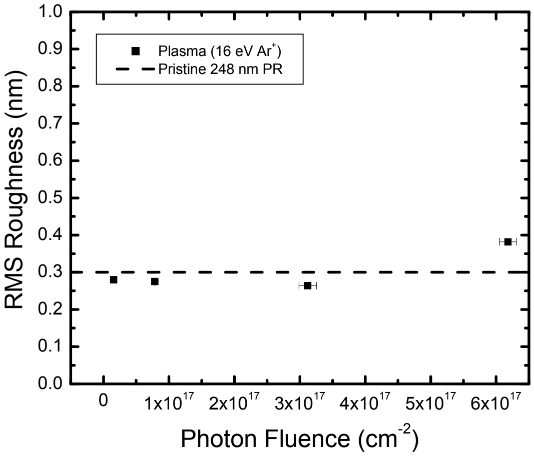

Figure 8.17 RMS surface roughness of 248 nm PR measured with AFM after exposure to an Ar plasma at 10 mT, 70 W. Substrate temperature: 50 °C.

8.5.3 Simultaneous VUV and Ion Exposures

8.5.3.1 Effect of VUV photon fluence

The synergistic effects of VUV-photon and ion bombardment on 193 nm PR were investigated in the ICP system (*cf* Table 8.1, condition 2) and compared to studies in the vacuum beam system (*cf* Table 8.2, condition 6). The FTIR absorbance spectra for plasma and simultaneous VUV and ion exposed samples are shown in Figure 8.18.

As observed with the VUV-only exposure cases, there is a rapid depletion of C=O and C-O-C bond structures that increases with VUV fluence and the variation between experiments is attributed to the difference in photon wavelengths, as discussed in the previous section. Note, that reproducibility in the vacuum beam system can vary as shown in the two 60 min exposure cases. The greatest difference between Xe-beam and Ar-ICP exposed samples are observed in the CH_2/CH_3 regions. A significant decrease in the CH_2/CH_3 peaks for the plasma-exposed samples indicate film etching occurs with the presence of 120 eV Ar^+ in the plasma system, as opposed to samples bombarded with 150 eV Ar^+ in the vacuum beam system. Measurements of ion mass spectra (Figure 8.19) and optical emission spectra show the presence of small concentrations of O-, and H-containing species with 120 eV Ar^+ bombardment. O^+, H^+, H_2O^+, CO^+, CO_2^+ and $CH_xO_y^+$ are observed at levels several orders of magnitude below the dominant Ar^+ ion signal. These species appear to be from etch products formed during plasma exposure[55,113]. The lack of film etching in the vacuum beam system with similar ion and photon fluences suggests that the presence of these small concentrations of O- and H-containing species are themselves responsible for the observed etching rather than just being evidence of low levels of etching.

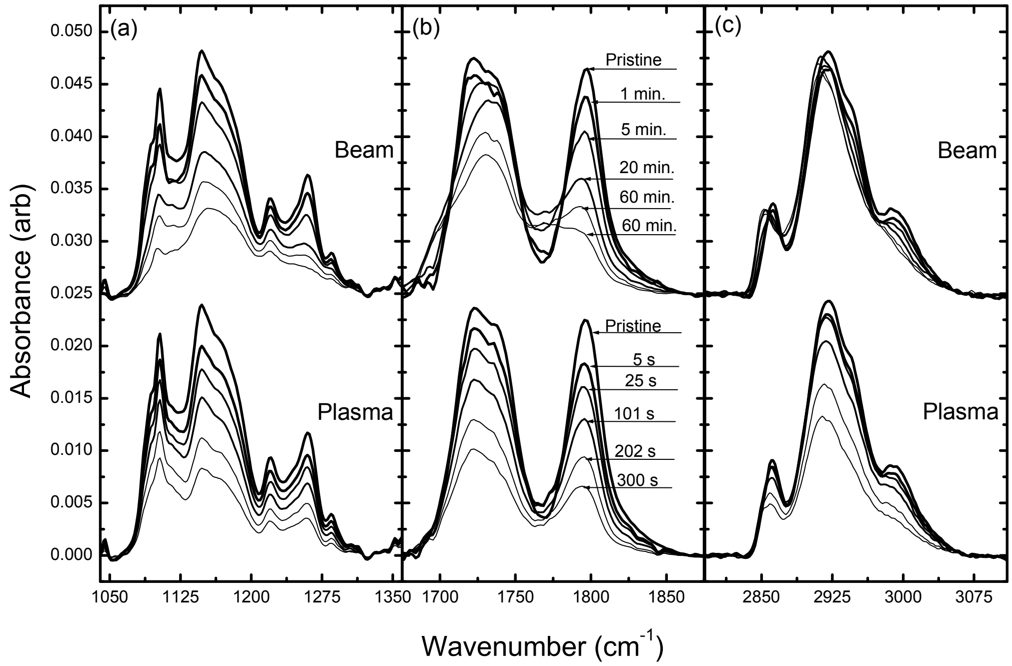

Figure 8.18 FTIR spectra of 193 nm PR: (a) C-O-C region, (b) C=O region, (c) CH_2/CH_3 stretch region. Ar plasma samples processed at 10 mT, 70 W, 50 °C, with 120 eV ions for 5 s – 300 s. Vacuum beam system samples are processed at 65 °C with Xe photons and 150 eV Ar^+ for 1 min – 60 min.

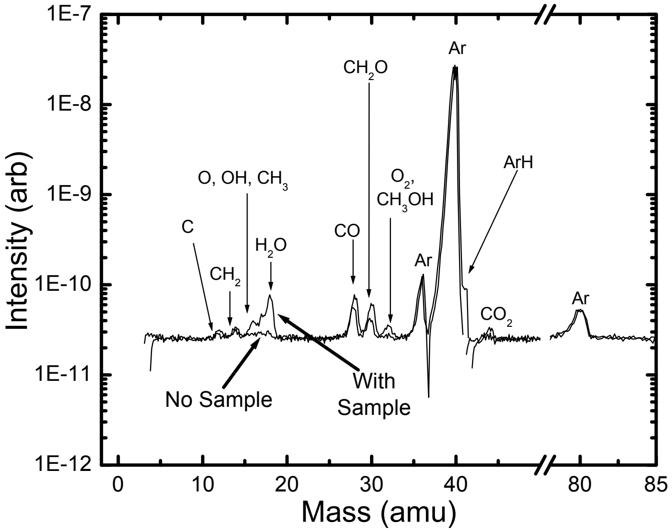

Figure 8.19 Ion mass spectrometer measurements for a 10 mT, 70 W Ar plasma, with and without 193 nm PR sample *in-situ*.

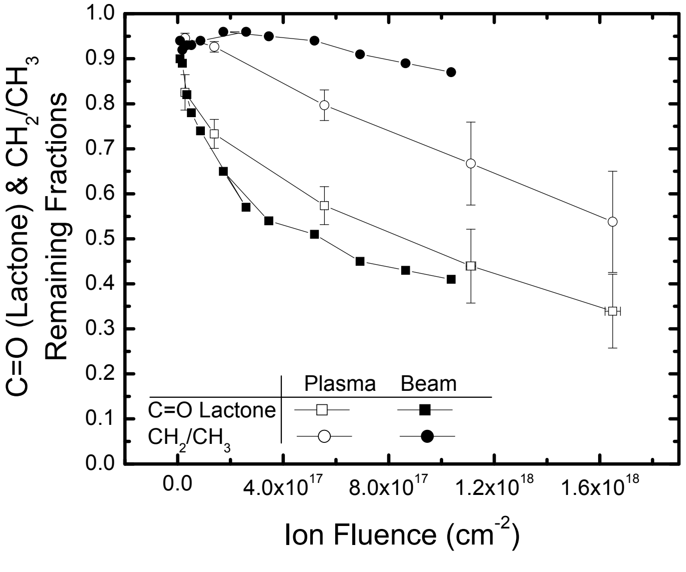

Figure 8.20 Remaining C=O and CH_2/CH_3 fractions in 193 nm PR, calculated from FTIR peak intensities. Ar plasma condition: 10 mT, 70 W, 50 °C, 120 eV ions. Vacuum beam condition: 65 °C, Xe photons and 150 eV Ar^+.

The observed changes in the C=O and CH_2/CH_3 peaks in the FTIR spectra are plotted in Figure 8.20 as a function of ion fluence and compared to the vacuum beam experimental results. The primary difference observed when comparing to the VUV-only exposure case (*cf* Figure 8.14) is the significant loss of CH_2/CH_3 species in the plasma-exposure case. As a result of the etching, the remaining fraction of C=O species does not saturate at 1×10^{18} photons/cm^2 in the Ar-ICP case as it does for the Xe-beam case. (Note, photon-to-ion ratio is 0.52 and 0.66 for the plasma and vacuum beam studies, respectively).

Previous results have demonstrated that the RMS roughness values of simultaneously VUV and ion-exposed PRs generally increase with time[6,62]. The increased roughening of PRs processed in both the vacuum beam (Table 8.2, condition 6) and ICP system (Table 8.1, condition 2) are shown in Figure 8.21. Under both conditions, the roughening increases with time and does not appear to saturate at 1×10^{18} ions/cm^2 as observed with the C=O depletion in the FTIR absorbance spectra. The increase in roughness with VUV fluence (PI ratio for Xe-beam and Ar-ICP cases are 0.66 and 0.52, respectively), is attributed to the changing mechanical properties of the PR[8,11]. As the photons penetrate the PR, CO bonds are rapidly scissioned causing a decrease in T_g[8,11]. As the scissioned layer continues to grow with exposure (up to ~100 nm), a larger volume of the PR is modified and induces stress within the top ~2 nm of the PR that has been graphitized by ion bombardment[99,110]. The mechanical properties of this 2 nm surface layer have also been altered from its pristine state and typically exhibit an increased molecular weight and T_g[109,114,115].

As a check, 248 nm PRs were processed in both the vacuum beam and ICP systems under identical VUV and ion exposure conditions. Although not shown here, the FTIR and analyses demonstrated no significant chemical modification was observed while AFM analysis (Figure 8.22) similarly shows insignificant change to the surface morphology and roughness. Therefore, the roughening results observed with the 193 nm PRs are unique to the PR chemical structure.

Representative AFM images of processed 193 nm PR samples from both the vacuum beam and ICP systems are shown in Figure 8.23. A comparison between the vacuum beam and ICP processed materials demonstrate similar roughening structures. As the VUV fluence is increased, the roughness transitions from the initial, smooth surface (pristine sample ~0.33 nm RMS) to a “pebble-like” structure. With continued VUV irradiation, the “pebble” structure transitions into a “yarn-like” structure. Therefore, even with the additional species (etch-products, radicals, neutrals) observed in the Ar-ICP system, the roughening behavior and structure are reproduced with the vacuum beam system for simultaneous VUV photon and ion exposure.

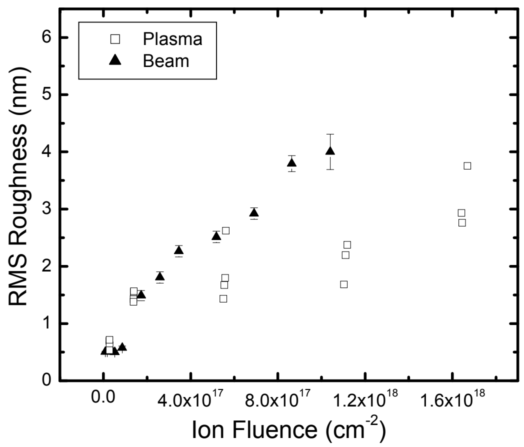

Figure 8.21 RMS surface roughness of 193 nm PR measured with AFM after processing in an Ar plasma at 10 mT, and 70 W with 120 eV ions. Sample temperature: 50 °C. Vacuum beam system: Xe photons and 150 eV Ar$^+$. Sample temperature: 65 °C.

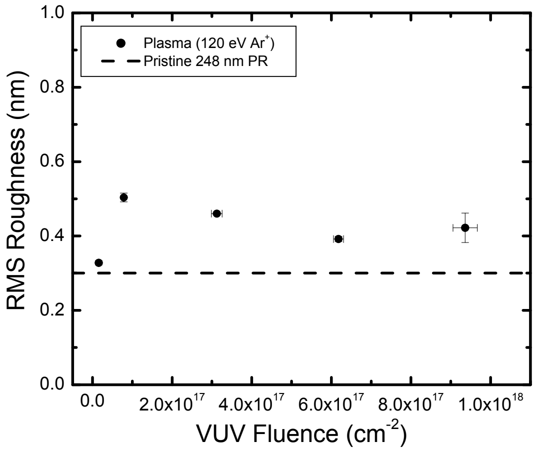

Figure 8.22 RMS surface roughness of 248 nm PR measured with AFM after processing in an Ar plasma at 10 mT, and 70 W with 120 eV ions. Sample temperature: 50 °C.

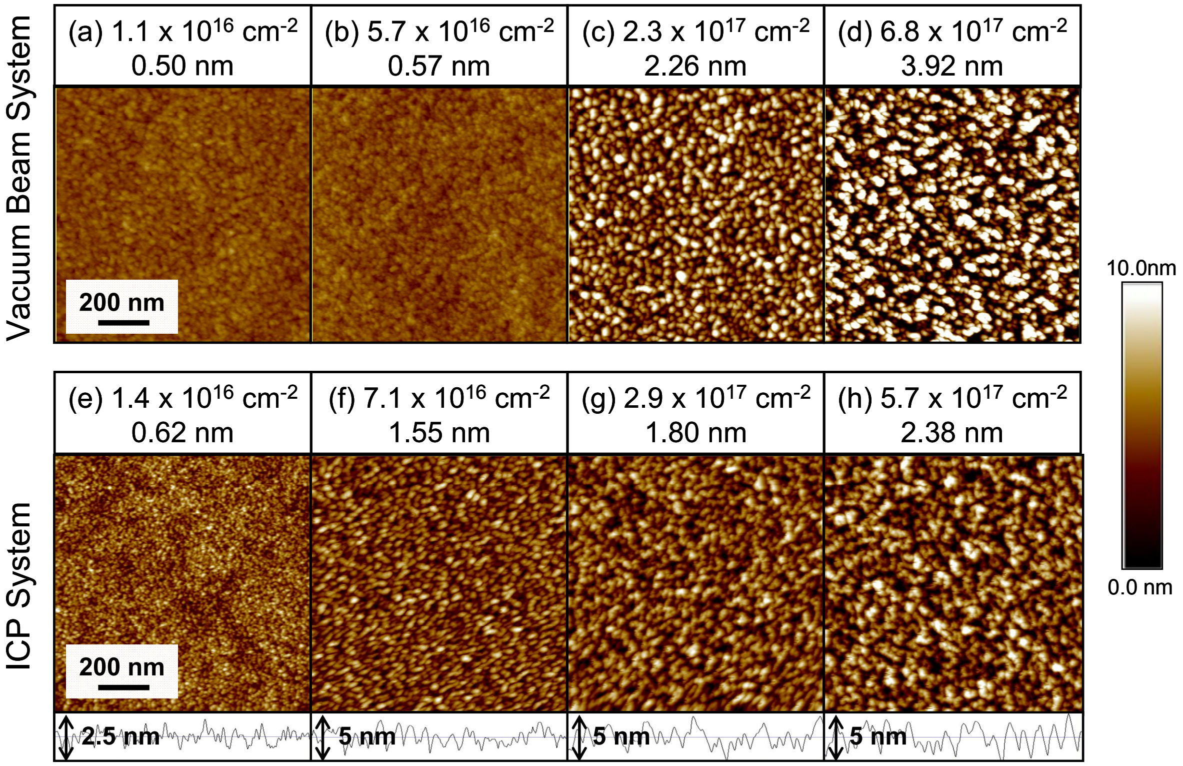

Figure 8.23 AFM images displaying typical roughening structure and RMS values for 193 nm PR materials processed in the vacuum beam (a – d) and ICP (e – h) systems. The VUV fluence for each condition is given. Materials in the vacuum beam system are exposed to Xe VUV photons (Resonance source) and 150 eV Ar$^+$ at 65 °C. PR in the ICP system are exposed to Ar VUV and 120 eV Ar$^+$ at 50 °C. All images are plotted on a 10 nm scale.

8.5.3.2 Effects of Ion Energy

The effect of ion energy on PR surface roughening was studied by varying the applied bias voltage to the sample holder in the plasma system. Initially, PR samples were exposed to an Ar plasma (10 mT, 70 W) at 50 °C for a range of processing times. Processed samples were measured with FTIR spectroscopy to determine the amount of etching (CH_2/CH_3 loss) and AFM to determine surface roughness. Formation of a graphitized layer for each sample was determined with THF dips.

FTIR analysis (Figure 8.24) demonstrated that application of larger bias voltages (i.e. increasing ion energy above the plasma potential) resulted in increased etching of the PR. For all bias voltages applied, there is an initial lag CH_2/CH_3 depletion. However as the C=O species are preferentially removed due to VUV photoabsorption, the concentrated CH_2/CH_3 remaining in the top ~100 nm of the PR is continuously etched away and is a function of the ion energy and fluence.

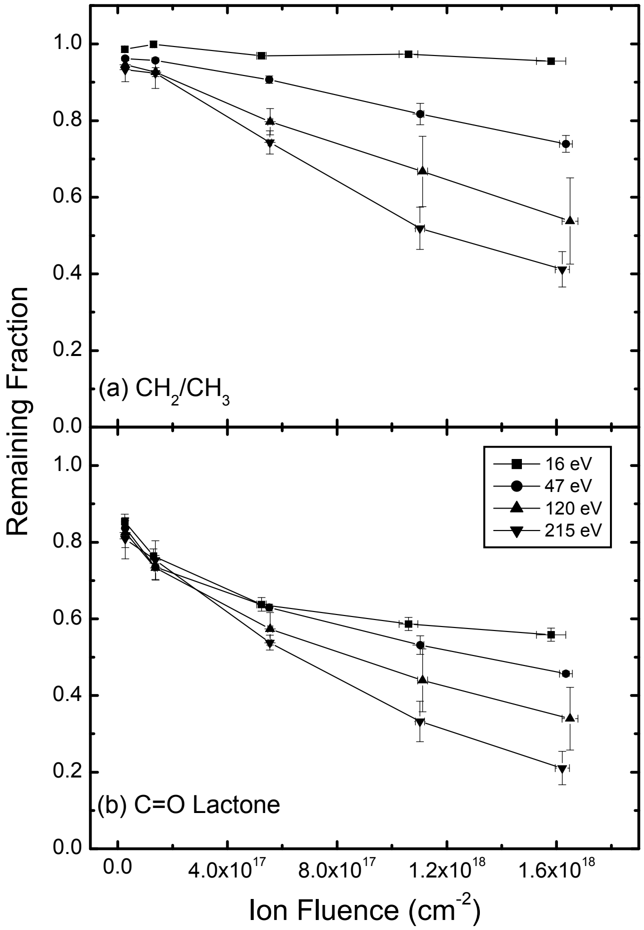

Figure 8.24 Remaining (a) CH_2/CH_3 and (b) C=O fractions in 193 nm PR, calculated from FTIR peak intensities of 193 nm PR processed in an Ar plasma at 10 mT and 70 W. Substrate temperature: 50 °C. Ion energies varied: 16 eV, 47 eV, 120 eV and 215 eV ions.

The RMS surface roughness of the PR increases with larger bias voltage application although the total VUV photon and ion fluences are similar (Figure 8.25). The sudden increase in PR roughness between processing with 47 eV ions and 150 eV ions appeared to indicate that a threshold energy must be overcome to initiate PR roughening. The threshold energy was determined by processing PR samples in an Ar plasma (10 mT, 70 W) at 50 °C for 5 min (~ 8 – 9 × 10^{17} photons/cm^2), under various ion energies. The results are plotted in Figure 8.26. For comparison, a sample processed in the vacuum beam system with 150 eV Ar^+ at 65 °C for ~7 × 10^{17} Xe photons/cm^2 (PI = 0.66) is also plotted.

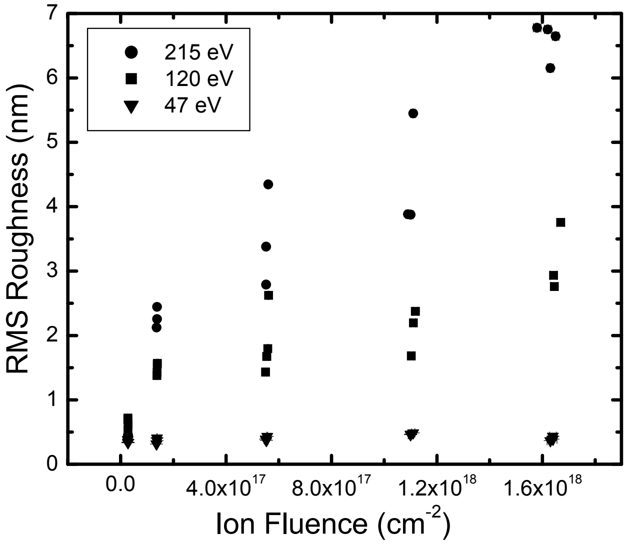

Figure 8.25 RMS surface roughness of 193 nm PR measured with AFM after processing in an Ar plasma at 10 mT and 70 W with 47 eV, 120 eV, and 215 eV ions. Sample temperature 50 °C.

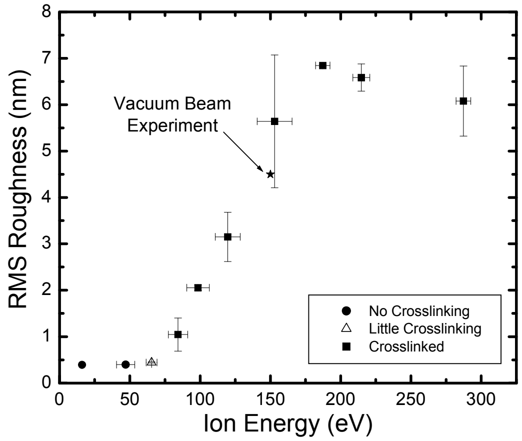

Figure 8.26 RMS surface roughness of 193 nm PR measured with AFM after processing in an Ar plasma at 10 mT and 70 W. Samples processed for 5 min: ~8 – 9 × 10^{17} photons/cm^2. Sample temperature: 50 °C.

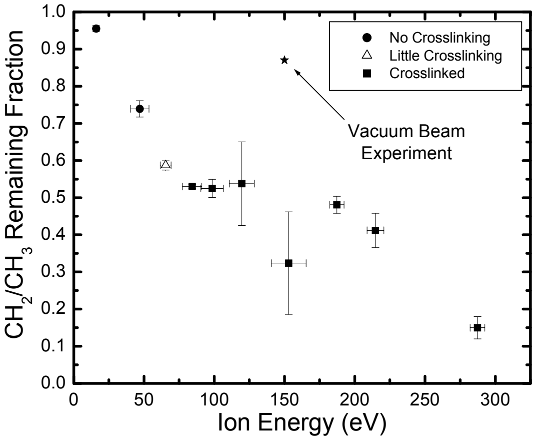

Figure 8.27 Remaining CH_2/CH_3 fraction in 193 nm PR, calculated from FTIR peak intensities after processing in an Ar plasma at 10 mT and 70 W. Samples processed for 5 min: ~8 – 9 × 10^{17} photons/cm^2. Sample temperature: 50 °C.

PR samples remain smooth and demonstrate no etching when bombarded with plasma potential ions (16 eV). These samples show no evidence that a strong graphitized layer has formed when irradiated with primarily VUV photons. As the ion energy is increased to ~65 eV, the etching rate increases, however the PR samples remain smooth and THF dips show little-to-no graphitized layer formation. When the bombarding ion energy is increased beyond 65 eV, there is increased PR roughening. Furthermore, THF dips indicate that a strongly graphitized layer has formed on the PR surface. A maximum roughness is observed around 150 – 175 eV and then appears to decrease at energies beyond ~200 eV. Vacuum beam studies of 193 nm PR exposure to energetic ions demonstrate a decrease in roughening with increasing ion energy. This decrease in roughening may suggest an annealing effect of high energy ions.

The transition from a relatively smooth PR surface with ion energies < 65 eV to a rough surface for ions > 65 eV suggests a kind of "threshold energy" or minimal ion energy necessary to induce PR roughening. Concurrently, the lack of a graphitized layer for ion energies < 65 eV and the formation of the graphitized layer > 65 eV indicates that a graphitized surface layer may be the necessary precursor to induce PR roughening. This is further evidenced by the continuous formation of the graphitized layer at higher energies, although the etch rate increases substantially with ion energy (Figure 8.27).

It is hypothesized that the ~ 1 – 2 nm ion bombardment-induced graphitized layer at the PR surface may be in compressive stress due to the ions. Research has shown that the mechanical properties of tetrahedral amorphous carbon (diamond like carbon) or hydrogenated tetrahedral amorphous carbon films deposited from carbon ions impacting substrates are dependent upon the carbon ion energies[116-118]. As the carbon ion energy increases, the mass density, sp^3 fraction and intrinsic stress of the film increases. The intrinsic stress is typically biaxial and compressive. However, above a certain threshold energy, the deposited film mass density begins to decrease, as well as the sp^3 fraction and intrinsic stress[118]. The relation between compressive stress developed in a thin diamond film as a function of ion energy has also been explored by molecular dynamic (MD) simulations[116]. MD simulations demonstrated that for low energy ions impacting a surface, (e.g. < 20 eV) the ions are reflected from the film without any change. For intermediate energies (e.g. 20 – 80 eV), a local compressive stress was observed due to penetration of incident atoms. At higher energies (e.g. 80 – 100 eV), incident atoms penetrated deeply and induced knock-on collisions. McKenzie *et al.* attributed this behavior as a "thermal spike" where localized melting and rapid chilling of a small region occurs[116]. As the bombarding energy increases, the impacts create a region large enough to flow that relieves the accumulated stress.

Since it is known that 100 eV Ar ions transfer energy with > 90 % efficiency to C atoms, the top graphitized layer consisting of C atoms should be of an equivalent energy[119]. Thus as the ion bombardment energy in the plasma experiments is increased from 65 eV to 150 eV, the density of the graphitized layer probably increases, as does the intrinsic stress, and an increase in PR roughening is observed. Above the observed threshold of 150 eV where PR roughening begins to slightly decrease, the graphitized film may have likely transitioned to a slightly decreased density, lower fraction of sp^3 production and due to a "thermal spike" yields a decreased intrinsic stress in the film.

8.5.3.3 Effects of Photon-to-Ion Flux Ratios

The effects of photon-to-ion flux (PI) ratio was investigated in the ICP system by varying the deposition power (0 – 200 W) and pressure (10 mT and 50 mT) conditions. Any dependence of surface roughness on PI ratio is complex as the PI ratio itself is complex and behaves differently for different pressures (Figure 8.28)[36]. It is possible that at higher pressures as the VUV photons become trapped and re-absorbed in the plasma the effect of ions becomes increasingly important. Coupled with an increasing number of C/H/O-type etch-products and contaminants in the system at higher pressures, the slightest change in ion composition may alter the response of PR roughening (e.g. by competing etching and graphitization rates) and dependence on PI ratio. XPS measurements of polymer samples processed in O_2-plasmas have demonstrated that oxygen radical species may prevent the formation of a dehydrogenated, graphitized layer[120]. Interestingly, Figure 8.29 shows for a 50 mT, 25 W Ar plasma, the estimated mass loss (from FTIR measurements) is much greater than the mass loss for samples processed in 50 mT, 190 W and 10 mT 70 W Ar plasmas, all with 120 eV ions. THF dips of the PR samples for this 50 mT, 25 W condition show no formation of a graphitized layer and the surface morphology remains smooth (Figure 8.30). It is possible that the rate of mass loss is greater than the rate of formation of the graphitized layer.

The occurrence of enhanced surface roughening in 193 nm PR, however, appears to necessitate a PI ratio between 0.1 and 0.7. As demonstrated earlier, a VUV-only flux (PI = ∞) yields a smooth surface structure. Similarly early studies of ion-only exposures (PI = 0) conducted in the vacuum beam system demonstrated roughening notably less than simultaneous ion and VUV exposure[6,62]. In order to generate enhanced roughening of 193 nm PR samples in the vacuum beam system, PI ratios were maintained between 0.1 and 0.7. Specifically, ratios of 0.66, 0.37, and 0.19 were utilized for the conditions investigated in Table 8.2, all of which clearly demonstrated roughening of PR surfaces.

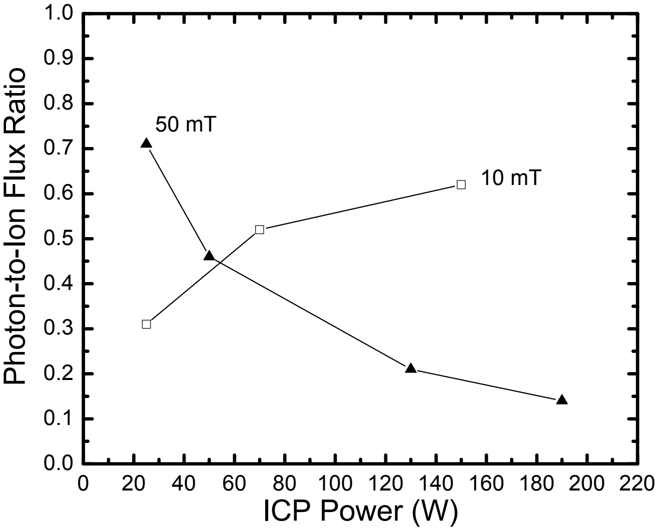

Figure 8.28 Photon-to-Ion flux ratio in a 10 mT and 50 mT Ar plasma.

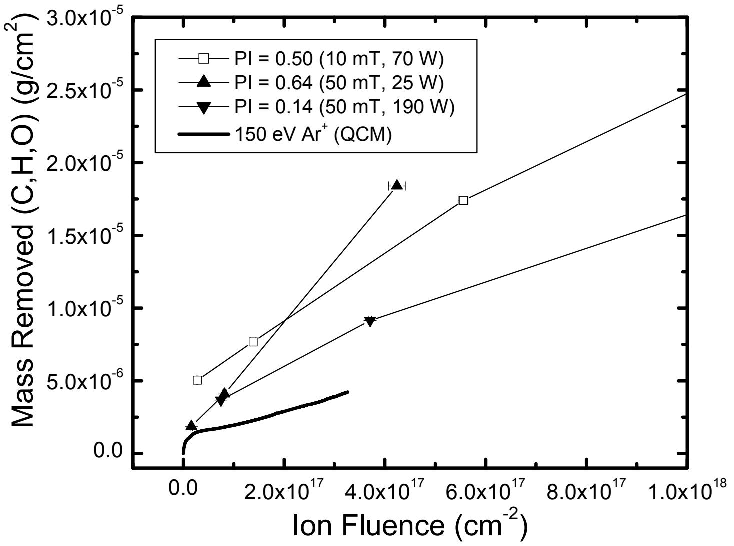

Figure 8.29 Estimated mass loss (from FTIR spectra) for 193 nm PR samples processed with 120 eV ions in a 10 mT, 70 W plasma and a 50 mT, 25 W and 190 W plasma. Mass loss is compared to QCM measurements for 193 nm PR processed with 150 eV Ar^{+} in the vacuum beam system.

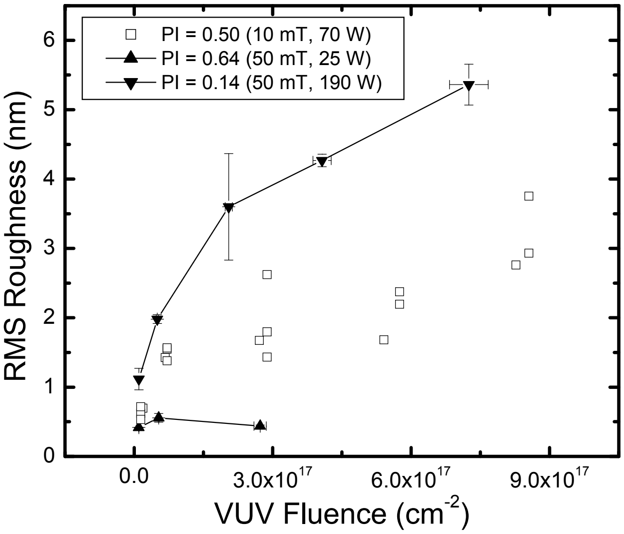

Figure 8.30 RMS surface roughness measurements for 193 nm PR samples processed with 120 eV ions in a 10 mT, 70 W plasma and a 50 mT, 25 W and 190 W plasma. PR samples processed at 50 mT, 25 W do not show formation of a graphitized layer.

8.5.3.4 Temperature Effects

The effect of temperature on 193 nm PR roughening was controlled by adjusting the sample holder temperature via a water-bath for constant ion and VUV fluence. All samples were attached to the sample holder with thermal paste to ensure good thermal contact. To monitor temperature control, sample temperatures in the ICP chamber were measured with Omega Four-Point irreversible temperature indicators attached to the sample. Temperature stickers indicated temperatures reached set-point values within 1 – 2 °C for plasma-off conditions. For sample temperatures greater than 50 °C, plasma-on conditions increased the sample temperature by ~ 10 °C for long time (5 min.) and high power exposures. This heating is attributed to ion bombardment[33,121].

FTIR absorption spectra (Figure 8.31) of 193 nm PR samples processed in the vacuum beam and ICP systems under identical VUV and ion fluences demonstrate that bulk modification is independent of temperature. AFM measurements, however, indicate surface roughness and morphology is sensitive to substrate temperature conditions. Figure 8.32 displays the RMS roughness values for 193 nm PR as a function of temperature for Ar-ICP experiments (Table 8.1, condition 2), and Ar VUV plus Ar^+ (Table 8.2, condition 4), and Xe VUV plus Ar^+ (Table 8.2, condition 5) vacuum beam exposures. As the temperature is increased, there is a nearly monotonic increase in RMS roughness. The total RMS roughness for samples processed in the vacuum beam system is comparatively smaller due to a slightly decreased exposure fluence.

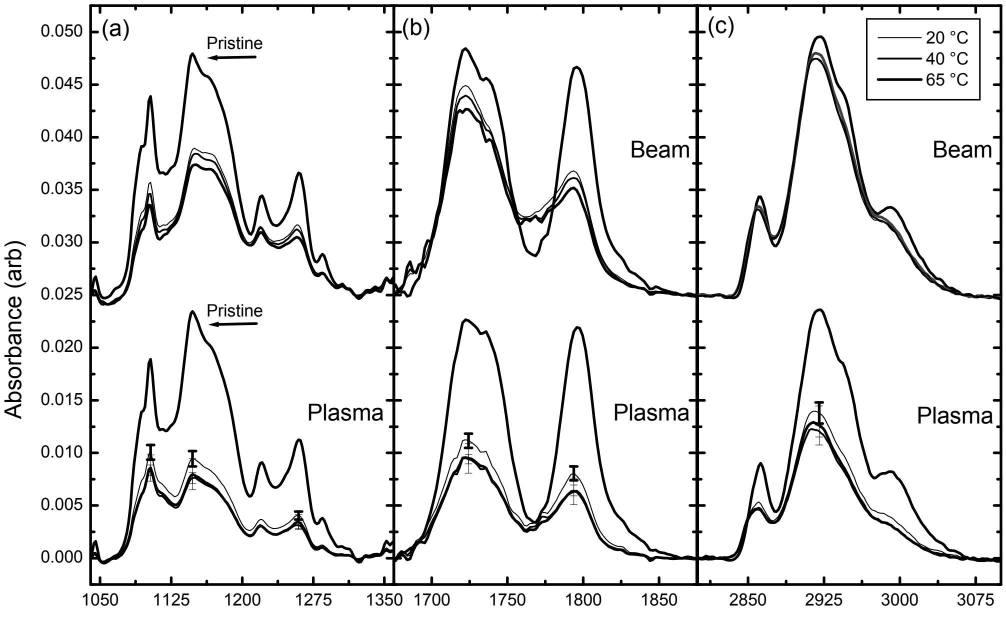

Figure 8.31 FTIR spectra of 193 nm PR: (a) C-O-C region, (b) C=O region, (c) CH_2/CH_3 stretch region. Ar plasma samples processed at 10 mT, 70 W, with 120 eV ions for 300 s. Vacuum beam system samples are processed with Xe photons and 150 eV Ar^+ (Table 8.2, condition 5). Sample temperatures are maintained at 20 °C, 40 °C, and 65 °C for the duration of each experiment.

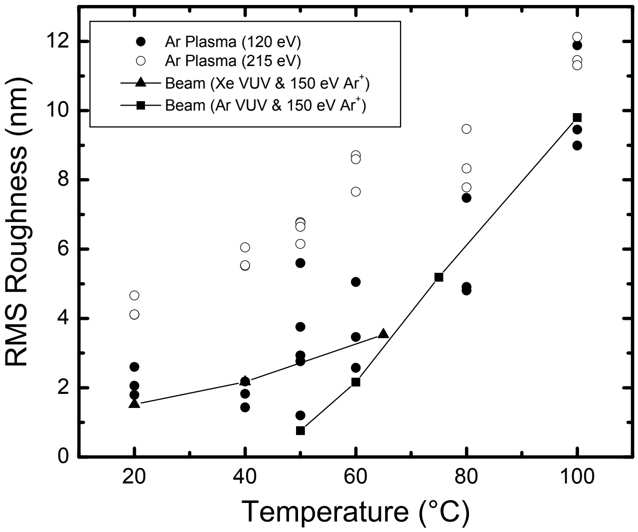

Figure 8.32 RMS surface roughness measurements as a function of temperature for 193 nm PR processed in an Ar plasma at 10 mT, 70 W, with 120 eV and 215 eV ions for 300 s. Vacuum beam system samples are processed with Xe photons and 150 eV Ar$^+$ (triangles) and Ar photons and 150 eV Ar$^+$ (squares) (Table 8.2, conditions 4 and 5).

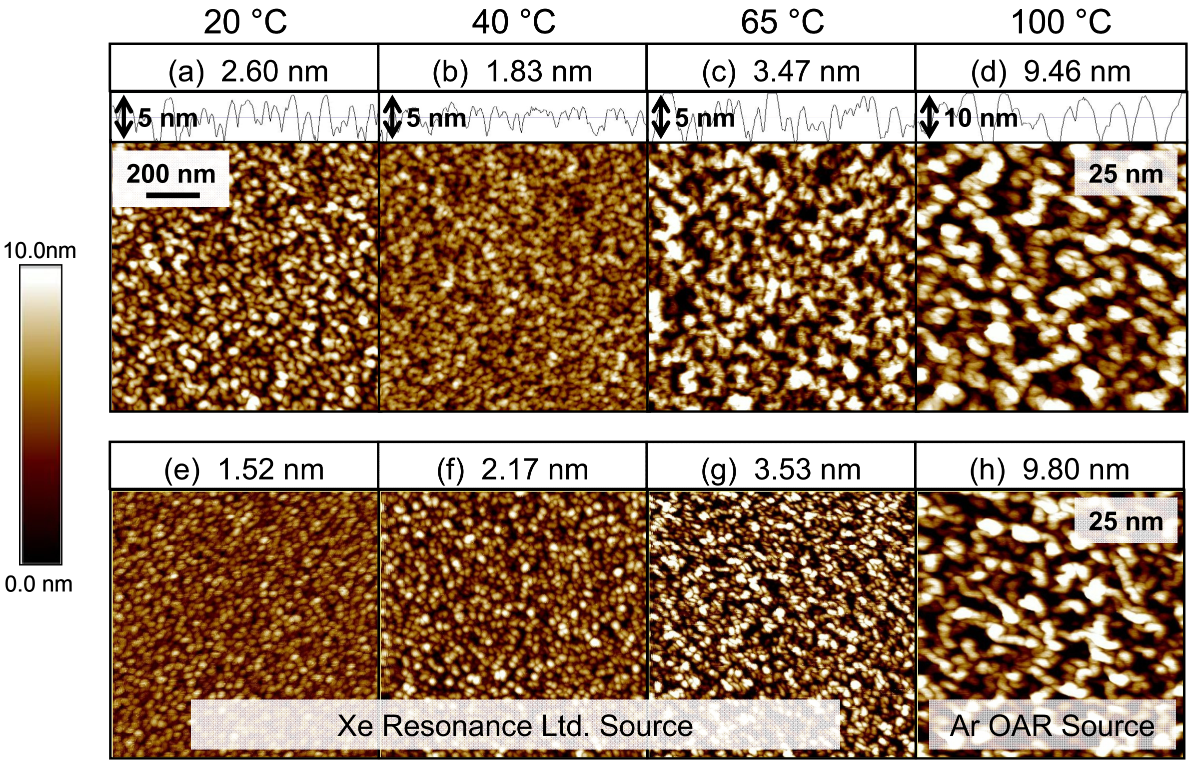

Figure 8.33 AFM roughness images for samples processed in the (a – d) Ar-ICP system. Samples receive a VUV fluence of 8 – 9 × 10^{17} photons/cm^2 and 120 eV ions (Table 8.1, condition 2); (e – g) vacuum beam system with the Xe-line Resonance source. Samples receive 3.7 × 10^{17} photons/cm^2 and 150 eV ions (Table 8.2, condition 5); and (h) Ar-lamp OAR source (Table 8.2, condition 4). AFM images are 1 µm × 1 µm. Color scale is 10 nm unless otherwise noted.

The physical characteristics of 193 nm PR roughness (i.e. grain-size and shape) are similar in both vacuum beam and ICP systems. Figure 8.33 displays the AFM images for samples processed at various temperatures in the ICP and vacuum beam systems. At 20 °C and 40 °C, the feature size is small and roughness ranges from 1.5 – 2.5 nm. Samples processed in the vacuum beam system (e and f) are exposed to Xe VUV photons at 3.7×10^{17} cm^{-2} vs. Ar VUV photons in the ICP system (a and b) at $8 - 9 \times 10^{17}$ cm^{-2}. Due to the larger VUV fluence in the ICP system, the resulting features are less pebble-like and more "yarn-like." As the temperature is increased to 65 °C and 100 °C, the roughening continues. In both beam (h, Ar OAR source) and plasma (d) results, the roughness produces similar "yarn-like" features on the same scale ~ 9 – 10 nm.

Increasing substrate temperature may contribute to the compressive stresses generated in the ion and VUV modified layers. Measurements have shown that the T_g values of VUV-scissioned PRs decrease with VUV fluence[8,11]. Simultaneously, due to ion bombardment of the surface layer, the top ~2 nm is dehydrogenated and highly graphitized[99,109], therefore contributing to an increased T_g. The combination of a top surface region in compressive stress and an underlying layer with a greater tendency to relax may lead to the wrinkled surfaces described as enhanced PR roughening.

8.5.4 Wrinkling Mechanism

The results above demonstrate the experimental conditions necessary to initiate PR roughening and provides some insight to a possible roughening mechanism. The exact mechanism still requires further investigation since mechanical properties of the processed PRs must be measured and complex plasma systems still require study. Thus far, however, experimental and MD results demonstrate the formation of an ion modified graphitized layer, ~ 2 nm thick, with increased T_g, density, and viscosity above a thick (~100 nm) VUV-scissioned layer with decreased T_g, density, and viscosity. Given the significant difference in the resulting mechanical properties of each layer, wrinkling may occur to relieve the intrinsic stress that develops within the top graphitized layer due to ion bombardment[116-118].

The formation of this bilayer system with differing mechanical properties may be the cause, or at least the initiation, of polymer wrinkling. For example, unlike 193 nm PR, 248 nm PR demonstrates little roughening when exposed to similar VUV photon and ion fluence conditions. The 248 nm PR will form the same ion-induced surface graphitized (cross-linked) layer, but the absence of significant C-O bonds in this material precludes the deeper scissioning that occurs in 193 nm PR. Rather, the VUV will act to cross-link the 248 nm PR, thus reducing the likelihood of surface wrinkles forming. Numerous authors report the formation of wrinkles (e.g. herring-bone patterns) for polymer films only in the presence of a top compressively stressed layer in a bilayer system in which the underlying layer can deform either elastically or viscoelastically[122-128].

8.5.4.1 Compressive Stress Calculations

The minimum compressive stress necessary to initiate wrinkling of 193 nm PR is estimated from elastic-viscoelastic bilayer systems used to model thin metal/polymer film systems[123,124,129]. Huang *et al.*[123-125] shows the critical condition for wrinkling and the extent of wrinkling (amplitude and wavelength) are dependent on the film and underlayer thicknesses, h_f and H, respectively. For thick viscoelastic (i.e. VUV-scissioned) layers (H) and thin films (h_f), the effect of H decreases as $H/h_f \rightarrow \infty$. The experimental conditions studied for 193 nm PR processing (Ar 10 mT, 70 W, 5 s – 300 s) results in photoabsorption penetration depths of 38 – 90 nm (see simulation study in Chapter 7), while the graphitized layer is ~ 2 nm. Therefore analysis of the critical condition can be taken in the limit $H/h_f \rightarrow \infty$.

The critical stress (σ_{c0}), for $H/h_f \rightarrow \infty$ is defined as:

$$\sigma_{c0} = -E_f \left(\frac{9}{16\left(1-\nu_f^2\right)\left(1-\nu\right)^2} \right)^{1/3} \left(\frac{\mu_0}{E_f} \right)^{2/3} \tag{8.1}$$

where E_f, ν_f, and μ_0 are the Young's modulus, Poisson's ratio, and relaxation modulus of the film, respectively, and ν is Poisson's ratio for the underlying layer. The wrinkling wavelength (L_0) and amplitude (A_0) for $\sigma_0 > \sigma_{c0}$ are:

$$L_0 = 2\pi h_f \left(\frac{\left(1-\nu\right)E_f}{6\left(1-\nu_f^2\right)\mu_0} \right)^{1/3} \tag{8.2}$$

$$A_0 = h_f \sqrt{\frac{\sigma_0}{\sigma_{c0}} - 1} \tag{8.3}$$

Mechanical properties of the modified 193 nm PR are estimated from published literature. The graphitized layer is approximated as tetrahedral amorphous carbon (ta-C)[116,118], while the VUV-scissioned layer is modeled as poly-methyl methacrylate (PMMA) (Table 8.3).

The critical stress is dependent on the relaxation modulus, which is a function of time. However in the limits of the glassy and rubbery cases, the critical stresses are ~ 5 GPa and 11 MPa, respectively (Table 8.4). For the glassy case, this results in a wrinkling wavelength of ~ 28 nm and amplitude of ~ 4 nm. This is in rather good agreement with AFM images (eg. Figure 8.23 and 8.33) where RMS roughness values are ~3 – 4 nm, and granular/pebble formation is on the order of 20 – 40 per 1 μm in length measured. Additionally, a critical compressive stress value of 5 GPa for wrinkling of 193 nm PR is not unreasonable when experimental and calculated compressive stresses for buckling of plasma-modified polymers are on the order of 15 – 20 GPa[130].

Experimental results demonstrate there is a clear dynamic dependence on processing time. Not only are the thicknesses of each modified layer changing with time (due to etching and photoabsorption), but the mechanical properties and compressive stresses are changing as well. Assuming constant E_f, the growth of the winkling amplitude can be found as a function of σ_0 and μ (Figure 8.34), i.e. as a function of processing time. Short time vacuum beam system measurements are normalized to the results, demonstrating the lag between the initial exposure time (at 0 s) and initial onset of PR wrinkling (5 min) may be due to the time dependent change in μ and growth of σ_0. Clearly, a deeper understanding of the material mechanical properties is required.

Table 8.3 Mechanical properties of ta-C and PMMA

Property	ta-C	PMMA
Glassy Modulus (Pa): $\mu_{0,r}$	10^9	
Rubbery Modulus (Pa): $\mu_{0,g}$	10^5	
Young's Modulus (Pa): E	1×10^{11}	3×10^9
Poisson's Ratio: v	0.202	0.35
Height (nm):	2	100

Table 8.4 Calculated critical compressive stresses, wavelengths, and amplitudes for bi-layer ta-C and PMMA polymer wrinkling.

	Glassy Limit	Rubbery Limit
Critical Film Stress (GPa): σ_{c0}	5.18	0.0112
Critical Wavelength (nm): L_0	28.2	607.4
Amplitude for $\sigma_0 > \sigma c_0$ (nm): A_0	4.09	21.03

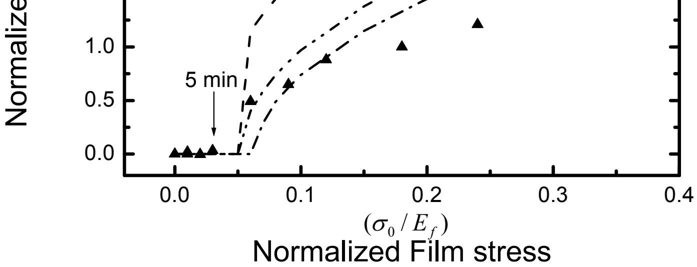

Figure 8.34 Wrinkle amplitudes calculated as a function of compressive film stress for fixed values of E_f. Calculated results are compared to the normalized vacuum beam system experimental data for 193 nm PR samples processed with 150 eV Ar^+ and Xe VUV photons for 30 s to 1 hr.

8.5.4.2 Temperature Considerations

Experimental results clearly demonstrate that the magnitude of PR roughening is temperature dependent and may possibly reflect some changes in the mechanical properties of the PR and the mismatch between sandwiched layers. Table 8.5 summarizes how physical and chemical modifications to pure PMMA (e.g. cross-linking, scissioning, etching) will affect some thermo-mechanical properties.

The stresses induced by thermal mismatch between the graphitized – VUV scissioned – pristine PR tri-layer were considered by calculating the induced stress from each layer and summing them by the principle of superposition[131]. The flexural stress in layer "a" with respect to "b" and "b" with respect to "a" is calculated as follows:

$$\sigma_a = -\frac{E_a(\alpha_b - \alpha_a)\Delta T}{(1-\nu_a)K}\left[3\left(\frac{t_a}{t_b}\right)+2\left(\frac{t_a}{t_b}\right)^2 - \frac{E_b}{E_a}\frac{t_b}{t_a}\left(\frac{1-\nu_a}{1-\nu_b}\right)\right] \qquad (8.4)$$

$$\sigma_b = -\frac{E_b(\alpha_b - \alpha_a)\Delta T}{(1-\nu_b)K}\left[3\left(\frac{t_a}{t_b}\right)+2 - \frac{E_a}{E_b}\left(\frac{t_b}{t_a}\right)^3\left(\frac{1-\nu_b}{1-\nu_a}\right)\right] \qquad (8.5)$$

where K is define as:

$$K = 4 + 6\left(\frac{t_a}{t_b}\right)+4\left(\frac{t_a}{t_b}\right)^2 + \frac{E_a}{E_b}\left(\frac{t_b}{t_a}\right)^3\left(\frac{1-\nu_b}{1-\nu_a}\right)+\frac{E_a}{E_b}\left(\frac{t_a}{t_b}\right)\left(\frac{1-\nu_a}{1-\nu_b}\right) \qquad (8.6)$$

The variables t, ν, α, and E are the layer thickness, Poisson's ratio, coefficient of thermal expansion and Young's modulus, respectively.

Assuming, however, the mechanical properties are temperature independent, the induced stresses for ΔT = 25 °C (i.e. 50 °C experimental condition) are calculated. Because α values for the graphitized and scissioned layers were unknown, estimated values were used based on pure PMMA (6×10^{-5} K^{-1}). With these approximations ($\alpha_{scissioned} = 8 \times 10^{-5}$ K^{-1}), a compressive stress of ~ 20 MPa is generated in the graphitized layer by the thermal mismatch with the VUV-scissioned layer. Although this compressive stress << critical compressive stress (5 GPa), calculations assume the mechanical properties are not varying with time. As previously examined, the dynamic time dependency of the mechanical properties must be considered, which is now further complicated by its dependency on temperature.

Table 8.5 Changes in the thermal and mechanical properties of PMMA properties due to material modification.

For Pure PMMA, as:	Changes to properties:
Temperature increases	Young's modulus (E) decreases[132] Poisson's ratio increases[132]
Film thickness decreases	Glass transition temperature (T_g) increases[133] Coefficient of thermal expansion (CTE) increases[133]
Cross-linking increases	Specific volume decreases[134] MW increases[135] T_g increases[134] Viscosity increases[135] For $T > T_g$, CTE decreases[136] For $T < T_g$, CTE is constant[136]
Scissioning increases	MW decreases[136,137] Viscosity increases[137] van der Walls bonds increase[136,138] Broken covalent bonds increase[138] T_g decreases[136] Thermal conductivity decreases[136,138] CTE increases with increasing T[138]

8.5.5 Patterned 193 nm Photoresist Samples

193 nm PR patterned samples were processed in the ICP system under experimental conditions similar to the blanket PR studies (Table 8.1). The effects of VUV photons (plasma cure), fluence, ion energy and temperature on LWR were measured with SEM and compared to RMS surface roughness measurements. Analysis of line-segments varying in length (40 nm – 540 nm) provided low and high frequency LWR values.

8.5.5.1 Plasma Cure Treatment

Treatment of patterned samples in the plasma cure condition (Ar 10 mT, 70 W, 50 °C, zero-bias) is consistent with the previous blanket PR studies and with cure processes studied by other groups[7,11]. All PR samples demonstrate a smoothing of the PR surface and LWR with increasing exposure time. The smoothing of the PR sample surface correlates well with the decrease in both low and high frequency LWR, indicating that the VUV photons are likely responsible for smoothing the PR (Figure 8.35). Typically the observed low frequency LWR is greater than the high frequency LWR by several nm. As exposure time increases, the difference between low and high frequency LWR decreases from 4 nm (at 4 s) to 2 nm (at 270 s) (Figure 8.36).

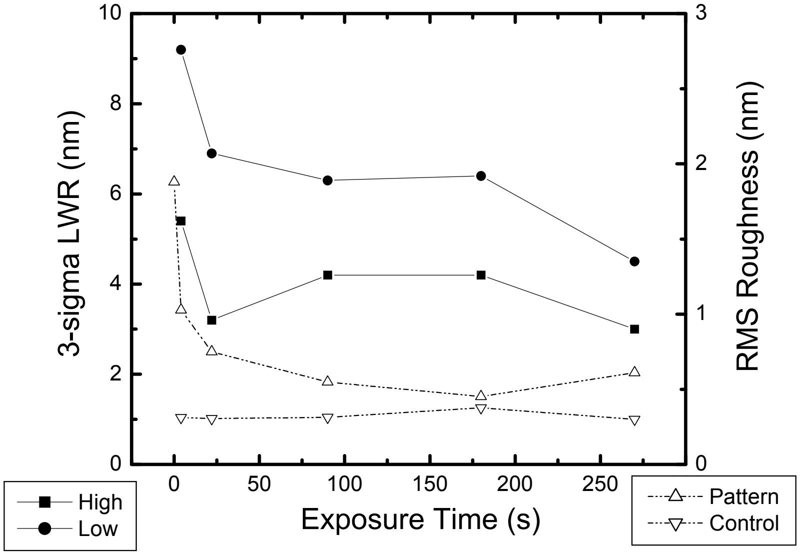

Figure 8.35 RMS surface roughness of patterned 193 nm PR measured with AFM after processing in a 10 mT, 70 W Ar plasma. Sample temperature: 50 °C. Zero-bias is applied (plasma cure treatment). Measurements are compared to surface roughness of control blanket 193 nm PR. High and low frequency LWR measured with SEM.

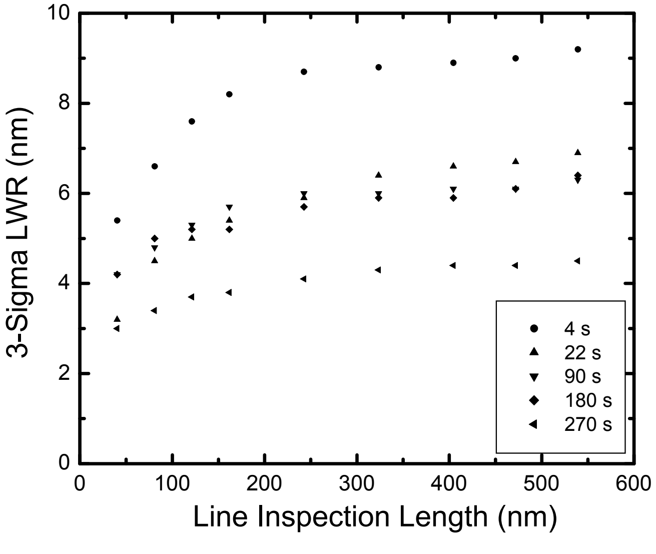

Figure 8.36 LWR values vs. line inspection length. Ar plasma cure: 10 mT, 70 W. Sample temperature 50 °C.

8.5.5.2 Synergistic VUV Photon and Ion Effects

The synergistic effects of high energy ion and VUV photon irradiation on LWR is observed on the patterned samples by biasing the sample holder. Patterned samples receive 110 eV ions in a 10 mT, 70 W, Ar plasma (Table 8.1, condition 2). Unlike the previous blanket sample studies, it appears that both LWR and surface roughness decreases with exposure time and begins to increase only after ~ 200 s (Figure 8.37). This apparent discrepancy may be explained by the use of 110 eV ions, which is close to the threshold energy (70 eV) (Figure 8.38). Control blanket samples processed with the 110 eV ions show a similar delay in generating enhanced PR roughness. Additionally, the initial decrease in LWR and surface roughness may be due to the pre-existing roughness of the patterned PR. It is possible that the mechanical properties of the film have been previously altered with prior photolithography steps or the initial roughness may influence how the compressive stress in the graphitized layer accumulates with time.

Both high and low frequency LWR correlate well with surface roughness as a function of ion energy (Figure 8.39). At ion energies below the 70 eV threshold, both LWR and surface roughness smooth and is consistent with the plasma cure conditions. The difference between high and low frequency LWR is also minimized to ~ 2 nm (Figure 8.40). Above 70 eV, both LWR and surface roughness increase. Beyond 200 eV, however, surface roughness tends to stop and is similar to the observations made in the blanket sample studies. In contrast, LWR significantly increases indicating that the roughness may depend on the geometry and resulting boundary conditions imposed on the compressively stressed layer. Additionally, at these higher energies, the difference between low and high frequency LWR is increasing, up to ~ 5 nm. Representative SEM and AFM images are shown in Figures 8.41 and 8.42.

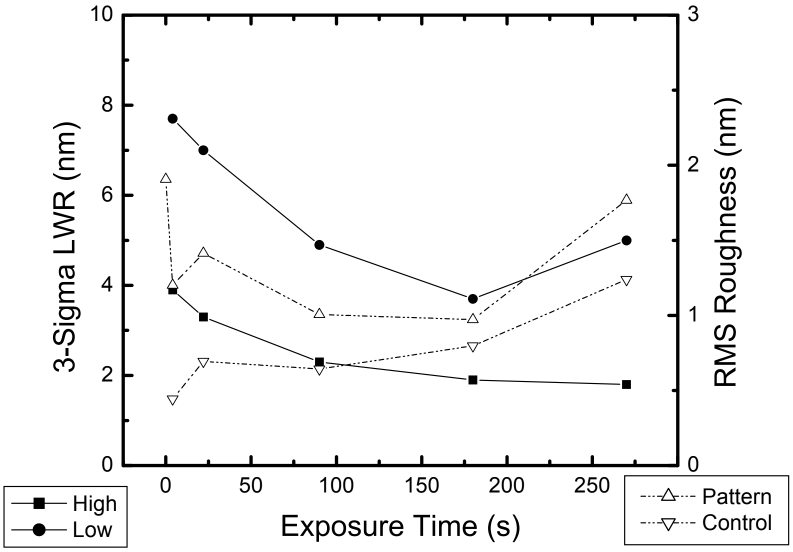

Figure 8.37 RMS surface roughness of patterned and control blanket 193 nm PR measured with AFM. High and low frequency LWR measured with SEM. Ar plasma: 10 mT, 70 W, 110 eV ions. Sample temperature: 50 °C.

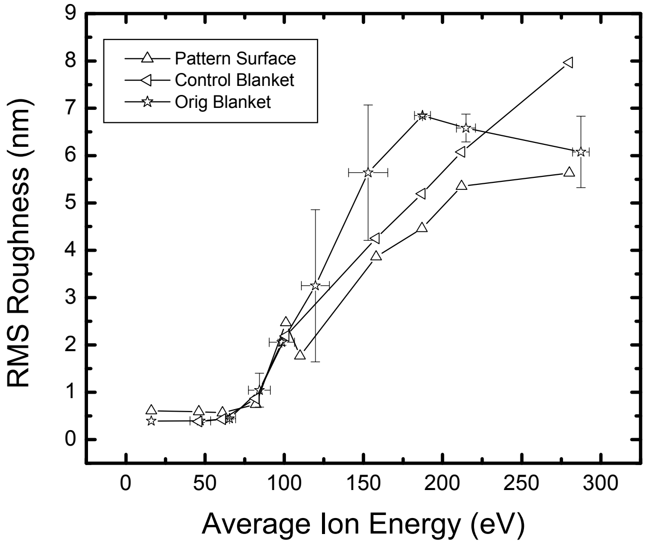

Figure 8.38 Comparison between RMS surface roughness of patterned and blanket 193 nm PR samples at varying ion energies. Ar plasma: 10 mT, 70 W, 5 min exposure. Sample temperature: 50 °C.

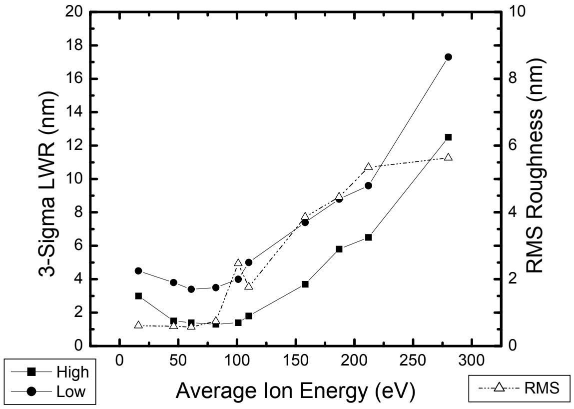

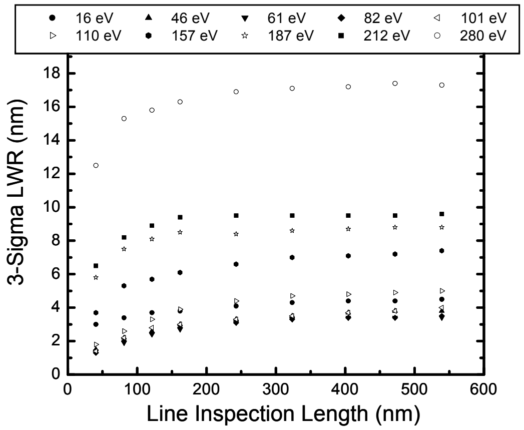

Figure 8.39 RMS surface roughness of patterned 193 nm PR measured with AFM. High and low frequency LWR measured with SEM. Ar plasma: 10 mT, 70 W. Constant ion and VUV fluences (270 s exposure times). Sample temperature: 50 °C.

Figure 8.40 LWR values as a function of line inspection length. Ar plasma: 10 mT, 70 W. Sample temperature: 50 °C. 270 s exposures.

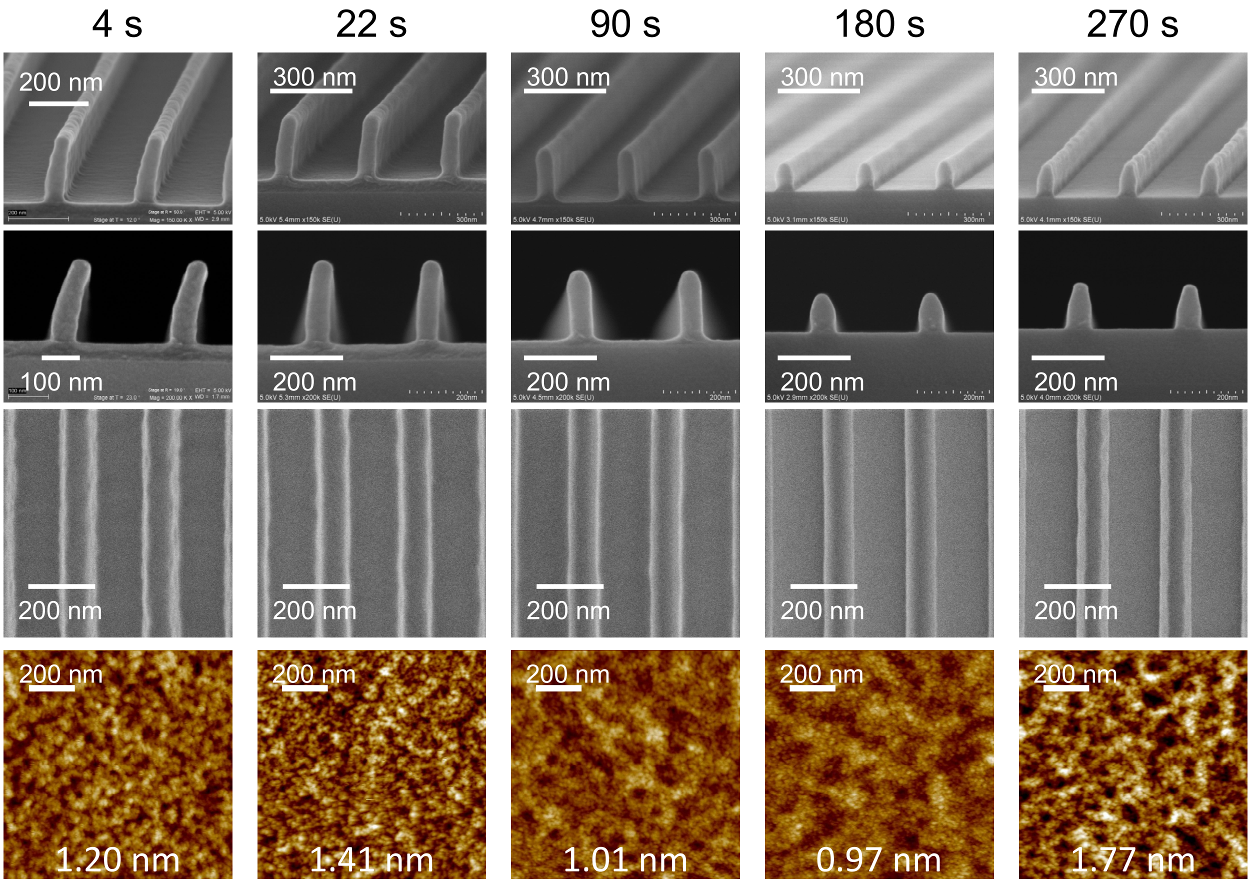

Figure 8.41 CD SEM and AFM images of patterned lines processed in a 10 mT, 70 W Ar plasma for 4 - 270 s. Ion energy: 110 eV. Sample temperature: 50 °C. VUV flux: 3×10^{15} cm^{-2} s^{-1}. AFM images are 1 μm^2 with a 10 nm color scale.

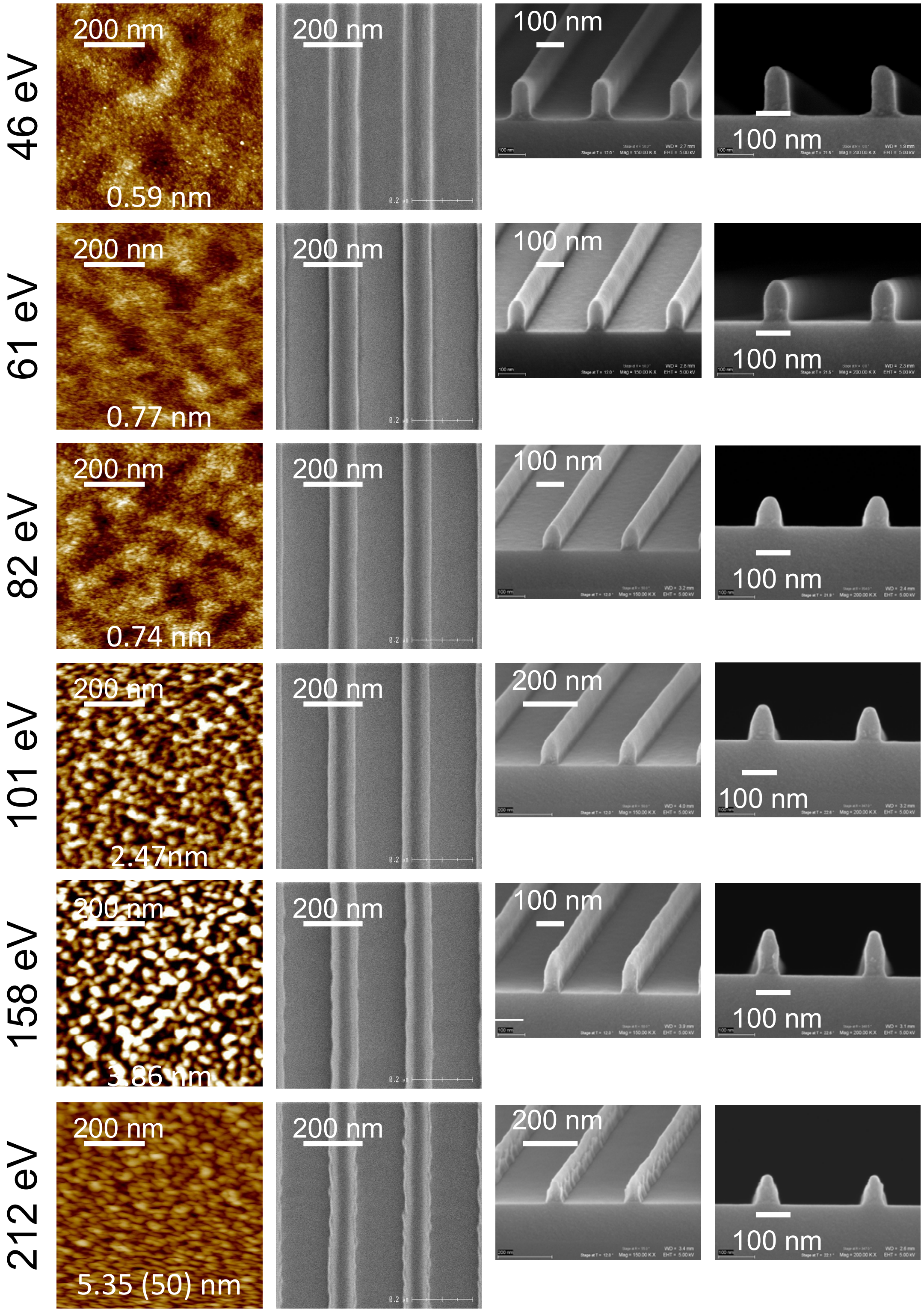

Figure 8.42 CD SEM and AFM images of patterned lines processed in a 10 mT, 70 W Ar plasma for 270 s. Ion energy was varied from 46 eV to 280 eV. Sample temperature: 50 °C. VUV flux: 3.26×10^{15} cm^{-2} s^{-1}. AFM images are 1 μm^2 with a 10 nm color scale unless otherwise indicated.

8.5.5.3 Temperature Effects

SEM analysis demonstrates that both high and low frequency LWR are independent of temperatures ranging 20 °C to 80 °C for samples processed in a 10 mT, 70 W Ar plasma with 110 eV ions for 270 s (Figure 8.43). The difference (~ 2 nm) in high and low frequency LWR is generally small for T < 80 °C. Only for T > 80 °C is there an acute dependence of LWR on temperature while the difference between high and low frequency LWR increases to ~ 5 nm. This is in contrast to the surface roughness measurements of the patterned samples where surface roughness increases linearly with temperature and is consistent with previously observed blanket PR studies. Further analysis will be required to understand why surface roughness and LWR dependence on temperature appear unrelated. Representative SEM and AFM images are shown in Figure 8.44.

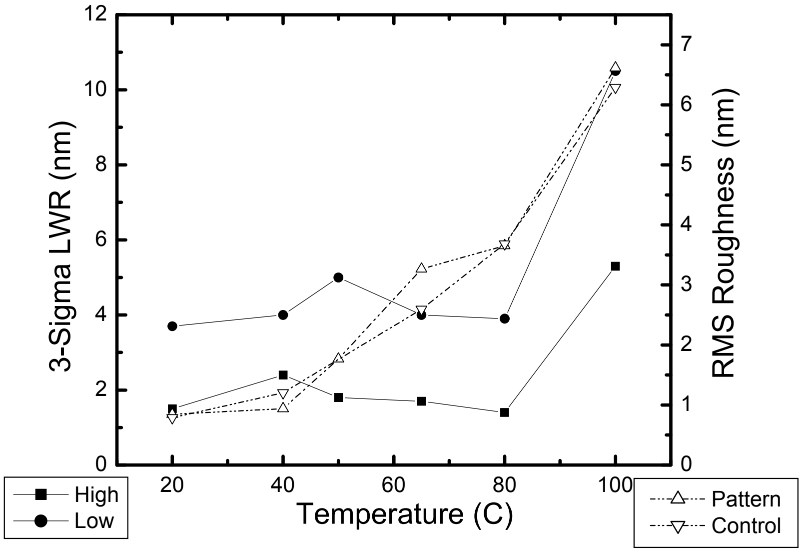

Figure 8.43 RMS surface roughness of patterned and control blanket 193 nm PR samples measured with AFM. High and low frequency LWR measured with SEM. Ar plasma: 10 mT, 70 W, 110 eV ions, 270 s exposure.

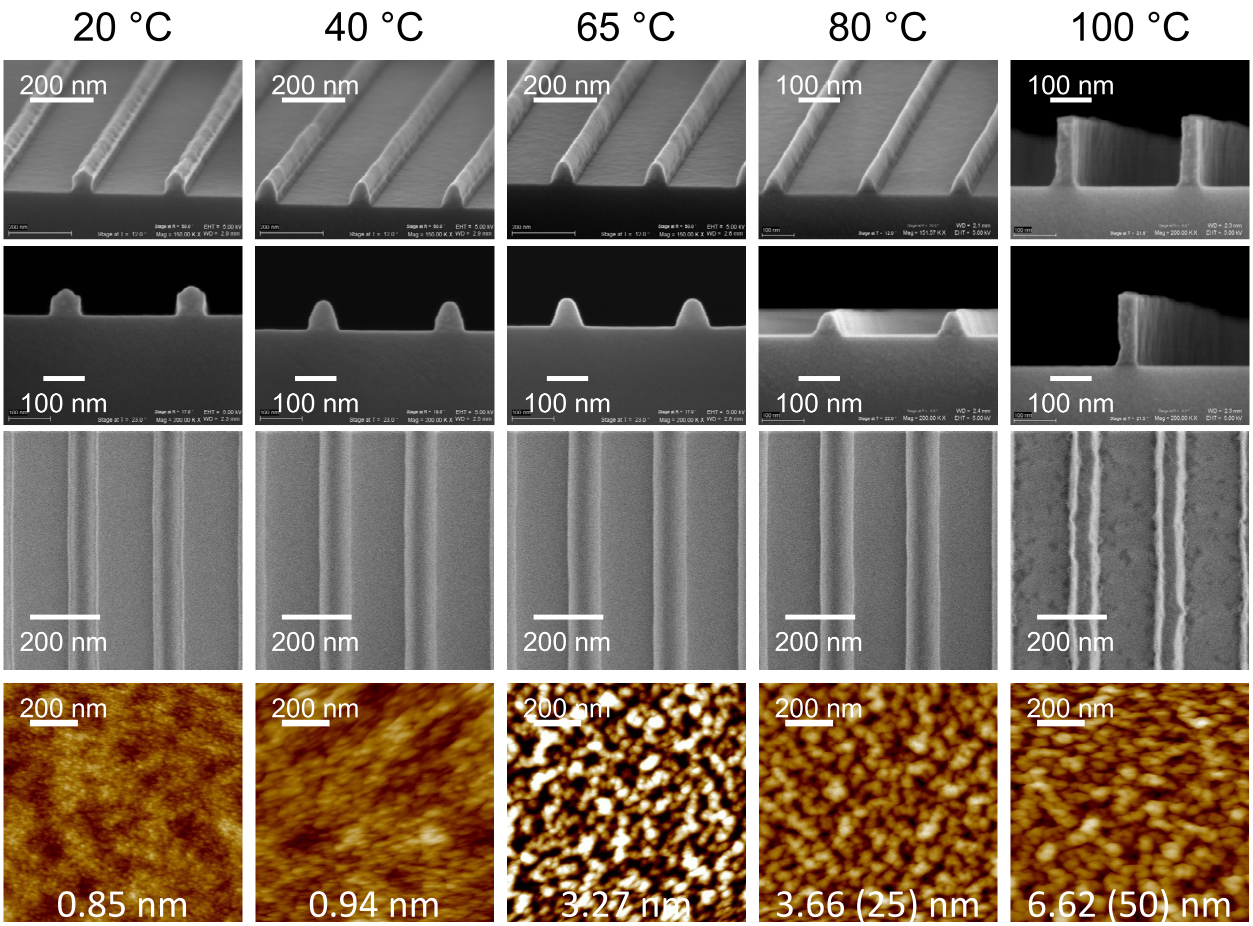

Figure 8.44 CD SEM and AFM images of patterned lines processed in a 10 mT, 70 W Ar plasma for 270 s with 110 eV ions. Sample temperature varied from 20 - 100 °C. VUV flux: 3.15 × 10^{15} cm^{-2} s^{-1}. AFM images are 1 μm^2 with a 10 nm color scale unless otherwise indicated.

8.6 Conclusions

Blanket 193 nm PR samples were processed in an ultra-high vacuum beam and ICP systems. Samples exposed to VUV-only or simultaneous VUV-photon and ion fluxes were analyzed with FTIR spectroscopy and AFM. The ion energy, photon flux, ion flux and sample temperature were controlled and measured. In addition, patterned 193 nm PR samples were processed in the ICP system under similar experimental conditions to study effects of process control variables on LWR development.

Under Xe-line VUV, and Ar-lamp VUV in the vacuum beam systems and Ar VUV (16 eV plasma potential ions) in the ICP system, 193 nm PR did not roughen. RMS roughness values were near the unprocessed blanket sample ~ 0.3 nm. A significant amount of C=O lactone and ester loss (40 – 60 %) was observed with FTIR analysis under both processing conditions. This loss was attributed to the scissioning of CO bonds due to penetrating VUV photons, ~ 100 nm deep. The difference in FTIR absorption spectra of vacuum beam (Xe – photons) and ICP (Ar – photons) VUV-only exposed samples were attributed to the difference in photon wavelengths and resulting photochemistry. Significant etching did not occur, interpreted with minimal – to – no CH_2/CH_3 decrease in FTIR spectra.

Blanket samples simultaneously exposed to high energy ions and VUV photons significantly roughened. As the VUV fluence (and ion fluence) was increased, an increased roughening was observed in both the vacuum beam and ICP processed samples, up to ~ 4 nm for 8×10^{17} photons/cm^2. FTIR analysis, however, showed that samples processed in the beam system did not etch significantly while samples in the ICP system experienced significant etching. The etching in the ICP system is attributed to the C-, O-, and H-based ions generated from gaseous products and residual chamber contamination, although less than 0.7 % of the total positive ion fraction. The reactive species present in the ICP system contributed to the increased etch rate; however, it did not change the roughening behavior or structure of the surface layer, transitioning from a smooth, to pebble-like, and ultimately yarn-like network. This demonstrates that the addition of trace amount of reactive chemistry significantly changes the plasma behavior, thus complicating the study of 193 nm PR in an inert plasma. Therefore, vacuum beam-based studies can be viewed as useful tools that can deconvolute and simplify an otherwise complex, reactive system.

The formation of surface roughness is correlated to the ion energy and formation of an ion-induced graphitized layer. For ion energies < 65 eV, the PR remains smooth with roughness levels equivalent to its pristine state and a graphitized layer does not form. As the ion energy is increase to 65 eV, a graphitized layer is produced on the top 2 nm of the PR and the surface begins to roughen. Increased roughening and formation of a graphitized layer is observed until ~150 eV. For energies > 150 eV, the rate of roughening declines slightly. This roughening behavior is attributed to the intrinsic stress developed in the graphitized layer that is a function of the bombarding ion energy, coupled with the lower layer relaxing.

193 nm PR roughness studies demonstrated a dependence on substrate temperature and photon-to-ion flux (PI) ratios. The PI ratio is dependent upon the power and pressure of the generated plasma. In order to produce surface roughness with RMS > 1 nm, a PI ratio ranging

from 0.1 to 0.7 must be present. As the temperature of the samples were increased, the surface roughness increased, up to RMS values of ~10 nm for 100 °C substrate temperature in both vacuum beam and ICP systems. The monotonic increase in surface roughness for constant VUV and ion fluences is attributed to the changing mechanical properties of the irradiated polymer. As the surface layer is bombarded with high energy ions, the top 2 nm becomes dehydrogenated and heavily graphitized, thus increasing the T_g value. In contrast, the VUV photons penetrate the PR and scission the CO bonds, causing a decrease in T_g values.

The necessary experimental conditions to produce PR roughening on blanket have been identified. Further studies of the mechanical properties of the films will be required to investigate the theory of wrinkling for elastic-viscoelastic bilayer systems to determine if the resulting changes to the PR during plasma exposures are sufficient in causing the roughening observed.

Lastly, preliminary investigations of patterned 193 nm PR samples in an inert Ar plasma demonstrated a correlation between LWR and surface roughness measurements for plasma cure and VUV-ion synergy cases. Plasma cures show that LWR and surface roughness decreases with VUV fluence and is consistent with blanket PR studies. VUV-ion synergy studies show LWR and surface roughness strongly depend on ion energy. A threshold energy of ~ 70 eV must be exceeded to see enhanced LWR and surface roughness. However, at energies above 200 eV, LWR continues to increase while surface roughness remains unaffected or decreases slightly. This may demonstrate how LWR is geometry and boundary condition dependent, but requires further study. Dependence of LWR on temperature is negligible except for temperatures greater than 80 °C while surface roughness remains linearly dependent on temperature. Clearly surface roughness and LWR are related; however, the exact roughening mechanism still remains unclear. Improvement in our understanding would surely benefit from numerical modeling analysis of different geometry configurations.

Appendix A:
PlasmaTemp$^{\text{TM}}$ Study – Supplemental Data

A.1 PlasmaTemp^{TM} Sensor Configuration

Sensor numbers 28, 1, 4, 3, and 8 were used for all PlasmaTemp^{TM} analyses in Chapter 4.

Table A.1.1 PlasmaTemp^{TM} sensor coordinates

Sensor	X (mm)	Y (mm)
1	-19.8	0
2	-38.5	-38.5
3	-54.8	0
4	-34.4	19.8
5	0	19.8
6	0	39.6
7	-45.5	-45.5
8	-64.7	0
9	-59.5	-24.5
10	-59.5	24.5
11	-24.5	59.5
12	-45.5	45.5
13	24.5	-59.5
14	-24.5	-59.5
15	0	-64.7
16	0	64.7
17	45.5	45.5
18	24.5	59.5
19	0	-54.8
20	45.5	-45.8
21	38.5	-38.5
22	38.5	38.5
23	-38.5	38.5
24	0	54.8
25	0	-19.8
26	-34.4	-19.8
27	0	-39.6
28	0	0
29	49.5	0
30	19.8	0

Figure A.1.1 PlasmaTemp^{TM} sensor layout

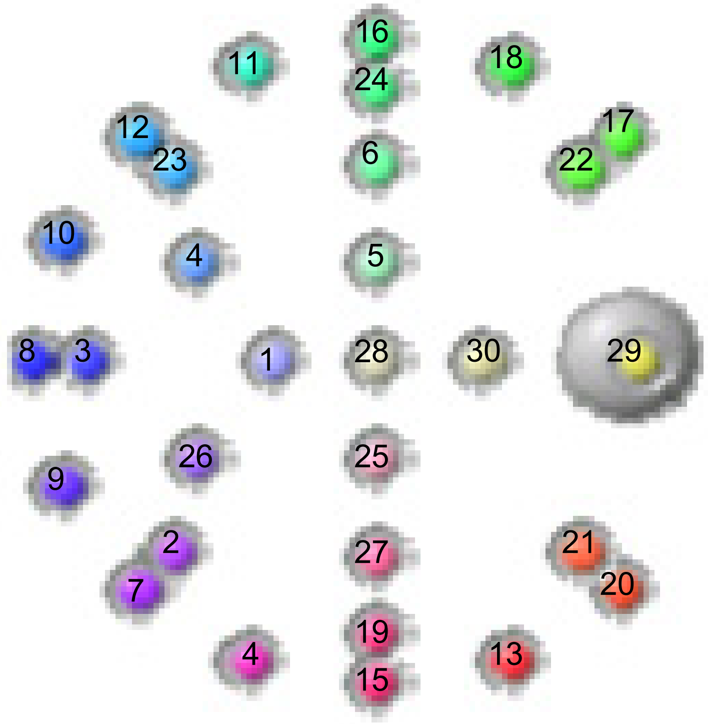

A.2 Supplemental Experimental Conditions – Langmuir Probe Measurements

Table A.2.1 Experimental Ar plasma conditions utilized in the PlasmaTemp^{TM} study. Langmuir probe measurements are 2.54 cm above the lower electrode and with respect to the chamber radius, i.e. chamber center: (r = 0 cm), middle, wall.

Pressure	Flow Rate	ICP Power	Ion Probe Reading	Ion Current	Plasma Potential (eV)			Electron Density (n_e/cm^3)			T_e (eV)		
(mT)	sccm	(W)	(mA)	($/cm^2/s$)	Center	Middle	Edge	Center	Middle	Edge	Center	Middle	Edge
50	70	220	1.06	1.7E+19				5.6E+11	5.0E+11	2.3E+11	2.3	2.3	2.2
70	75	70	0.19	3.0E+18				1.8E+11	1.5E+11	5.5E+10	2.3	2.3	2.2
70	75	70	0.26	4.1E+18	12.3	11.9	10.0	1.8E+11		6.0E+10	2.2	2.1	2.1
70	75	80	0.276	4.3E+18	12.3	11.9	10.0	2.0E+11	1.7E+11	6.6E+10	2.2	2.2	2.1
70	75	80	0.26	4.1E+18				2.4E+11	2.0E+11	8.0E+10	2.2	2.2	2.2
70	75	90	0.329	5.1E+18				3.1E+11	2.3E+11	1.0E+11	2.2	2.1	2.1
70	75	120	0.474	7.4E+18				4.0E+11	3.4E+11	1.5E+11	2.1	2.1	2.1
71	75	160	0.767	1.2E+19				6.2E+11	5.3E+11	2.4E+11	2.1	2.1	2.0
70	75	180	0.938	1.5E+19	11.9	11.5	10.0	5.6E+11	4.7E+11	2.1E+11	2.1	2.0	2.0
71	75	190	0.975	1.5E+19				6.5E+11	6.3E+11	2.9E+11	2.1	2.1	2.0
70	75	190	1.022	1.6E+19	11.9	11.5	10.0	5.9E+11	5.1E+11	2.3E+11	2.1	2.0	2.0
80	75	65	0.18	2.8E+18				2.0E+11	1.6E+11	5.6E+10	2.2	2.2	2.1
80	75	75	0.245	3.8E+18				2.5E+11	2.1E+11	8.1E+10	2.2	2.1	2.1
80	75	80	0.257	4.0E+18				2.7E+11	2.3E+11	8.6E+10	2.1	2.1	2.1
80	75	105	0.414	6.5E+18				3.8E+11	3.1E+11	1.4E+11	2.0	2.0	2.0
81	75	135	0.675	1.1E+19				6.0E+11	5.0E+11	2.2E+11	2.0	2.0	1.9
81	75	150	0.753	1.2E+19				6.4E+11	4.6E+11	2.0E+11	2.1	2.0	1.9
81	75	195	1.024	1.6E+19				7.0E+11	5.9E+11	2.9E+11	2.1	2.0	1.9
90	75	65	0.19	3.0E+18				2.3E+11	1.9E+11	7.0E+10	2.1	2.1	2.1
90	75	70	0.252	3.9E+18	11.9	11.5	9.6	2.2E+11	1.9E+11	7.1E+10	2.1	2.1	2.0
90	75	70	0.222	3.5E+18				2.0E+11	1.6E+11	6.0E+10	2.1	2.1	2.0
90	75	70	0.235	3.7E+18				2.1E+11	1.8E+11	6.6E+10	2.1	2.0	2.0
91	75	100	0.38	5.9E+18				3.6E+11	3.0E+11	1.1E+11	2.0	2.0	1.9
91	75	140	0.63	9.8E+18				4.9E+11	4.1E+11	2.0E+11	1.9	1.9	1.9
91	75	160	0.785	1.2E+19				6.0E+11	5.0E+11	2.5E+11	1.9	1.9	1.9
90	75	190	1.08	1.7E+19	11.1	11.1	9.6	7.0E+11	6.7E+11	2.9E+11	1.9	1.9	1.8
91	75	200	1.157	1.8E+19				8.1E+11	6.5E+11	3.3E+11	1.9	1.9	1.9
90	75	200	1.18	1.8E+19	11.1	11.1	9.6	7.3E+11	7.1E+11	3.1E+11	1.9	1.9	1.8

Table A.2.2 Experimental Ar/O_2 plasma conditions utilized in the PlasmaTemp^{TM} study. Langmuir probe measurements are 2.54 cm above the lower electrode and with respect to the chamber radius, i.e. chamber center: (r = 0 cm), middle, wall.

Pressure (mT)	Chemistry (sccm) Ar	O_2	ICP Power (W)	Ion Probe Reading (mA)	Ion Current (/cm^2/s)	Plasma Potential (eV) Center	Middle	Edge	Electron Density (n_e/cm^3) Center	Middle	Edge	T_e (eV) Center	Middle	Edge
52	35	100	100	0.12	1.9E+18				1.5E+10	1.4E+10	8.9E+09	2.5	2.5	2.4
51	35	100	100	0.12	1.9E+18				1.5E+10	1.5E+10	8.8E+09	2.6	2.5	2.4
51	35	100	200	0.29	4.5E+18				3.2E+10	2.9E+10	2.5E+10	2.7	2.6	2.6
53	35	100	200	0.29	4.5E+18				3.3E+10	3.3E+10	2.2E+10	2.7	2.7	2.6
60	35	100	100	0.12	1.9E+18				1.7E+10	1.4E+16	9.2E+09	2.4	2.5	2.3
61	35	100	100	0.1	1.6E+18				1.6E+10	1.4E+10	8.9E+09	2.4	2.4	2.3
61	35	100	200	0.27	4.2E+18				3.4E+10	3.0E+10	2.2E+10	2.6	2.6	2.5
61	35	100	200	0.26	4.1E+18				3.3E+10	3.0E+10	2.1E+10	2.6	2.5	2.5
70	35	100	100	0.1	1.6E+18				1.4E+10	1.4E+10	9.0E+09	2.3	2.3	2.3
71	35	100	100	0.1	1.6E+18				1.6E+10	1.5E+10	8.9E+09	2.5	2.5	2.3
71	35	100	160	0.16	2.5E+18	11.5	11.1	10.4	1.8E+10	1.6E+10	1.1E+10	2.5	2.4	1.9
71	35	100	200	0.24	3.7E+18				3.3E+10	3.0E+10	1.9E+10	2.5	2.4	2.1
71	35	100	200	0.24	3.7E+18				3.4E+10	3.0E+10	1.9E+10	2.6	2.4	2.2
71	35	100	450	0.66	1.0E+19	12.3	11.9	10.7	5.9E+10	5.9E+10	3.9E+10	2.7	3.2	2.6
71	35	100	460	0.688	1.1E+19	11.9	11.9	10.7	6.5E+10	6.4E+10	4.0E+10	2.7	2.7	2.5
81	35	100	100	0.08	1.2E+18				1.4E+10	1.3E+10	8.4E+09	2.3	2.3	2.1
80	35	100	100	0.09	1.4E+18				1.5E+10	1.3E+10	8.5E+09	2.5	2.4	2.2
81	35	100	200	0.21	3.3E+18				3.3E+10	2.9E+10	1.8E+10	2.5	2.3	2.1
81	35	100	200	0.2	3.1E+18				3.2E+10	2.9E+10	1.8E+10	2.5	2.4	2.2
90	35	100	100	0.08	1.2E+18				1.5E+10	1.3E+10	8.1E+09	2.3	2.2	2.1
91	35	100	100	0.07	1.1E+18				1.4E+10	1.2E+10	7.9E+09	2.3	2.3	2.1
90	35	100	160	0.11	1.7E+18	10.7	10.4	9.2	1.5E+10	1.3E+10	8.2E+09	2.3	2.2	2.1
91	35	100	200	0.19	3.0E+18				3.2E+10	2.8E+10	1.7E+10	2.4	2.3	2.1
91	35	100	200	0.19	3.0E+18				3.2E+10	2.8E+10	1.7E+10	2.4	2.3	2.1
91	35	100	540	0.65	1.0E+19	11.5	11.1	10.0	7.0E+10	6.7E+10	3.9E+10	2.7	2.7	2.4

Table A.2.3 Experimental Ar/O_2/N_2 plasma conditions. Langmuir probe measurements are 2.54 cm above the lower electrode and with respect to the chamber radius, i.e. chamber center: (r = 0 cm), middle, wall.

Pressure (mT)	Chemistry (sccm) Ar	O_2	N_2	ICP Power (W)	Ion Probe Reading (mA)	Ion Current (/cm^2/s)	Electron Density (n_e/cm^3) Center	Middle	Edge	T_e (eV) Center	Middle	Edge
71	35	100	6	195	~	~	2.6E+10	2.3E+10	1.6E+10	2.3	2.3	2.0
81	35	100	6	200	0.16	2.5E+18	2.5E+10	2.2E+10	1.5E+10	2.3	2.2	2.1
91	35	100	6	200	0.17	2.6E+18	2.6E+10	2.5E+10	1.5E+10	2.1	2.2	1.9

Table A.2.4 Experimental Ar//N_2 plasma conditions. Langmuir probe measurements are 2.54 cm above the lower electrode and with respect to the chamber radius, i.e. chamber center: (r = 0 cm), middle, wall.

Pressure (mT)	Chemistry (sccm) Ar	O_2	N_2	ICP Power (W)	Ion Probe Reading (mA)	Ion Current (/cm^2/s)	Electron Density (n_e/cm^3) Center	Middle	Edge	T_e (eV) Center	Middle	Edge
70	75	0	3.5	90	0.19	3.0E+18	1.3E+11	1.1E+11	4.5E+10	2.3	2.3	2.2
80	75	0	3.5	90	0.19	2.9E+18	1.5E+11	1.2E+11	5.0E+10	2.3	2.2	2.1
90	75	0	3.5	90	0.19	3.0E+18	1.8E+11	1.5E+11	5.8E+10	2.2	2.2	2.1

A.3 Heat Flux Contributions in Pure Ar Plasmas

Table A.3.1 Percent heat flux contribution to wafer heating in Ar plasmas

Pressure (mT)	Power (W)	Ion Current (mA/cm^2)	Kinetic Energy	I/e Recomb.	Electron Thermal Energy	Metastable Quenching	Presheath Energy	Total Modeled Heat Flux (W/m^2)
70	70	0.65	32.6 %	49.7 %	13.6 %	0.8 %	3.4 %	586
70	70	1.18	32.3 %	50.2 %	13.5 %	0.6 %	3.4 %	1,022
70	80	0.65	33.0 %	49.1 %	13.7 %	0.8 %	3.4 %	597
70	95	0.82	32.7 %	49.6 %	13.6 %	0.7 %	3.4 %	738
70	160	1.93	32.1 %	50.6 %	13.4 %	0.5 %	3.3 %	1,607
70	170	2.35	31.6 %	51.4 %	13.2 %	0.5%	3.3 %	1,893
70	190	2.44	31.9 %	51.1 %	13.3 %	0.5 %	3.3 %	1,990
90	70	0.55	31.5 %	51.3 %	13.1 %	0.8 %	3.3 %	487
90	70	0.58	31.5 %	51.3 %	13.1 %	0.8 %	3.3 %	510
90	70	0.63	31.8 %	50.9 %	13.2 %	0.7%	3.3 %	551
90	100	0.95	31.2 %	51.8 %	13.0 %	0.6 %	3.3 %	799
90	130	1.57	30.8 %	52.6 %	12.8 %	0.5 %	3.2 %	1,268
90	150	1.96	30.8 %	52.7 %	12.8 %	0.5 %	3.2 %	1,558
90	190	2.65	30.4 %	53.40%	12.6 %	0.5%	3.2 %	2,025
90	200	2.90	30.7 %	52.9 %	12.8 %	0.4 %	3.2 %	2,242

A.4 Radiation Heating Calculation

Wafer heating contributions from photon irradiation was estimated using the methodology presented by Piejak *et al.*[64]. The heat flux is calculated according to equation A.4.1.

$$Q_{rad} = \Gamma_{h\nu}\varepsilon\gamma \tag{A.4.1}$$

where Γ_{hv} is the photon flux, ε is the excitation energy (Ar^* ~ 11.6 eV) and γ is the absorption probability (here $\gamma = 1$). The photon flux is calculated according to equation A.4.2.

$$\Gamma_{hv} = \frac{n^*}{k_0\tau_i} \tag{A.4.2}$$

Here, n^* is the excited state density, τ_i is the imprisonment time and k_0 is the absorption coefficient.

$$\tau_i = \frac{1}{A}\frac{1}{\theta} = \frac{1}{A}\frac{4k_0R\sqrt{\ln(k_0/R)}}{\sqrt{\pi}} \tag{A.4.3}$$

The imprisonment time is a function of the natural life time (A) and the escape factor (θ). R is the chamber radius. For a 100 mT Ar plasma, with R = 10 cm,

	k_0 (m^{-1})	τ_i (s)
$^1P_1$	140000	0.0001
$^1P_3$	31400	0.000096

The excited state density is estimated based on the ICP simulation results. At the time of this study, only the metastable states ($^1P_1$ and $^3P^1$) were tracked in the ICP model. As a rough estimate the generation of resonance states (i.e. photon generating states) was approximated as equivalent to the generation of metastable states. Thus five reactions for the generation and consumption of Ar^* were tracked (see Appendix C), and the excited state density was estimated:

$$e + Ar \xrightarrow{k_i} e + Ar^* \xrightarrow{kq} e + Ar + hv \tag{A.4.4}$$

$$\frac{dn^*}{dt} = n_e n_{Ar}\sum_i k_i - k_q n^* - \frac{n^*}{\tau_i} \tag{A.4.5}$$

The heat flux due to photon irradiation was ~ 1 W/m^2 for estimated photon fluxes on the order of 10^{12} cm^{-2} $s^{-1}$and was therefore considered negligible. Note, if this approximated flux is compared to later work studying VUV emissions, the photon flux is most likely an underestimate by a few orders of magnitude. For a 50 mT, Ar plasma, the experimentally measured VUV flux is ~ 10^{15} cm^{-2} s^{-1}; although at higher pressures will likely be less due to radiative trapping and quenching. Based on this experimental VUV flux, the equivalent heat flux to the wafer surface is ~ 18 W/m^2. With this consideration, the heat flux is at most ~ 3 % of the total heat flux and still considered a negligible heat source.

A.5 Evolution of Wafer Temperature in Pulsed Plasmas

The 3D numerical model of the sensor wafer can be utilized to monitor the temperature evolution of the wafer for pulsed plasma conditions, i.e. plasma on – off – on. Figure A.5.1 – A.5.2 demonstrates the model fitted to the PlasmaTemp™ temperature rise for exposure to an Ar plasma at 70 mT, 80 W, 0.65 mA/cm^2. The lag between model and experiment (few seconds) is primarily due to the PlasmaTemp™ data acquisition software. There is an inherent delay between software initiation and communication with the hardware, making it difficult to define *t* = 0 s. In addition, due to simplifications and assumptions the model may not entirely account for the thermal lag of the complex 3D sensor wafer.

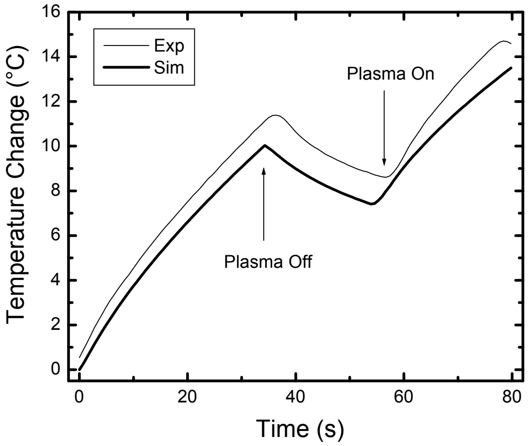

Figure A.5.1 PlasmaTemp™ and simulation temperature rise in a 70 mT, 80 W, Ar plasma.

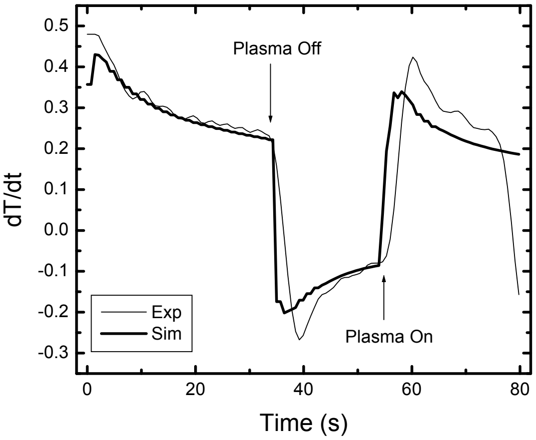

Figure A.5.2 PlasmaTemp™ and simulation evolution of ∂T/∂t with t in a 70 mT, 80 W, Ar plasma.

A.6 PlasmaTemp^{TM} Thermal Model – User Guide

The COMSOL^{TM} simulation consists of 9 subdomains and 57 boundaries that are permanently defined, according to Tables A.6.1 and A.6.2. The main modification required by the user is isolated to the "Scalar Expressions" dialog box, defined in Table A.6.3.

Table A.6.1 Subdomains and respective physical constants defined in the PlasmaTemp^{TM} thermal model.

	Quartz Module	Polyimide Coatings	Silicon Wafer	Gap (center)	Gap (edge)	Stainless Steel Chuck
Subdomain #	9	5-8	3	4	2	1
Thermal Conductivity: k (W/m/K)	3	kcoating	131	0.0005	0.002	13.4
Density: ρ (kg/m^3)	2600	rhocoating	2330	0.0001625	0.0001625	8238
Heat Capacity: C_p (J/kg/K)	820	Cpcoating	710.8	5193	5193	468

Table A.6.2 Boundary conditions defined in the PlasmaTemp^{TM} thermal model.

Boundary Condition	Boundary #
Insulated	1, 2, 4, 5, 7, 8, 11, 15, 16, 19, 21, 22, 25, 27, 28, 31, 33, 34, 37 – 41, 45, 48 – 50, 52, 53, 55, 57
Heat Flux: qtot	10, 18, 20, 24, 26, 30, 32, 36, 42, 44, 47
Constant Temperature: T0	3

Table A.6.3 Scalar expressions defined in the PlasmaTemp^{TM} thermal model.

Variable	Expression	Definition
kcoating	0.01	Polyimide coating: thermal conductivity (W/m/K)
rhocoating	1650	Polyimide coating: density (kg/m^3)
cpcoating	1060	Polyimide coating: heat capacity (J/kg/K)
T0	27	Initial temperature (°C)
t1	((a)+(b)*r-(c)*r^2-(d)*r^3+(e)*r^4)	Neutral Gas Temperature: T_g
k1	((a)+(b)*r-(c)*r^2-(d)*r^3+(e)*r^4)	Neutral Gas Thermal Conductivity: k
mfp1	((a)+(b)*r-(c)*r^2-(d)*r^3+(e)*r^4)	Neutral Gas Mean Free Path: λ
qion1	((a)+(b)*r-(c)*r^2-(d)*r^3+(e)*r^4)	Heat Flux: Ions
qcond1	16/15/3.14*k1/mfp1*((t1/(T+273))^0.5)*(t1-(T+273))	Heat Flux: Thermal conductivity
qrc1	((a)+(b)*r-(c)*r^2-(d)*r^3+(e)*r^4)	Heat Flux: O-atom Recombination
qtot	qion1+qcond1+qrc1	Total Heat Flux
r	(x^2+y^2)^0.5	Coordinate Conversion

The total heat flux to the wafer and module surface is defined by the variable *qtot* and is the sum of three terms: the ion/metastable heat flux (*qion1*), the thermal conduction heat flux (*qcond1*), and the O-atom recombination heat flux (*qrc1*). The heat flux expressions are defined below for reference. Recall, that n_i is the ion density, u_B is the Bohm velocity, k is the neutral gas thermal conductivity, λ is the neutral gas mean free path, and T_g is the neutral gas temperature, all of which are a function of chamber radius. Note in the model, *qion1* = $q_{Ar/O2.}$

$$q_{Ar/O2} = q_{Ar} + n_{O2^+} u_{B,O2^+} e\left(\Phi_p + 0.5T_e + 2T_e + \varepsilon_{O2,iz}\right) + n_{O^+} u_{B,O^+} e\left(\Phi_p + 0.5T_e + 2T_e + \varepsilon_{O,iz}\right) \quad \text{(A.6.1)}$$

$$q_{rec} = \frac{1}{4} n_O \bar{v}_O \gamma_{rec} \varepsilon_{O2,diss} \quad \text{(A.6.2)}$$

$$q_{cond} = \frac{16}{15\pi} \frac{k}{\lambda} \left(\frac{T_g}{T_w}\right)^{1/2} \left(T_g - T_w\right) \quad \text{(A.6.3)}$$

Since heat flux is dependent on the spatial variation of the ion and neutral species, i.e. *qtot(r)*, it is necessary to use the numerical simulation of the ICP chamber to obtain $n_i(r)$, $u_B(r)$, $k(r)$, $\lambda(r)$, and $T_g(r)$. As discussed in Chapter 4, the ICP model simulation is adjusted (through the applied source power) until the simulation wall ion current is equivalent to the experimentally measured ion current. This normalizes the experiment to model. Tables A.6.4 and A.6.5 list the required ICP simulation power to achieve wall ion currents equivalent to experiment. In general, the required power for a given wall ion current in a pure Ar plasma can be estimated via a linear relationship (Figure A.6.1). The ion current in the Ar/O_2 case, however, does not scale linearly with power and requires a trial and error approach to obtain the desired wall ion current. The simulated $n_i(r)$, $u_B(r)$, $k(r)$, $\lambda(r)$, and $T_g(r)$ profiles above the wafer surface are fitted with forth-order polynomial expressions (e.g. *k1*, *mfp1*, *t1*) that are used to calculate the total heat flux to the wafer surface.

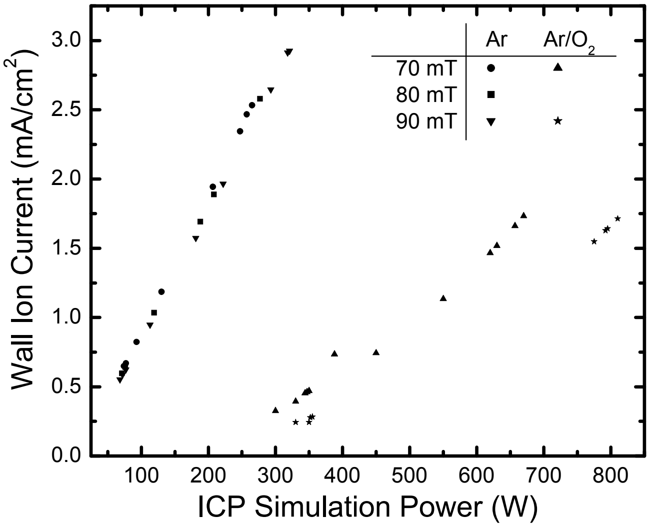

Figure A.6.1 The ICP power required in the numerical ICP simulation to generate a wall ion current (at r = 0.099 m and z = 0.0254 m) equivalent to experimental values in 70 – 90 mT Ar and Ar/O_2 plasmas

Table A.6.4 ICP model required power to normalize simulation wall ion current (r = 0.099 m, z = 0.0254 m) to experiment. For pure Ar plasmas only.

Ar	Experiment		Simulation		
Pressure	Power (W)	Ip (mA/cm^2)	Power (W)	Ip (mA/cm^2)	% Match
70	80	0.65	74	0.649	1.001
70	80	0.68	77	0.670	1.015
70	90	0.8225	92.75	0.824	0.998
70	120	1.18	130	1.186	0.995
70	160	1.925	206.5	1.944	0.990
70	180	2.35	247	2.345	1.002
70	190	2.44	257	2.468	0.989
70	190	2.54	265	2.533	1.003
80	75	0.6	71	0.598	1.004
80	80	0.645	76	0.642	1.004
80	105	1.04	119	1.035	1.005
80	135	1.693	188	1.693	1.000
80	150	1.88	208	1.889	0.995
80	195	2.5725	276.75	2.580	0.997
90	70	0.555	68	0.552	1.005
90	70	0.5825	72	0.587	0.993
90	70	0.625	77	0.624	1.001
90	100	0.95	113	0.948	1.002
90	140	1.575	181	1.574	1.001
90	160	1.9625	222	1.965	0.999
90	190	2.65	293	2.646	1.002
90	200	2.9	318	2.913	0.996
90	200	2.93	321	2.926	1.001

Table A.6.5 ICP model required power to normalize simulation wall ion current (r = 0.099 m, z = 0.0254 m) to experiment. For Ar/O_2 mix plasmas.

Ar/O_2	Experiment		Simulation		
Pressure	Power (W)	Ip (mA/cm^2)	Power (W)	Ip (mA/cm^2)	% Match
70	160	0.398	330	0.394	1.009
70	450	1.66	657	1.662	0.999
70	460	1.73	670	1.734	0.998
90	160	0.279	352	0.278	1.002
90	160	0.284	355	0.283	1.003
90	540	1.62	792	1.628	0.995
90	540	1.64	795	1.642	0.999

Appendix B:
PlasmaVolt$^{\text{TM}}$ Study – Supplemental Data

B.1 Supplemental Experimental Conditions – Langmuir Probe Measurements

B.2 Sheath Simulation – Current Profiles

B.3 Sheath Simulation – Sheath Thickness vs. Ion Mean Free Path

B.4 Sheath Simulation – User Guide

B.5 Sheath Simulation – Ion Energy Distribution Function

B.6 Ion Energy Distribution Script

B.1 Supplemental Experimental Conditions – Langmuir Probe Measurements

Table B.1.1 Langmuir probe measurements (2.54 cm above the lower electrode surface) for a pure Ar plasma. Conditions utilized in the PlasmaVolt^{TM} study.

Pressure (mT)	Flow Rate sccm	ICP Power (W)	Ion Probe Reading (mA)	Ion Current (/cm^2/s)	Plasma Potential (eV)		Electron Density (n_e/cm^3)		T_e (eV)	
					Wafer Center	Wafer Edge	Wafer Center	Wafer Edge	Wafer Center	Wafer Edge
10	50	35	0.05	7.7E+17	16.2	15.0	5.5E+09	3.4E+09	3.1	3.3
10	50	65	0.15	2.4E+18	15.8	14.6	3.1E+10	2.0E+10	3.4	3.7
10	50	160	0.63	9.9E+18	15.8	14.6	9.3E+10	6.7E+10	3.4	3.5
10	50	290	1.40	2.2E+19	15.8	15.0	1.9E+11	1.5E+11	3.4	3.5
10	50	420	2.20	3.4E+19	16.2	15.0	2.8E+11	2.1E+11	3.6	3.4
20	50	40	0.08	1.3E+18	13.9	12.7	1.7E+10	1.1E+10	3.1	3.1
20	50	65	0.14	2.2E+18	13.9	12.7	3.2E+10	2.1E+10	3.1	3.1
20	50	170	0.67	1.0E+19	13.9	12.7	1.6E+11	1.1E+11	2.9	2.9
20	50	290	1.39	2.2E+19	13.9	13.1	2.8E+11	2.1E+11	2.9	2.9
20	50	430	2.31	3.6E+19	14.3	13.5	4.5E+11	3.4E+11	3.0	2.9
50	95	40	0.08	1.2E+18	12.3	10.7	3.7E+10	2.1E+10	2.8	2.7
50	95	65	0.16	2.5E+18	12.3	10.7	8.9E+10	4.8E+10	2.5	2.5
50	95	110	0.38	6.0E+18	12.3	11.1	2.2E+11	1.3E+11	2.4	2.3
50	95	290	1.71	2.7E+19	11.9	11.1	6.8E+11	4.5E+11	2.2	2.2
50	95	430	2.81	4.4E+19	11.9	11.5	9.2E+11	7.1E+11	2.2	2.2
80	95	55	0.13	2.0E+18	11.5	10.4	1.0E+11	6.1E+10	2.2	2.2
80	95	90	0.31	4.8E+18	11.5	10.4	2.8E+11	1.58.81e11	2.0	2.0
80	95	170	0.90	1.4E+19	11.1	10.4	5.6E+11	3.7E+11	1.8	1.9
80	95	290	1.84	2.9E+19	11.1	10.4	9.7E+11	6.4E+11	1.9	1.9
80	95	430	3.02	4.7E+19	11.1	10.7	1.3E+12	9.3E+11	1.9	1.9

B.2 Sheath Simulation – Current Profiles

The displacement, ion and electron current profiles for the 1D sheath domain are plotted in Figure B.2.1. The profiles are generated for a 10 mT, Ar plasma for a low (I_{rf} = 0.2 A) and high (I_{rf} = 1.0 A) bias voltage application. In both cases, electrons are repelled from the electrode surface, x = 0.0020 m, and the electron current is nearly zero. The total current in the sheath to the wafer surface is the sum of the displacement and ion currents.

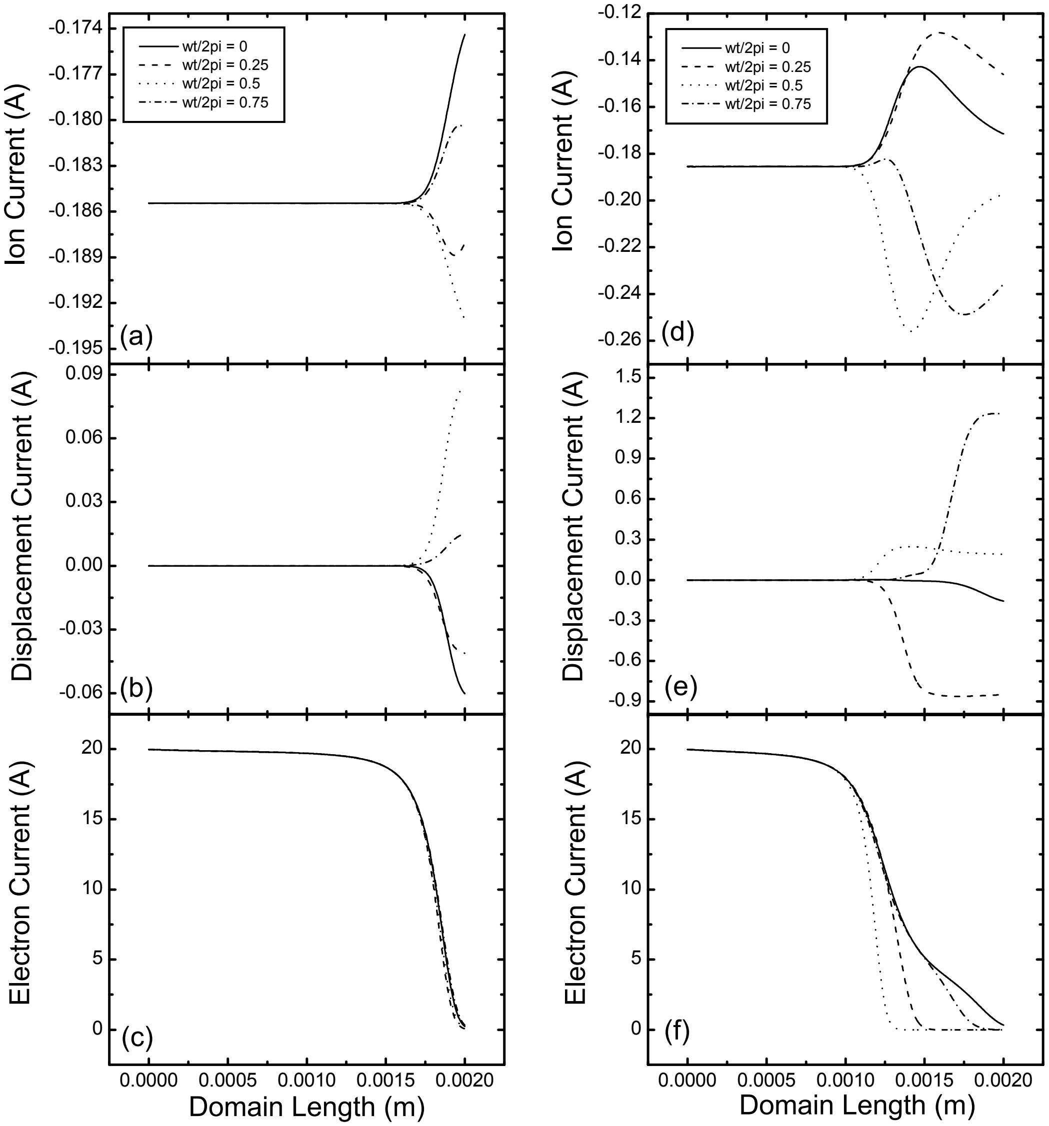

Figure B.2.1 Sheath simulation results: Displacement, ion and electron currents in the 1D sheath domain for low bias voltages, I_{rf} = 0.2 (a – c) and high bias voltages, I_{rf} = 1.0 (d – f).

B.3 Sheath Simulation – Sheath Thickness vs. Ion Mean Free Path

The sheath thickness oscillates during the RF-cycle as demonstrated in Chapter 5. It was assumed the ion species traverse the sheath with little–to–no collisions during expansion and contraction of the sheath. Plotting the instantaneous sheath thickness vs. the ion mean free path demonstrates that under low pressure conditions (< 10 mT), the sheath is collisionless. As the pressure increases (~ 20 mT), the sheath becomes collisional during the expansion phase. For pressures > 50 mT, the sheath grows increasingly collisional during both expansion and contraction phases.

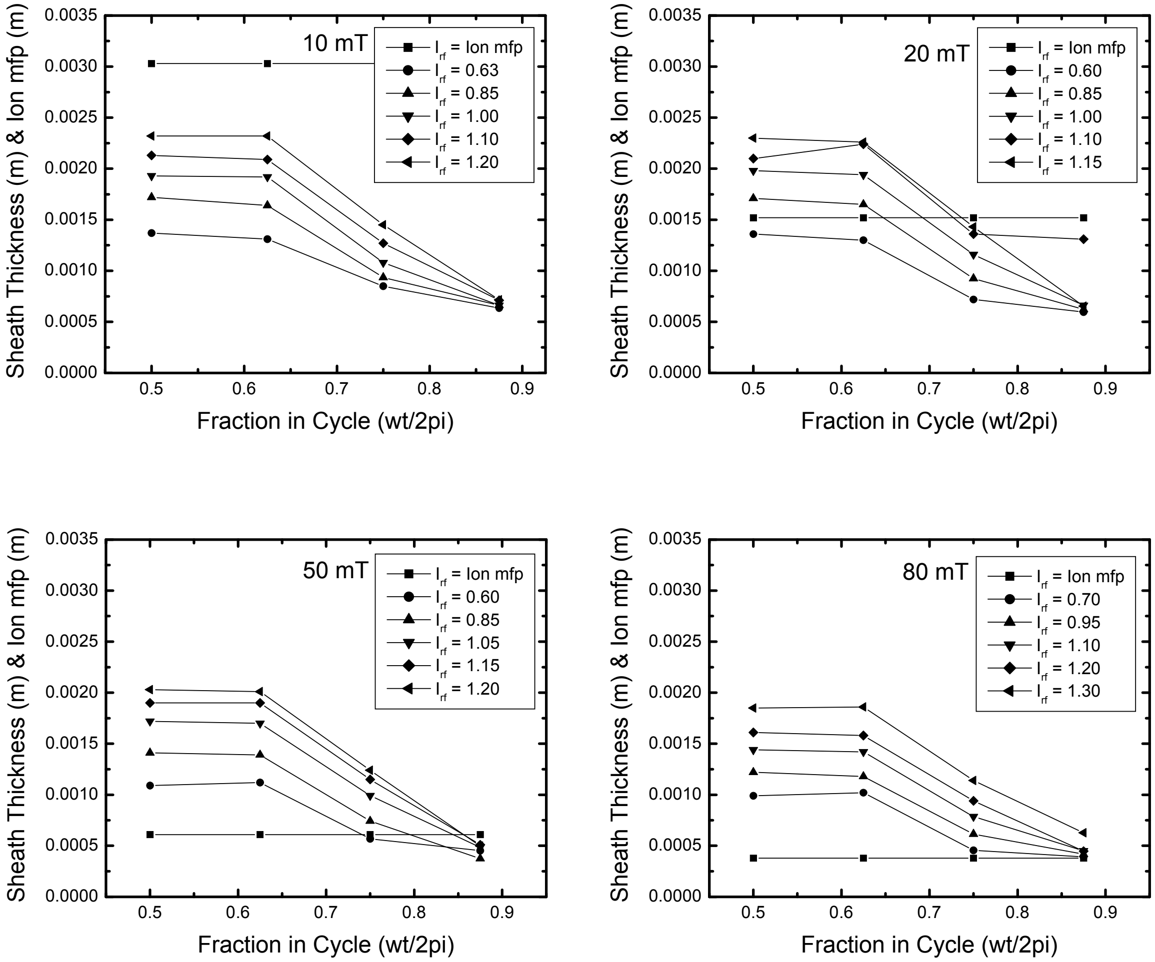

Figure B.3.1 Instantaneous sheath thickness compared to the ion mean free path for an Ar plasma at 10 mT, 20 mT, 50 mT, and 80 mT, for a range of bias voltages (I_{rf} values). For $s < \lambda_i$, the sheath is collisionless. For $s > \lambda_i$, the sheath is increasingly collisional.

B.4 Sheath Simulation – User Guide

This section provides a guide to running the 1D sheath simulation in COMSOL^{TM} and describes the steps necessary to achieve fast convergence. Note, the outlined steps are for the RF-current driven electrode simulation (not the voltage driven simulation).

There are two approaches that may be taken when using the sheath simulation and the approach depends on what input parameters are being changed. If only the RF-current, I_{rf}, is being changed, then the user may start with a previously solved transient-state simulation. The 1D sheath models, used for a number of Ar plasma experimental conditions explored in Chapter 5, are listed in Tables B.4.1 and B.4.2. For users wishing to explore, similar conditions, it is recommended to start with one of these converged transient solution simulations. If however, a new plasma condition is being explored, i.e. new T_e and n_p, (here $n_p = n_{es}$), then the user should start with a steady-state simulation, labeled as "1D Sheath Model Startup". Once the steady-state model is solved with the desired T_e and n_p values, then the transient solution can be obtained for a desired bias voltage.

Table B.4.1 Existing 1D sheath simulations for 10 mT and 50 mT Ar plasmas generated for the PlasmaVolt^{TM} study. The required I_{rf} values for desired peak-to-peak bias voltages (V_{pp}) are listed.

10 mT										50 mT			
25 W		50 W		100 W		200 W		400 W		50W		200 W	
n_p = 6.25e15		n_p = 1.44e16		n_p = 2.9e16		n_p = 5.6e16		n_p = 1.05e17		n_p = 8.96e15		n_p = 3.44e16	
I_{rf}	V_{pp}	I_{rf}	V_{pp}	I_{rf}	V_{pp}	I_{rf}	V_{pp}	I_{rf}	V_{pp}	I_{rf}	V_{pp}	I_{rf}	V_{pp}
0.29	33	0.24	10	0.38	10	0.60	9	1.00	11	0.22	14	0.53	12
0.51	99	0.36	20	0.57	18	0.70	11	1.62	20	0.36	31	0.64	18
0.57	127	0.50	35	0.78	35	0.98	20	1.85	29	0.58	86	0.72	23
0.61	151	0.67	66	0.90	50	1.25	37	2.02	36	0.66	121	0.95	47
0.68	206	0.78	89	1.12	82	1.49	53	2.18	46	0.73	154	1.18	76
0.715	234	0.925	134	1.28	114	1.98	118	2.51	65	0.78	185	1.35	110
		1.02	174	1.41	144	2.17	155	2.80	92	0.82	214	1.52	157
		1.09	206	1.50	170	2.33	191	3.00	102	0.86	240	1.64	200
		1.15	235	1.58	198	2.58	256	3.10	130			1.68	212
				1.70	238	2.60	264	3.20	146			1.70	216
								3.50	198				
								4.00	311				

Table B.4.2 Additional 1D sheath simulations for 10 mT Ar plasmas generated for the PlasmaVolt^{TM} study. The required I_{rf} values for desired peak-to-peak bias voltages (V_{pp}) are listed.

V_{pp}	75 W	160 W	290 W	420 W
	n_p = 8.2e15	n_p = 3.41e16	n_p = 7.78e16	n_p = 1.18e17
40	0.38	0.93	1.6	2.3
86	0.55	1.3	2.2	3
126	0.65	1.5	2.5	3.4
158	0.73	1.63	2.66	3.6
194	0.8	1.74	2.87	3.78

For a new plasma condition, i.e. new T_e and n_p, the following steps are recommended:

1. Open the start-up model: "1D Sheath Model Startup". The start-up model is a steady-state, high voltage sheath model.

2. Adjust the domain length such that the solution will converge quickly. Domain length is dependent on the plasma/sheath interface density. Between 5 – 10 mm is recommended.

3. Change plasma/sheath interface density (n_p) defined in the "Constants" dialog box.

4. Change electron temperature (T_e) defined in the "Constants" dialog box.

5. Change pressure (P) defined in the "Constants" dialog box.

6. Change electrode voltage (V_e). For $n_p \sim 10^{16}$ m^{-3} then $V_e \sim 100$ V. For $n_p \sim 10^{15}$ m^{-3} then V_e ~50 V.

7. Run model; this quickly produces a converged solution under the desired plasma conditions and generates initial conditions for the transient state model.

8. Change Solver Parameter to "Transient" state, and input desired number of cycles. Start with 10 cycles for quick convergence.

9. Change the BC for Poisson's equation: Input the rf-current BC

10. Change I_{rf} current value in "Constants" dialog box. Make sure I_{rf} is small for quick convergence. Slowly increase I_{rf} until the desired V_{pp} (at electrode) value is obtained. The simulation will typically fail to converge if the I_{rf} increments were too large.

Note: It is possible to update a previously converged transient simulation (with the RF-current BC) with new n_p and T_e values as long as Δn_p and ΔT_e are small. If the values are too large, instabilities will arise and the simulation may fail to converge, or several hundred cycles must be run to remove the instability.

The simulation domains and boundary conditions are defined as follows:

	Expression	Initial Condition	BC @ x = 0 (interface)	BC @ x = L (electrode)
Poisson's Equation	$\frac{\partial^2\Phi}{\partial x^2} = -\frac{e}{\varepsilon_0}(n_i - n_e)$	phi0	0	RF-current balance
Ion Continuity	$\frac{\partial n_i}{\partial t} + \frac{\partial(n_i u_i)}{\partial x} = 0$	ni0	nibc	Convective flux
Ion Momentum	$\frac{\partial u_i}{\partial t} + u_i \frac{\partial u_i}{\partial x} = \frac{eE}{m_i} - \nu_m u_i$	ui0	uibc	Convective flux

The RF-current balance is defined as:

$$I_{rf}\sin(\omega_{pi}t)+en_iu_iA-eAn_pu_e\exp\left(\frac{\Phi}{T_e}\right)-\varepsilon_0A\frac{\partial^2\phi}{\partial x\partial t}=0 \qquad \text{(B.4.1)}$$

The constants and variables in COMSOL^{TM} are defined in the "Constants" and "Scalar Expressions" dialog boxes (Tables B.4.3 and B.4.4).

Table B.4.3 Scalar expressions defined in the 1D sheath simulation

Variable	Expression	Description
ne	np*exp(phi/Te)	Electron Density Boltzmann Distribution (m^{-3})
ue	(e*Te/pi/m/2)^0.5	Electron Thermal Velocity (m/s)
Ie	e*A*np*ue*exp(phi/Te)	Electron Current (A)
Id	epsilon0*A*phixt	Displacement Current (A)
Ve	-50	Steady-state Voltage at Electrode (V)
Ii	-e*A*ni*ui	Ion Current (A)
It	Irf*sin(wpi*t)	Total RF Current (A)
vm	ui/(300*P*100)	Krook Collision Term (s^{-1})

Table B.4.4 Constants defined in the 1D sheath simulation

Constant	Value	Description
kb	1.3807e-23	Boltzmann Constant (J/K)
N	6.022e23	Avogadro's number
e	1.6022e-19	Electron Charge (C)
m	9.1095e-31	Electron Mass (kg)
mu0	4*pi*10^-7	(H/m)
freq	13.56e6	Driving Frequency (Hz)
R	0.075	Electrode Radius (m)
mi	6.63367e-26	Ar ion mass (kg)
A	pi*R^2	Electrode area (m^2)
ub	(e*Te/mi)^0.5	Bohm velocity (m/s)
np	1.78e16	Plasma-sheath interface density (m^{-3})
Te	3.47514	Electron Temperature (eV)
epsilon0	8.8542e-12	Permittivity (F/m)
wpi	freq*2*pi	(Hz)
Debye	(epsilon0*Te/e/np)^0.5	Debye Length (m)
uibc	1*ub	Momentum BC (m/s)
nibc	np	Ion Continuity BC (m^{-3})
P	10/1000	Pressure (Torr)
phi0	-e*np*ub*A	Potential Initial Condition
ni0	np	Ion Density Initial Condition
ui0	ub	Velocity Initial Condition
Irf	-1	Total RF-Current amplitude

B.5 Sheath Simulation – Ion Energy Distribution Function

The ion energy distribution (IED) is an important parameter that affects surface reactions and film etching rates. The ion bombarding energy over the wafer surface is determined by the spatial and temporal evolution of the electric fields within the expanding and collapsing sheath. As the applied RF-bias voltage increases, the oscillations of the sheath potential increases, resulting in a larger fraction of time spent at large negative potentials while the time the potential is pinned at the floating potential decreases. Simultaneously, the sheath thickness increases with RF-bias voltage. Ions entering a thick sheath near the plasma potential, will not be accelerated to high enough velocities to traverse the sheath. Consequently, the ions will remain in the sheath when the potential becomes increasingly negative. As a result, ions are accelerated by a larger electric field and will bombard the wafer with larger energies[2,87,90]. Ions entering thin sheaths, however, will traverse the sheath with high enough velocity and will strike the wafer with energies near the plasma potential. This dynamic behavior will typically produce bimodal IEDs. Experimentally, the IED can be measured with gridded ion energy analyzers[88,90]. The IED, however, can also be predicted with a self-consistent sheath model. The numerical sheath model provides profiles for the spatially varying potential drop, ion velocity and charge densities as a function of various RF-bias voltages (I_{rf}) and plasma densities (n_{es}). With values for the ion flux ($n_i u_i$) and ion kinetic energy gained (assuming it is equivalent to the sheath potential drop (Φ)) at every instant in the RF-cycle, the IED can be calculated. A MATLAB™ script (IEDF_calculations.m) was written to calculate the IED for experimental conditions investigated in the PlasmaVolt™ study. The script determines the number of times an ion bombards the electrode surface with a specific energy.

Figure B.5.1 shows the potential drop for a 20 mT, 75 W Ar plasma ($n_p = 1.74 \times 10^{10}$ cm^{-3}, $T_e = 3.0$ eV) for varying bias voltages (i.e. I_{rf} is varied). As the bias voltage is increased, the sheath potential increases and the time the potential is pinned at the floating potential (~ 9 eV) decreases. This trend is observed in the IED (Figure B.5.2). The low energy peak position is ~ constant (9 eV) because the voltage waveform is pinned near the floating potential. As the bias voltage is increased, ions in the low energy peak shift toward the high energy peak due to the expanding sheath. The high energy peak increases linearly with the bias power (Figure B.5.3) and agrees well with the IED simulation studies of Edelberg[90].

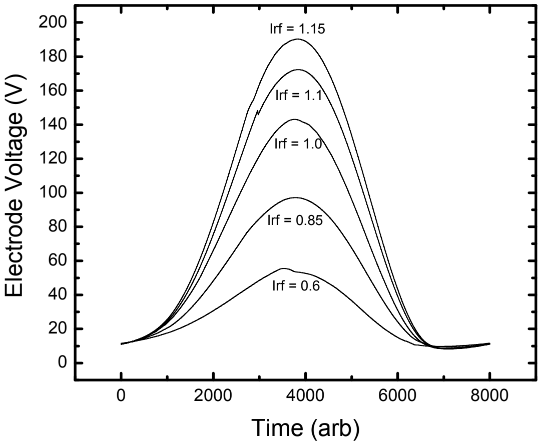

Figure B.5.1 Simulated sheath potential for a 20 mT, 75 W Ar plasma, for varying bias voltage (I_{rf}) values (driven at 13.56 MHz).

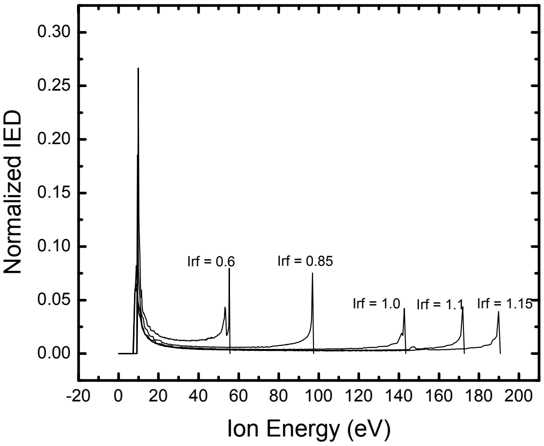

Figure B.5.2 Simulated ion energy distributions for a 20 mT, 75 W Ar plasma at varying bias voltages.

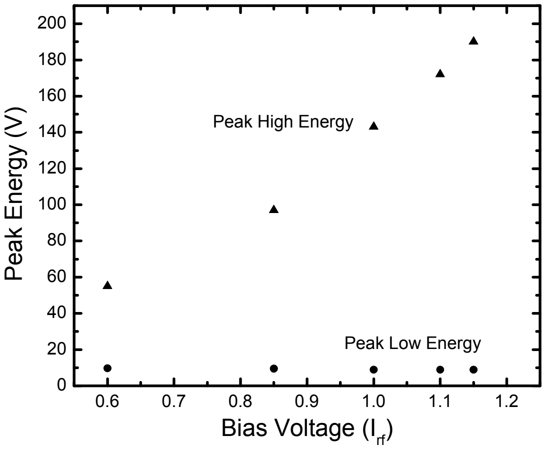

Figure B.5.3 Position in energy for the high and low energy peaks corresponding to the IEDs plotted in Figure B.5.2.

B.6 Ion Energy Distribution Script

The MATLAB^{TM} script (IEDF_calculations.m) generates an IEDF plot using post-processing data from the converged solution of the 1D sheath simulation. In order to create an IEDF plot, export and save the ion flux values and instantaneous potential drop through the sheath in columns one and two, respectively, of an excel file.

```
% open excel file where column 1 data = flux, column 2 data = energy
data = xlsread('C:\IEDF\10mT_Irf378_highnp_phi.xls');
flux = data(:,1);
energy = data(:,2);
energymax = max(energy);
delE = 200;
num = zeros(delE,1);

% count how many data points fall into an energy bin,
% then sum up the flux of ions of each bin
for j = 1:length(flux)-1
   ni = min(floor(energy(j)/energymax*delE)+1,delE);
   num(ni) = num(ni)+flux(j);
end

% defining the iedf, flux basis, adding zeros before and after for plotting purposes
iedf = [0;num;0];

% defining the energy (x-axis) values and accounting for center point of the
% bin for plotting purposes
eindx = [0 linspace(0,energymax,delE+1)+0.5*energymax/delE] ;

% normalizing the data
nrm = 0;
for j = 1:delE+2
   nrm = nrm+iedf(j); % sum = total ion flux within period
end
 de = energymax/delE;
 for j = 1:delE+2
   iedf(j) = iedf(j)/nrm/de;
end

eindxtrans = eindx';
plot(eindxtrans,iedf)
output = [eindxtrans iedf];
```

Appendix C:
Inductively Coupled Plasma Numerical Model

C.1 Introduction

This appendix contains documentation for the inductively coupled plasma (ICP) numerical model utilized in the PlasmaTemp^{TM}, PlasmaVolt^{TM}, and VUV studies presented in Chapters 4 – 8. The numerical model was originally developed in Femlab^{TM}, a commercial software now called COMSOL^{TM}, by previous graduate student Cheng-Che Hsu. The 2-dimensional, axisymmetric model was designed to represent the experimental ICP system and to study Ar, Ar/O_2, and Ar/O_2/Cl_2 plasma characteristics. For the purpose of this dissertation, the ICP model was modified for three specific intentions:

1. Model the flux of Ar-metastables: In the PlasmaTemp^{TM} study, the effect of Ar-metastables (Ar^m) on wafer heating was investigated. The flux of Ar^m could not be experimentally measured and was therefore necessary to estimate with the model. The original ICP model did not track the generation or consumption of Ar^m species.

2. Account for the thermal properties of Ar/O_2 mixed plasmas: The PlasmaTemp^{TM} study also investigated the heat flux contributions from the neutral gas species in Ar/O_2 plasmas. In the first version of the model, the physical properties (e.g. thermal conductivity, heat capacity, viscosity, etc.) of the neutral gas species were a function of Ar only.

3. Model vacuum ultraviolet (VUV) emissions: The degree of VUV photon spatial variation in the ICP chamber and the effects of power and pressure were investigated in the 193 nm PR studies. Experimental measurements with the VUV spectrometer provided line-of-sight measurements from which spatial variation could not be determined. Therefore a model of Ar-resonance state generation in the ICP chamber would provide information about VUV emissions. The original ICP model did not track the generation or consumption of Ar-resonance states.

A detailed discussion of the original ICP model and comparison to experiment, is found in the dissertation of Hsu[48]. The model structure, language, and interfacing capabilities with MATLAB^{TM} are also provided in his work and will not be reviewed here.

Emphasis will be placed on the additions, modifications, and resulting changes to the modeled plasma characteristics. Two updated working models will be presented. The first updated ICP model (called ArM) utilized in the PlasmaTemp^{TM} studies will demonstrate modification of the physical properties (k, C_v, ρ) of the neutral species and incorporation of Ar^m (section C.2). The second updated model (called ArMSR) used in the VUV studies will show the addition of Ar-resonance states (section C.3).

C.2 ICP Model Set-up: Domains and Boundaries

The ICP simulation is a fluid model, solving a series of partial differential equations coupling Ar, Ar/O_2 and Ar/O_2/Cl_2 neutral chemistry and transport to plasma characteristics. The model is a 2D axisymmetric representation of the ICP chamber (r = 10 cm, h = 10 cm) and consists of 11 domains (Figure C.1). Processing gas enters the top annular region (subdomain 11) and exits through the lower radial annulus (subdomain 9). Power is deposited through the top 5-turn coil (subdomains 4 – 8) through the dielectric window (subdomain 2). Capacitive coupling is minimized with a Faraday shield in experimental practice and therefore capacitive effects are excluded in the model. All walls, including the lower electrode are grounded.

The ICP model solves for the neutral gas flow (u, v), temperature (T), pressure (p), and neutral specie densities (w_i). The deposited ICP power for electron excitation (E_θ) and electron power balance (T_e) is also solved. Positively and negatively charged ion species (n_i) are also solved and electron density (n_e) is determined by the difference between the sum of all positive and negative ions. The complete derivation, simplifications, and assumptions of each model equation are given in the dissertation of Hsu in addition to the model nomenclature, constants, and scalar expression definitions.

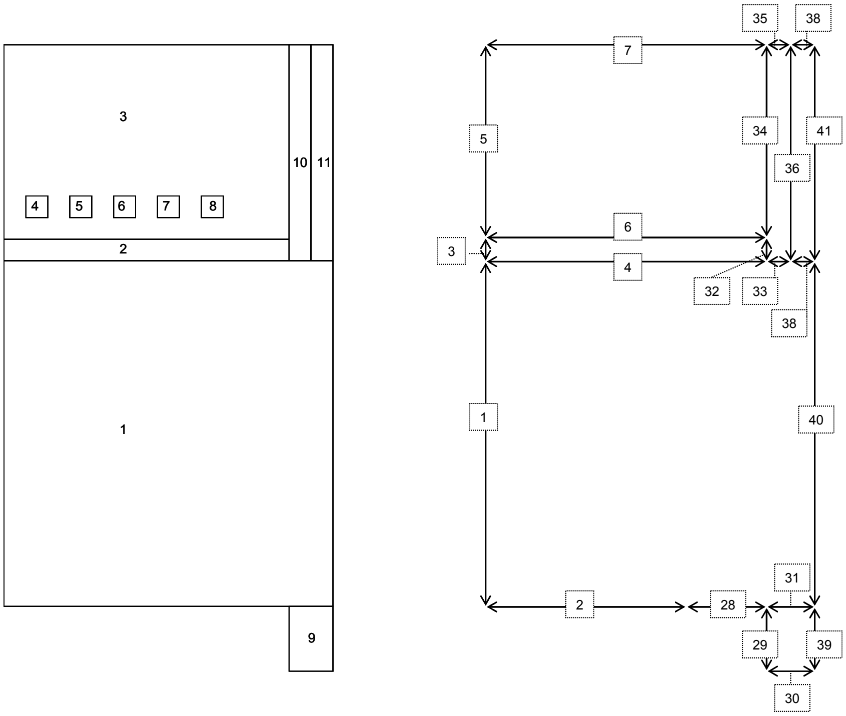

Figure C.2.1 Diagram of the 2D axisymmetric ICP model identifying the 9 subdomains and 41 boundaries.

C.3 ArM ICP Model:

C.3.1 Including Ar-Metastable (Ar^m) Species

The generation and consumption of the Ar-metastable specie (Ar^m) were tracked in the updated ICP model with the reaction expressions listed in Table C.3.1. Electron – excitation reactions account for Ar^m generation; these expressions were part of original model to account for consumption/loss of neutral Ar species. The model was updated with Ar^m loss mechanisms such as metastable pooling, neutral quenching, electron quenching, stepwise ionization and surface quenching[139-143].

The Ar^m density (*ng1m*) was modeled with a neutral species balance, similar to the Ar, O_2, and O neutral specie balances[48]. In COMSOL™ the mass fraction of Ar^m (*w1m*) is written according to Equation C.3.1.

$$d_a \frac{\partial w1m}{\partial t} + \nabla \cdot \Gamma = F \qquad \text{(C.3.1)}$$

where

da = 1

Γ(r) = w1m*rho*u-rho*D1m*w1mr-w1m*sumJr (C.3.2)

Γ(z) = w1m*rho*v-rho*D1m*w1mz-w1m*sumJz (C.3.3)

F = -(w1m*rho*u-rho*D1m*w1mr-w1m*sumJr)/r+r1m (C.3.4)

u is the neutral specie r-momentum, *v* is the neutral specie z-momentum, and *D1m* is the Ar^m diffusion rate. *r* and *r1m* are the Ar and Ar^m source terms (creation minus loss). *sumJr* and *sumJz* arise in the derivation of the neutral species balance and are defined in Appendix D.

Table C.3.1 Modeled Ar^m reaction rate expressions

ID	Reaction		Rate Constant (cm^3/s)	Ee (eV)
1	$e + Ar \rightarrow Ar^+ + 2e$	Excitation	$1.235 \times 10^{-7} \exp(-18.96/Te)$	15.6
2	$e + Ar \rightarrow Ar^m + 2e$	Excitation	$0.371 \times 10^{-7} \exp(-15.06/Te)$	11.6
3	$e + Ar \rightarrow Ar^m + 2e$	Excitation	$0.06271 \times 10^{-7} \exp(-14.27/Te)$	14.3
4	$e + Ar \rightarrow Ar^m + 2e$	Excitation	$0.0352 \times 10^{-7} \exp(-15.07/Te)$	14.15
5	$e + Ar \rightarrow Ar^m + 2e$	Excitation	$0.009237 \times 10^{-7} \exp(-16.66/Te)$	14.1
6	$e + Ar \rightarrow Ar^m + 2e$	Excitation	$0.002501 \times 10^{-7} \exp(-15.92/Te)$	14.3
a	$Ar^m + Ar^m \rightarrow Ar^+ + Ar + e$	Metastable Pooling	6.2×10^{-10}	
b	$Ar^m + Ar \rightarrow 2Ar$	Neutral Quenching	3.0×10^{-15}	
c	$e + Ar^m \rightarrow Ar^{rad} + e$	Electron Quenching	2.0×10^{-7}	0.18
d	$e + Ar^m \rightarrow Ar + e$	Electron Quenching	1.0×10^{-9}	-11.6
e	$e + Ar^m \rightarrow Ar^+ + 2e$	Stepwise Ionization	$6.8 \times 10^{-9}\, Te^{0.67} \exp(-4.2/Te)$	4.2

Table C.3.2 Defined boundary conditions for the ArM ICP model in COMSOL^{TM}

Boundary #	Description	Boundary Condition	Boundary Value
1	Symmetry	Neumann	0
2	Electrode	Neumann	srxn1m
4	Dielectric	Neumann	srxn1m
28, 29, 33, 36, 39 – 41	Walls	Neumann	srxn1m
30	Outlet	Neumann	w1m*rho*v
38	Inlet	Dirichlet	-w1m+w1m0

The initial condition, *x1mo* = 0. The inlet boundary condition is a Dirichlet condition while the outlet condition is that the axial flux is equal to the convective flux. It is assumed that all Ar^m species quench on the stainless steel, dielectric and electrode surfaces with unity probability (Equation C.3.5). At the radial mid-plane, axisymmetry is defined (Table C.3.2). The updated and new terms defined in the "Constants," "Scalar Expressions," and "Subdomain Expressions" are given in Appendix D.

srxn1m = -gammaAr*w1si*rho*vbar1/4 (C.3.5)

C.3.2 Ar/O$_2$ – Mixed Thermal Properties: Updating k, C$_v$, & μ

The thermal properties of the original model are a function of the Ar neutral gas specie only. To determine the temperature effects on a wafer for a mixed Ar/O$_2$ plasma (as in the PlasmaTemp^{TM} study), the thermal properties were redefined for a neutral gas mixture. The constant volume heat capacity (C_v), viscosity (μ_{mix}) and thermal conductivity (k_{mix}) of a mixed gas are defined in Equations C.3.6 – C.3.8.

$$C_v = \sum_{\alpha} C_{vref,\alpha} x_\alpha \,, \tag{C.3.6}$$

$$\mu_{mix} = \sum_{\alpha=1}^{N} \frac{x_\alpha \mu_\alpha}{\sum_{\beta} x_\beta \phi_{\alpha\beta}} \,, \tag{C.3.7}$$

$$k_{mix} = \sum_{\alpha=1}^{N} \frac{x_\alpha k_\alpha}{\sum_{\beta} x_\beta \phi_{\alpha\beta}} \,, \tag{C.3.8}$$

where

$$\mu_\alpha = 2.6693 \cdot 10^{-5} \frac{\sqrt{MT}}{\sigma^2 \Omega_\mu} \,, \tag{C.3.9}$$

$$k_{monatomic} = \frac{15}{4} \frac{R}{M} \mu \,, \tag{C.3.10}$$

$$k_{polyatomic} = \left(C_p + \frac{5}{4}\frac{R}{M} \right)\mu \, , \tag{C.3.11}$$

$$\phi_{\alpha\beta} = \frac{1}{\sqrt{8}}\left(1 + \frac{M_\alpha}{M_\alpha}\right)^{-1/2}\left[1 + \left(\frac{\mu_\alpha}{\mu_\beta}\right)^{1/2}\left(\frac{M_\beta}{M_\alpha}\right)^{1/4}\right]^2 . \tag{C.3.12}$$

R is the gas constant (8.314 J/mol/K), *M* is the atomic mass, *σ* is the specie diameter, C_p is the heat capacity, and *Ω* is the dimensionless integral for viscosity or thermal conductivity (Table C.3.3). The updated *k*, *μ*, and C_v variables defined in the "Scalar Expressions," dialog box are given in Appendix D.

Table C.3.3 Ar and O_2 properties for calculating μ_{mix} and k_{mix}.

	Ar	O_2
σ (Å)	3.432	3.433
M	40	32
C_p (J/kg/K)	520.337	145.483
Ω_{μ} & $\Omega_{,k}$	1	1

C.3.3 Ar^m Simulation Results

The ArM ICP simulation results were compared to the work by Kiehlbauch[81] for a 40 mT, 80 W Ar plasma. Ar^m generated profiles qualitatively and near-quantitatively agree with his dissertation work. The metastable species are generated by electron impact excitation from the ground state, near the power coils where electron temperature peaks (Figure C.3.1) while Ar^m is depleted due to neutral gas heating electron and surface quenching[81]. Due to electron kinetics and neutral transport, the net gas phase source term for Ar^m is zero near the center of the reactor and is positive near surfaces[81](Figure C.3.2).

The peak Ar^m density is ~ 1.4×10^{11} cm^{-3} and the volume averaged density is ~ 5.4×10^{11} cm^{-3}. The peak Ar^m mole fraction is ~1.34×10^{-4}. The peak neutral gas temperature is ~ 437 K. The Ar^m density calculated by Kiehlbauch[81] is 1.1×10^{11} cm^{-3} for his 40 mT, 80 W Ar plasma simulation. The volume averaged Ar^m mole fraction is 1.5×10^{-4} and the peak neutral gas temperature is ~ 680 K.

The addition of the new Ar^m specie does not significantly alter previously established trends and values (in the original ICP model) for ion and electron density profiles, and electron temperature. The quantitative differences between the ArM simulation and Kiehlbauch's model may be attributed to a number of simplifications and assumptions. For example, the EEDF in Kiehlbauch's model utilizes a parameterized EEDF, whereas the COMSOL™ model employs a Maxwellian EEDF. Certainly there is room for improvement but the general agreement in density profiles and values provide a first step approximation for estimating Ar^m fluxes to substrate surfaces

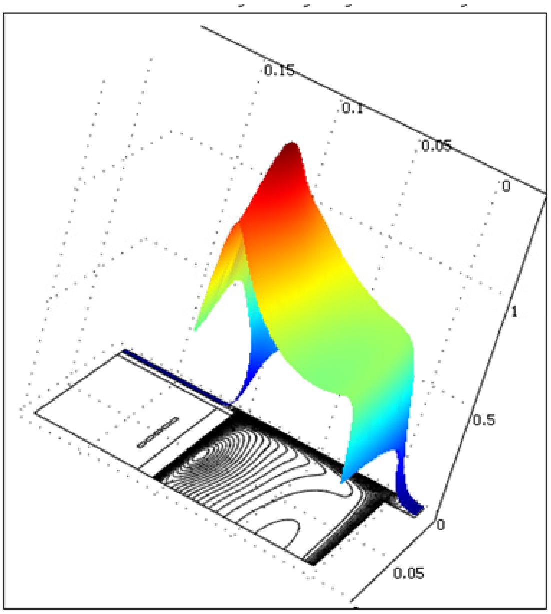

Figure C.3.1 Ar^m density profile in a 40 mT, 80 W Ar plasma. The peak density ~ 1.4×10^{11} cm^{-3}.

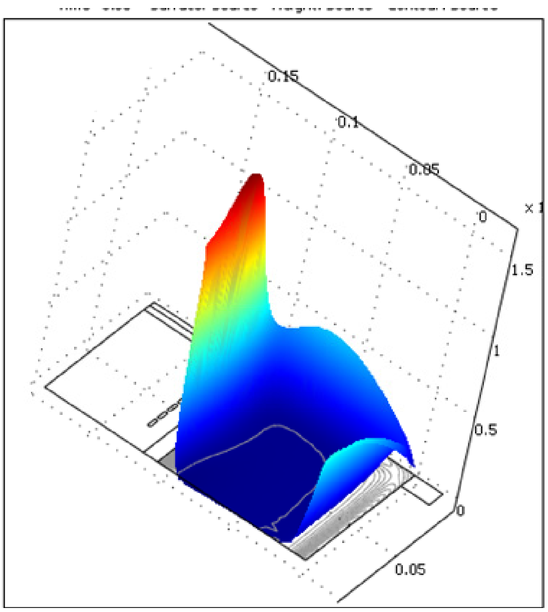

Figure C.3.2 Ar^m source terms (generation) profile in a 40 mT, 80 W Ar plasma.

C.4 ArMSR – ICP Model

C.4.1 Mass Balance

The original ICP model was again updated with four new continuity equations to track Ar metastable ($1s_3$ and $1s_5$) and Ar resonance ($1s_2$ and $1s_4$) state species (Table C.4.1). The 1s levels are populated from the ground state and upper 1p levels (Figure C.4.1).

Table C.4.1 Definition of argon states and level characteristics

Effective Level (n)	Designation	Paschen Notation	E (eV)	g^*	J	λ (nm)
1 (ground)	$3p^6$	$1p_0$	0.0	1	1	--
2 (metastable)	$4s[3/2]_2$	$1s_5$	11.548	5	2	--
3 (resonance)	$4s[3/2]_1$	$1s_4$	11.624	3	1	106.6
4 (metastable)	$4s'[1/2]_0$	$1s_3$	11.723	1	0	--
5 (resonance)	$4s'[1/2]_1$	$1s_2$	11.828	3	1	104.8
Ar^+ (ion)	$3p^5$		15.6			--

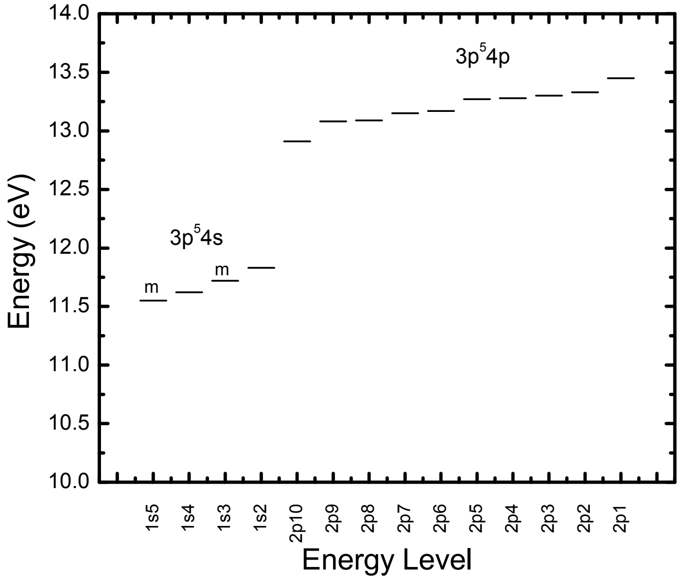

Figure C.4.1 Energy level diagram of the $3p^5 4s$ and $3p^5 4p$ manifolds of argon

The mass balance is given by:

$$\frac{\partial n_i}{\partial t} = \alpha_i n_e N_0 - \beta_i n_e n_i - \chi n_e n_i + n_e \sum_{j=1,\neq i}^{4} \left(a_{ji} n_j - b_{ij} n_i \right) - \gamma_i n_i \sum_{j=1}^{4} n_j - A_{eff} n_i - \frac{D}{\Lambda^2} n_i - \eta_i n_i N_0 \tag{C.4.1}$$

for i = $1s_2$, $1s_3$, $1s_4$, and $1s_5$. α, β, χ, a, b, γ, and η are reaction rate coefficients. n_e, and N_0 are electron and Ar atom densities, respectively. The eight generation and loss terms on the right side of the equation represent:

(1) Excitation by electron collisions with ground state Ar atoms.
(2) De-excitation to ground state by super-elastic electron collisions
(3) Stepwise ionization
(4) Conversion between states due to electron collisions
(5) Destruction due to collisions between 1s states (e.g. metastable pooling)
(6) Radiative decay from $1s_2$ and $1s_4$ to ground states with trapping
(7) Diffusion
(8) Neutral quenching

Many numerical models also include generation and loss mechanisms such as Penning ionization, and three-body collisions with thermal argon ground state atoms, fast argon ions, fast argon atoms, or electrons[69,140]. For simplicity, however, these terms were not included because they play insignificant roles in comparison to the main populating and depopulating mechanisms[140,144]. The radiative decay term (6) is dropped in the metastable mass balance equations and is only included in the resonance state balance equations. A_{eff} is defined as the product of the Einstein coefficient and escape factor that accounts for radiation trapping[64]. The diffusion and neutral quenching terms (7 and 8) were included only in the metastable balance equations. The diffusion term is defined similarly to the Ar atom diffusion coefficient. The reaction rate expressions used for each state are defined in Table C.4.2.

Table C.4.2 Reaction rate constants for $1s_2$ – $1s_5$ argon states

Rxn	Term	Reaction	Rate Expression / Constant (m^3/s)	Reference
200	1	e + Ar --> e + Ar(1s2)	2.5*10^-15*Te^0.74*exp(-11.56/Te)	142
201	2	e + Ar(1s2) --> e + Ar	4.3*10^-16*Te^0.74	142
202	3	e + Ar(1s2) --> 2e + Ar+	6.8*10^-15*Te^0.67*exp(-4.2/Te)	142
203	4	e + Ar(1s2) --> e + Ar(1s3)	3.43568*10^-14*exp(-4.1633140*10^-17/Te)*(1/Te)^0.04	140,144,145
204	4	e + Ar(1s3) --> e + Ar(1s2)	1.0307*10^-13*exp(-0.105/Te)*(1/Te)^0.04	140,144
205	4	e + Ar(1s2) --> e + Ar(1s4)	3.43568*10^-14*exp(2.498*10^-16/Te)*(1/Te)^0.04	140,144,145
206	4	e + Ar(1s4) --> e + Ar(1s2)	3.43568*10^-14*exp(-0.204/Te)*(1/Te)^0.04	140,144
207	4	e + Ar(1s2) --> e + Ar(1s5)	3.43568*10^-14*exp(-3.33067*10^-16/Te)*(1/Te)^0.04	140,144,145
208	4	e + Ar(1s5) --> e + Ar(1s2)	2.06141*10^-14*exp(-0.28/Te)*(1/Te)^0.04	140,144
209	5	Ar(1s2) + Ar(1s2) --> e + Ar + Ar+	5*10^-16	69
210	5	Ar(1s2) + Ar(1s3) --> e + Ar + Ar+	5*10^-16	69
211	5	Ar(1s2) + Ar(1s4) --> e + Ar + Ar+	5*10^-16	69
212	5	Ar(1s2) + Ar(1s5) --> e + Ar + Ar+	5*10^-16	69
	6	Aeff (Ar(1s2) --> Ar +hv)	A*EscapeFactor	140,144

400	1	e + Ar --> e + Ar(1s4)	2.5*10^-15*Te^0.74*exp(-11.56/Te)	142
401	2	e + Ar(1s4) --> e + Ar	4.3*10^-16*Te^0.74	142
402	3	e + Ar(1s4) --> 2e + Ar+	6.8*10^-15*Te^0.67*exp(-4.2/Te)	142
403	4	e + Ar(1s4) --> e + Ar(1s2)	3.43568*10^-14*exp(-0.204/Te)*(1/Te)^0.04	142
404	4	e + Ar(1s2) --> e + Ar(1s4)	3.43568*10^-14*exp(2.498*10^-16/Te)*(1/Te)^0.04	140,144,145
405	4	e + Ar(1s4) --> e + Ar(1s3)	1.14523*10^-14*exp(-0.099/Te)*(1/Te)^0.04	140,144
406	4	e + Ar(1s3) --> e + Ar(1s4)	5.72613*10^-14*exp(1.249*10^-16/Te)*(1/Te)^0.04	140,144,145
407	4	e + Ar(1s4) --> e + Ar(1s5)	3.43568*10^-13*exp(-9.71445*10^-17/Te)*(1/Te)^0.04	140,144,145
408	4	e + Ar(1s5) --> e + Ar(1s4)	2.06141*10^-13*exp(-0.075*Te)*(1/Te)^0.04	140,144
409	5	Ar(1s4) + Ar(1s2) --> e + Ar + Ar+	5*10^-16	69
410	5	Ar(1s4) + Ar(1s3) --> e + Ar + Ar+	5*10^-16	69
411	5	Ar(1s4) + Ar(1s4) --> e + Ar + Ar+	5*10^-16	69
412	5	Ar(1s4) + Ar(1s5) --> e + Ar + Ar+	5*10^-16	69
	6	Ar(1s4) --> Ar +hv	A*EscapeFactor	140,144
300	1	e + Ar --> e + Ar(1s3)	2.5*10^-15*Te^0.74*exp(-11.56/Te)	142
301	2	e + Ar(1s3) --> e + Ar	4.3*10^-16*Te^0.74	142
302	3	e + Ar(1s3) --> 2e + Ar+	6.8*10^-15*Te^0.67*exp(-4.2/Te)	142
303	4	e + Ar(1s3) --> e + Ar(1s2)	1.0307*10^-13*exp(-0.105/Te)*(1/Te)^0.04	140,144
304	4	e + Ar(1s2) --> e + Ar(1s3)	3.43568*10^-14*exp(-4.1633140*10^-17/Te)*(1/Te)^0.04	140,144,145
305	4	e + Ar(1s3) --> e + Ar(1s4)	5.72613*10^-14*exp(1.249*10^-16/Te)*(1/Te)^0.04	140,144,145
306	4	e + Ar(1s4) --> e + Ar(1s3)	1.14523*10^-14*exp(-0.099/Te)*(1/Te)^0.04	140,144
304	4	e + Ar(1s3) --> e + Ar(1s5)	3.43568*10^-14*exp(2.498*10^-16/Te)*(1/Te)^0.04	140,144,145
308	4	e + Ar(1s5) --> e + Ar(1s3)	6.87135*10^-15*exp(-0.175/Te)*(1/Te)^0.04	140,144
309	5	Ar(1s3) + Ar(1s2) --> e + Ar + Ar+	5*10^-16	69
310	5	Ar(1s3) + Ar(1s3) --> e + Ar + Ar+	5*10^-16	69
311	5	Ar(1s3) + Ar(1s4) --> e + Ar + Ar+	5*10^-16	69
312	5	Ar(1s3) + Ar(1s5) --> e + Ar + Ar+	5*10^-16	69
	7	D	Same as Ar-atom Diffusion Coefficient	
313	8	Ar(1s3) + Ar --> 2Ar	2.30E-21	140,144
500	1	e + Ar --> e + Ar(1s5)	2.5*10^-15*Te^0.74*exp(-11.56/Te)	142
501	2	e + Ar(1s5) --> e + Ar	4.3*10^-16*Te^0.74	142
502	3	e + Ar(1s5) --> 2e + Ar+	6.8*10^-15*Te^0.67*exp(-4.2/Te)	142
503	4	e + Ar(1s5) --> e + Ar(1s2)	2.06141*10^-14*exp(-0.28/Te)*(1/Te)^0.04	140,144
504	4	e + Ar(1s2) --> e + Ar(1s5)	3.43568*10^-14*exp(-3.33067*10^-16/Te)*(1/Te)^0.04	140,144,145
505	4	e + Ar(1s5) --> e + Ar(1s3)	6.87135*10^-15*exp(-0.175/Te)*(1/Te)^0.04	140,144
506	4	e + Ar(1s3) --> e + Ar(1s5)	3.43568*10^-14*exp(2.498*10^-16/Te)*(1/Te)^0.04	140,144,145
507	4	e + Ar(1s5) --> e + Ar(1s4)	2.06141*10^-13*exp(-0.075*Te)*(1/Te)^0.04	140,144
508	4	e + Ar(1s4) --> e + Ar(1s5)	3.43568*10^-13*exp(-9.71445*10^-17/Te)*(1/Te)^0.04	140,144,145
509	5	Ar(1s5) + Ar(1s2) --> e + Ar + Ar+	5*10^-16	69
510	5	Ar(1s5) + Ar(1s3) --> e + Ar + Ar+	5*10^-16	69
511	5	Ar(1s5) + Ar(1s4) --> e + Ar + Ar+	5*10^-16	69
512	5	Ar(1s5) + Ar(1s5) --> e + Ar + Ar+	5*10^-16	69
	7	D	Same as Ar-atom Diffusion Coefficient	
513	8	Ar(1s5) + Ar --> 2Ar	2.30E-21	140,144

C.4.2 Boundary Conditions for i = $1s_2$, $1s_3$, $1s_4$, and $1s_5$

The boundary conditions utilized in the ArMSR ICP model for each specie are given in Table C.4.3 (*cf* Figure C.1.1). All species are assumed to quench at surfaces with unity probability, i.e. *gammaAr* = 1.0. The surface quenching reaction is:

srxn1si = -gammaAr*w1si*rho*vbar1/4 (C.4.2)

Table C.4.3 Boundary conditions defined in the ArMSR ICP model for i = $1s_2 – 1s_5$ argon states

Boundary #	Description	Boundary Condition	Boundary Value
1	Symmetry	Neumann	0
2	Electrode	Neumann	srxn1si
4	Dielectric	Neumann	srxn1si
28, 29, 33, 36, 39 – 41	Walls	Neumann	srxn1si
30	Outlet	Neumann	w1si*rho*v
38	Inlet	Dirichlet	-w1si+w1si0

C.4.3 Modified Constants & Expressions

There are several constants, and scalar/subdomain expressions that must be updated or included for this new ICP model. The new constants and expressions are given in Appendix E.

C.4.4 ArMSR Simulation Results

Qualitative agreement between ArMSR simulation results and literature is obtained. The general dependence of the $1s_2 – 1s_5$ species on power and pressure will be reviewed here.

Figure C.4.3 – C.4.5 plots the 3-D density profiles of the $1s_2 – 1s_5$ species for a 10 mT, 200 W Ar plasma. A major source of metastable species is near the rf-coil region where T_e is the greatest: $k = k(T_e)$. It follows that due to mixing, resonance species will also have a large density near the rf-coil region. As the pressure is increased (50 mT, 200 W) plasma density and neutral gas temperatures increase resulting in a decrease of $1s_3$ and $1s_5$ species at the chamber center (Figure C.4.6 – C.4.9). The density profiles resemble the caldera-type feature similar to the Ar-metastable profiles simulated by Kiehlbauch[81,141]. $1s_2$ and $1s_4$ profiles are more peaked than $1s_3$ and $1s_5$ profiles due to different production and loss mechanisms; e.g. radiation trapping and electron collisional excitation, which are radially dependent.

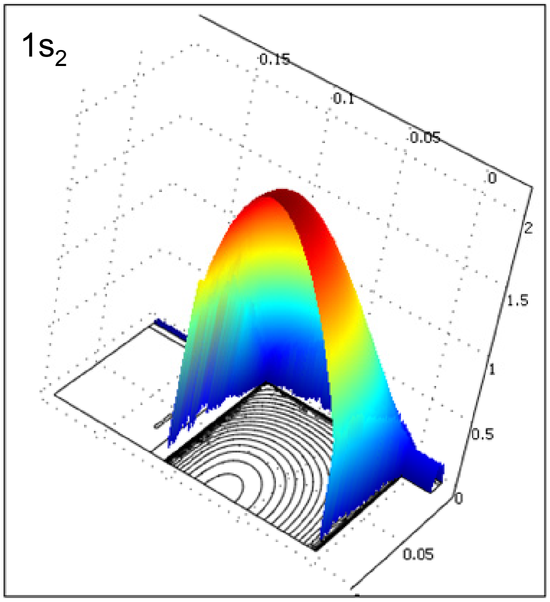

Figure C.4.2 Simulated 1s$_2$ density profile for a 10 mT, 200 W-experiment (140 W simulated) Ar plasma.

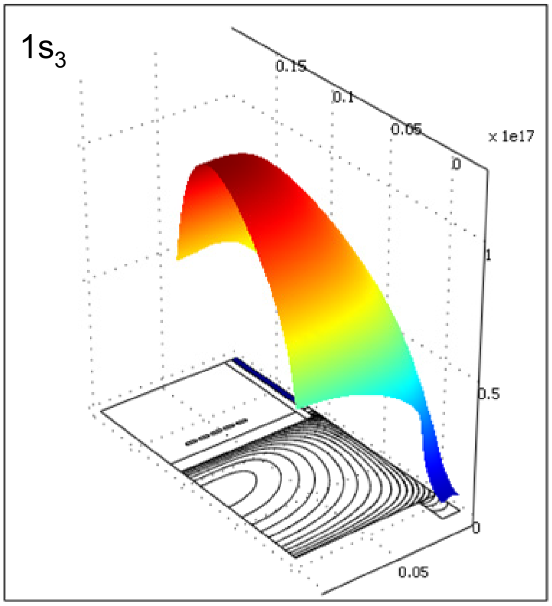

Figure C.4.3 Simulated 1s$_3$ density profile for a 10 mT, 200 W-experiment (140 W simulated) Ar plasma.

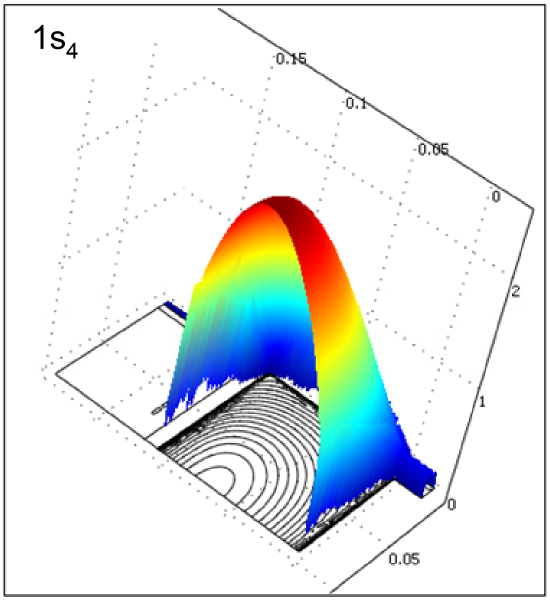

Figure C.4.4 Simulated 1s$_4$ density profile for a 10 mT, 200 W-experiment (140 W simulated) Ar plasma.

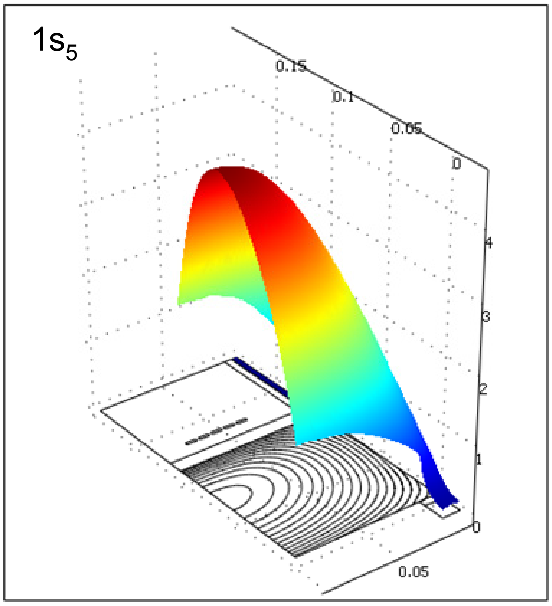

Figure C.4.5 Simulated 1s$_5$ density profile for a 10 mT, 200 W-experiment (140 W simulated) Ar plasma.

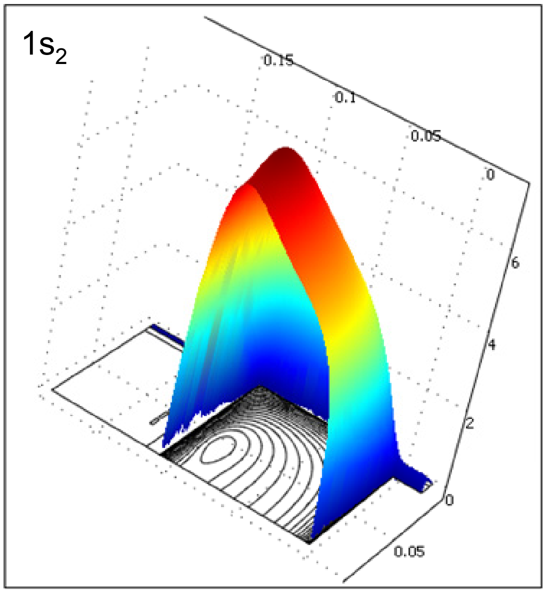

Figure C.4.6 Simulated 1s$_2$ density profile for a 50 mT, 200 W-experiment (140 W simulated) Ar plasma.

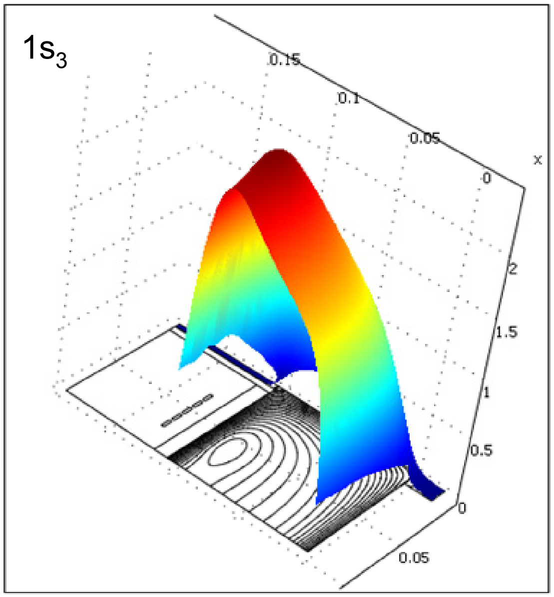

Figure C.4.7 Simulated 1s$_3$ density profile for a 50 mT, 200 W-experiment (140 W simulated) Ar plasma.

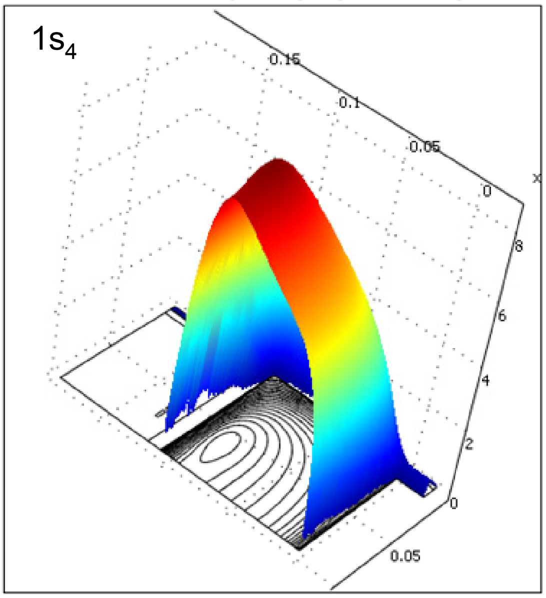

Figure C.4.8 Simulated 1s$_4$ density profile for a 50 mT, 200 W-experiment (140 W simulated) Ar plasma.

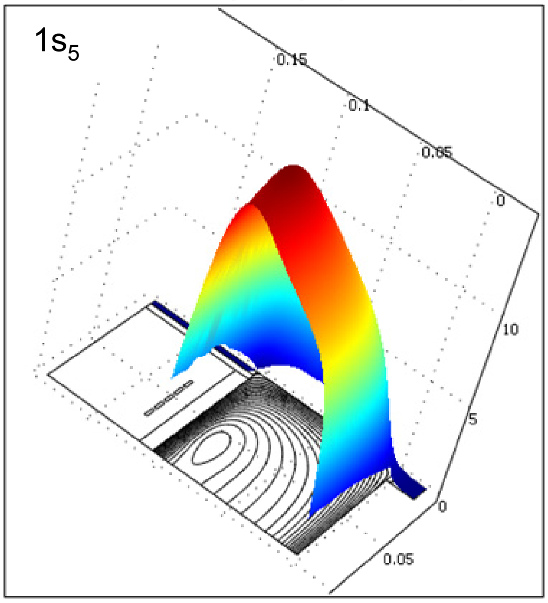

Figure C.4.9 Simulated 1s$_5$ density profile for a 50 mT, 200 W-experiment (140 W simulated) Ar plasma.

Simulation studies of Ar metastables and resonance states found in literature demonstrate that as plasma powers are increased, the $1s_3$ and $1s_5$ profiles broaden and the edge densities tend to increase due to increasing generation and diffusion rates[146]. This results in a more uniform line integrated density. Although not shown here, this behavior is observed in the ArMSR simulation results. For a 10 mT, Ar plasma as power is increased from 100 W – 300 W, the overall $1s_5$ density in the system increases from 3.3e17 m^{-3} to 5.0e17 m^{-3}. The chamber center to edge density variation, however, decreases from ~ 5.5 to ~ 3.5 for the 100 W and 300 W cases, respectively. This increase in the edge density results in a more uniform integrated line density.

Comparing the $1s_2 – 1s_5$ densities at a fixed pressure for varying powers demonstrate that $1s_5 > 1s_4 > 1s_2 > 1s_3$ (Figure C.4.10). For highly excited levels, more energy is required to produce the same amount of excitation, compared to lower levels. Therefore it is expected that $1s_5$ (E = 11.548 eV) will have a higher density than the $1s_2$, $1s_3$, and $1s_4$ (E =11.828, 11.723, 11.624) states. The same trend holds for fixed power and varying pressures (Figure C.4.11) and is in agreement with literature results[69,146,147]. For the Ar 10 mT case, $1s_5$ density is about three times greater than the $1s_3$ case. As pressure is increased, the ratio of $1s_5$ to $1s_3$ is ~5 and is in good agreement with the statistical weights of both levels (which predict a factor of 5 difference in specie density)[144]. As observed in the 3D density profiles (*cf* Figures C.4.6 – C.4.9), as the pressure is increased (e.g. 50 ~ 70 mT) the $1s_3$ and $1s_5$ densities begin to decrease due to neutral gas heating effects. In contrast, the $1s_2$ and $1s_4$ densities continuously increase with pressure due to radiation trapping. This is also consistent with the simulation results observed by Hebner[69,146] and Gorchakov[147].

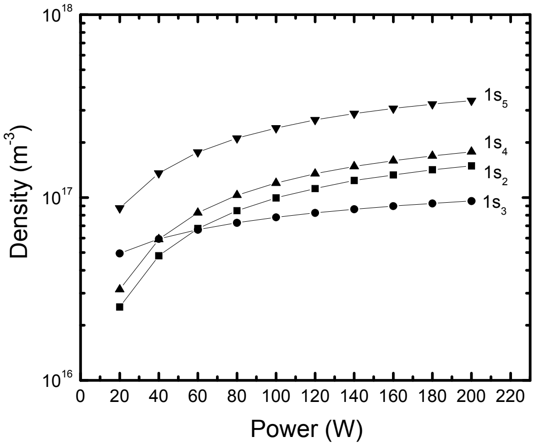

Figure C.4.10 Simulated $1s_2 – 1s_5$ densities (line-average) at z = 0.05 m (chamber center) for a 10 mT, Ar plasma and varying powers.

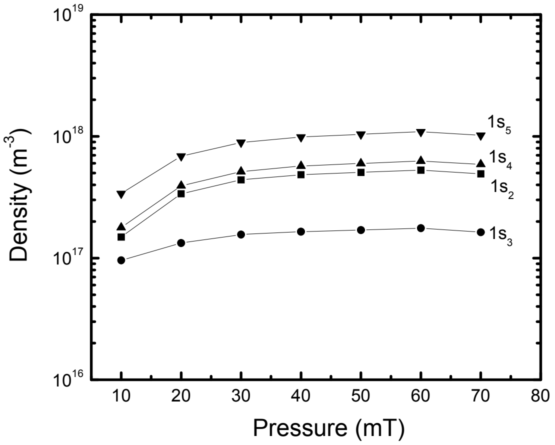

Figure C.4.11 Simulated $1s_2 – 1s_5$ densities (line-average) at z = 0.05 m (chamber center) for a 200 W, Ar plasma and varying pressures.

The vacuum ultraviolet (VUV) photon flux emitted from the $1s_2$ and $1s_4$ states are estimated with equation C.4.3.

$$\Gamma_{hv} = \frac{n^*}{k_0 \tau_i} \tag{C.4.3}$$

Here, n^* are the $1s_2$ and $1s_4$ state densities, τ_i is the imprisonment time and k_0 is the absorption coefficient. The imprisonment time is a function of the natural life time (A) and the escape factor (θ). R is the chamber radius. The density, absorption coefficient, and escape factor values are obtained from the model (expressions are defined in Appendix E).

$$\tau_i = \frac{1}{A}\frac{1}{\theta} = \frac{1}{A}\frac{4k_0 R\sqrt{\ln(k_0/R)}}{\sqrt{\pi}} \tag{C.4.4}$$

Figures C.4.12 – C.4.15 plot the simulated photon flux for varying powers and pressures; the trend qualitatively agrees with experimentally measured VUV flux (104.8 nm and 106.7 nm) from an Ar plasma. The simulated VUV photon flux emitted from the $1s_2$ and $1s_4$ states, however, underestimate the true VUV flux by ~10^2. This is likely due to omission of species from other Ar manifolds (e.g. $3p^5 4p$) that populate $1s_2$ and $1s_4$ states.

The general qualitative agreement, however, suggests the ArMSR ICP model can be a useful tool for predicting the behavior of VUV emissions for a given operating condition, relative to other plasma characteristics, e.g. ion flux (Figure C.4.14 – C.4.15) or plasma density. The ArMSR ICP model values for T, T_e, are within 2 – 10 % of the original model, while n_e and $ng1m$ are underestimated by ~1.6-1.7 times. This is expected due to the addition of several new reaction terms, which no doubt omits many other resonance and metastable state creation and loss mechanisms.

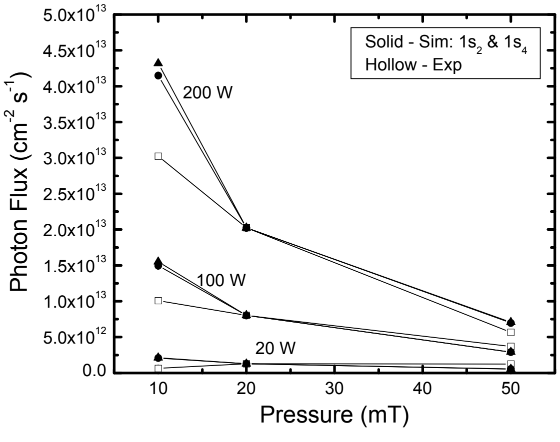

Figure C.4.12 Simulated VUV photon flux emitted from $1s_2$ and $1s_4$ Ar resonance states in a 20 W, 100 W, and 200 W plasma. Experimental VUV flux is normalized to simulation results.

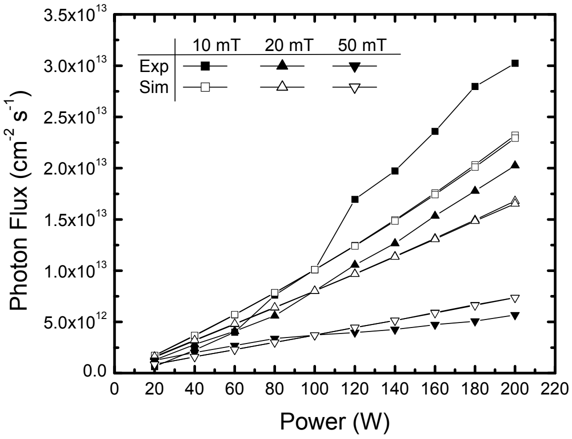

Figure C.4.13 Simulated VUV photon flux emitted from $1s_2$ and $1s_4$ Ar resonance states in a 10 mT, 20 mT, and 50 mT plasma. Experimental VUV flux is normalized to simulation results.

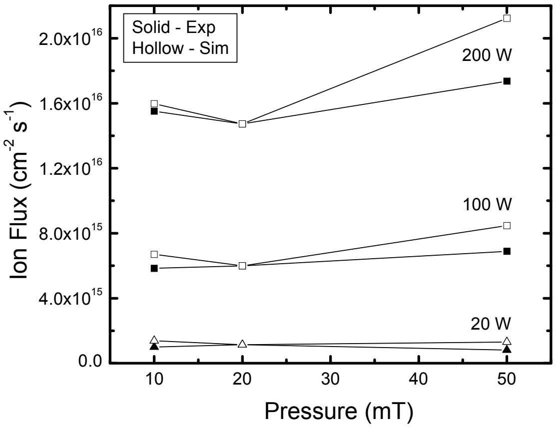

Figure C.4.14 Simulated ion flux emitted in a 20 W, 100 W, and 200 W plasma. Experimental ion flux is normalized to simulation results.

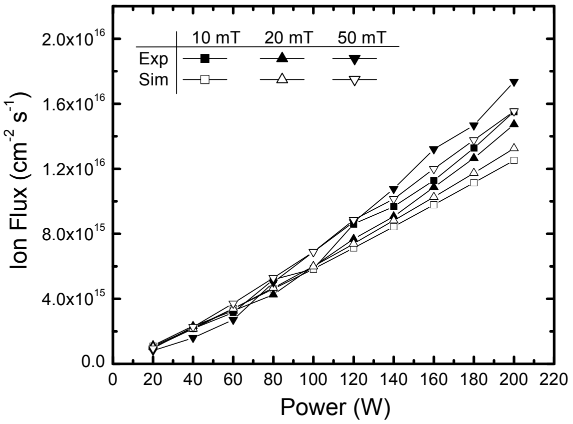

Figure C.4.15 Simulated ion flux emitted in a 10 mT, 20 mT, and 50 mT plasma. Experimental ion flux is normalized to simulation results.

Appendix D:
ArM ICP Simulation Constants and Expressions

D.1 Scalar Expressions

Table D.1 Scalar Expressions defined in COMSOL^{TM}: ArM ICP Model

Variable	Expression	Definition
x1	w1/M1/(w1/M1+w1m/M1+w2/M2+w2a/M2+w2b/M2+w3/M3+w3D/M3+w4/M4+w5/M5+w6/M6)	Mole Fraction: Ar
x2	w2/M2/(w1/M1+w1m/M1+w2/M2+w2a/M2+w2b/M2+w3/M3+w3D/M3+w4/M4+w5/M5+w6/M6)	Mole Fraction: O_2
x3	w3/M3/(w1/M1+w1m/M1+w2/M2+w2a/M2+w2b/M2+w3/M3+w3D/M3+w4/M4+w5/M5+w6/M6)	Mole Fraction: O
x2a	w2a/M2/(w1/M1+w1m/M1+w2/M2+w2a/M2+w2b/M2+w3/M3+w3D/M3+w4/M4+w5/M5+w6/M6)	Mole Fraction: O_2 (a^1D)
x2b	w2b/M2/(w1/M1+w1m/M1+w2/M2+w2a/M2+w2b/M2+w3/M3+w3D/M3+w4/M4+w5/M5+w6/M6)	Mole Fraction: O_2 ($b^1\Sigma$)
x3D	w3D/M3/(w1/M1+w1m/M1+w2/M2+w2a/M2+w2b/M2+w3/M3+w3D/M3+w4/M4+w5/M5+w6/M6)	Mole Fraction: O (^1D)
x4	w4/M4/(w1/M1+w1m/M1+w2/M2+w2a/M2+w2b/M2+w3/M3+w3D/M3+w4/M4+w5/M5+w6/M6)	Mole Fraction: Cl_2
x5	w5/M5/(w1/M1+w1m/M1+w2/M2+w2a/M2+w2b/M2+w3/M3+w3D/M3+w4/M4+w5/M5+w6/M6)	Mole Fraction: Cl
x6	w6/M6/(w1/M1+w1m/M1+w2/M2+w2a/M2+w2b/M2+w3/M3+w3D/M3+w4/M4+w5/M5+w6/M6)	Mole Fraction: ClO
w1o	x1o*M1/(x1o*M1+x1mo*M1+x2o*M2+x2ao*M2+x2bo*M2+x3o*M3+x3Do*M3+x4o*M4+x5o*M5+x6o*M6)	Initial Mass Fraction: Ar
w2o	x2o*M2/(x1o*M1+x1mo*M1+x2o*M2+x2ao*M2+x2bo*M2+x3o*M3+x3Do*M3+x4o*M4+x5o*M5+x6o*M6)	Initial Mass Fraction: O_2
w2ao	x2ao*M2/(x1o*M1+x1mo*M1+x2o*M2+x2ao*M2+x2bo*M2+x3o*M3+x3Do*M3+x4o*M4+x5o*M5+x6o*M6)	Initial Mass Fraction: O_2 (a^1D)
w2bo	x2bo*M2/(x1o*M1+x1mo*M1+x2o*M2+x2ao*M2+x2bo*M2+x3o*M3+x3Do*M3+x4o*M4+x5o*M5+x6o*M6)	Initial Mass Fraction: O_2 ($b^1\Sigma$)
w3o	x3o*M3/(x1o*M1+x1mo*M1+x2o*M2+x2ao*M2+x2bo*M2+x3o*M3+x3Do*M3+x4o*M4+x5o*M5+x6o*M6)	Initial Mass Fraction: O
w3Do	x3Do*M3/(x1o*M1+x1mo*M1+x2o*M2+x2ao*M2+x2bo*M2+x3o*M3+x3Do*M3+x4o*M4+x5o*M5+x6o*M6)	Initial Mass Fraction: O (^1D)
w4o	x4o*M4/(x1o*M1+x1mo*M1+x2o*M2+x2ao*M2+x2bo*M2+x3o*M3+x3Do*M3+x4o*M4+x5o*M5+x6o*M6)	Initial Mass Fraction: Cl_2
w5o	x5o*M5/(x1o*M1+x1mo*M1+x2o*M2+x2ao*M2+x2bo*M2+x3o*M3+x3Do*M3+x4o*M4+x5o*M5+x6o*M6)	Initial Mass Fraction: Cl
w6o	x6o*M6/(x1o*M1+x1mo*M1+x2o*M2+x2ao*M2+x2bo*M2+x3o*M3+x3D	Initial Mass Fraction: ClO

	o*M3+x4o*M4+x5o*M5+x6o*M6)	
w1	1-w1m-w2-w2a-w2b-w3-w3D-w4-w5-w6	Mass Fraction: Ar
w1r	-w1mr-w2r-w2ar-w2br-w3r-w3Dr-w4r-w5r-w6r	Derivative of w1 wrt r
w1z	-w1mz-w2z-w2az-w2bz-w3z-w3Dz-w4z-w5z-w6z	Derivative of w1 wrt z
sumJr	-rho*(D1*w1r+D1*w1mr+D2*w2r+D3*w3r+D2a*w2ar+D2b*w2br+D3D*w3Dr+D4*w4r+D5*w5r+D6*w6r)	Derived from neutral species mass fraction expression
sumJz	-rho*(D1*w1z+D1*w1mz+D2*w2z+D3*w3z+D2a*w2az+D2b*w2bz+D3D*w3Dz+D4*w4z+D5*w5z+D6*w6z)	Derived from neutral species mass fraction expression
M	x1*M1+x1m*M1+x2*M2+x3*M3+x2a*M2+x2b*M2+x3D*M3+x4*M4+x5*M5+x6*M6	Total Mass
R	r1+r1m+r2+r2a+r2b+r3+r3D+r4+r5+r6	Sum of Neutral Specie Source Terms
sumsrxns	srxn1+srxn1m+srxn2+srxn2a+srxn2b+srxn3+srxn3D+srxn4+srxn5+srxn6	Sum of all Surface Reactions (metal)
sumsrxns_1	srxn1+srxn1m+srxn2_1+srxn2a+srxn2b+srxn3_1+srxn3D_1+srxn4_1+srxn5_1+srxn6_1	Sum of all Surface Reactions (electrode)
sumsrxns_2	srxn1+srxn1m+srxn2_2+srxn2a+srxn2b+srxn3_2+srxn3D_2+srxn4_1+srxn5_1+srxn6_1	Sum of all Surface Reactions (dielectric)
srxn1	nsrxn1+isrxn1-srxn1m	Surface reaction: Ar
rxn1	1.235e-13*exp(-18.69/Te)*ne*ng1	e-impact reactions for Ar
rxn2	0.371e-13*exp(-15.06/Te)*ne*ng1	e-impact reactions for Ar
rxn3	0.06271e-13*exp(-14.27/Te)*ne*ng1	e-impact reactions for Ar
rxn4	0.03520e-13*exp(-15.07/Te)*ne*ng1	e-impact reactions for Ar
rxn5	0.009237e-13*exp(-15.66/Te)*ne*ng1	e-impact reactions for Ar
rxn6	0.002501e-13*exp(-15.92/Te)*ne*ng1	e-impact reactions for Ar
x1m	w1m/M1/(w1/M1+w1m/M1+w2/M2+w2a/M2+w2b/M2+w3/M3+w3D/M3+w4/M4+w5/M5+w6/M6)	Ar-metastable mole fraction
w1mo	x1mo*M1/(x1o*M1+x1mo*M1*x2o*M2+x2ao*M2+x2bo*M2+x3o*M3+x3Do*M3+x4o*M4+x5o*M5+x6o*M6)	Ar-metastable initial mass fraction
ng1m	w1m*rho/M1	Ar-metastable number density
D1m	D1	Ar-metastable Diffusion rate (same as neutral Ar)
srxn1m	-(gammaAr)*w1m*rho*vbar1/4	Ar-metastable/Surface Quenching Reaction
rxna	6.2*10^(-16)*ng1m*ng1m	Ar-Metastable Pooling Reaction
rxnb	3.0*10^(-21)*ng1m*ng1	Ar-metastable/Neutral Quenching Reaction
rxnc	2.0*10^(-13)*ne*ng1m	Ar-metastable/Electron Quenching Reaction
rxnd	1.0*10^(-15)*ne*ng1m	Ar-metastable/Electron Quenching Reaction
rxne	(6.8*10^(-15))*Te^0.67*exp(-4.2/Te)*ne*ng1m	Ar-metastable Stepwise Ionization Reaction

Ee	-e*(EE1*rxn1+EE2*rxn2+EE3*rxn3+EE4*rxn4+EE5*rxn5+EE6*rxn6+EE10*rxn10+EE11*rxn11 +EE12*rxn12+EE13*rxn13+EE14*rxn14+EE15*rxn15+EE16*rxn16+EE17*rxn17+EE18*rxn18+EE19*rxn19+EE20*rxn20+EE21*rxn21+EE22*rxn22+EE31*rxn31+EE40*rxn40+EE41*rxn41+EE43*rxn43+EE44*rxn44+EE45*rxn45+EE46*rxn46+EE47*rxn47+EE50*rxn50+EE51*rxn51+EE52*rxn52+EE53*rxn53+EE54*rxn54+EE55*rxn55+EE56*rxn56+EE60*rxn60+EE61*rxn61+EE62*rxn62+EE65*rxn65+EE66*rxn66+EE67*rxn67+EE68*rxn68+EE69*rxn69+EE70*rxn70+EE71*rxn71+EE72*rxn72+EE73*rxn73+EE74*rxn74+EE75*rxn75+EE76*rxn76+EE81*rxn81+EE90*rxn90+EE95*rxn95+Eec*rxnc+Eed*rxnd+Eee*rxne)	Total electron energy losses per rxn#
Eec	0.18	Electron Energy Loss: rxn c
Eed	-11.6	Electron Energy Loss: rxn d
Eee	4.2	Electron Energy Loss: rxn e
muAr	2.6693e-6*sqrt(M1*1000*6.022e23*T)/sigma1^2/1e20/omegamu	Viscosity: Ar
kAr	(Cp1ref+5/4*kb/M1)*2.6693e-6*sqrt(M1*1000*6.022e23*T)/sigma1^2/1e20/omegamu	Thermal Conductivity: Ar
Cv	x1*Cv1ref+x2*Cv2ref+x3*Cv3ref	Heat Capacity: Mixture
muO2	2.6693e-6*sqrt(M2*1000*6.022e23*T)/sigma2^2/1e20/omegamu	Viscosity: O_2
muO	2.6693e-6*sqrt(M3*1000*6.022e23*T)/sigma3^2/1e20/omegamu	Viscosity: O
PhiArO2	1/sqrt(8)*(1+M1/M2)^(-1/2)*(1+(muAr/muO2)^(1/2)*(M2/M1)^(1/4))^2	Dimensionless term for k(mix) and μ(mix) calculation
PhiO2Ar	1/sqrt(8)*(1+M2/M1)^(-1/2)*(1+(muO2/muAr)^(1/2)*(M1/M2)^(1/4))^2	Dimensionless term for k(mix) and μ(mix) calculation
PhiO2O	1/sqrt(8)*(1+M2/M3)^(-1/2)*(1+(muO2/muO)^(1/2)*(M3/M2)^(1/4))^2	Dimensionless term for k(mix) and μ(mix) calculation
PhiArO	1/sqrt(8)*(1+M1/M3)^(-1/2)*(1+(muAr/muO)^(1/2)*(M3/M1)^(1/4))^2	Dimensionless term for k(mix) and μ(mix) calculation
PhiOO2	1/sqrt(8)*(1+M3/M2)^(-1/2)*(1+(muO/muO2)^(1/2)*(M2/M3)^(1/4))^2	Dimensionless term for k(mix) and μ(mix) calculation
PhiOAr	1/sqrt(8)*(1+M3/M1)^(-1/2)*(1+(muO/muAr)^(1/2)*(M1/M3)^(1/4))^2	Dimensionless term for k(mix) and μ(mix) calculation
mu	(x1*muAr)/(x1+x2*PhiArO2+x3*PhiArO)+(x2*muO2)/(x1*PhiO2Ar+x2+x3*PhiO2O)+(x3*muO)/(x3+x2*PhiOO2+x1*PhiOAr)	Viscosity: Mixture
kO2	(Cp2ref+5/4*kb/M2)*2.6693e-6*sqrt(M2*1000*6.022e23*T)/sigma1^2/1e20/omegamu	Thermal Conductivity: O_2
kO	(15/4*kb/M1)*2.6693e-6*sqrt(M3*1000*6.022e23*T)/sigma1^2/1e20/omegamu	Thermal Conductivity: O
k	(x1*kAr)/(x1+x2*PhiArO2+x3*PhiArO)+(x2*kO2)/(x1*PhiO2Ar+x3*PhiO2O+x2)+(x3*kO)/(x2*PhiOO2+x1*PhiOAr+x3)	Thermal Conductivity: Mixture

D.2 Constants

Table D.2 Constants defined in COMSOL^{TM}: ArM ICP Model

Constant	Value	Definition
x1mo	0	Initial Mole Fraction: Ar-metastable
gammaAr	1	Ar-metastable/Surface Quenching Probability

D.3 Subdomain Expressions

Table D.3 Subdomain Expressions defined in COMSOL^{TM}: ArM ICP Model

Variable	Expressions	Definition
r1	M1*(cerxn1+cerxn1a+cerxn1b+cerxn2+cerxn3+cerxn6+cerxn7+cerxn8-rxn1-rxn2-rxn3-rxn4-rxn5-rxn6+rxna+rxnb+rxnc+rxnd)	Ar neutral – source term: Generation minus Loss
r1m	M1*(rxn2-2*rxna-rxnb-rxnc-rxnd-rxne)	Ar metastable – source term: Generation minus Loss

Appendix E:
ArMSR ICP Simulation Constants and Expressions

E.1 Scalar Expressions

Table E.1 Scalar Expressions defined in COMSOL^{TM}: ArMSR ICP Model

Variable	Expression	Definition
x1	w1/M1/(w1/M1+w1s2/M1+w1s3/M1+w1s4/M1+w1s5/M1+w2/M2+w2a/M2+w2b/M2+w3/M3+w3D/M3+w4/M4+w5/M5+w6/M6)	Mole Fraction: Ar
x2	w2/M2/(w1/M1+w1s2/M1+w1s3/M1+w1s4/M1+w1s5/M1+w2/M2+w2a/M2+w2b/M2+w3/M3+w3D/M3+w4/M4+w5/M5+w6/M6)	Mole Fraction: O_2
x3	w3/M3/(w1/M1+w1s2/M1+w1s3/M1+w1s4/M1+w1s5/M1+w2/M2+w2a/M2+w2b/M2+w3/M3+w3D/M3+w4/M4+w5/M5+w6/M6)	Mole Fraction: O
x2a	w2a/M2/(w1/M1+w1s2/M1+w1s3/M1+w1s4/M1+w1s5/M1+w2/M2+w2a/M2+w2b/M2+w3/M3+w3D/M3+w4/M4+w5/M5+w6/M6)	Mole Fraction: O_2 (a^{1}D)
x2b	w2b/M2/(w1/M1+w1s2/M1+w1s3/M1+w1s4/M1+w1s5/M1+w2/M2+w2a/M2+w2b/M2+w3/M3+w3D/M3+w4/M4+w5/M5+w6/M6)	Mole Fraction: O_2 (b$^1\Sigma$)
x3D	w3D/M3/(w1/M1+w1s2/M1+w1s3/M1+w1s4/M1+w1s5/M1+w2/M2+w2a/M2+w2b/M2+w3/M3+w3D/M3+w4/M4+w5/M5+w6/M6)	Mole Fraction: O (^{1}D)
x4	w4/M4/(w1/M1+w1s2/M1+w1s3/M1+w1s4/M1+w1s5/M1+w2/M2+w2a/M2+w2b/M2+w3/M3+w3D/M3+w4/M4+w5/M5+w6/M6)	Mole Fraction: Cl_2
x5	w5/M5/(w1/M1+w1s2/M1+w1s3/M1+w1s4/M1+w1s5/M1+w2/M2+w2a/M2+w2b/M2+w3/M3+w3D/M3+w4/M4+w5/M5+w6/M6)	Mole Fraction: Cl
x6	w6/M6/(w1/M1+w1s2/M1+w1s3/M1+w1s4/M1+w1s5/M1+w2/M2+w2a/M2+w2b/M2+w3/M3+w3D/M3+w4/M4+w5/M5+w6/M6)	Mole Fraction: ClO
w1o	x1o*M1/(x1o*M1+x1s2o*M1+x1s3o*M1+x1s4o*M1+x1s5o*M1+x2o*M2+x2ao*M2+x2bo*M2+x3o*M3+x3Do*M3+x4o*M4+x5o*M5+x6o*M6)	Initial Mass Fraction: Ar
w2o	x2o*M2/(x1o*M1+x1s2o*M1+x1s3o*M1+x1s4o*M1+x1s5o*M1+x2o*M2+x2ao*M2+x2bo*M2+x3o*M3+x3Do*M3+x4o*M4+x5o*M5+x6o*M6)	Initial Mass Fraction: O_2
w2ao	x2ao*M2/(x1o*M1+x1s2o*M1+x1s3o*M1+x1s4o*M1+x1s5o*M1+x2o*M2+x2ao*M2+x2bo*M2+x3o*M3+x3Do*M3+x4o*M4+x5o*M5+x6o*M6)	Initial Mass Fraction: O_2 (a^{1}D)
w2bo	x2bo*M2/(x1o*M1+x1s2o*M1+x1s3o*M1+x1s4o*M1+x1s5o*M1+x2o*M2+x2ao*M2+x2bo*M2+x3o*M3+x3Do*M3+x4o*M4+x5o*M5+x6o*M6)	Initial Mass Fraction: O_2 (b$^1\Sigma$)
w3o	x3o*M3/(x1o*M1+x1s2o*M1+x1s3o*M1+x1s4o*M1+x1s5o*M1+x2o*M2+x2ao*M2+x2bo*M2+x3o*M3+x3Do*M3+x4o*M4+x5o*M5+x6o*M6)	Initial Mass Fraction: O
w3Do	x3Do*M3/(x1o*M1+x1s2o*M1+x1s3o*M1+x1s4o*M1+x1s5o*M1+x2o*M2+x2ao*M2+x2bo*M2+x3o*M3+x3Do*M3+x4o*M4+x5o*M5+x6o*M6)	Initial Mass Fraction: O (^{1}D)
w4o	x4o*M4/(x1o*M1+x1s2o*M1+x1s3o*M1+x1s4o*M1+x1s5o*M1+x2o*M2+x2ao*M2+x2bo*M2+x3o*M3+x3Do*M3+x4o*M4+x5o*M5+x6o*M6)	Initial Mass Fraction: Cl_2
w5o	x5o*M5/(x1o*M1+x1s2o*M1+x1s3o*M1+x1s4o*M1+x1s5o*M1+x2o*M2+x2ao*M2+x2bo*M2+x3o*M3+x3Do*M3+x4o*M4+x5o*M5+x6o*M6)	Initial Mass Fraction: Cl
w6o	x6o*M6/(x1o*M1+x1s2o*M1+x1s3o*M1+x1s4o*M1+x1s5o*M1+x2o*M2+x2ao*M	Initial Mass Fraction: ClO

	2+x2bo*M2+x3o*M3+x3Do*M3+x4o*M4+x5o*M5+x6o*M6)	
w1	1-w1s2-w1s3-w1s4-w1s5-w2-w2a-w2b-w3-w3D-w4-w5-w6	Mass Fraction: Ar
w1r	-w1s2r-w1s3r-w1s4r-w1s5r-w2r-w2ar-w2br-w3r-w3Dr-w4r-w5r-w6r	Derivative of w1 wrt r
w1z	-w1s2z-w1s3z-w1s4z-w1s5z-w2z-w2az-w2bz-w3z-w3Dz-w4z-w5z-w6z	Derivative of w1 wrt z
sumJr	-rho*(D1*w1r+D1s2*w1s2r+D1s3*w1s3r+D1s4*w1s4r+D1s5*w1s5r+D2*w2r+D3*w3r+D2a*w2ar+D2b*w2br+D3D*w3Dr+D4*w4r+D5*w5r+D6*w6r)	Derived from neutral species mass fraction expression
sumJz	-rho*(D1*w1z+D1s2*w1s2z+D1s3*w1s3z+D1s4*w1s4z+D1s5*w1s5z+D2*w2z+D3*w3z+D2a*w2az+D2b*w2bz+D3D*w3Dz+D4*w4z+D5*w5z+D6*w6z)	Derived from neutral species mass fraction expression
M	x1*M1+x1s2*M1+x1s3*M1+x1s4*M1+x1s5*M1+x2*M2+x3*M3+x2a*M2+x2b*M2+x3D*M3+x4*M4+x5*M5+x6*M6	Total Mass
R	r1+r1s2+r1s3+r1s4+r1s5+r2+r2a+r2b+r3+r3D+r4+r5+r6	Sum of Neutral Specie Source Terms
sumsrxns	srxn1+srxn1s2+srxn1s3+srxn1s4+srxn1s5+srxn2+srxn2a+srxn2b+srxn3+srxn3D+srxn4+srxn5+srxn6	Sum of all Surface Reactions (metal)
sumsrxns_1	srxn1+srxn1s2+srxn1s3+srxn1s4+srxn1s5+srxn2_1+srxn2a+srxn2b+srxn3_1+srxn3D_1+srxn4_1+srxn5_1+srxn6_1	Sum of all Surface Reactions (electrode)
sumsrxns_2	srxn1+srxn1s2+srxn1s3+srxn1s4+srxn1s5+srxn2_2+srxn2a+srxn2b+srxn3_2+srxn3D_2+srxn4_1+srxn5_1+srxn6_1	Sum of all Surface Reactions (dielectric)
srxn1	nsrxn1+isrxn1-srxn1s2-srxn1s3-srxn1s4-srxn1s5	Surface reaction: Ar
ri1	rxn1-cerxn1-cerxn1a-cerxn1b-cerxn2-cerxn3-cerxn6-cerxn7-cerxn8+rxn202+rxn209+rxn210+rxn211+rxn212+rxn302+rxn309+rxn310+rxn311+rxn312+rxn402+rxn409+rxn410+rxn411+rxn412+rxn502+rxn509+rxn510+rxn511+rxn512	Sum of Ar-ion Source Terms
Ee	-e*(Ee1*rxn1+Ee2*rxn2+Ee3*rxn3+Ee4*rxn4+Ee5*rxn5+Ee6*rxn6+Ee10*rxn10+Ee11*rxn11+Ee12*rxn12+Ee13*rxn13+Ee14*rxn14+Ee15*rxn15+Ee16*rxn16+Ee17*rxn17+Ee18*rxn18+Ee19*rxn19+Ee20*rxn20+Ee21*rxn21+Ee22*rxn22+Ee31*rxn31+Ee40*rxn40+Ee41*rxn41+Ee43*rxn43+Ee44*rxn44+Ee45*rxn45+Ee46*rxn46+Ee47*rxn47+Ee50*rxn50+Ee51*rxn51+Ee52*rxn52+Ee53*rxn53+Ee54*rxn54+Ee55*rxn55+Ee56*rxn56+Ee60*rxn60+Ee61*rxn61+Ee62*rxn62+Ee65*rxn65+Ee66*rxn66+Ee67*rxn67+Ee68*rxn68+Ee69*rxn69+Ee70*rxn70+Ee71*rxn71+Ee72*rxn72+Ee73*rxn73+Ee74*rxn74+Ee75*rxn75+Ee76*rxn76+Ee81*rxn81+Ee90*rxn90+Ee95*rxn95+Ee200*rxn200+Ee201*rxn201+Ee202*rxn202+Ee203*rxn203+Ee204*rxn204+Ee205*rxn205+Ee206*rxn206+Ee207*rxn207+Ee208*rxn208+Ee300*rxn300+Ee301*rxn301+Ee302*rxn302+Ee303*rxn303+Ee304*rxn304+Ee305*rxn305+Ee306*rxn306+Ee307*rxn307	Total electron energy losses per rxn#

	+Ee308*rxn308+Ee400*rxn400+Ee401*rxn401+Ee402*rxn402+Ee403*rxn403+Ee404*rxn404+Ee405*rxn405+Ee406*rxn406+Ee407*rxn407+Ee408*rxn408+Ee500*rxn500+Ee501*rxn501+Ee502*rxn502+Ee503*rxn503+Ee504*rxn504+Ee505*rxn505+Ee506*rxn506+Ee507*rxn507+Ee508*rxn508)	
D1s3	D1	Diffusion: Ar-metastable state ($1s_3$)
D1s5	D1	Diffusion: Ar-metastable state ($1s_5$)
D1s2	0	Diffusion: Ar-resonance state ($1s_2$)
D1s4	0	Diffusion: Ar-resonance state ($1s_4$)
x1s2	w1s2/M1/(w1/M1+w1s2/M1+w1s3/M1+w1s4/M1+w1s5/M1+w2/M2+w2a/M2+w2b/M2+w3/M3+w3D/M3+w4/M4+w5/M5+w6/M6)	Mole Fraction: Ar-resonance state ($1s_2$)
x1s3	w1s3/M1/(w1/M1+w1s2/M1+w1s3/M1+w1s4/M1+w1s5/M1+w2/M2+w2a/M2+w2b/M2+w3/M3+w3D/M3+w4/M4+w5/M5+w6/M6)	Mole Fraction: Ar-metastable state ($1s_3$)
x1s4	w1s4/M1/(w1/M1+w1s2/M1+w1s3/M1+w1s4/M1+w1s5/M1+w2/M2+w2a/M2+w2b/M2+w3/M3+w3D/M3+w4/M4+w5/M5+w6/M6)	Mole Fraction: Ar-resonance state ($1s_4$)
x1s5	w1s5/M1/(w1/M1+w1s2/M1+w1s3/M1+w1s4/M1+w1s5/M1+w2/M2+w2a/M2+w2b/M2+w3/M3+w3D/M3+w4/M4+w5/M5+w6/M6)	Mole Fraction: Ar-metastable state ($1s_5$)
w1s2o	x1s2o*M1/(x1o*M1+x1s2o*M1+x1s3o*M1+x1s4o*M1+x1s5o*M1+x2o*M2+x2ao*M2+x2bo*M2+x3o*M3+x3Do*M3+x4o*M4+x5o*M5+x6o*M6)	Initial Mass Fraction: Ar-resonance state ($1s_2$)
w1s3o	x1s3o*M1/(x1o*M1+x1s2o*M1+x1s3o*M1+x1s4o*M1+x1s5o*M1+x2o*M2+x2ao*M2+x2bo*M2+x3o*M3+x3Do*M3+x4o*M4+x5o*M5+x6o*M6)	Initial Mass Fraction: Ar-metastable state ($1s_3$)
w1s4o	x1s4o*M1/(x1o*M1+x1s2o*M1+x1s3o*M1+x1s4o*M1+x1s5o*M1+x2o*M2+x2ao*M2+x2bo*M2+x3o*M3+x3Do*M3+x4o*M4+x5o*M5+x6o*M6)	Initial Mass Fraction: Ar-resonance state ($1s_4$)
w1s5o	x1s5o*M1/(x1o*M1+x1s2o*M1+x1s3o*M1+x1s4o*M1+x1s5o*M1+x2o*M2+x2ao*M2+x2bo*M2+x3o*M3+x3Do*M3+x4o*M4+x5o*M5+x6o*M6)	Initial Mass Fraction: Ar-metastable state ($1s_5$)
ng1s2	w1s2*rho/M1	Neutral Mass Density: $1s_2$
ng1s3	w1s3*rho/M1	Neutral Mass Density: $1s_3$
ng1s4	w1s4*rho/M1	Neutral Mass Density: $1s_4$
ng1s5	w1s5*rho/M1	Neutral Mass Density: $1s_5$
srxn1s2	-(gammaAr)*w1s2*rho*vbar1/4	$1s_2$/Surface – Quenching Reaction
srxn1s3	-(gammaAr)*w1s3*rho*vbar1/4	$1s_3$/Surface – Quenching Reaction
srxn1s4	-(gammaAr)*w1s4*rho*vbar1/4	$1s_4$/Surface – Quenching Reaction
srxn1s5	-(gammaAr)*w1s5*rho*vbar1/4	$1s_5$/Surface – Quenching Reaction
k200	2.5*10^-15*Te^0.74*exp(-11.56/Te)	Reaction Rate Constant for $1s_2$ species
k201	4.3*10^-16*Te^0.74	"
k202	6.8*10^-15*Te^0.67*exp(-4.2/Te)	"
k203	3.43568*10^-14*exp(-(4.1633*10^-17)/Te)*(1/Te)^0.04	"
k204	1.0307*10^-13*exp(-0.105/Te)*(1/Te)^0.04	"
k205	3.43568*10^-14*exp((2.498*10^-16)/Te)*(1/Te)^0.04	"
k206	3.43568*10^-14*exp(-0.204/Te)*(1/Te)^0.04	"

k207	3.43568*10^-14*exp((-3.33067*10^-16)/Te)*(1/Te)^0.04	“
k208	2.06141*10^-14*exp(-0.28/Te)*(1/Te)^0.04	“
k209	5*10^-16	“
k210	5*10^-16	“
k211	5*10^-16	“
k212	5*10^-16	“
rxn200	k200*ne*ng1	Reaction Rate Expression for $1s_2$ species
rxn201	k201*ne*ng1s2	“
rxn202	k202*ne*ng1s2	“
rxn203	k203*ne*ng1s2	“
rxn204	k204*ne*ng1s3	“
rxn205	k205*ne*ng1s2	“
rxn206	k206*ne*ng1s4	“
rxn207	k207*ne*ng1s2	“
rxn208	k208*ne*ng1s5	“
rxn209	k209*ng1s2*ng1s2	“
rxn210	k210*ng1s2*ng1s3	“
rxn211	k211*ng1s2*ng1s4	“
rxn212	k212*ng1s2*ng1s5	“
k400	2.5*10^-15*Te^0.74*exp(-11.56/Te)	Reaction Rate Constant for $1s_4$ species
k401	4.3*10^-16*Te^0.74	“
k402	6.8*10^-15*Te^0.67*exp(-4.2/Te)	“
k403	3.43568*10^-14*exp(-0.204/Te)*(1/Te)^0.04	“
k404	3.43568*10^-14*exp((2.498*10^-16)/Te)*(1/Te)^0.04	“
k405	1.14523*10^-14*exp(-.099/Te)*(1/Te)^0.04	“
k406	5.72613*10^-14*exp((1.249*10^-16)/Te)*(1/Te)^0.04	“
k407	3.43568*10^-13*exp((-9.71445*10^-17)/Te)*(1/Te)^0.04	“
k408	2.06141*10^-13*exp(-0.075/Te)*(1/Te)^0.04	“
k409	5*10^-16	“
k410	5*10^-16	“
k411	5*10^-16	“
k412	5*10^-16	“
rxn400	k400*ne*ng1	Reaction Rate Expression for $1s_4$ species
rxn401	k401*ne*ng1s4	“
rxn402	k402*ne*ng1s4	“
rxn403	k403*ne*ng1s4	“
rxn404	k404*ne*ng1s2	“
rxn405	k405*ne*ng1s4	“

rxn406	k406*ne*ng1s3	“
rxn407	k407*ne*ng1s4	“
rxn408	k408*ne*ng1s5	“
rxn409	k409*ng1s4*ng1s2	“
rxn410	k410*ng1s4*ng1s3	“
rxn411	k411*ng1s4*ng1s4	“
rxn412	k412*ng1s4*ng1s5	“
k300	2.5*10^-15*Te^0.74*exp(-11.56/Te)	Reaction Rate Constant for $1s_3$species
k301	4.3*10^-16*Te^0.74	“
k302	6.8*10^-15*Te^0.67*exp(-4.2/Te)	“
k303	1.0307*10^-13*exp(-0.105/Te)*(1/Te)^0.04	“
k304	3.43568*10^-14*exp((-4.16334*10^-17)/Te)*(1/Te)^0.04	“
k305	5.72613*10^-14*exp((1.249*10^-16)/Te)*(1/Te)^0.04	“
k306	1.14523*10^-14*exp(-.099/Te)*(1/Te)^0.04	“
k307	3.43568*10^-14*exp((2.498*10^-16)/Te)*(1/Te)^0.04	“
k308	6.87135*10^-15*exp(-0.175/Te)*(1/Te)^0.04	“
k309	5*10^-16	“
k310	5*10^-16	“
k311	5*10^-16	“
k312	5*10^-16	“
k313	2.30E-21	“
rxn300	k300*ne*ng1	Reaction Rate Expression for $1s_3$species
rxn301	k301*ne*ng1s3	“
rxn302	k302*ne*ng1s3	“
rxn303	k303*ne*ng1s3	“
rxn304	k304*ne*ng1s2	“
rxn305	k305*ne*ng1s3	“
rxn306	k306*ne*ng1s4	“
rxn307	k307*ne*ng1s3	“
rxn308	k308*ne*ng1s5	“
rxn309	k309*ng1s3*ng1s2	“
rxn310	k310*ng1s3*ng1s3	“
rxn311	k311*ng1s3*ng1s4	“
rxn312	k312*ng1s3*ng1s5	“
rxn313	k313*ng1s3*ng1	“
k500	2.5*10^-15*Te^0.74*exp(-11.56/Te)	Reaction Rate Constant for $1s_5$species
k501	4.3*10^-16*Te^0.74	“
k502	6.8*10^-15*Te^0.67*exp(-4.2/Te)	“

k503	2.06141*10^-14*exp(-0.28/Te)*(1/Te)^0.04	“
k504	3.43568*10^-14*exp((-3.33067*10^-16)/Te)*(1/Te)^0.04	“
k505	6.87135*10^-15*exp(-0.175/Te)*(1/Te)^0.04	“
k506	3.43568*10^-14*exp((2.498*10^-16)/Te)*(1/Te)^0.04	“
k507	2.06141*10^-13*exp(-0.075/Te)*(1/Te)^0.04	“
k508	3.43568*10^-13*exp((-9.71445*10^-17)/Te)*(1/Te)^0.04	“
k509	5*10^-16	“
k510	5*10^-16	“
k511	5*10^-16	“
k512	5*10^-16	“
k513	2.30E-21	“
rxn500	k500*ne*ng1	“
rxn501	k501*ne*ng1s5	“
rxn502	k502*ne*ng1s5	“
rxn503	k503*ne*ng1s5	“
rxn504	k504*ne*ng1s2	“
rxn505	k505*ne*ng1s5	“
rxn506	k506*ne*ng1s3	“
rxn507	k507*ne*ng1s5	“
Ee200	11.828	Electron Energy Loss per Rxn#
Ee201	-11.828	“
Ee202	3.772	“
Ee203	-0.105	“
Ee204	0.105	“
Ee205	-0.204	“
Ee206	0.204	“
Ee207	-0.28	“
Ee208	0.28	“
Ee400	11.624	“
Ee401	-11.624	“
Ee402	3.976	“
Ee403	0.204	“
Ee404	-0.204	“
Ee405	0.099	“
Ee406	-0.099	“
Ee407	-0.075	“
Ee408	0.075	“
Ee300	11.723	“

Ee301	-11.723	“
Ee302	3.877	“
Ee303	0.105	“
Ee304	-0.105	“
Ee305	-0.099	“
Ee306	0.099	“
Ee307	-0.175	“
Ee308	0.175	“
Ee500	11.548	“
Ee501	-11.548	“
Ee502	4.052	“
Ee503	0.28	“
Ee504	-0.28	“
Ee505	0.175	“
Ee506	-0.175	“
Ee507	0.075	“
Ee508	-0.075	“
A1s2	5.1e8	Einstein Transition Probability: 1s$_2$
A1s4	1.19e8	Einstein Transition Probability: 1s$_4$
ko1s2	(2.1*10^-17)*3*A1s2*ng1/(11.828^3)/sqrt(T)/100^3	(ko1s2*R) = optical depth for 1s$_2$
ko1s4	(2.1*10^-17)*3*A1s4*ng1/(11.624^3)/sqrt(T)/100^3	(ko1s4*R) = optical depth for 1s$_4$
a1s2	A1s2*(1+(3.225*10^-14)*3*ng1/(100^3)/11.828^3)*(4.839*10^-9)/(sqrt(T)*11.828)	Damping Coefficient: 1s$_2$
a1s4	A1s4*(1+(3.225*10^-14)*3*ng1/(100^3)/11.624^3)*(4.839*10^-9)/(sqrt(T)*11.624)	Damping Coefficient: 1s$_4$
TD1s2	1/(100*ko1s2*.1*sqrt(3.14*log(100*.1*ko1s2)))	Transmission Coeff. for Doppler Broadening: 1s$_2$
TD1s4	1/(100*ko1s4*.1*sqrt(3.14*log(100*.1*ko1s4)))	Transmission Coeff. for Doppler Broadening: 1s$_4$
TC1s2	sqrt(a1s2/(sqrt(3.14)*100*.1*ko1s2))	Transmission Coeff. for Collisional Broadening: 1s$_2$
TC1s4	sqrt(a1s4/(sqrt(3.14)*100*.1*ko1s4))	Transmission Coeff. for Collisional Broadening: 1s$_4$
TCD1s2	2*a1s2/(3.14*sqrt(log(100*.1*ko1s2)))	Coeff. for Collisional & Doppler Broadening: 1s$_2$
TCD1s4	2*a1s4/(3.14*sqrt(log(100*.1*ko1s4)))	Coeff. for Collisional & Doppler Broadening: 1s$_4$
Escape1s2	1.9*TD1s2*exp(-3.14*TCD1s2^2/4/TC1s2^2)+1.3*TC1s2*erf(sqrt(3.14)*TCD1s2/2/TC1s2)	Escape Factor: 1s$_2$
Escape1s4	1.9*TD1s4*exp(-3.14*TCD1s4^2/4/TC1s4^2)+1.3*TC1s4*erf(sqrt(3.14)*TCD1s4/2/TC1s4)	Escape Factor: 1s$_4$

rxn1s2decay	A1s2*Escape1s2*ng1s2	Radiative Decay Reaction Rate: $1s_2$
rxn1s4decay	A1s4*Escape1s4*ng1s4	Radiative Decay Reaction Rate: $1s_4$

E.2 Constants

Table E.2 Constants defined in COMSOL^{TM}: ArMSR ICP Model

Constant	Value	Definition
x1s2o	0	Initial Mole Fraction: Ar-resonance state 1s2
x1s3o	0	Initial Mole Fraction: Ar-metastable state 1s3
x1s4o	0	Initial Mole Fraction: Ar- resonance state 1s4
x1s5o	0	Initial Mole Fraction: Ar-metastable state 1s3
gammaAr	1	Ar-metastable/Surface Quenching Probability

E.3 Subdomain Expressions

Table E.3 Subdomain Expressions defined in COMSOL^{TM}: ArMSR ICP Model

Variable	Expressions	Definition
r1	M1*(cerxn1+cerxn1a+cerxn1b+cerxn2+cerxn3+cerxn6+cerxn7+cerxn8-rxn1-rxn2-rxn3-rxn4-rxn5-rxn6-rxn300+rxn301+rxn309+rxn310+rxn311+rxn312+rxn313-rxn500+rxn501+rxn509+rxn510+rxn511+rxn512+rxn513-rxn200+rxn201+rxn209+rxn210+rxn211+rxn212-rxn400+rxn401+rxn409+rxn410+rxn411+rxn412+rxn1s2decay+rxn1s4decay)	Ar neutral – source term: Generation minus Loss
r1s2	M1*(rxn200-rxn201-rxn202-rxn203+rxn204-rxn205+rxn206-rxn207+rxn208-rxn209-rxn210-rxn211-rxn212+rxn403-rxn404-rxn409+rxn303-rxn304-rxn309+rxn503-rxn504-rxn509-rxn1s2decay)	Ar $1s_2$ – source term: Generation minus Loss
r1s3	M1*(rxn300-rxn301-rxn302-rxn303+rxn304-rxn305+rxn306-rxn307+rxn308-rxn309-rxn310-rxn311-rxn312-rxn313+rxn203-rxn204-rxn210+rxn405-rxn406-rxn410+rxn505-rxn506-rxn510)	Ar $1s_3$ – source term: Generation minus Loss
r1s4	M1*(rxn400-rxn401-rxn402-rxn403+rxn404-rxn405+rxn406-rxn407+rxn408-rxn409-rxn410-rxn411-rxn412+rxn205-rxn206-rxn211+rxn305-rxn306-rxn311+rxn507-rxn508-rxn511-rxn1s4decay)	Ar $1s_4$ – source term: Generation minus Loss
r1s5	M1*(rxn500-rxn501-rxn502-rxn503+rxn504-rxn505+rxn506-rxn507+rxn508-rxn509-rxn510-rxn511-rxn512-rxn513+rxn207-rxn208-rxn212+rxn407-rxn408-rxn412+rxn307-rxn308-rxn312)	Ar $1s_5$ – source term: Generation minus Loss

Appendix F:
Matlab^{TM} scripts for the ArM ICP model

The Matlab^{TM} scripts required to run the ArM simulation are provided in this Appendix; they are modified from the original ICP model to include the new Ar-metastable specie. Scripts are located in the "ICPScripts_ArMetastables" folder. The pdep.m, pdepdataexchange.m, regulargridcoordinates.m, and results.m are original files. Modifications are only made in the run_ArO2.m and iter_ArO2 files. See the dissertation of Hsu[48] for the user guides.

runArO2.m

```
%Directory to save the solution files
parentdirectory = 'E:\Monica\';

%input # of iterations....
iteration1=3;

%Input Fresh Start OR Iterations, dd=1 for fresh start, dd=2 for iterations
dd = 1;

%Input Directory Name
a = '20080808_SimTest';

b = 'cd ';
c = horzcat([b parentdirectory a]);
cc = horzcat([parentdirectory a]);

    mkdir(parentdirectory,a);
   eval(c)
   addpath(cc)

 times = linspace(0,3e-2,20);

if dd == 1
   tic
   q = iteration1;

   counter = 0;
   d = num2str(counter);
   e = 'iter';
   f = horzcat([e d]);

   disp('Initializing FEM')
   fem.sol = asseminit(fem);
   fem0 = fem;
   flsave(f,'fem')

   counter = counter +1
   d = num2str(counter);  %number to string, p. 11-14
   e = 'iter';
   f = horzcat([e d]);

%Tracks how the value at the chamber center changes over iterations
rr(counter,1) = postinterp(fem,'Te',[0.099/2; 0.105]);  % Te
rr(counter,2) = postinterp(fem,'ni1',[0.099/2; 0.105/2]);  % ni1, Ar+
rr(counter,3) = postinterp(fem,'ni2',[0.099/2; 0.105/2]);  % ni2, O2+
rr(counter,4) = postinterp(fem,'ni3',[0.099/2; 0.105/2]);  % ni3, O+
rr(counter,5) = postinterp(fem,'ni3neg',[0.099/2; 0.105/2]);  % ni3neg, O-
rr(counter,11) = postinterp(fem,'Eth',[0.099/2; 0.105]);  % Eth
rr(counter,12) = postinterp(fem,'u',[0.099/2; 0.105/2]);  % u
rr(counter,13) = postinterp(fem,'v',[0.099/2; 0.105/2]);  % v
rr(counter,14) = postinterp(fem,'p',[0.099/2; 0.105/2]);  % p
rr(counter,15) = postinterp(fem,'T',[0.099/2; 0.105/2]);  % T
```

```
rr(counter,16) = postinterp(fem,'w2',[0.099/2; 0.105/2]);  % w2, O2
rr(counter,17) = postinterp(fem,'w2a',[0.099/2; 0.105/2]);  % w2a, O2a
rr(counter,18) = postinterp(fem,'w2b',[0.099/2; 0.105/2]);  % w2b, O2b
rr(counter,19) = postinterp(fem,'w3',[0.099/2; 0.105/2]);  % w3, O
rr(counter,20) = postinterp(fem,'w3D',[0.099/2; 0.105/2]);  % w3D, OD
rr(counter,21) = postinterp(fem,'w1m',[0.099/2; 0.105/2]);  % w1m, Ar ms
```

%Start solving by Femlab

%Solve for neutral uvpT

```
disp('Start Solving....')
   [fem.sol, stop] = femnlin(fem, ...
                'init',fem0.sol, ...
                'solcomp',{'u','v','p','T'}, ...
                'outcomp',{'u','v','p','T','w1m','w2','w3','w2a','w2b','w3D','Eth','Te','ni1','ni2','ni3','ni3neg'}, ...
                'ntol',1E-6, ...
                'maxiter',150, ...
                'nonlin','on', ...
                'hnlin','off', ...
                'out',{'sol' 'stop'});
   t(counter,1) = toc/3600

   if stop == 1
      save('stopped','t','fem')
      break
   end

   flsave(f,'fem')
   save(f,'t')
```

%Solve for neutral composition

```
   [fem.sol, stop] = femnlin(fem, ...
                'init',fem.sol, ...
                'solcomp',{'w1m','w2','w3','w2a','w2b','w3D'}, ...
                'outcomp',{'u','v','p','T','w1m','w2','w3','w2a','w2b','w3D','Eth','Te','ni1','ni2','ni3','ni3neg'}, ...
                'ntol',1E-6, ...
                'maxiter',150, ...
                'nonlin','on', ...
                'hnlin','off', ...
                'out',{'sol' 'stop'});
        t(counter,2) = toc/3600

   if stop == 1
      save('stopped','t','fem')
      break
   end

   flsave(f,'fem')
   save(f,'t')
```

%Solve for Eth

```
   [fem.sol, stop] = femlin(fem, ...
             'init',fem.sol, ...
             'solcomp',{'Eth'}, ...
```

```
            'outcomp',{'u','v','p','T','w1m','w2','w3','w2a','w2b','w3D','Eth','Te','ni1','ni2','ni3','ni3neg'}, ...
            'out',{'sol' 'stop'});
   t(counter,3) = toc/3600

   if stop == 1
      save('stopped','t','fem')
      break
   end

   regulargridcoordinates
   pdepdataexchange

   disp('Int P=')
   postint(fem,'2*pi*r*P','Edim',2,'Dl',1)
   disp('Int Pdep, Before=')
   postint(fem,'2*pi*r*Pdep','Edim',2,'Dl',1)
   pdepdataexchange
   disp('Int Pdep, After=')
   postint(fem,'2*pi*r*Pdep','Edim',2,'Dl',1)

   flsave(f,'fem')
   save(f,'t','pdepdata')
```

%Solve for Te and charge species

```
   [fem.sol, stop] = femtime(fem, ...
            'init',fem.sol, ...
            'solcomp',{'ni1','ni2','ni3','ni3neg','Te'}, ...
            'outcomp',{'u','v','p','T','w1m','w2','w3','w2a','w2b','w3D','Eth','Te','ni1','ni2','ni3','ni3neg'}, ...
            'tlist',times, ...
            'tout','tlist', ...
            'out',{'sol' 'stop'});
   t(counter,4) = toc/3600

   if stop == 1
      save('stopped','t','fem')
      break
   end

   flsave(f,'fem')
   save(f,'t','pdepdata')
```

%Plot the ne profile

```
     hold on
     postcrossplot(fem,1,[0 0.1;0.025 0.025],'lindata','ne','cont','on','solnum',1)
     drawnow
```

%Tracks how the value at the chamber center changes over iterations

```
rr(counter+1,1) = postinterp(fem,'Te',[0.099/2; 0.105]);  % Te
rr(counter+1,2) = postinterp(fem,'ni1',[0.099/2; 0.105/2]);  % ni1
rr(counter+1,3) = postinterp(fem,'ni2',[0.099/2; 0.105/2]);  % ni2
rr(counter+1,4) = postinterp(fem,'ni3',[0.099/2; 0.105/2]);  % ni3
rr(counter+1,5) = postinterp(fem,'ni3neg',[0.099/2; 0.105/2]);  % ni3neg
rr(counter+1,11) = postinterp(fem,'Eth',[0.099/2; 0.105]);  % Eth
rr(counter+1,12) = postinterp(fem,'u',[0.099/2; 0.105/2]);  % u
rr(counter+1,13) = postinterp(fem,'v',[0.099/2; 0.105/2]);  % v
```

```
rr(counter+1,14) = postinterp(fem,'p',[0.099/2; 0.105/2]);  % p
rr(counter+1,15) = postinterp(fem,'T',[0.099/2; 0.105/2]);  % T
rr(counter+1,16) = postinterp(fem,'w2',[0.099/2; 0.105/2]);  % w2
rr(counter+1,17) = postinterp(fem,'w2a',[0.099/2; 0.105/2]);  % w2a
rr(counter+1,18) = postinterp(fem,'w2b',[0.099/2; 0.105/2]);  % w2b
rr(counter+1,19) = postinterp(fem,'w3',[0.099/2; 0.105/2]);  % w3
rr(counter+1,20) = postinterp(fem,'w3D',[0.099/2; 0.105/2]);  % w3D
rr(counter+1,21) = postinterp(fem,'w1m',[0.099/2; 0.105/2]);  % w1m

   flsave(f,'fem')
   save(f,'t','pdepdata','rr')
   counter = counter + 1
   fem0 = fem;
```

%Start iteration

```
   for i = 1:q
      iter_ArO2
      counter = counter + 1
      % plot ne
      hold on
      postcrossplot(fem,1,[0 0.1;0.025 0.025],'lindata','ne','cont','on','solnum',1)
      drawnow
   end
end
```

%Start Iteration

```
if dd == 2
   counter = input('Set "counter" at?');
    q = iteration1;
   fem0 = fem;

   for i = 1:q
      iter_ArO2
      counter = counter + 1
      % plot ni1
      hold on
      postcrossplot(fem,1,[0 0.1;0.025 0.025],'lindata','ne','cont','on','solnum',1)
      drawnow
   end

end
```

%Add Label to each rr column

```
results
save(f,'t','pdepdata','rr','result')
```

iter_ArO2.m

```
tic

d = num2str(counter);
e = 'iter';
f = horzcat([e d]);

%Solves one iteration for plasma model
[fem.sol, stop] = femnlin(fem, ...
                'init',fem0.sol, ...
                'solcomp',{'u','v','p','T'}, ...
                'outcomp',{'u','v','p','T','w1m','w2','w3','w2a','w2b','w3D','Eth','Te','ni1','ni2','ni3','ni3neg'}, ...
                'ntol',1E-6, ...
                'maxiter',150, ...
                'nonlin','on', ...
                'hnlin','off', ...
                'out',{'sol' 'stop'});
   t(counter,1) = toc/3600

   if stop == 1
      save('stopped','t','fem')
      break
   end

   flsave(f,'fem')
   save(f,'t')

   [fem.sol, stop] = femnlin(fem, ...
                'init',fem.sol, ...
                'solcomp',{'w1m','w2','w3','w2a','w2b','w3D'}, ...
                'outcomp',{'u','v','p','T','w1m','w2','w3','w2a','w2b','w3D','Eth','Te','ni1','ni2','ni3','ni3neg'}, ...
                'ntol',1E-6, ...
                'maxiter',150, ...
                'nonlin','on', ...
                'hnlin','off', ...
                'out',{'sol' 'stop'});
   t(counter,2) = toc/3600

   if stop == 1
      save('stopped','t','fem')
      break
   end

   flsave(f,'fem')
   save(f,'t')

   [fem.sol, stop] = femlin(fem, ...
             'init',fem.sol, ...
             'solcomp',{'Eth'}, ...
             'outcomp',{'u','v','p','T','w1m','w2','w3','w2a','w2b','w3D','Eth','Te','ni1','ni2','ni3','ni3neg'}, ...
             'out',{'sol' 'stop'});
   t(counter,3) = toc/3600

   if stop == 1
```

```
      save('stopped','t','fem')
      break
   end

   pdepdataexchange

   disp('Int P=')
   postint(fem,'2*pi*r*P','Edim',2,'Dl',1)
   disp('Int Pdep, Before=')
   postint(fem,'2*pi*r*Pdep','Edim',2,'Dl',1)
   pdepdataexchange
   disp('Int Pdep, After=')
   postint(fem,'2*pi*r*Pdep','Edim',2,'Dl',1)

   flsave(f,'fem')
   save(f,'t','pdepdata')

   [fem.sol, stop] = femtime(fem, ...
            'init',fem.sol, ...
            'solcomp',{'ni1','ni2','ni3','ni3neg','Te'}, ...
            'outcomp',{'u','v','p','T','w1m','w2','w3','w2a','w2b','w3D','Eth','Te','ni1','ni2','ni3','ni3neg'}, ...
            'tlist',times, ...
            'tout','tlist', ...
            'out',{'sol' 'stop'});
   t(counter,4) = toc/3600

   if stop == 1
      save('stopped','t','fem')
      break
   end

   flsave(f,'fem')
   save(f,'t','pdepdata')
```

%Tracks how values change over iterations

```
rr(counter+1,1) = postinterp(fem,'Te',[0.099/2; 0.105]);  % Te
rr(counter+1,2) = postinterp(fem,'ni1',[0.099/2; 0.105/2]);  % ni1
rr(counter+1,3) = postinterp(fem,'ni2',[0.099/2; 0.105/2]);  % ni2
rr(counter+1,4) = postinterp(fem,'ni3',[0.099/2; 0.105/2]);  % ni3
rr(counter+1,5) = postinterp(fem,'ni3neg',[0.099/2; 0.105/2]);  % ni3neg
rr(counter+1,11) = postinterp(fem,'Eth',[0.099/2; 0.105]);  % Eth
rr(counter+1,12) = postinterp(fem,'u',[0.099/2; 0.105/2]);  % u
rr(counter+1,13) = postinterp(fem,'v',[0.099/2; 0.105/2]);  % v
rr(counter+1,14) = postinterp(fem,'p',[0.099/2; 0.105/2]);  % p
rr(counter+1,15) = postinterp(fem,'T',[0.099/2; 0.105/2]);  % T
rr(counter+1,16) = postinterp(fem,'w2',[0.099/2; 0.105/2]);  % w2
rr(counter+1,17) = postinterp(fem,'w2a',[0.099/2; 0.105/2]);  % w2a
rr(counter+1,18) = postinterp(fem,'w2b',[0.099/2; 0.105/2]);  % w2b
rr(counter+1,19) = postinterp(fem,'w3',[0.099/2; 0.105/2]);  % w3
rr(counter+1,20) = postinterp(fem,'w3D',[0.099/2; 0.105/2]);  % w3D
rr(counter+1,21) = postinterp(fem,'w1m',[0.099/2; 0.105/2]);  % w1m

    flsave(f,'fem')
   save(f,'t','pdepdata','rr')
   fem0 = fem;
```

Appendix G:
Matlab^{TM} scripts for the ArMSR ICP model

The Matlab^{TM} scripts are modified from the original ICP model to include the $1s_2$, $1s_3$, $1s_4$, and $1s_5$ species. Scripts are located in the "ICPScripts_ArMSR" folder. The pdep.m, pdepdataexchange.m, and regulargridcoordinates.m are original files. Modifications are only made in the run_ArO2.m, iter_ArO2.m and results.m files. See the dissertation of Hsu[48] for the user guides.

```
%Directory to save the solution files
parentdirectory = 'E:\Monica\';

%input # of iterations....
iteration1=10;

%Input Fresh Start OR Iterations, dd=1 for fresh start, dd=2 for iterations
dd = 1;

%Input Directory Name
a = '20090205_Test2_ArMSR_1mT_20Wexp';

b = 'cd ';
c = horzcat([b parentdirectory a]);
cc = horzcat([parentdirectory a]);

    mkdir(parentdirectory,a);
    eval(c)
    addpath(cc)


times = linspace(0,3e-2,20);

if dd == 1
    tic
    q = iteration1;

    counter = 0;
    d = num2str(counter);
    e = 'iter';
    f = horzcat([e d]);

    disp('Initializing FEM')
    fem.sol = asseminit(fem);
    fem0 = fem;
    flsave(f,'fem')

    counter = counter +1
    d = num2str(counter);  %number to string, p. 11-14
    e = 'iter';
    f = horzcat([e d]);

%Tracks how the value at the chamber center changes over iterations
rr(counter,1) = postinterp(fem,'Te',[0.099/2; 0.105]);  % Te
rr(counter,2) = postinterp(fem,'ni1',[0.099/2; 0.105/2]);  % ni1, Ar+
rr(counter,3) = postinterp(fem,'Eth',[0.099/2; 0.105]);  % Eth
rr(counter,4) = postinterp(fem,'u',[0.099/2; 0.105/2]);  % u
rr(counter,5) = postinterp(fem,'v',[0.099/2; 0.105/2]);  % v
rr(counter,6) = postinterp(fem,'p',[0.099/2; 0.105/2]);  % p
rr(counter,7) = postinterp(fem,'T',[0.099/2; 0.105/2]);  % T
rr(counter,8) = postinterp(fem,'w1s2',[0.099/2; 0.105/2]);  % w1m, Ar R
rr(counter,9) = postinterp(fem,'w1s3',[0.099/2; 0.105/2]);  % w1m, Ar ms
rr(counter,10) = postinterp(fem,'w1s4',[0.099/2; 0.105/2]);  % w1m, Ar R
rr(counter,11) = postinterp(fem,'w1s5',[0.099/2; 0.105/2]);  % w1m, Ar ms
```

%Start solving by Femlab

%Solve for neutral uvpT

```
disp('Start Solving....')
   [fem.sol, stop] = femnlin(fem, ...
               'init',fem0.sol, ...
               'solcomp',{'u','v','p','T'}, ...
               'outcomp',{'u','v','p','T','w1s2','w1s3','w1s4','w1s5','Eth','Te','ni1'}, ...
               'ntol',1E-6, ...
               'maxiter',150, ...
               'nonlin','on', ...
               'hnlin','off', ...
               'out',{'sol' 'stop'});
   t(counter,1) = toc/3600

   if stop == 1
      save('stopped','t','fem')
      break
   end

   flsave(f,'fem')
   save(f,'t')
```

%Solve for neutral composition

```
   [fem.sol, stop] = femnlin(fem, ...
               'init',fem.sol, ...
               'solcomp',{'w1s2','w1s3','w1s4','w1s5'}, ...
               'outcomp',{'u','v','p','T','w1s2','w1s3','w1s4','w1s5','Eth','Te','ni1'}, ...
               'ntol',1E-6, ...
               'maxiter',150, ...
               'nonlin','on', ...
               'hnlin','off', ...
               'out',{'sol' 'stop'});
         t(counter,2) = toc/3600

   if stop == 1
      save('stopped','t','fem')
      break
   end

   flsave(f,'fem')
   save(f,'t')
```

%Solve for Eth

```
   [fem.sol, stop] = femlin(fem, ...
            'init',fem.sol, ...
            'solcomp',{'Eth'}, ...
            'outcomp',{'u','v','p','T','w1s2','w1s3','w1s4','w1s5','Eth','Te','ni1'}, ...
            'out',{'sol' 'stop'});
   t(counter,3) = toc/3600

   if stop == 1
      save('stopped','t','fem')
      break
   end
```

```
   regulargridcoordinates
   pdepdataexchange

   disp('Int P=')
   postint(fem,'2*pi*r*P','Edim',2,'Dl',1)
   disp('Int Pdep, Before=')
   postint(fem,'2*pi*r*Pdep','Edim',2,'Dl',1)
   pdepdataexchange
   disp('Int Pdep, After=')
   postint(fem,'2*pi*r*Pdep','Edim',2,'Dl',1)

   flsave(f,'fem')
   save(f,'t','pdepdata')
```

%Solve for Te and charge species

```
   [fem.sol, stop] = femtime(fem, ...
            'init',fem.sol, ...
            'solcomp',{'ni1','Te'}, ...
            'outcomp',{'u','v','p','T','w1s2','w1s3','w1s4','w1s5','Eth','Te','ni1'}, ...
            'tlist',times, ...
            'tout','tlist', ...
            'out',{'sol' 'stop'});
   t(counter,4) = toc/3600

   if stop == 1
      save('stopped','t','fem')
      break
   end

   flsave(f,'fem')
   save(f,'t','pdepdata')
```

%Plot the ne profile

```
      hold on
      postcrossplot(fem,1,[0 0.1;0.025 0.025],'lindata','ne','cont','on','solnum',1)
      drawnow
```

%Tracks how the value at the chamber center changes over iterations

```
rr(counter+1,1) = postinterp(fem,'Te',[0.099/2; 0.105]);  % Te
rr(counter+1,2) = postinterp(fem,'ni1',[0.099/2; 0.105/2]);  % ni1
rr(counter+1,3) = postinterp(fem,'Eth',[0.099/2; 0.105]);  % Eth
rr(counter+1,4) = postinterp(fem,'u',[0.099/2; 0.105/2]);  % u
rr(counter+1,5) = postinterp(fem,'v',[0.099/2; 0.105/2]);  % v
rr(counter+1,6) = postinterp(fem,'p',[0.099/2; 0.105/2]);  % p
rr(counter+1,7) = postinterp(fem,'T',[0.099/2; 0.105/2]);  % T
rr(counter+1,8) = postinterp(fem,'w1s2',[0.099/2; 0.105/2]);  % w2
rr(counter+1,9) = postinterp(fem,'w1s3',[0.099/2; 0.105/2]);  % w2a
rr(counter+1,10) = postinterp(fem,'w1s4',[0.099/2; 0.105/2]);  % w2b
rr(counter+1,11) = postinterp(fem,'w1s5',[0.099/2; 0.105/2]);  % w3

   flsave(f,'fem')
   save(f,'t','pdepdata','rr')
   counter = counter + 1
   fem0 = fem;
```

```
 %Start iteration
    for i = 1:q
       iter_ArO2
       counter = counter + 1
       % plot ne
       hold on
       postcrossplot(fem,1,[0 0.1;0.025 0.025],'lindata','ne','cont','on','solnum',1)
       drawnow
   end
end

%Start Iteration
if dd == 2
   counter = input('Set "counter" at?');
    q = iteration1;
   fem0 = fem;

   for i = 1:q
       iter_ArO2
       counter = counter + 1
       % plot ni1
       hold on
       postcrossplot(fem,1,[0 0.1;0.025 0.025],'lindata','ne','cont','on','solnum',1)
       drawnow
   end

end

%Add Label to each rr column
results
save(f,'t','pdepdata','rr','result')
```

iter_ArO2.m

```
tic

d = num2str(counter);
e = 'iter';
f = horzcat([e d]);

%Solves one iteration for plasma model
[fem.sol, stop] = femnlin(fem, ...
                'init',fem0.sol, ...
                'solcomp',{'u','v','p','T'}, ...
                'outcomp',{'u','v','p','T','w1s2','w1s3','w1s4','w1s5','Eth','Te','ni1'}, ...
                'ntol',1E-6, ...
                'maxiter',150, ...
                'nonlin','on', ...
                'hnlin','off', ...
                'out',{'sol' 'stop'});
   t(counter,1) = toc/3600

   if stop == 1
      save('stopped','t','fem')
      break
   end

   flsave(f,'fem')
   save(f,'t')

   [fem.sol, stop] = femnlin(fem, ...
                'init',fem.sol, ...
                'solcomp',{'w1s2','w1s3','w1s4','w1s5'}, ...
                'outcomp',{'u','v','p','T','w1s2','w1s3','w1s4','w1s5','Eth','Te','ni1'}, ...
                'ntol',1E-6, ...
                'maxiter',150, ...
                'nonlin','on', ...
                'hnlin','off', ...
                'out',{'sol' 'stop'});
   t(counter,2) = toc/3600

   if stop == 1
      save('stopped','t','fem')
      break
   end

   flsave(f,'fem')
   save(f,'t')

   [fem.sol, stop] = femlin(fem, ...
             'init',fem.sol, ...
             'solcomp',{'Eth'}, ...
             'outcomp',{'u','v','p','T','w1s2','w1s3','w1s4','w1s5','Eth','Te','ni1'}, ...
             'out',{'sol' 'stop'});
   t(counter,3) = toc/3600

   if stop == 1
```

```
    save('stopped','t','fem')
    break
  end

  pdepdataexchange

  disp('Int P=')
  postint(fem,'2*pi*r*P','Edim',2,'Dl',1)
  disp('Int Pdep, Before=')
  postint(fem,'2*pi*r*Pdep','Edim',2,'Dl',1)
  pdepdataexchange
  disp('Int Pdep, After=')
  postint(fem,'2*pi*r*Pdep','Edim',2,'Dl',1)

  flsave(f,'fem')
  save(f,'t','pdepdata')

  [fem.sol, stop] = femtime(fem, ...
            'init',fem.sol, ...
            'solcomp',{'ni1','Te'}, ...
            'outcomp',{'u','v','p','T','w1s2','w1s3','w1s4','w1s5','Eth','Te','ni1'}, ...
            'tlist',times, ...
            'tout','tlist', ...
            'out',{'sol' 'stop'});
  t(counter,4) = toc/3600

  if stop == 1
    save('stopped','t','fem')
    break
  end

  flsave(f,'fem')
  save(f,'t','pdepdata')
```

%Tracks how values change over iterations

```
rr(counter+1,1) = postinterp(fem,'Te',[0.099/2; 0.105]);  % Te
rr(counter+1,2) = postinterp(fem,'ni1',[0.099/2; 0.105/2]);  % ni1
rr(counter+1,3) = postinterp(fem,'Eth',[0.099/2; 0.105]);  % Eth
rr(counter+1,4) = postinterp(fem,'u',[0.099/2; 0.105/2]);  % u
rr(counter+1,5) = postinterp(fem,'v',[0.099/2; 0.105/2]);  % v
rr(counter+1,6) = postinterp(fem,'p',[0.099/2; 0.105/2]);  % p
rr(counter+1,7) = postinterp(fem,'T',[0.099/2; 0.105/2]);  % T
rr(counter+1,8) = postinterp(fem,'w1s2',[0.099/2; 0.105/2]);  % w2
rr(counter+1,9) = postinterp(fem,'w1s3',[0.099/2; 0.105/2]);  % w2a
rr(counter+1,10) = postinterp(fem,'w1s4',[0.099/2; 0.105/2]);  % w2b
rr(counter+1,11) = postinterp(fem,'w1s5',[0.099/2; 0.105/2]);  % w3


  flsave(f,'fem')
  save(f,'t','pdepdata','rr')
  fem0 = fem;
```

results.m

```
[rrm rrn]=size(rr);

result(1,:)={'Te' 'ni1' 'Eth' 'u' 'v' 'p' 'T' 'w1s2' 'w1s3' 'w1s4' 'w1s5'};

for i=2:rrm+1
   for j=1:rrn
      result{i,j}=rr(i-1,j);
   end
end
```

References

[1] ITRS, 2009 ed. (ITRS, 2009).

[2] M. A. Lieberman and A. J. Lichtenberg, *Principles of Plasma Discharges and Materials Processing*, 2nd ed. (Wiley, New York, 2005).

[3] M. Kameyama, M. McCallum, and S. Owa, *Evolution of Wavelength Shrinkage in Lithography*, **7281**. 2009 SPIE conference proceedings.

[4] L. Capodieci, *From Optical Proximity Correction to Lithography-Driven Physical Design (1996-2006): 10 years of Resolution Enhancement Technology and the roadmap enablers for the next decade*, **6154**. 2006 SPIE conference proceedings.

[5] S. Englemann, R. L. Bruce, T. Kwon, R. Phaneuf, G. S. Oehrlein, Y. C. Bae, C. Andes, D. Graves, D. Nest, E. A. Hudson, P. Lazzeri, E. Iacob, and M. Anderle, J. Vac. Sci. Technol. A **25,** 1353 (2007).

[6] D. Nest, T. Y. Chung, D. B. Graves, S. Engelmann, R. L. Bruce, F. Weilnboeck, G. Oehrlein, D. Wang, C. Andes, and E. Hudson, Plasma Processes and Polymers **6,** 649 (2009).

[7] E. Pargon, M. Martin, K. Menguelti, L. Azarnouche, J. Foucher, and O. Joubert, Appl. Phys. Letters **94,** 103111 (2009).

[8] A. Bazin, E. Pargon, X. Mellahoui, D. Perret, B. Mortini, and O. Joubert, in *Impact of HBr and Ar cure plasma treatments on 193nm photoresists*, **6923**. 2008 SPIE conference proceedings.

[9] H.-W. Kim, J.-Y. Lee, J. Shin, S.-G. Woo, H.-K. Cho, and J. T. Moon, IEEE Trans. Electron. Devices **51,** 1984 (2004).

[10] D. Nest, D. B. Graves, S. Engelmann, R. L. Bruce, F. Weilnboeck, G. S. Oehrlien, C. Andes, and E. A. Hudson, Appl. Phys. Letters **92,** 153113 (2008).

[11] E. Pargon, K. Menguelti, M. Martin, A. Bazin, O. Chaix-Pluchery, C. Sourd, S. Derrough, T. Lill, and O. Joubert, J. Appl. Phys. **105,** 094902-1 (2009).

[12] M. Sumiya, R. Bruce, S. Engelmann, F. Weilnboeck, and G. S. Oehrlein, J. Vac. Sci. Technol. B **26,** 1637 (2008).

[13] M. J. Titus, D. Nest, T. Y. Chung, and D. Graves, J. Phys. D: Applied Physics **42,** 152001 (2009).

[14] L. Berry, H. Maynard, P. Miler, T. Moore, M. Pendley, V. Resta, D. Sparks, and Q. Yang, J. Vac. Sci. Technol. A **18,** 2806 (2000).

[15] M. A. Sobolewski, J. Vac. Sci. Technol. A **24,** 1892 (2006).

[16] M. D. Baker, F. R. Williams, and G. S. May, IEEE Trans.Semi. Manuf. **11,** 254 (1998).

[17] T. F. Edgar, S. W. Butler, and W. J. Campbell, Automatica **36,** 1567 (2000).

[18] J. J. Moslehi, R. A. Chapman, M. Wong, and e. al, IEEE Trans. Electron. Devices **39,** 4 (1992).

[19] M. Freed, M. Druger, C. J. Spanos, and P. Kameshwar, IEEE Trans.Semi. Manuf. **14,** 255 (2001).

[20] T. E. Benson, L. I. Kamlet, and S. M. Ruegsegger, J. Vac. Sci. Technol. B **14,** 483 (1995).

[21] P. Klimecky, C. Garvin, and C. G. Glarza, J. Electrochem. Soc. **148,** C35 (2001).

[22] J. J. Chambers, K. Min, and G. N. Parsons, J. Vac. Sci. Technol. B **16,** 2996 (1998).

[23] V. Jacobsen, B. Menges, R. Forch, S. Mittler, and W. Knoll, Thin Solid Films **409,** 185 (2002).

[24] M. Freed, M. Kruger, K. Poola, and C. J. Spanos, IEEE Trans.Semi. Manuf. **18,** 148 (2005).

[25] N. S. J. Braithwaite, J. P. Booth, and G. Cunge, Plasma Sources Sci. Technol. **5,** 677 (1996).

[26] J. W. Coburn and M. Chen, J. of Appl. Phys. **5,** 3134 (1980).

[27] H. Singh and D. B. Graves, J. Appl. Phys. **87,** 4098 (2000).

[28] E. J. Tonnis and D. B. Graves, J. Vac. Sci. Technol. A **20,** 1787 (2002).

[29] M. J. Titus, C.-C. Hsu, and D. Graves, J. Vac. Sci. Technol. A **28,** 139 (2009).

[30] S. Vallon, O. Joubert, L. Vallier, F. Ferrieu, B. Drevillon, and N. Blayo, J. Vac. Sci. Technol. A **15,** 865 (1997).

[31] S. J. Hon and S. M. Gary, IEEE Trans. Industrial Electronics **52,** 1063 (2005).

[32] E. A. Rying, M. C. Ozturk, G. L. Bilbro, and J. Lu, IEEE Trans. Semi. Manuf. **18,** 112 (2005).

[33] C. C. Hsu, M. J. Titus, and D. B. Graves, J. Vac. Sci. Technol. A **25** 607 (2007).

[34] K. Pangal and J. C. Sturm, *Correlation of Plasma-Induced Charging Voltage Measured In-Situ by Microelectromechanical Sensors with Device Degradation*, 1997.

[35] M. Schulze, A. Yangua-Gil, A. v. Keudell, and P. Awakowicz, J. Phys. D: Applied Physics **41,** 065206 (2008).

[36] M. J. Titus, D. Nest, and D. B. Graves, Applied Physics Letters **94,** 171501 (2009).

[37] I. C. Abraham, J. R. Woodworth, M. E. Riley, P. A. Miller, and R. J. Shul, J. Vac. Sci. Technol. B **21,** 1112 (2003).

[38] V. A. Godyak, R. B. Piejak, and B. M. Alexandrovich, Plasma Sources Sci. Technol. **1,** 36 (1992).

[39] Y.-M. Ling, J. Phys. D **39,** 3305 (2006).

[40] M. J. Sowa, M. G. Blain, R. L. Jarecki, and J. E. Stevens, Appl. Phys. Letters **80,** 932 (2002).

[41] Y. Ishikawa, Y. Katoh, M. Okigama, and S. Samukawa, J. Vac. Sci. Technol. A **23,** 1509 (2005).

[42] T. W. Kim and E. S. Aydil, IEEE Trans. Plasma Sci. **30,** 120 (2002).

[43] T. W. Kim and E. S. Aydil, Plasma Sources Sci. Technol. **12,** 148 (2003).

[44] T. W. Kim, S. J. Ullal, V. Vahedi, and E. S. Aydil, Review of Scientific Instruments **73,** 3494 (2002).

[45] V. Loryuenyong, Thesis, University of California, Berkeley, 2006.

[46] Z. S. Luo, Thesis, University of California, Berkeley, 2005.

[47] M. Kiehlbauch and D. B. Graves, J. Vac. Sci. Technol. A **21,** 660 (2003).

[48] C.-C. Hsu, Thesis, University of California, Berkeley, 2006.

[49] V. Vahedi, Thesis, University of California, Berkeley, 1993.

[50] M. A. Sobloewski, J. K. Olthoff, and Y. Wang, J. of Appl. Phys. **85,** 3966 (1999).

[51] M. A. Sobolewski, Phys. Rev. E **62,** 8540 (2000).

[52] S. Kuhn, K.-U. Riemann, N. Jelic, D. D. Tskhakaya, D. J. Tskhakaya, and M. Stanojevic, Phys. of Plasmas **13,** 013503 (2006).

[53] J. P. Chang, A. P. Mahorowala, and H. H. Sawin, J. Vac. Sci. Technol. A **16,** 217 (1998).

[54] J. J. Vegh, Thesis, University of California, Berkeley, 2007.

[55] J. O. Choi, J. A. Moore, J. C. Corelli, J. P. Silverman, and H. Bakhru, J. Vac. Sci. Technol. B **6,** 2286 (1988).

[56] S. Engelmann, R. L. Bruce, M. Sumiya, T. Kwon, R. Phaneuf, G. S. Oehrlein, C. Andes, D. Graves, D. Nest, and E. A. Hudson, J. Vac. Sci. Technol. B **27,** 92 (2009).

[57] L. Ling, X. Hua, X. Li, G. S. Oehrlein, E. A. Hudson, P. Lazzeri, and M. Anderle, J. Vac. Sci. and Technol. B **22,** 2594 (2004).

[58] M. Padmanaban, E. Alemy, R. Dammel, W. K. Kim, T. Kudo, S. H. Lee, D. Rahman, W. L. Chen, R. M. Sadjadi, W. Livesay, and M. Ross, J. of Photopolymer Sci. and Technol. **15,** 1521 (2002).

[59] H. Singh, Thesis, University of California, Berkeley, 2000.

[60] F. F. Chen, Phys. Plasmas **8,** 3029 (2001).

[61] F. F. Chen, J. D. Evans, and D. Arnush, Phys. Plasmas **9,** 1449 (2002).

[62] D. Nest, Thesis, University of California, Berkeley, 2009.

[63] E. Rosa, *Photometric Units and Nomenclature*, Vol. 6 (Department of Commerce and Labor, Washington Government Printing Office, 1910) p 543-572.

[64] R. Piejak, V. Godyak, B. Alexandrovich, and N. Tishchenko, Plasma Sources Sci. Technol. **7,** 590 (1998).

[65] M. A. Sobolewski and J.-H. Kim, J. Appl. Phys. **102,** 113302-1 (2007).

[66] D. Barton, J. W. Bradley, K. J. Gibson, D. A. Steele, and R. D. Short, J. Phys. Chem. **104,** 7150 (2000).

[67] T. Yunogami, T. Mizutani, K. Suzuki, and S. Nishimatsu, Japanese J. Appl. Phys. **28,** 2172 (1989).

[68] S. Samukawa, Y. Ishikawa, S. Kumagai, and M. Okigawa, Japanese J. Appl. Phys. **40,** 1346 (2001).

[69] G. A. Hebner and P. A. Miller, J. Appl. Phys. **87,** 8304 (2000).

[70] A. Hatta, J. Light Vis. Env. **29,** 79 (2005).

[71] Y. Tanaka, A. S. Jursa, and F. LeBlanc, J. Chem. Phys. **26,** 862 (1957).

[72] F. Truica-Marasescu and M. R. Wertheimer, J. Appl. Polymer Sci. **91,** 3886 (2003).

[73] Y. K. Pu, Z. G. Guo, Z. D. Kang, J. Ma, Z. C. Guan, G. Y. Zhang, and E. G. Wang, Pure Appl. Chem. **74,** 459 (2002).

[74] J. R. Woodworth, M. E. Riley, V. A. Amatucci, T. W. Hamilton, and B. P. Aragon, J. Vac. Sci. Technol. A **19,** 45 (2000).

[75] A. Durandet, O. Joubert, J. Pelletier, and M. Pichot, J. of Appl. Phys. **67,** 3862 (1989).

[76] T. Jasinski and S. Kang, J. Vac. Sci. Technol. A **10,** 1065 (1992).

[77] H. Kersten, H. Deutsch, H. Steffen, G. M. W. Kroesen, and R. Hippler, Surf. Eng., Surf. Instr. Vac. Technol. **63,** 385 (2001).

[78] D. Tretheway and E. Aydil, J. Electrochem. Soc. **143,** 3674 (1996).

[79] D. Kim and D. J. Economou, IEEE Trans. Plasma Sci. **30,** 2048 (2003).

[80] V. M. Donnelly and M. V. Malyshev, Appl. Phys. Letters **77,** 2467 (2000).

[81] M. W. Kiehlbauch, Thesis, University of California, Berkeley, 2001.

[82] C. Lee, D. B. Graves, M. A. Lieberman, and D. W. Hess, J. Electrochem. Soc. **141,** 1546 (1994).

[83] S. Gomez, P. G. Steen, and W. G. Graham, Appl. Phys. Letters **81,** 19 (2002).

[84] E. S. Aydil and D. J. Economou, J. Electrochem. Soc. **140,** 1471 (1993).

[85] Y.-R. Luo, in *CRC Handbook of Chemistry and Physics*, 88th ed. (CRC Press/Taylor Francis, Baton Roca, 2008).

[86] I. C. Abraham, J. R. Woodworth, M. E. Riley, P. A. Miller, T. W. Hamilton, and B. P. Aragon, J. Vac. Sci. Technol. A **20,** 1759 (2002).

[87] E. A. Edelberg, A. Perry, N. Benjamin, and E. S. Aydil, J. Vac. Sci. Technol. A **17,** 506 (1998).

[88] J. R. Woodworth, I. C. Abraham, M. E. Riley, P. A. Miller, T. W. Hamilton, B. P. Aragon, R. J. Shul, and C. G. Willison, J. Vac. Sci. Technol. A **20,** 873 (2002).

89 S.-B. Wang and A. E. Wendt, IEEE Trans. Plasma Sci. **27,** 1358 (1999).

90 E. A. Edelberg and E. S. Aydil, J. Appl. Phys. **86,** 4799 (1999).

91 T. E. Nitschke, Thesis, University of California, Berkeley, 1995.

92 A. C. Fozza, A. Kruse, A. Hollander, A. Ricard, and M. R. Wertheimer, J. Vac. Sci. Technol. A **16,** 72 (1998).

93 M. R. Wertheimer, A. C. Fozza, and A. Hollander, Nuclear Instruments and Methods in Physics Research B **151,** 65 (1999).

94 G. E. Morfill, T. Shimizu, B. Steffes, and H.-U. Schmidt, New Journal of Physics **11,** 115019 (2009).

95 F. E. Truica-Marasescu and M. R. Wertheimer, Macromolecular Chemistry and Physics **206,** 744 (2005).

96 J. Kim, Y. S. Chae, W. S. Lee, J. W. Shon, C. J. Kang, W. S. Han, and J. T. Moon, J. Vac. Sci. Technol. B **21,** 790 (2003).

97 M. C. Kim, D. Shamiryan, Y. Jung, W. Boullart, C. J. Kang, and H. K. Cho, J. Vac. Sci. Technol. A **24,** 2645 (2006).

98 E. Sarantopoulou, J. Kovac, Z. Kollia, I. Raptis, S. Kobe, and A. C. Cefalas, Surface and Interface Analysis **40,** 400 (2008).

99 J. J. Vegh, D. Nest, D. B. Graves, R. Bruce, S. Engelmann, T. Kwon, R. J. Phaneuf, G. S. Oehrlein, B. K. Long, and C. G. Wilson, Appl. Phys. Letters **91,** 233113 (2007).

100 V. E. Skurat and Y. I. Dorofeev, Die Angewandte Makromolekulare Chemie **216,** 205 (1994).

101 V. Skurat, Nuclear Instruments and Methods in Physics Research B **208,** 27 (2003).

102 M. Schwell, H.-W. Jochims, H. Baumgartel, F. Dulieu, and S. Leach, Planetary and Space Science **54,** 1073 (2006).

103 M. Suto, X. Wang, and L. C. Lee, J. Phys. Chem. **92,** 3764 (1988).

104 T. Adam and R. Zimmermann, Anal. Bioanal Chem. **389,** 1941 (2007).

105 N. Negishi, H. Takesue, M. Sumiya, T. Yoshida, Y. Momonoi, and M. Izawa, J. Vac. Sci. Technol. B **23,** 217 (2005).

106 X. Hua, S. Engelmann, G. S. Oehrlein, P. Jiang, P. Lazzeri, E. Iacob, and M. Anderle, J. Vac. Sci. Technol. B **24,** 1850 (2006).

107 A. P. Mahorowala, K. J. Chen, R. Sooriyakumaran, A. Clancy, D. Murthy, and S. Rasgon, in *Line edge roughness reduction by plasma curing photoresists*, **5753,** 2005 SPIE conference proceedings.

108 K. Takeda, H. Asahara, T. Hanawa, K. Tsujita, H. Okumura, and N. Hishinuma, J. Photopolymer Sci. Technol. **16,** 511 (2003).

109 Y. Koval, J. Vac. Sci. Technol. B **22,** 843 (2004).

110 J. J. Vegh, D. Nest, D. B. Graves, R. Bruce, s. Engelmann, T. Kwon, R. J. Phaneuf, G. S. Oehrlein, B. K. Long, and C. G. Willson, J. Appl. Phys. **104,** 034308-1 (2008).

[111] J. A. R. Samson, *Techniques of Vacuum Ultraviolet Spectroscopy* (John Wiley & Sons, Inc., 1967).

[112] M. J. Titus, D. Nest, and D. B. Graves, J. Phys. D. FTC **42,** 152001 (2009).

[113] J. M. Yu, X. M. Tao, H. Y. Tam, and M. S. Demokan, Appl. Surf. Sci. **252,** 1283 (2005).

[114] S. Beauvois, D. Renaut, R. Lazzaroni, L. D. Laude, and J. L. Bredas, Appl. Surf. Sci. **109,** 218 (1997).

[115] E. Kesters, M. Claes, Q. T. Le, M. Lux, A. Franquet, G. Vereecke, P. W. Mertens, M. M. Frank, R. Carleer, P. Adriaensens, J. J. Biebuyk, and S. Bebelman, Thin Solid Films **516,** 3454 (2008).

[116] D. R. McKenzie, D. Muller, and B. A. Pailthorpe, Phys. Rev. Letters **67,** 773 (1991).

[117] O. Tsuda, M. Ishihara, Y. Koga, S. Fujiwara, Y. Setsuhara, and N. Sato, J. Phys. Chem. B **109,** 4917 (2005).

[118] M. Weiler, S. Sattel, T. Giessen, K. Jung, and H. Ehrhardt, Phys. Rev. B **53,** 1594 (1996).

[119] H. Coufal, H. F. Winters, and H. L. Bay, Phys. Rev. B: Condensed Matter **44,** 4747 (1991).

[120] J. Chai, F. Lu, B. Li, and K. D. Y., Langmuir **20,** 10919 (2004).

[121] M. J. Titus and D. B. Graves, J. Vac. Sci. Technol. A **26,** 1154 (2008).

[122] S. K. Basu, A. M. Bergstreser, L. F. Francis, L. E. Scriven, and A. V. McCormick, J. Appl. Phys. **98,** 063507 (2005).

[123] R. Huang, J. of Mech. and Phys. of Solids **53,** 63 (2005).

[124] R. Huang and S. H. Im, Phys. Rev. E **74,** 026214 (2006).

[125] R. Huang and Z. Suo, J. of App. Phys. **91,** 1135 (2001).

[126] Z. Huang, W. Hong, and Z. Suo, Phys. Rev. E **70,** 030601 (2004).

[127] P.-C. Lin and S. Yang, Appl. Phys. Letters **90,** 241903 (2007).

[128] C. M. Stafford, B. D. Vogt, C. Harrison, D. Julthongpiput, and R. Huang, Macromolecules **36,** 5095 (2006).

[129] S. H. Im and R. Huang, J. Appl. Mech. **72,** 955 (2005).

[130] R. L. Bruce, F. Weilnboeck, T. Lin, R. Phaneuf, G. Oehrlein, B. K. Long, C. G. Willson, J. J. Vegh, D. Nest, and D. Graves, (submitted 2009).

[131] N. Sharma, V. K. Sharma, and K. N. Tripathi, Optics and Lasers in Engineering **46,** 514 (2008).

[132] I. W. Gilmour, A. Trainor, and R. N. Haward, J. Appl. Poly. Sci. **23,** 3129 (1979).

[133] L. Singh, P. J. Ludovice, and C. L. Henderson, in *Influence of Film Thickness, Molecular Weight, and Substrate on the Physical Properties of Photoresist Polymer Thin Films*, **5039**. 2003 SPIE conference proceedings.

[134] P. Mason, Polymer Degradation and Stability **12,** 625 (1964).

[135] A. R. Shultz, P. I. Roght, and G. B. Rathmann, J. Polymer Science **22,** 495 (1956).

[136] W. Knappe and O. Yamamoto, Kolloid-Z. u.Z. Polymere **240,** 775 (1970).

[137] D. J. T. Hill and J. H. O'Donnell, J. Chem. Education **58,** 174 (1981).

[138] H. N. Subrahmanyam and S. V. Subramanyam, Polymer **28,** 1331 (1987).

[139] S. Ashida, C. Lee, and M. A. Lieberman, J. Vac. Sci. Technol. A. **13,** 2498 (1995).

[140] A. Bogaerts and R. Gijbels, Phys. Rev. A **52,** 3743 (1995).

[141] M. W. Kiehlbauch and D. Graves, J. Appl. Phys. **91,** 3539 (2002).

[142] M.-H. Lee, S.-H. Jang, and C.-W. Chung, Phys. Plasmas **13,** 053502-1 (2006).

[143] T. Sato and T. Makabe, J. Appl. Phys. **98,** 113304-1 (2005).

[144] A. Bogaerts, R. Gijbels, and J. Vlcek, J. Appl. Phys. **84,** 121 (1998).

[145] V. O. Papanyan, G. T. Nerisisyan, S. A. Ter-Avetisyan, and F. K. Tittel, J. Phys. B: Mol. Opt. Phys. **28,** 807 (1995).

[146] G. A. Hebner, J. Appl. Phys. **80,** 2624 (1996).

[147] S. Gorchakov, D. Loffhagen, and D. Uhrlandt, Phys. Rev. E **74** 066401 (2006).